Trinity College Dublin
Coláiste na Tríonóide, Baile Átha Cliath
The University of Dublin

DEVELOPMENT OF A PREDICTIVE MAINTENANCE SOLUTION FOR A PUMP-AS-TURBINE HYDROPOWER SYSTEM

CALVIN STEPHEN

Thesis submitted for the fulfilment of the requirements for the
Degree of Doctor of Philosophy in Engineering
to the University of Dublin, Trinity College

March 2026

Supervisor: Prof. Aonghus McNabola

Co-Supervisor: Prof. Biswajit Basu

Department of Civil, Structural & Environmental Engineering,
University of Dublin, Trinity College, Dublin

Declaration

I declare that this thesis has not been submitted as an exercise for a degree at this or any other university and it is entirely my own work.

I agree to deposit this thesis in the University's open access Institutional repository or allow the library to do so on my behalf, subject to the Irish Copyright Legislation and Trinity College Library conditions of use and acknowledgements.

I consent to the examiner retaining a copy of the thesis beyond the examination period, should they so wish (EU GDPR May 2018).

Date: *04 / 03 / 2026*

Signed:

(Calvin Stephen)

Abstract

The increasing demand for reliable and cost-effective small-scale hydropower systems, alongside the evolving dynamics of renewable energy integrated electric grids, has led to a growing adoption of Pump-as-Turbine (PAT) systems. While PATs offer economic and operational advantages over conventional turbines, their practical deployment is often hindered by insufficient research into their operation and maintenance, particularly regarding hydrodynamic failures such as cavitation. This PhD research addresses this gap through the development of a predictive maintenance system tailored for PAT-based micro-hydropower systems, with a strong emphasis on the detection and diagnosis of cavitation.

The study pursued four core objectives: numerical analysis of cavitation in PATs using Computational Fluid Dynamics (CFD), experimental investigations of PAT vibration responses under cavitating flows, evaluation of the suitability of Machine Learning (ML) models in cavitation diagnosis and the development of a software platform to integrate the findings of the study. CFD simulations revealed that cavitation onset varies between design and off-design conditions, and it evolves through four distinct stages, influencing PAT performance differently depending on the flow regime. Experimental investigations confirmed the narrow safe operating range of PATs and led to the development of a modified Deviation from Normal Distribution (DND) method for real-time cavitation detection, adapted from gearbox monitoring techniques.

In the machine learning domain, Decision Trees (DT), Artificial Neural Networks (ANN) and Support Vector Machines (SVM) were assessed, with ANN achieving the highest prediction accuracy and DT being competitive while offering greater interpretability. A hybrid ANN-DT model was proposed to balance predictive performance with interpretability of predictions to improve transparency of decisions and trust in ML methods. These models alongside other findings from the study were embedded in a modular software platform built in MATLAB App Designer, structured according to ISO 13374:2003 and capable of time and frequency domain analysis for accurate cavitation classification.

The developed system significantly enhances the operational reliability and sustainability of PAT-based micro-hydropower by enabling proactive maintenance through digital diagnostics. The outcomes of this research not only contribute new knowledge to the field of PAT operation and condition monitoring but also advance the digitalization of hydropower, supporting global efforts to build resilient, intelligent and sustainable energy infrastructure.

Acknowledgements

First and foremost, I would like to express my sincere gratitude to my academic supervisor, Professor Aonghus McNabola, for his unwavering guidance and support throughout this research journey. His patience, encouragement and belief in my potential were instrumental in helping me achieve this milestone. His prompt feedback, expert and his friendly demeanour made working with him both enjoyable enriching. The lessons I have learnt under his supervision will continue to guide me well beyond the PhD.

I am equally grateful to my co-supervisor, Professor Biswajit Basu, whose intellectual brilliance and thoughtful guidance were vital in shaping the direction of this work. His constructive feedback and support at key stages of the research were invaluable to its successful completion.

I extend my heartfelt thanks to the technical staff of the Department of Civil, Structural and Environmental Engineering, David McAuley, Robert Fitzpatrick and Michael Grimes, for their tremendous assistance during the experimental phase. Their readiness to help and patience in responding to my many requests created a supportive and pleasant working environment.

I would also like to acknowledge my colleague and friend, Madhavan Vasudevan, for his constant support, especially during the challenging COVID-19 period, when everything seemed to come to a standstill. His friendship and willingness to lend an ear to my frustrations meant more than words can express.

A very special thanks goes to my wonderful wife, Amogelang and our beautiful daughters Yamasa and Marang. Your love, understanding and emotional support have made this journey truly meaningful. I am grateful to my parents, sibling, uncles, aunts and cousins, each of you contributed in your own way to the achievement of this goal.

Finally, I would like to sincerely thank Trinity College Dublin's Provost Awards for the generous financial support that made this research possible.

Table of Contents

List of Figures

List of Tables

1. INTRODUCTION

This chapter gives an overview of the research topic, provides an explanation of the problem the thesis addresses, gives the purpose and objectives of the thesis and presents the research questions. It also outlines the scope and the limitations of the research and gives the outline of the thesis.

1.1. BACKGROUND TO THE RESEARCH

Global warming and climate change are some of the most significant challenges facing the whole world, as such there is a need for environmentally friendly and sustainable means of providing necessities. The world's major economies have developed and implemented policies that will aid in the reduction or slowing down of these global issues. The Intergovernmental Panel on Climate Change (IPCC) suggests that the emission of carbon dioxide (CO_2) and other greenhouse gases must be halved by 2050 to remain under the 2°C global warming limit [1]. This is in comparison with the 2019 levels. There is a need for radical action to combat this situation or else the world risks a difficult and costly future.

Renewable energy is one of the available means necessary to reduce the CO_2 and other greenhouse gas emissions hence slowing down the effects of climate change [2] as technologies such as hydropower, solar and wind are said to be preventing substantial CO_2 emissions and have been responsible for 11% of the world energy supply in 2019[3]. Of the available renewable energy technologies, hydropower is the most popular having supplied over 60% of all renewable energy generated in 2019, accounting for around 7% of the global world energy [3].

Hydropower technologies have evolved over the years catering for the society's concerns while contributing to the amount of energy generated through renewable means. This has given rise to realisation of many factors associated with hydropower technologies including environmental impacts of large hydropower plants, social and economic factors associated with such. However, the current scope for new large hydropower plants in Europe, the US or other parts of the developed world is limited due to challenges in complying with environmental legislation such as the water framework directive or nature restoration law among other factors. As such the focus for new hydropower has shifted to smaller scales and niche applications in the built rather than natural environment.

A boom in the hydropower industry was realised in the early 2000's when high income economies introduced some incentives to attract independent power producers to venture into renewable energy production means. In the United Kingdom for example, the government introduced feed-in tariffs (FITs) to promote the uptake of renewable and low carbon electricity generation in April 2010 [4].

As a result, there was an increased number of newly developed hydropower producers who wanted to take advantage of the scheme. Most of the developed plants consisted of large hydropower turbines which have been the basis for hydropower generation for years including Kaplan, Francis and Pelton. In recent years the FITs have been reducing in value as depicted by the decline in the UK's values from 23.39p/kWh in 2014 to 8.03p/kWh in 2019 [4].

As of April 2019, the UK government has since terminated the FIT scheme to new applicants [4], indicating that for existing FIT beneficiaries to take advantage of the scheme, low-cost hydropower turbines need to be taken advantage of. This kind of decline in FITs has forced a shift in the type of hydropower turbines used to maximize the possible returns. Small-scale micro-hydropower (MHP) usage has increased partly due to this and due to development of other application areas. MHP has been implemented on water supply networks, wastewater treatment plants, irrigation systems, alcohol breweries and underground mining [5].

Improving sustainability of water supplies has been a major subject of interest in recent years, especially with the fight to reduce the rate of climate change being prioritised. Sustainability of water supply is hindered by both increased energy consumption and carbon dioxide emissions of water treatment and supply processes [6]. As such, means of reducing these factors in water supply processes are appreciable.

Methods of reducing energy consumption in water treatment and water supply processes have been widely studied. This involves methods such as biogas capture for both heating and power needs [7], anaerobic bioreactors for energy production [8], waste heat recovery [9], energy efficient treatment processes [10, 11]) and harvesting of rainwater [12]. In addition to these methods, more relatively new methods are being investigated in literature.

The water sector and the energy sector form the most important water-energy nexus, where water supply requires energy and energy production requires water. However, the water industry has been deemed the 4th most energy intensive sector in the EU [13]. That being so, water sector can be attributed to considerable contributions to CO_2 emissions and climate change.

Reduction in the amount of energy consumed by water treatment and supply processes can lead to the reduction in the industry's carbon footprint. Most of the CO_2 emissions attributed to the water sector come from the use of fossil-based energy generation techniques which contribute most of the green-house gases in the atmosphere. Therefore, reducing mass consumption of energy by water treatment and supply processes will contribute to the reduction of carbon dioxide emissions associated with the water industry.

Pumping of water is the most energy intensive activity within water supply. With the possibility of recovering energy via the application of micro-hydro power technologies in water infrastructure on areas of high excess pressure, energy consumption from such activities can be minimised. Pumps-as-Turbine (PATs) offer that capability of energy recovery at low cost. They have been deemed the most economical option for energy recovery in micro or pico-hydropower applications across a wide range of heads and flows such as within water supply networks or in run-of-river schemes [14]. PATs offer a very low-cost alternative which is readily available in all sizes that can be required within the micro- or pico-hydropower scales. PAT cost competitiveness is valid up to around 300kW of which between 100-300kW there is an overlap in the potential turbine choices [15].

Other advantages include less complexity, mass production, availability for a wide range of heads and flows, shorter delivery times and availability in a variety of standard sizes [16]. One of the shortcomings of PATs is their efficiency which is lower than that of conventional turbines, however, this is typically only two or three percent [17] and its impact on the pay-back periods is very minimal for fixed flow rates. PATs also have limited regulation capability on their own which dents their suitability for energy generation, but the benefits they offer often outweigh these shortcomings.

1.2. PROBLEM DESCRIPTION

Pump manufacturers rarely supply the performance curves of pumps operating as turbines, but significant efforts have been made in recent years to characterize pump performance in turbine mode. Hence improving their potential and usability. However, PATs like any other hydraulic machines require regular maintenance, and maintenance problems are known to greatly reduce efficiency, with consequent environmental impacts. PATs operate in conditions for which the pump was not designed for, and the service life and maintenance requirements are as such unknown. Limited efforts have been made to address this problem hence creating a need to close this gap in literature.

Moving towards a less energy intensive, CO_2 free, smart and reliable water supply system requires a holistic approach to maintenance that will alleviate maintenance problems. One such approach to improving the efficiency of PATs and reducing their environmental impact is the implementation of predictive maintenance. This is the use of machine condition data to predict machinery failures and schedule for repairs before the failure occurs.

Despite hydropower's long-established role in the global energy mix, significant gaps remain in the digitalization and predictive maintenance of hydropower systems, particularly for small-scale and emerging technologies such as PAT systems. While large conventional hydro units are increasingly being integrated into digital frameworks across Europe as part of the energy transition, comprehensive digital solutions for condition monitoring, fault diagnosis and performance optimization are still lacking especially for micro- and pico- hydropower applications.

Recent initiatives in Europe have accelerated the development of predictive maintenance tools for large -scale hydroelectric facilities. However, these advances have yet to trickle down to smaller, distributed hydropower units. In the case of PATs, despite their rapid growth due to their affordability and ease of integration into existing infrastructure, have received limited attention in terms of smart diagnostics and automated anomaly detection. In a micro-hydropower system, PATs are the most critical component of the system, which means their loss to failure will halt energy generation immediately leading to a direct loss in revenue and a potential high-pressure loss of water if installed in pressurised systems. As such the adoption of predictive maintenance would safeguard against these eventualities.

Condition monitoring differs from one machine to another, as the operating environment plays a vital role in dictating the machine's dynamics. During operation of rotating machines in general, PATs included, unbalanced forces are generated, and their energies are released in the form of vibration. Bianchini et al. [18] stated that vibration is familiar as an effective condition monitoring parameter for these machines. In PATs, sources of vibration can be either mechanical or hydrodynamic in nature. For vibrations of mechanical nature, various reliable techniques for predictive maintenance have been developed over the years and can be generalised from one rotating machine to another. In contrast, vibrational response due to hydrodynamic sources such as cavitation, turbulence and pressure pulsations varies from one fluid machine to another due to the variety and complexity of the phenomena involved in the interaction between machine components and the flowing fluid [19], hence techniques for their predictive maintenance cannot be easily generalised to all types of fluid machines.

An understanding of hydrodynamic sources of vibration such as cavitation in PATs is important as it would aid in the design of effective predictive maintenance solutions. Alatorre-Frenk [20] explored the incidence of cavitation in PATs by comparing their critical Thoma number with that of conventional turbines and showed that cavitation is slightly worse in PATs than in conventional turbines of similar specific speed. This is an important finding that demonstrates the need for a detailed understanding of cavitation in PATs, a phenomenon that has not been deeply studied in literature, hence the need for the current work.

1.3. PURPOSE AND OBJECTIVES

This study aims to use signal processing techniques to develop and test a predictive maintenance system for PATs. Predictive maintenance has been lauded for bringing about material cost savings while increasing the equipment uptime. To take full advantage of this maintenance strategy, there is a need for the development of predictive maintenance systems that do not only consider mechanical causes of machine failure but also hydrodynamic causes. To achieve this, the following objectives were set to be completed in this thesis:

- To numerically investigate the necessary conditions for cavitation to occur in PATs and analyse the evolution of pressure pulsations resulting from cavitation.
- To experimentally study the vibration characteristics associated with cavitation in PATs and develop a real-time detection method using signal processing techniques.
- To evaluate and implement machine learning algorithms for the detection and diagnosis of cavitation in PATs.
- To develop a software platform that integrates experimental findings and Machine Learning-based analyses for predictive maintenance of PATs.

1.4. RESEARCH QUESTIONS

The research questions to be addressed in this PhD project are centred on the development of a predictive maintenance system for PATs that will ensure that faults due to hydrodynamics forces are taken into consideration. Four research questions were devised to help in meeting the aim:

Research Question 1 – What are the necessary conditions for cavitation to occur inside a PAT and how do pressure pulsations evolve as a result?
Research Question 2 – What vibration characteristics are indicative of cavitation in PATs and how can they be used to detect cavitation in real-time?
Research Question 3 – What Machine Learning algorithms are best suited for detecting and diagnosing cavitation in PATs?
Research Question 4 – How can results of the experimental and Machine Learning based analyses be integrated into a software platform for predictive maintenance of PATs?

1.5. SCOPE AND LIMITATIONS

The research focuses on the development of a predictive maintenance solution for operation, monitoring and maintenance of PATs. It proposes a strategy for fault detection and diagnostic using real-time monitoring of machine faut condition.

Limitations of the research include the following:

- This research focuses on the predictive maintenance of pico-scale PATs, and findings may not be directly transferable to larger-scale PATs or other types of hydraulic machines.

- The study is limited to cavitation as a representative fault in PATs and does not address other potential failure mechanisms, such as mechanical wear, flow induced vibrations or bearing failures.
- The numerical model used in this study approximates the real PAT system, as it was developed independently and may not capture all real-world complexities.
- The numerical simulations are subject to computational limitations such as mesh resolution, solver accuracy and processing power, which may impact the fidelity of the cavitation modelling.
- The accuracy and reliability of cavitation detection depend on the quality and sensitivity of the sensors used for vibration measurements. Any noise or inaccuracies in sensor data may affect the analysis
- The developed software platform is a prototype and may require further testing, validation and refinement before being integrated into industrial predictive maintenance systems.

To minimise these limitations, future research will focus on overcoming these limitations and enhancing the study's applicability.

1.6. OVERVIEW OF THE THESIS

This thesis develops a predictive maintenance solution for Pump-as-Turbine (PAT) hydropower systems, with a particular focus on cavitation detection and diagnosis. The work comprises eight chapters structured around three core activities advancing our understanding of i) cavitation, ii) cavitation detection and diagnosis, and iii) application. These three activities require linking numerical modelling, experimental investigation and practical implementation of developed algorithms in a software platform. Following herewith is an overview of each subsequent chapters of the thesis.

Chapter 2 – Theoretical Background to the Research

This chapter provides a comprehensive review of available knowledge around the main study topic of this thesis. It covers such areas as hydropower, pumps-as-turbine, common failure mechanisms in pumps and turbines, maintenance strategies, vibration-based signal analysis techniques and machine learning base fault classification techniques. Additionally, the analysed existing research on cavitation, PATs and vibration analysis highlight existing gaps.

Chapter 3 – Research Methodology

This chapter is brief and it presents the methodology adopted to achieve the study objective. It is divided into four short subsections covering research strategy, research model, description of the experimental test-rig and the method of study.

Chapter 4 – Numerical Analysis of Cavitation in PATs

This is the first chapter presenting the full results of the work conducted in this thesis. The focus of the chapter is in addressing the fundamental gap of how cavitation evolves in PATs. While cavitation is well studied in conventional turbines, PATs operate under reverse flow conditions and off-design regimes, meaning their cavitation characteristics cannot be assumed to follow that of pumps of a similar size or conventional turbines. Computational Fluid Dynamics simulations were developed to identify cavitation onset conditions, track cavitation evolution and analyse the resultant pressure pulsations and flow instabilities under design and off-design operation.

The numerical analysis is used to obtain an overview of the process evolution from 'no cavitation' conditions to '*full cavitation*' conditions. Consequently, physical insights into where cavitation forms, how it evolves and what operating conditions are most suitable for its occurrence were obtained. Also, an understanding of pressure pulsation characteristics associated with cavitation in PATs was developed, which directly informed what should be observable using vibration measurements.

Chapter 5 – Experimental Investigation and Detection of Cavitation in PATs

Building on the numerical analysis insights, the research moves to the experimental stage where a dedicated PAT test rig was used to study cavitation under controlled conditions. The key role of the experimental work was to validate the qualitative insights obtained from the numerical analysis and generate the necessary data for automating detection and diagnosis function using machine learning techniques. Vibration measurements were collected across a wide range of operating points, corresponding to three cavitation stages of '*no cavitation*', '*inception cavitation*' and '*full cavitation*'. Visual observations provided ground truth for validating these different cavitation stages.

Standard vibration metrics were shown to be insufficient for reliable cavitation detection in PATs. In response, a modified Deviation from Normal Distribution (DND) method was developed. This method quantifies how vibration signals deviate statistically from a '*no cavitation*' baseline as cavitation evolves. The experimental results demonstrated that cavitation in PATs produces repeatable statistical changes in vibration signals that could be monitored for detection purposes. The modified DND method was found to be reliable in the detection of cavitation and its severity as it progresses, making it suitable for real-time implementation in monitoring systems.

Chapter 6 – Fault Diagnosis and Application of Machine Learning Approaches

In this chapter, the analysis of experimental vibration data progressed to diagnosis and decision support using machine learning. Conventional frequency domain-based analysis of vibration signals to assess cavitation dependent frequency parameters is conducted resulting in no clear cavitation excited frequency components. This is extended with a development of a structured vibration feature framework, which is then used to train multiple machine learning models to classify cavitation severity.

The performance evaluation of the models reveals that ANNs provided high diagnostic accuracy while Decision Trees provide competitive diagnostic accuracy coupled with vivid interpretability of predictions. A hybrid ANN-Decision Tress diagnostic framework was proposed to achieve a balance between diagnostic accuracy and transparency in predictions.

Chapter 7 – Development of a Software Platform for Predictive Maintenance

The developed detection and diagnostic methods proposed in Chapters 5 and 6 were then integrated into a predictive maintenance software platform, developed in MATLAB and aligned with ISO 13374 standards. The platform brings together data acquisition, signal processing, cavitation detection, machine learning based diagnosis and health state visualisation.

The key role of this application focused work was to demonstrate that the research findings can be operationalised into a practical, industry-relevant predictive maintenance tool. So, rather than being separate studies each part of the thesis feeds directly into the next i.e., numerical simulations provided qualitative insights on the cavitation process, experiments converted these insights into detectable signals that quantify insights about the machine condition while machine learning added diagnostic intelligence. The software platform integrates these elements together into a robust predictive maintenance solution for PATs.

Chapter 8 – Conclusions and Future Work

Finally, Chapter 8 summarises the key findings of the thesis and discusses their implications. It also provides recommendations for future research and improvements in predictive maintenance of PATs.

2. THEORETICAL BACKGROUND TO THE STUDY

The chapter describes the state-of-the-art in research conducted around the study area. It is organised in such a way that general principles and the topic are first introduced; and more specific studies related to the study are then covered in-depth. It begins with an explanation of hydropower, different hydropower schemes and the various types of turbines used to convert available head into power. It then concentrates on PATs, their operation theory and performance characterization. Next, some common failure mechanisms in both pumps and turbines are studied leading to the description of cavitation and the cavitation modelling techniques in turbomachinery. The relevant literature that deals with cavitation are analysed identifying some gaps in literature that this thesis will address.

The next section provides a brief description of maintenance strategies for taking care of machinery covering reactive, preventive and predictive maintenance. Vibration analysis techniques are then covered with emphasis on time domain techniques and frequency domain techniques. This is linked to the study of cavitation in turbines and gaps identified that this thesis would deal with concentrating on the signal processing of the vibration data indicative of cavitation in PATs.

Lastly, the available fault diagnosis techniques are described with emphasis mostly being on machine learning approaches that consume the machine condition data and output a classification of the machine condition. The chapter end with a summary of the gaps identified in literature that are going to be addressed by this PhD thesis.

2.1. HYDROPOWER

Hydropower involves generating energy from the flow of water. Water in storage systems contains potential energy, which through the use of correct equipment and infrastructure can be transformed into other forms of energy. This potential energy can be transformed into mechanical energy through a turbine to drive other mechanical equipment. The driven equipment can be a generator, producing electricity as the output.

Hydroelectricity is categorised as a renewable means alongside such sources of energy as solar, wind, bioenergy and geothermal. It has been pointed out that hydropower is the most common and accepted forms of renewable energy with Kavadias & Apostolou [21] maintaining that over 16.5% of the world's electricity currently comes from hydropower, a figure that well surpasses the contribution of other renewable energy sources at 7.9% and that of nuclear energy at 10.6%.

At the forefront of global energy demand is the use of fossil fuel-based electricity with over 65% of the market share [21]. This raises a concern as this kind of electricity production technologies are detrimental to the environment having been associated with over 0.9 kg CO_2e/kWh of energy used in the water sector as compared to 0.1 kg CO_2e/kWh from nuclear and renewable energy sources [22]. Increasing the usage of hydropower can help offset CO_2e/kWh of energy used and Rothausen & Conway [23] found that a 20% decrease in emissions can be realised with an increased renewable energy usage.

There is a myriad of other advantages offered using hydropower to produce electricity. Such advantages include meeting peak load demands, frequency control and grid management, low cost as compared to fossil fuel-based sources, multipurpose usage and ability to be used as energy storage [24]. In a day the electricity demand curve has two peaks, one in the morning when everyone is getting ready to go to work and the other one in the evening when everyone is back home from work. At these times electricity demand is at its highest and it can surpass supply. It is at these times that hydropower becomes more useful as compared to other forms of energy as it can quickly respond to load changes [24] in comparison with other energy sources.

In circumstances where the demand surpasses the load and there is no feed in of additional power, the frequency of the supply drops to below acceptable limits resulting in a power cut to avoid damage to distribution systems. In this situation, Pandit & Thatte [24] note that hydropower capacity that is adequate can provide the required frequency control and grid steadying.

As compared to other sources of energy, hydropower has been deemed as a low-cost option. One would argue that solar energy and wind energy uses the resources that are abundantly available and therefore might be the cheapest option, but in fact the investment required to setup such energy sources coupled with payback periods makes them more costly. According to Pandit & Thatte [24], as of 2018, hydropower is considered the most economic source when looking at the scale of potential for development and use in comparison with other forms of renewable energy.

The dams used as potential energy storage for hydropower generation also serves other purposes such as flood control and water storage for irrigation [24]. This offers flexibility in their use based on the need. If the power demand is high water is released to drive the turbine which in turn drives a generator for electricity generation. And the same water can be used for other purposes. This elucidates the advantage it offers by being multipurpose.

Recently, there has been an increase in research in energy storage systems and hydropower is considered one of the few means that energy can be stored for future use. The use of pumped hydro storage plants is considered as the most mature and most deployed energy storage technology [25] as they are the only technically proven and cost effective technology [26-28]. During times of less energy demand, excess energy from the grid is used to pump water to storage locations at higher potentials. It is during peak hours that the water is released via turbine generator units for electricity supply of the peak loads.

Even though hydropower is associated with such advantages, it also presents negative aspects that need to be taken into consideration before the actual implementation of hydropower in a selected site. Okot [29] divided these negative aspects into environmental, economic and social. The environmental aspects of hydropower include impact on fish population which may find it difficult to migrate upstream past dams to spawning grounds, competition for land with other uses which may end up leading to humans, flora and fauna losing their habitat and concerns regarding hydropower impact on water quality.

Negative economic aspects of hydropower include the high capital cost associated with building powerplants, the requirement for long term planning and high reimbursements cost to the community if the planned hydropower sites may impinge upon local cultures and historic sites and involves relocation of inhabitants. The social issues associated with hydropower includes the need for resettlement, changes in the landscape and management of competing water uses [29].

In order to cater for the fish population when designing hydropower facilities, it has been taken into consideration that downstream and upstream fish passages and turbine intake screens and racks need to be part of the designs. To deal with the problem of water quality impacts due to low dissolved oxygen levels in the water, various aeration techniques have been developed.

2.1.1. Hydropower Schemes

Hydropower schemes can be divided into run-of-river, storage-based, and pumped-storage based schemes. The increased uptake of the application of PATs has resulted in possibly a new scheme known as 'multi-purpose hydro systems'.

Run-of-River Hydropower

In this hydropower scheme, water flowing through a river is diverted in areas where the geography is elevated and directed to pass through a turbine at a low elevation area to generate electricity. The difference in elevation of the diversion point and the powerhouse ensures a suitable head is obtained for power generation.

In this scenario there is no water storage even though in some cases a tiny pondage [30] will be incorporated in the whole system. The purpose of the pondage will be to provide a little amount of flow regulation. Breeze [30] suggests that the significance of the availability of a pondage is minimum and it doesn't affect the plant's classification as Run-of-River.

Water is diverted to the powerhouse via a headrace, which consists of a special design for topology exploitation leading to reduced head loss along its length. It will then fall into a hydraulic turbine via a penstock. The turbine will then convert the hydraulic energy into mechanical energy to drive the electricity generator. The penstock is designed in such a way as to avoid further loss of energy due to turbulence.

Turbine rotation is due to the pressure generated at the bottom of the penstock by the water head and the kinetic energy of the flowing water. The water is then returned to the river to continue with its natural flow via a tailrace. This type of a hydropower scheme provides the advantages of being cheap mainly due to the level of simplicity applied. Many cost elements from other scheme types are eliminated by the amount of civil engineering works involved.

On the contrary, run-of-river schemes present some disadvantages to the power consumers as it solely relies on the natural flow of water. This might be unreliable in times where the flow fluctuates as the generated power will also be fluctuating. In times of drought no power will be generated and during floods most of the water will flow past the diversion hence presenting little or zero potential energy harvest.

Storage-based Hydropower

Contrary to the run-of-river scheme, in storage-based hydropower schemes, a reservoir or a dam is built to act as a means of storing energy. The reservoir or dam can be built at the area of high elevation as compared to the powerhouse elevation or the reservoir height can be enough to provide suitable head for power generation. For power generation, water from the reservoir is sent into the powerhouse located at a lower altitude via a penstock and discharged out to the river via a tailrace.

Storage based hydropower schemes offer the advantages of water flow control. Flow in the river can be controlled as well as the flow through the turbine. This is an advantage as most turbines have a specific range of flow rates that their performance is at its best and flow control capabilities ensures that the water will always flow at a rate which supports attainment of maximum efficiency.

The increased water flow control capabilities also enable better management of water. In floods water is stored avoiding or reducing the effects of flood damages and the water can then be used during drought periods. When used alongside other means of renewable energy, wind or solar, storage-based hydropower can provide backup and balance. Wind and solar energy are intermittent as such addition of storage-based hydropower alongside those can help provide energy in times where there is no sunlight or when wind energy is at its minimum.

Some disadvantages associated with this scheme include the increased cost associated with the construction of dams. The need for geological surveys for geological faults and unsuitable substrata identification [30] before dam construction, make this cost of civil engineering projects to be high. Breeze also indicated that the construction of a dam alone will account for up to two thirds of the total project costs. Furthermore, for dams that are fed by rivers they will also be a need for cleaning to remove sediments that are swept by the river. Storage-based hydropower has also been associated with negative environmental impact.

Pumped Hydro Storage

Pumped hydro schemes are not classified as a primary source of energy as their most intended use is the transfer of energy for energy storage [24]. These schemes consist of two reservoirs at differing altitudes for useful head creation. During off peak hours of electricity supply, surplus energy is used to pump water from the lower altitude reservoir to the high-altitude reservoir. This helps to preserve the energy for use during peak hours where demand is high. At these hours water is run down from the higher reservoir to the lower reservoir via a turbine to produce electricity.

The energy storage aspect of pumped hydro power schemes allows for grid stabilisation in times of variable electricity supply hence providing a balance of supply to the grid. Even though the construction of such a hydro scheme can be quite expensive, large quantities of energy can be stored effectively and later used when need arise. The requirement for a pump to drive water to higher altitudes and a turbine for energy generation can also play a major role in overshooting this scheme's cost.

Multi-purpose Hydro Systems

The benefits brought about by the application of the pumps-as-turbine in recovering energy has led to a number of applications that forms this category of hydropower systems. In this scheme, a pump is operated as a hydraulic turbine in applications that were never thought of being potential hydropower sites in its earlier years. The examples of this application include energy recovery in water supply networks, sewage systems, irrigation systems, alcohol breweries, underground mining and desalination plants [31].

Novara [32] gave a collection of case studies providing a significant insight on this hydropower application. Some of the covered examples are the Al-Jubail reverse osmosis plant in Saudi Arabia with a nominal shaft power of 760 kW, a 112 kW PAT installed in the water supply system of the city of La Habra in California, a 220kW PAT installed in a treated water discharge for the city of Nyon in Switzerland and a maximum 300 kW output power PAT of Breech power station, Germany.

2.1.2. Operational Principles

The amount of power generated from a hydropower plant is dependent on several factors such as water flow rate, hydraulic head, specific gravity and overall efficiency of the plant. The equation below gives a mathematical relationship between the produced power and these parameters, where

P is power in watts, γ is specific gravity of water in N/m^3, Q is the water flow rate in m^3/s, H is the hydraulic head in meters and η is the overall plant efficiency.

$$P = \gamma.Q.H.\eta \tag{2.1-1}$$

Hydraulic head and water flow rate are the two parameters that could be varying in the above relationship and can be associated with the variability of the amount of power produced. The water flow rate is the most variable parameter as it is dependent on other factors such as precipitation, weather data and plant type [21]. On the other hand, hydraulic head is dependent on the plant design parameters. It can be thought of as the difference between the gross head and the associated losses. The head losses can occur because of friction in pipes and geometric changes in the piping systems.

The value of the overall efficiency is dependent on a number of efficiencies that occur throughout the plant system. Water into the turbine is subjected to several losses in the turbine and the generator such as the possible losses in the water volume, hydraulic losses, friction losses in mechanical parts of the turbine and electrical losses in the generator. These losses affect the amount of electricity produced in a hydropower plant. Kavadias and Apostolou [21] stated that due to these losses the amount of electricity sent to the grid for a given time is expressed as;

$$E = \int_{t_0}^{t_0+\Delta t} P(t).dt \tag{2.1-2}$$

Where E is the electricity sent to the grid at any given time and *P(t)* is the power produced from a hydropower plant as a function of time.

2.1.3. Hydropower Turbines

Hydropower turbines are used to capture the potential energy from the stored water at high elevation. There are two main classifications of hydropower turbines namely the impulse and the reaction turbines. Some relatively new types of turbines such as the reversible pump turbines are often considered as a third or special category of hydropower turbines [21], they can always be classed as reaction turbines as they depict some features of this class of turbines. They have of late garnered much attention in research as there is a shift from larger hydropower plants to MHPs.

Impulse Turbines

Pelton turbines are the only available type of impulse turbine. Impulse turbines depend on the conversion of the kinetic energy from the water jet to mechanical energy at the output. There is no realisable change in static energy across the runner. Pressure energy is converted to kinetic energy of a jet of water in a nozzle. The jet loses all the kinetic energy as it strikes the moving runner blades. Pelton turbines are more suited to areas portraying high heads and low volume rate of flow. They may achieve a maximum efficiency value between 85 - 90% [33].

The available head is converted to kinetic energy using one or more nozzles, the number dependent on the orientation of the machine with a maximum of two for horizontal and six for vertical machines [33]. The jet of water shoots tangentially to the pitch circle onto runner buckets resulting in work done on the runner and energy transfer.

The bucket is designed in such a way that the interception of the jet of water by the incoming bucket is minimised. This is via the cutaway on the bucket towards the tip. The nozzle is used to control the flow, this is made possible by the availability of the spear. Water from the penstock is accelerated to a certain velocity which it is desirable to be kept constant. The volume flow rate will then be regulated by altering the area of the water jet by making the spear to protrude through the nozzle hence keeping the velocity constant and increasing or decreasing flow.

When the nozzle is completely closed by the spear fully protruding covering the whole jet area, the amount of water striking the bucket reduces to zero. But because of inertia, the runner continues to rotate without stopping. To counteract this effect and bring the runner to a stop in a short duration, a smaller nozzle is used to provide a water jet to the back side of the bucket, hence providing the braking effect.

Reaction Turbines

This class of hydropower turbines differ in operating principle to impulse turbines as the working fluid is completely covering the runner passages. The fluid pressure at the runner blades is different from atmospheric pressure since the fluid is completely enclosed. Furthermore, unlike impulse turbines, reaction turbines use only a fraction of the head available for fluid transfer from the reservoir before reaching the turbine.

One typical example of this class of turbines is the *Francis turbine*. It operates effectively at medium heads ranging from 15m - 300m [21, 33], power loads of up to 100MW [21] achieving overall efficiencies of over 90% [33]. In reaction turbines the fluid enters the turbine via a volute which is designed to keep the velocity of the fluid constant by adopting a reducing cross-sectional area. On its way to the turbine, the fluid passes through guide vanes where it is being directed to the runner at the rightful angle. Through the runner the fluid is deflected changing its angular momentum in the process.

The fluid exits the runner at the centre in an axial direction via the draft tube. To avoid further head losses, its ensured that the draft tube lower end is submerged in water under all operating conditions. Another type of reaction turbines is referred to as *axial-flow reaction turbines or propeller turbines*. The working principle of this turbines is the same with that of Francis Turbines besides that their design is based on the principle that in order to achieve greatest flow rates the flow needs to be parallel to the axis of rotation of the runner [33].

Since the direction of flow into the turbine is radial, flow in propeller turbines changes direction by 90^0 after passing through the guide vanes before reaching the impeller. This ensures that it reaches the impeller parallel to the axis of rotation. A *Kaplan turbine* is another form of axial-flow reaction turbines. It is similar to the propeller turbine in operation with the difference being that it consists of adjustable guide vane blades and impeller vane blades ensuring the possibility of achieving high efficiencies over a wide range of operating conditions.

2.2. PUMPS-AS-TURBINES (PATs)

The first use of a pump as a turbine can be traced back to the 1930s when Thoma and Kittredge [34] carried out lab experiments and identified the potential for a common pump to be operated efficiently in reverse to produce work. Since then several studies have been undertaken on the application of pumps in reverse operation as hydraulic turbines indicating that they can be a good alternative to conventional turbines [35] taking into account both practical and economic considerations [36].

As compared with conventional turbines of the same power, pumps-as-turbines offer a very cheap alternative which is readily available in all sizes that can be required. One of the shortcomings of PATs is their efficiency which is lower than that of conventional turbines, however, this is typically only two or three percent [35] and its impact on the pay-back periods is very minimal for fixed flow rates. PATs also lack regulation capabilitiesy which is one of its major shortcomings. Regardless of these shortcomings, PATs have been deemed the most economical option for energy recovery in micro or pico-hydropower applications such as within water supply networks or in run-of-river schemes [37].

2.2.1. PAT Theory

Understanding the energy conversion in pump mode can aide the understanding in turbine mode. The velocity triangles obtained for both pump and PAT mode are shown in Fig 2.2-1 [38]. Velocities u_i are the peripheral velocities of the impeller at the inlet and outlet respectively in each case. In pump mode, the fluid flows into the impeller at velocity c_1 and exits at the outlet at velocity c_2. When operated as a turbine the flow is reversed and the liquid enters the impeller at speed c_2. As a result of the blade design there would be a resultant relative velocity w_i.

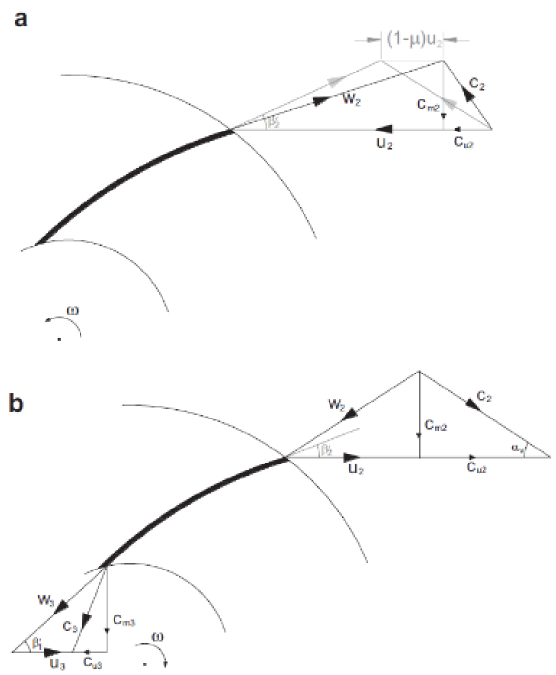

Figure 2.2-1. a) Outlet velocity triangle in pump mode b) impeller inlet and outlet velocity triangles in turbine mode

As a result of the effect of the magnitude and direction of the relative velocity w_i, the absolute velocity at the outlet will deviate from the flow velocity at the entry [35]. With reference to Fig. 2.2-1 above, in the case of pump mode the flow velocity at entry is c_1 (not shown) and the resultant absolute velocity is depicted as c_2. In turbine operation flow velocity at entry is c_2 and the resultant absolute velocity is c_3.

It must be noted that even though the flow is reversed there is a change in velocity triangles. The inlet flow angle to the impeller in a PAT cannot be thought of as equal to the outlet flow angle of the impeller in the pump mode [31]. It is estimated to be equal to the volute angle in turbine mode [31, 38]. In pump mode, if the law of conservation of momentum is applied in the fluid flow through the impeller, the head imparted by the impeller to the fluid, often termed the Euler head, can be obtained by:

$$\Delta H = \frac{u_2.c_{2u} - u_1.c_{1u}}{g} \tag{2.2-1}$$

Ideally the value of c_{1u} can be said to be equal to zero and the resultant equation for the imparted head becomes,

$$\Delta H = \frac{u_2.c_{2u}}{g} \tag{2.2-2}$$

The head, H, developed by the pump can be thought of as being the difference between Net Head at the pump outlet and the Net head at the inlet. Due to the frictional losses by the fluid, the value of H and ΔH are not equal. Their ratio yields the manometric efficiency, η_m. The mechanical efficiency of the pump, η_{mech}, is the ratio of the power the impeller receives from the shaft to the shaft power. Therefore, the product of the manometric efficiency and the mechanical efficiency yields the overall efficiency of the pump.

2.2.2. PAT Performance Characteristics

PAT Characterisation and selection has been widely studied. Several methods have been presented in literature, and these can be summed into experimental, theoretical and numerical investigations. In [39], Budris suggested the following conversion ratios for obtaining BEPs of a pump operating in reverse:

$$Q_{T(BEP)} = Q_{P(BEP)}/\eta_{P(BEP)}$$
$$H_{T(BEP)} = H_{P(BEP)}/\eta_{P(BEP)} \quad (2.2\text{-}3)$$

where $Q_{(BEP)}$ is the best efficiency flow rate, $H_{(BEP)}$ is the best efficiency head and $\eta_{(BEP)}$ is the best efficiency point of the machine. The subscript T and P refers to the Turbine and Pump mode respectively. It must be noted that this conversion assumes the efficiency during pump operation is equal to the efficiency during turbine mode.

On the other hand, in some studies [31, 40, 41] the BEP of the turbine was obtained from pump mode BEP using the conversion ratios. These ratios are presented below:

$$h = H_{T(BEP)}/H_{P(BEP)}$$
$$q = Q_{T(BEP)}/Q_{P(BEP)} \quad (2.2\text{-}4)$$

where h and q are the head and flow conversion ratios respectively, $Q_{(BEP)}$ is the flow rate at BEP, $H_{(BEP)}$ is the head at BEP and subscript T and P denote turbine and pump mode respectively.

Derakhshan & Nourbakhsh [41] plotted the BEP values obtained using the aforementioned ratios for four PATs at different specific speeds and concluded that pumps with high specific speeds portray lower values of h and q. Furthermore, they developed some dimensionless parameters for the estimation of the BEP in turbine mode from BEP values in pump mode that are only valid at low pump specific speeds. These parameters are indicated below,

$$\gamma = 0.0233\alpha_P + 0.6464$$
$$\alpha_T = 0.9413\alpha_P - 0.6065 \quad (2.2\text{-}5)$$

where α_P is the specific speed in pump mode. Using the value of γ yields the PAT head at the BEP and the value of α_T gives the flow rate of the PAT at the BEP. They later used different methods of estimating the PAT BEP to compare with experimental data, which indicated that none of the methods clearly resemble the experimental pattern throughout the whole range of specific speeds.

Thus, in agreement with findings of Williams [42] that concluded that no method could predict accurately the turbine characteristics from pump characteristics for all machines.

In reaching the same conclusion, Lydon et al [37] compared the results of applying the different available BEP conversion ratios with experimentally established BEP of a prototype PAT and none of the applied BEP conversion ratios could successfully predict the PATs BEP as most of the predictions fell outside of the pumps operating range of flow and head.

Yang et al [38] also made use of the head and flow ratios presented in Eqns. 2.2-3 and 2.2-4 respectively coupled with empirical correlations to develop new head and flow ratios that are dependent on the pump mode efficiency values. These relationships are presented below,

$$h = \frac{1.2}{\eta_P^{1.1}}$$
$$q = \frac{1.2}{\eta_P^{0.55}} \qquad (2.2\text{-}6)$$

where η_P is the efficiency in pump mode. The output from these formulas was compared to the ones from other methods and indicated better agreement with experimental data.

Mitrovic et al [43] assessed the accuracy of the Yang et al [38] model for predicting the PAT's best efficiency point from the pump's best efficiency point after it was pointed out as one of the best in literature [32]. Their assessment revealed that the Yang et al [38] model could yield average relative absolute errors of 10.28% in predicting H_{BEP} and 6.42% in predicting Q_{BEP}. This is a significant finding, and it invalidates the earlier findings of Williams [42] and Lydon [37] described earlier in this chapter.

In their study Singh & Nestmann [44] developed experimental relationship between pump mode and turbine mode specific speeds utilising the BEPs of 13 PATs. Their developed relationship is given by the following equation:

$$N_{qt} = 0.94N_{qp} - 3.12 \qquad (2.2\text{-}7)$$

where N_{qt} is the turbine mode specific speed and N_{qp} is the pump mode specific speed. With the net head and flow rate of the application site known the turbine specific speed can be obtained at different rotational speeds then the above relationship used to predict the pump that will yield these characteristics when operated in reverse.

Carravetta et al [45] obtained the BEPs of machines similar to a prototype machine whose characteristics curves were known using turbo-machinery affinity laws. They also used the prototype data to calculate Suter parameters [46, 47] for assessing performance curves of similar

PATs. This approach assumes the same efficiency for both pump and turbine mode. However, Gulich [48] has indicated that the efficiencies of the two modes of operation can differ by ±0.02%.

The Common Affinity Law was used to establish the BEP for similar machines with different diameters and rotational speeds from experimental results obtained from a laboratory PAT prototype [37]. Relaxation of the Affinity Equation (RAE) as developed by Fecarotta [49] was also applied in this work to obtain the BEP values for these machines and the results compared to those of the affinity laws. The results could not be conclusive as RAE was fixed to the changes in rotational speed only hence the adoption of the affinity law as the study was based on the impact of diameter change.

Lydon et al [37] also applied Suter parameters and the use of dimensionless curves as suggested by Fecarotta et al [49] to generate approximate characteristics and efficiency curves for PAT BEP established experimentally with a prototype PAT. Results obtained from Sutter parameters differed substantially with experimental results while results from dimensionless curves could replicate the testing results with a high degree of accuracy.

Throughout literature it is evident that the use of theoretical approaches to predict pump performance in turbine mode is always associated with deficiencies which make it difficult to devise a method that can be applicable to all cases. This is evidenced by most of the works discussed above which either present methods that are either not in agreement with experimental data or are only true for a certain class of pumps. This clearly indicates that the best technique to obtain performance characteristics of a pump in turbine mode is via experiments.

The downside of obtaining PAT performance characteristics through experimentation lies on the cost of carrying out the experiments. The use of numerical models has provided a better alternative, even though the models are not always a 100% representation of the PAT operating environment. Several studies have focused on obtaining PAT performance characteristics using numerical modelling approaches. These have resulted in better correlation between predicted and experimental performance characteristics, often better than what can be provided using theoretical approaches.

Frosina et al [50] presented a methodology for obtaining reverse characteristics of a pump from CFD simulations. They compared the results of their model to both experimental data and results of theoretical approaches. The CFD model offered good accuracy of the performance characteristics in both direct and reverse mode. When compared to the results of theoretical prediction approaches, it was evident that theoretical means of obtaining performance characteristics were either overestimating or underestimating the real PAT performance.

The problem associated with CFD studies is that these are usually limited to just one pump as it can be very complex to model even just a single pump making it very time and resource consuming to have an accurate representation of a family of pumps, or a large group required for practical PAT design activity. Denton [51] discussed some limitations of CFD in turbomachinery applications and noted that errors can arise from numerical discretization, complex flow physics, unknown boundary conditions, approximated geometry and the steady state assumption for flows.

This indicates that no matter the cost implications that come with the use of experimentation in predicting pump performance in turbine mode it will always be superior to the other described methods. This is due to fact that experimentation also takes into consideration the environment in which the machine operates in, an aspect that is only assumed or ignored in both theoretical and numerical approaches.

2.3. COMMON FAILURE MECHANISMS IN HYDRAULIC MACHINES

Smith [52] defines failure as non-conformance to some defined performance criterion. This implies that a system or machine is considered to be in a failure state when it can no longer fulfil its intended function or when its state deviate from the set state. Considering the above definition, it is worth noting that failure does not always imply a complete malfunction of a system or a component but also a deviation from the set performance criteria. Tinga [53] opine that it depends on the level that is being considered, for example, a malfunction of a particular subsystem or component does not necessarily mean the complete failure of that system.

Tinga [53] also point out that failures are usually a result of imbalance between loads in a system and the load carrying capacity of that system. Load carrying capacity referring to the built-in resistance to withstand loads without failing and loads in this context are dictated by the way the system is being operated. In most cases loads applied to the system are known as global loads applied to the system externally, which means that to assess the sufficiency of the local load carrying capacity, these external loads must be translated into internal loads.

It is also vital to define the phrase *failure mode* as it is sometimes confused with failure mechanisms. Failure mode refers to the way in which the system or component functionally fails to fulfil its intended purpose. It can be thought of as a description of the extent a function is not fulfilled. This means that failure modes usually relate to the performance requirements of the system or a component.

On the contrary, *failure mechanisms* refer to the physical or chemical processes that leads to the degradation of the component leading to physical failure [53]. Thus, failure mechanisms can be identified after carrying out root cause analysis of identified failure modes. It is also vital that during the root cause analysis process the origin of the loads that activate the failure mechanism be identified.

Failure modes of a component can be brought about by different failure mechanisms, which means that there exist a limited number of failure mechanisms which manifest themselves as almost infinite failure modes. As such it is an important practice to reduce a failure mode to its failure mechanism and the activating load in order to simplify the root cause analysis process. Thus, highlighting the importance of understanding different failure mechanisms of a component.

In the following subsection we describe the different failure mechanisms that are associated with failures in both pumps and turbines.

2.3.1. Fatigue

A high percentage of failures in machine elements results from fatigue. This is the case even though there are standardized design methods that are supposedly guarding against this failure mechanism. Fatigue damage results in the initiation and propagation of cracks leading to fracture of the machine component.

Fatigue failure has been defined as, "*a process in which there is progressive, localised, permanent microstructural change occurring in a structure when it is subjected to boundary conditions which produce fluctuating stresses and strains at some material point or points*" [54]. This implies that fatigue occurs in systems or machine elements that are subject to cyclic loading, be it due to thermal stresses or mechanical stresses.

The fatigue degradation model differs between the two categories of high cycle fatigue (HCF) and low cycle fatigue (LCF). In HCF the component is exposed to loads that result in stresses that are below the material yield stress and the degradation mechanism is controlled by the stress range ($\Delta\sigma$) [55]. Thus, the deformation is fully elastic and is usually a result of vibration of machine components. The resultant loads are relatively small but since they occur at high frequencies the number of cycles to failure are reached in relatively shorter durations.

HCF is represented using the S-N curves correlating the number of cycles and the characteristic stress level. The S-N curve can also be expressed as a numerical relation between applied stress range and number of cycles to failure, as proposed by Basquin:

$$\frac{\Delta\sigma}{2} = A(2N_F)^b \qquad (2.3\text{-}1)$$

Where *A* and *b* are constants to be determined from S-N data [53].

On the contrary, for LCF the stress level is above the yield stress limit resulting in plastic deformation. In this instance the degradation mechanism is controlled by the magnitude of the strain range ($\Delta\varepsilon$) [55]. The Manson-Coffin law is commonly used to represent this degradation mechanism. It considers that cyclic life depends on the deformation using a power law. In this case the material fatigue resistance must be provided as an ε-N curve instead of an S-N curve as indicated below [53], where $\Delta\varepsilon_p$ is the plastic strain range, c and ε_f are empirical constants.

$$\frac{\Delta\varepsilon_p}{2} = \varepsilon_f (2N_f)^c \quad (2.3\text{-}2)$$

As already indicated in the prior paragraphs fatigue damage leads to the formation of cracks leading to failure. Cracking usually initiates at a surface or subsurface discontinuity, such as a scratch, keyway, fillet, hole or intrusion [56]. Crack growth according to fracture mechanics is categorised into three regions namely, first region which describes initiation and slow crack growth, second region which describes crack growth becoming significant and constant, and the third region where the crack becomes unstable, and the propagation rate increases until fracture occurs.

The Paris Law is the most widely used model for crack growth, which was proposed based on experimental data that proved the correlation between crack length and number of cycles. It represents the second region of crack growth neglecting the crack initiation phase. The associated numerical equation of the Paris law is given below, with C and n being material coefficients, da/dN being the fatigue crack growth rate per cycle and ΔK is the range of the stress intensity factor.

$$\frac{da}{dN} = C(\Delta K)^n \quad (2.3\text{-}3)$$

The effect of design forms of machine elements on their endurance limit is represented in calculations by the stress concentration factor, K_σ, which is the proportion of the endurance limit for a smooth sample over the same for a sample of the same size containing a stress concentration point. Machine elements most frequently experience bending and torsional stress patterns as they mostly rotate under radial loads or they rotate transmitting torque [56], this is inclusive of both pumps and turbines.

The value of the stress concentration factor is small when the sample is exposed to pure cycle torsion as compared to when it is exposed to a bending or tension-compression load. This means that stress raisers are less dangerous in parts subjected to pure torsion than those exposed to bending or combined loads.

Ocampo [56] points out that the fracture in parts exposed to rotating bending loads occurs on surfaces that are perpendicular to the axis of rotation irrespective of the magnitude of the load. Cyclic twisting may result in fatigue failure at 45° to the torsion axis under low loads and perpendicular to the torsion axis under high loads.

Ocampo and Ruiz [57] presented case studies where they investigated fatigue failures in pumps highlighting inadequacies in design, manufacturing and repair malpractices. They considered fatigue fracture of diffuser fixing screws in a group of multistage centrifugal pumps illustrating design mistakes in the manufacturing of spare parts, fatigue fracture of impeller blades after repair by surface welding and fatigue fracture of a pump shaft demonstrating risks of repair and maintenance malpractice.

In [58] Ocampo provided further case studies in which fatigue failure of pump shaft and motor shaft was investigated. This led to conclusions that the main causal factor of stress concentration in both the shafts was that the degree of misalignment at the coupling was larger than the minimum values permitted for the kind of couplings. As such stress was concentrated at a change of section in the pump shaft and the corner of keyway in the motor shaft.

2.3.2. Wear

When two or more machine elements are in physical contact and there exists relative motion between them, chances are that wear will occur resulting in loss of material at the surface of at least one of the elements. This degradation mechanism can also occur due to the flow of either a gas or liquids at high velocities and/or temperatures near the surface of machine element.

These generally lead to a progressive degradation of the component resulting in failure, which is triggered by dimensional anomalies, functional failure and initiation of other failure mechanisms [53]. In turbomachinery, this failure mechanism is common in bearings and at interfaces between rotating and stationary components.

Wear can be classified into five major types namely, adhesive wear, abrasive wear, corrosive wear, surface fatigue and erosion. Adhesive wear takes place in relatively smooth surfaces when the bodies in contact display a similarity in hardness. Wear debris will be transferred between the two bodies resulting in the formation of structurally weak points which end up failing to perform their intended function or causing further damage to other components that they are in proximity with ultimately leading to complete machine failure. This type of wear is associated with high levels of friction causing a considerable heat generation, which also might be the cause of component failure.

Abrasive wear on the contrary, occurs at surface contacts that either display a considerable difference in hardness and the existence of a rough surface in the harder surface. This leads to material irregularities from the hardest surface penetrating the softer material resulting in scratches and furrows due to material loss. As a result, the softer material will be left being structurally weak and more prone to failure or initiation of other failure mechanisms.

When the physical contact between the two structures takes place under corrosive environments, corrosive wear takes place. In this case rubbing between the structures or machine elements will produce exposed surface which will lead to surface reactions resulting in formation of reaction products at the contact area. The continuation of the rubbing action will remove this reaction products leaving the contact more exposed. The process will repetitively continue until one of the structures has lost a significant amount of material leaving it prone to failure due to reduced structural strength in that location.

As already discussed in the previous section, fatigue failure develops when cyclic loads exist at a location over time. In rolling element surfaces, there exist stress distributions which vary in time causing cyclic loads that could initiate cracks. These cracks occur in the subsurface layer and will propagate and eventually reach the surface yielding material breakage and at times leads to pitting or spalling with the subsequent material removal. This piecewise loss of material can be classed as wear even though it started due to fatigue.

Unlike all the other types of wear discussed so far, erosion follows a different mechanism. It involves a single body and some flowing fluid or gas. Gas erosion occurs when a gas flows past a solid part at high velocities and generally high temperatures removing some material in the process. Prolonged exposure to these conditions generally leads to dimensional anomalies and subsequent failure. When the flowing medium is a fluid, the process is called fluid erosion. Due to high densities of fluids, material loss can occur at lower velocities as compared to gas erosion.

Wear is a very complex phenomenon to model, as such there exists limited numerical models to predict wear rates. This is because of the large number of influencing factors in physical contact situations with relative motion like hardness, surface roughness, friction coefficient, temperature, amount of lubrication etc [53]. When the contact surfaces are considered dry, wear can be modelled using the Archad Law [55] stated below which can help to model complex wear situation by modifying the value of *k;*

$$V = kF_n \Delta S \tag{2.3-4}$$

Where the volume loss V is proportional to the normal force F_n applied and the travelled distance ΔS. The variable k is the proportionality constant and is known as the specific wear rate [53] and it depends on the factors mentioned in the previous paragraph.

To reduce friction and wear, lubrication is applied hence increasing the machine, component or system lifetime. Lubricants play a major role also in condition monitoring of machine components as wear debris are trapped in the lubricant indicating the wearing components. There exist different lubrication regimes that are of utmost importance for different wear mechanisms namely, boundary lubrication, Hydrodynamic lubrication and mixed lubrication [53, 55].

These lubrication regimes are visualised in the Stribeck curve shown in Fig 2.3-1 below [55]. It is a graphical representation of the relationship between the rotational speed and the friction coefficient for a specific contact. Boundary lubrication is active when the pressure build-up is not enough to separate the different parts, therefore most of the load is transmitted through the contacts.

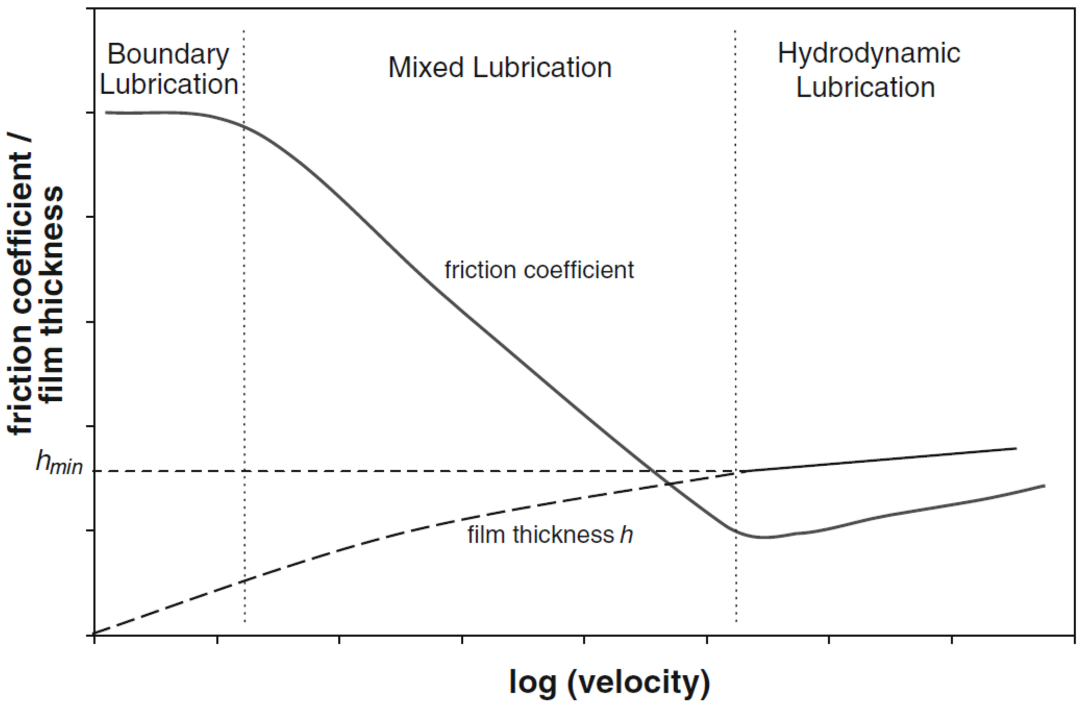

Figure 2.3-1. Stribeck curve showing the different lubrication regimes

In the mixed lubrication regime partial metal to metal contact occurs with load divided between being transmitted by the lubricant and some by the asperities in the contact area. Lastly, the lubrication regime where most hydrodynamic contacts in rotating machines (i.e., bearings) operate is the hydrodynamic lubrication. This is where the friction forces are exclusively a result of shear stresses of the lubricant, hence ensuring wear protection at high rotation speeds. This regime is only possible when the rotation speed is sufficiently high and the lubricant exceeds a critical thickness [53, 55].

2.3.3. Cavitation

Performance of hydraulic machines depend highly on the hydraulic characteristics of the fluid being transferred from one location to the other, which means that failure to ensure optimum hydraulic characteristics, the machine may become exposed to unfavourable conditions for their operation ultimately affecting their performance and their structural integrity.

Cavitation is one such phenomenon where the flow conditions are not favourable to achieve optimum energy conversion in hydraulic machines. It is defined as the process of rupturing a liquid by decreasing pressure at roughly constant temperature [59]. This involves the liquid changing its state of matter to a gaseous state. Liquids can also be ruptured by increasing their temperature, a process known as boiling, but cavitation achieves the same at constant temperature and a decreased pressure.

During the process of cavitation, a cavity filled with vapour is formed when the liquid's static pressure drops below its vapour pressure at the given temperature. This can occur when the fluid has been exposed to excess velocities to the extent that the liquid evaporates forming a two-phase flow in some parts of the flow field [48]. As soon as the vapour filled cavity has been transported to areas of lower velocity and increased pressures, it suddenly condenses emitting high energy [60] in the form of microjets, pressure fluctuations and uneven load distribution [61, 62].

If the cavitating zone is prolonged with two phase flows, head and efficiency can be impaired affecting overall machine performance. The resultant pressure pulsations can also result in noise and excitation of vibrations that can ultimately lead to failure from the prior discussed failure mechanisms. The tendency of the flow to cavitate can be characterized by the cavitation number, which is defined as follows:

$$C_a = \frac{p - p_v}{\frac{1}{2}\rho U^2} \tag{2.3-5}$$

where p is the reference pressure for the flow, p_v is the vapour phase pressure and the denominator represents the dynamic pressure. From the above relationship, it is evident that the tendency to cavitate is highly dependent on the reduction of the cavitation number. It is worth noting that cavitation is taken to be occurring at isothermal conditions.

Since cavitation involves the transportation of vapour bubbles, it is important that its description be accompanied by a description of bubble dynamics. In liquids, cavitation bubbles are formed when there exist nuclei. Nuclei exist in the liquid as accumulations of gas or vapour molecules of diameters in the range 10^{-3} to 10^{-1}mm [48]. Their interiors consist of both the contaminate gas and the liquid vapour, as such the pressure inside the bubble corresponds to sum of partial pressures of the constituents.

The radius of this nucleus grows when it enters an area of low pressure. The number of nuclei activated increases with decreasing pressure. More bubbles will be formed when the time the liquid is exposed to the low-pressure zone is increased and when the local pressure drops further. Transportation of these bubbles to flow zones where the local pressure exceeds the vapour pressure results in these bubbles collapsing as the phase equilibrium would have been disturbed.

$$C_i = \sqrt{\frac{2}{3} . \frac{p - p_B}{\rho} . (\frac{R_0^3}{R_e^3} - 1)} \tag{2.3-6}$$

The Rayleigh equation given by Eqn. 2.3-6 describes the velocity C_i reached by the bubble walls at the end of the implosion. The variable p_B represents the pressure in the bubble, R_0 the bubble radius at the start and R_e at the end of the implosion. This process results in extremely sharp pressure peaks which occur as a result of the water hammer effect [48] described by; $p_i = \rho a_o c_i$ where p_i is the implosion pressure peak and a_0 is the speed of sound in the liquid. These pressure peaks are time dependent and can exceed 1000bar, hence can exceed the strength of the material used in the machine.

The implosion pressure and the potential to cause damage to the machine increases with the bubble size at the start of the implosion R_0 and the pressure difference. Conversely, it decreases with an increase in the bubble radius at the end of the implosion R_e. The availability of other cavitation bubbles in the flow can have either positive or negative effect hence contributing to the local pressure difference that triggers the implosion.

2.3.3.1. Numerical Modelling of Cavitation

There are several ways that the cavitation phenomenon can be modelled in studying cavitation in engineering applications. A basic two-phase cavitation model consists of using the standard viscous flow equations governing the transport of a mixture and a conventional turbulence model. In modelling cavitation, the vapour transport equation given below governs the liquid-vapour mass transfer:

$$\frac{\partial}{\partial t}(\alpha \rho_v) + \nabla.(\alpha \rho_v V) = R_E - R_C \qquad (2.3\text{-}7)$$

Where V represents the vapour phase velocity, α represents the vapour volume fraction, ρ_v represents the vapour density, R_E and R_C representing the mass transfer source terms connected to the growth and collapse of vapour bubbles respectively. The available cavitation models derive these terms as described in the following sub-sections.

Rayleigh-Plesset Cavitation Model

Most of the available models used in cavitation modelling are based on this model, which describes the growth of a single vapour bubble in a liquid. This model is implemented in Ansys CFX in the multiphase framework as an interphase mass transfer model [63]. The Rayleigh-Plesset equation is as follows:

$$R_B \frac{d^2 R_B}{dt^2} + \frac{3}{2}(\frac{dR_B}{dt})^2 + \frac{2\sigma}{\rho_l R_B} = \frac{p_v - p}{\rho_l} \qquad (2.3\text{-}8)$$

Where R_B represents the bubble radius, p_v represents the pressure in the bubble which is assumed to be equal to the vapour pressure at the liquid temperature, p represents the pressure in the liquid surrounding the bubble, ρ_l represents the liquid density, and σ represents the surface tension coefficient between the liquid and the vapour.

When the second order terms and the surface tension are neglected, this equation reduces to the following form:

$$\frac{dR_B}{dt} = \sqrt{\frac{2}{3}\frac{p_v - p}{\rho_l}} \tag{2.3-9}$$

The rate of change of bubble volume follows as:

$$\frac{dV_B}{dt} = \frac{d}{dt}\left(\frac{4}{3}\pi R_B^3\right) = 4\pi R_B^2 \sqrt{\frac{2(p_v - p)}{3\rho_l}} \tag{2.3-10}$$

And the rate of change of bubble mass is:

$$\frac{dm_B}{dt} = \rho_g \frac{dV_B}{dt} = 4\pi R_B^2 \rho_g \sqrt{\frac{2(p_v - p)}{3\rho_l}} \tag{2.3-11}$$

If there are n bubbles per unit volume, the volume fraction α may be expressed as:

$$\alpha = V_B \times n = n \times \frac{4}{3}\pi R_B^3 \tag{2.3-12}$$

And the total interphase mass transfer rate per unit volume is:

$$R = n\frac{dm_B}{dt} = \frac{3\alpha\rho_g}{R_B}\sqrt{\frac{2(p_v - p)}{3\rho_l}} \tag{2.3-13}$$

This expression has been derived assuming bubble growth (vaporization). It can be generalised to include condensation as follows:

$$R_c = F_{cond}\frac{3\alpha_g\rho_g}{R_B}\sqrt{\frac{2|p_v - p|}{3\rho_l}}sgn(p_v - p) \tag{2.3-14}$$

Where F is an empirical factor that may be different depending on whether the modelled state is evaporation or condensation. It is designed to account for the fact that evaporation and condensation may occur at differing rates with condensation usually slower than evaporation [63]. When modelling the value of the bubble radius R_B is replaced by the nucleation site radius R_{nuc}.

Since vaporisation starts at nucleation sites and increase in vapour volume fraction leads to a decrease in the nucleation site density, the interphase mass transfer rate per unit volume expression for vaporisation needs further modification. The variable α_g is replaced by $\alpha_{nuc}(1 - \alpha_g)$ to give:

$$R_E = F_{vap}\frac{3\alpha_{nuc}(1 - \alpha_g)\rho_g}{R_{nuc}}\sqrt{\frac{2|p_v - p|}{3\rho_l}}sgn(p_v - p) \tag{2.3-15}$$

Where α_{nuc} is the volume fraction of the nucleation site. In ANSYS CFX the value of α_{nuc} = 5E-4, F_{vap}= 50, F_{cond}= 0.01 and R_{nuc} = 1μm [63, 64].

This model has been widely used in literature for cavitation modelling in turbomachinery applications. Fatah et al [60] used this model when studying the dynamic performance of a centrifugal pump in cavitation state. Likewise, Rakibuzzaman et al [65] used this model in their investigation of cavitation performance of a multistage centrifugal pump. The model validation yielded average deviation values of 5.34%, 6.35% and 8.22% for head, shaft power and efficiency respectively. In the study of cavitation in PATs, Rakibuzzaman et al [66] also used the Rayleigh-Plesset cavitation model coupled with the k-ω SST turbulence model to carry out a comparison study of cavitation performance in a centrifugal pump when being operated in both pump and turbine mode. Model validation yielded the average deviations of 3.01% and 3.63% for the head and efficiency respectively.

The Full Cavitation Model

In their work Singhal et al. [67] realised that the past models that were used in attempting to model cavitation lacked the robustness of numerical algorithms and the correlations or approaches used lack generality which resulted in these not being routinely used in practical CFD-based design optimization studies. They then proposed the full cavitation model which met all those requirements and later this was routinely used in industry.

The full cavitation model, like the Rayleigh-Plesset model, consists of using the standard viscous flow equations for variable fluid density and a conventional turbulence model. It accounts for all first order effects such as phase change, bubble dynamics, turbulent pressure fluctuations, and non-condensable gases. The model is capable of accounting for multiphase flows, the effects of slip velocities between the fluid and the gaseous phases, and the thermal effects and compressibility of both liquid and gas phases.

In this model fluid density is a function of vapour mass fraction f_v, which is computed by solving a transport equation coupled with the mass and momentum conservation equations. A transport equation like the vapour transport equation, Eqn. 2.3-7, governs the vapour mass fraction. The $\rho - f_v$ relationship is given by:

$$\frac{1}{\rho} = \frac{f_v}{\rho_v} + \frac{1 - f_v}{\rho_l} \tag{2.3-16}$$

And the vapour volume fraction α is deduced from f as:

$$\alpha = f_v \frac{\rho}{\rho_v} \tag{2.3-17}$$

Singhal et al. [67] assumed that most engineering application consists of plenty of nuclei for the inception of cavitation. As such they focused on accounting for bubble growth and collapse by utilising the Rayleigh-Plesset equation providing a physical approach to introduce the effects of bubble dynamics in their model. The Rayleigh-Plesset equation (Eqn. 2.3-8) can be considered as an equation for the void propagation and hence mixture density.

The following two-phase continuity equations were obtained to derive the expression for the net-phase change rate:

Liquid Phase,

$$\frac{\partial}{\partial t}[(1-\alpha)\rho_l] + \nabla.[(1-\alpha)\rho_l V] = -R \quad (2.3\text{-}18)$$

Vapour Phase,

$$\frac{\partial}{\partial t}(\alpha\rho_v) + \nabla.(\alpha\rho_v V) = R \quad (2.3\text{-}19)$$

Mixture,

$$\frac{\partial}{\partial t}(\rho) + \nabla(\rho V) = 0 \quad (2.3\text{-}20)$$

Where R is the net phase change, ρ is the mixture density and is defined by;

$$\rho = \alpha\rho_v + (1-\alpha)\rho_l \quad (2.3\text{-}21)$$

Creating a relationship between the mixture density and the vapour volume fraction α by combining all the above relationships we obtain:

$$\frac{D\rho}{Dt} = -(\rho_l - \rho_v)\frac{D\alpha}{Dt} \quad (2.3\text{-}22)$$

Taking the expression for the vapour volume fraction from the Rayleigh-Plesset model section and substituting it in the above equation we obtain:

$$\frac{D\rho}{Dt} = -(\rho_l - \rho_v)(4n\pi)^{\frac{1}{3}}(3\alpha)^{\frac{2}{3}}\frac{DR_B}{Dt} \quad (2.3\text{-}23)$$

Giving the following expression for the net phase change rate when combining with prior equations:

$$R = (4n\pi)^{\frac{1}{3}}(3\alpha)^{\frac{2}{3}}\frac{\rho_v\rho_l}{\rho}[\frac{2}{3}\left(\frac{P_B - P}{\rho_l}\right)]^{\frac{1}{2}} \quad (2.3\text{-}24)$$

In this relationship R represents the vapour generation or evaporation rate which is denoted by R_E in the vapour transport equation. In the above relationship all terms are either known constants or dependent variables except n. As such in the absence of a general model for estimation of the bubble number density, the phase change rate expression is written in terms of bubble radius (R_B) as follows:

$$R = \frac{3\alpha}{R_B}\frac{\rho_v\rho_l}{\rho}\sqrt{\frac{2}{3}\frac{P_B - P}{\rho_l}} \quad (2.3\text{-}25)$$

This indicates that the unit volume mass transfer rate is related to both vapour density, liquid density and the mixture density. This equation is exact since it has been derived from phase volume fraction equations and should accurately represent the evaporation or bubble growth phase of cavitation. During the condensation phase, this equation is often used by treating the right side as a sink term and using the absolute value of the pressure difference. In practical applications the bubble pressure is taken to be equal to the saturation vapour pressure in the absence of condensable gases, mass transport and viscous damping.

Singhal et al. [67] based on the above equation proposed a model where the vapour mass fraction is the dependent variable in the transport equation. This accommodates single-phase formulation where the transport equation becomes:

$$\frac{\partial}{\partial t}(f_v\rho) + \nabla.(f_v\rho V) = \nabla.(\Gamma\nabla f_v) + R_E - R_C \tag{2.3-26}$$

With Γ representing the diffusion coefficient. The mass transfer source terms are given by the following equations:

$$R_E = F_{vap}\frac{\max(1.0,\sqrt{k})(1-f_v-f_g)}{\sigma}\rho_l\rho_v\sqrt{\frac{2(P_v-P)}{3\rho_l}}\ \ if\ P \leq P_v, \tag{2.3-27}$$

and

$$R_c = F_{cond}\frac{\max(1.0,\sqrt{k})f_v}{\sigma}\rho_l\rho_v\sqrt{\frac{2(P_v-P)}{3\rho_l}}\ \ if\ P > P_v \tag{2.3-28}$$

Where k is the local kinetic energy, $F_{vap} = 0.02$, $F_{cond} = 0.01$. The saturation pressure is corrected by an estimation of the local values of the turbulent fluctuations;

$$P_v = P_{sat} + \frac{1}{2}(0.39\rho k) \tag{2.3-29}$$

This model has taken into consideration the effects of turbulent pressure fluctuations and the non-condensable gases while assuming the liquid-vapour mixture to be compressible. It was validated by Li [68] proving its capability in predicting inception cavitation with accuracy. The effect of considering the non-condensable gas has no effect on the head-NPSH$_A$ relationship until the concentration exceed above 15ppm.

Zwart-Gerber-Belamri Model

The Zwart-Gerber-Belamri model is also based on the Rayleigh-Plesset equation which describes the growth of a single vapour bubble in a liquid. In their model, they assumed that all bubbles in a system are of the same size, hence proposing that total interphase mass transfer rate per unit volume (R) is calculated using bubble density numbers n and the mass change rate of a single bubble [69]:

$$R = 4n\pi {R_B}^2\rho_v\frac{DR_B}{Dt} \tag{2.3-30}$$

Replacing n with the expression obtained from rearranging the equation for α in Eqn. 2.3-12, we obtain the following as an expression for the net mass transfer:

$$R = \frac{3\alpha\rho_v}{R_B}\sqrt{\frac{2}{3}\frac{P_B - P}{\rho_l}} \tag{2.3-31}$$

A comparison of this expression with the one obtained under the Singhal et al. [67] model points out that the only available difference is in the density terms. In the Zwart-Gerber-Belamri model, the unit volume mass transfer rate is only related to the vapour phase density with no dependency on both liquid phase and mixture densities.

The above formulation of R has been derived assuming bubble growth, hence the need for the following generalisation to be applicable to bubble collapse:

$$R = F\frac{3\alpha_v\rho_v}{R_B}\sqrt{\frac{2|P_B - P|}{3\rho_l}}sgn(P_B - P) \tag{2.3-32}$$

Where F is an empirical calibration coefficient of value 50 for bubble growth and 0.001 for bubble collapse. Even though the above expression for R was derived assuming bubble growth, it is physically incorrect and numerically unstable during evaporation phase. This is because it was assumed that cavitation bubbles do not interact with each other, an assumption that is only reasonable during the earliest stages of cavitation growth from the nucleation site. As the vapour fraction increases, the nucleation site density decreases accordingly. As such, Zwart et al. [69] proposed to replace α_v with $\alpha_{nuc}(1 - \alpha_v)$ in the above expression.

Therefore, if $P \leq P_v$,

$$R_E = F_{vap}\frac{3\alpha_{nuc}(1 - \alpha_v)\rho_v}{R_B}\sqrt{\frac{2(P_v - P)}{3\rho_l}} \tag{2.3-33}$$

If $P > P_v$,

$$R_c = F_{cond}\frac{3\alpha_v\rho_v}{R_B}\sqrt{\frac{2(P_v - P)}{3\rho_l}} \tag{2.3-34}$$

The value of R_B is assumed to be equal to 1×10^{-6}m and α_{nuc} is taken to be equal to 5×10^{-4}. This model, like the Rayleigh-Plesset model, has been widely used in cavitation modelling for turbomachinery. In the work of Lei et al. [61], the Zwart-Gerber-Belamri representation of the mass transfers for vaporisation and condensation rates was used in the modified cavitation model yielding a good quantitative agreement with experimental data in the range 0.76 to 1.2 of the design flow rate, with maximum errors smaller than 5%. Likewise, Wu et al. [70] and Fu et al. [62] utilised this model in their studies of cavitation in centrifugal pumps with a deviation between simulated and experimental data of within 3% and 6% respectively.

Tao et al. [71] made use of this cavitation model to study inception and critical cavitation in a pump-turbine unit and there was a good agreement between experimental and simulation data. The Zwart-Gerber-Belamri model makes a recommendation of the bubble diameter and the nucleation site volume fraction parameters that must be set. This model recognises that the dynamics of bubble collapse are complex and dependent upon a variety of factors such as surface tension, viscous effects and non-condensable effects [69].

Schnerr and Sauer Model

Schnerr and Sauer [72] follows a similar approach as Singhal et al. [67] to obtain the expression for the net mass transfer from liquid to vapour. The following is the general form of the equation for the vapour volume fraction they used:

$$\frac{\partial}{\partial t}(\alpha\rho_v) + \nabla.(\alpha\rho_v V) = \frac{\rho_v\rho_l}{\rho}\frac{D\alpha}{Dt} \tag{2.3-35}$$

In this equation, the net mass source term is represented by the right-hand side term:

$$R = \frac{\rho_v\rho_l}{\rho}\frac{D\alpha}{Dt} \tag{2.3-36}$$

Unlike the prior explained models, Schnerr and Sauer [72] connects the vapour volume fraction to the number of bubbles per volume of liquid using the following equation:

$$\alpha = \frac{n_b\frac{4}{3}\pi {R_B}^3}{1 + n_b\frac{4}{3}\pi {R_B}^3} \tag{2.3-37}$$

Following a similar approach to Singhal et al. [67] they obtained the following equation for the mass transfer rate *R*:

$$R = \frac{\rho_v\rho_l}{\rho}\alpha(1-\alpha)\frac{3}{R_B}\sqrt{\frac{2(P_v - P)}{3\rho_l}} \tag{2.3-38}$$

Where R_B is the bubble radius and is given by:

$$R_B = \left(\frac{\alpha}{1-\alpha}\frac{3}{4\pi}\frac{1}{n}\right)^{\frac{1}{3}} \tag{2.3-39}$$

From the above equation it can be inferred that the mass transfer rate is proportional to $\alpha(1-\alpha)$ in contrast to the Zwart-Gerber-Belamri model and the Singhal et al model. As such from the function $f(\alpha_v, \rho_v, \rho_l) = \frac{\rho_v\rho_l}{\rho}\alpha(1-\alpha)$ in the right-hand side of the above equation (Eqn. 2.3-38), it is noticeable that $f(\alpha_v, \rho_v, \rho_l)$ approaches zero when $\alpha = 0$ and when $\alpha = 1$, and reaches its maximum value in between.

The only unknown in the mass transfer rate equation (Eqn. 2.3-38) is the number of spherical bubbles per volume of fluid. As such if no bubbles are created or destroyed, the bubble number density would be constant. Consequently, using initial conditions for the nucleation site, volume fraction, and the equilibrium bubble radius, the bubble number density can be specified yielding the following form of this model, which is also applicable during bubble collapse:

$$R_{E,C} = \frac{\rho_v \rho_l}{\rho}\alpha(1-\alpha)\frac{3}{R_B}\sqrt{\frac{2(P_v - P)}{3\rho_l}} \tag{2.3-40}$$

The Schnerr and Sauer Model have not been widely used in modelling cavitation for turbomachinery applications.

2.3.3.2. Cavitation in Pumps and Turbines

Since the widespread use of PATs is relatively recent, much work has been focused on their hydraulic performance and much effort has been based on determining their optimum operation points. Binama et al. [73] provides a comprehensive review of such research works. Most of the research work on cavitation has been concentrated on the pumping mode of a centrifugal pump and Binama et al. [74] provides a review of such work.

Unsteady cavitation flows were studied under off-design conditions in pumping mode of a centrifugal pump in Lei et al. [61]. They combined the modified cavitation model and the RNG k-ε turbulence model to simulate the cavitation flows in a centrifugal pump. The modified cavitation model consisted of the use of transport equation based full cavitation model to solve the liquid-vapour mass transfer due to cavitation in which the mass transfers for vaporisation and condensation rates are modelled as per the Zwart-Gerber-Belamri model. The results indicate a shift of pressure pulsation's dominant frequency component from the rotational frequency, f_n, to $0.4f_n$ and $0.5f_n$ at partial discharge.

In Lu et al. [75], cavitation development and associated pressure pulsations in pump mode of a centrifugal pump, at both the inlet and outlet, were studied. The approach taken in this work was to use the full cavitation model to express cavitation coupled with the k-ε turbulence model. The changes in pump inlet and outlet pressure pulsations indicated the occurrence of cavitation with inlet pressure pulsations more consistent with cavitation occurrence. At pump inlet, pressure pulsations appeared as broadband pulsations with dominant component moving from the shaft rotation frequency towards the low frequency zone.

Li [68] numerically investigated the inception cavitation behaviour and cavitation performance of an experimental centrifugal pump using a combination of both a CFD code and the full cavitation model. The comparison of the predicted required net positive suction head ($NPSH_R$) and the experimental value shows dependency on the flow rate. The non-condensable gas is unable to change the head-$NPSH_A$ curve and the $NPSH_R$ until it surpasses 15ppm. The results also show consistency between observed cavitation inside the impeller and the CFD visualisations under the design conditions.

On the other hand, Rakibuzzaman et al. [65] investigated cavitation performance in a multistage centrifugal pump utilising both numerical and experimental techniques. They coupled the Rayleigh-Plesset cavitation model to the SST k-ω turbulence model to describe the fluid behaviour inside the pump. It was realised that cavitation occurred on the pump impeller blades at lower suction head leading to reduced efficiency. Cavitation first occurred at the blade leading edge in the suction side with the cavity increasing in length with reduction in $NPSH_a$.

Lu et al. [76] investigated pressure pulsations, vibration characteristics and internal flow instabilities under unsteady cavitating conditions both numerically and experimentally in a centrifugal pump. For the numerical modelling of cavitation inside the pump, they adopted the same approach used by Lu et al.[75]. Results reveals asymmetric and uneven cavity volume distributions on each blade as the $NPSH_A$ is reduced past cavitation inception. The dominant frequencies of the inlet and outlet pressure fluctuations are the shaft rotating frequency, f_n and the blade passing frequency (BPF). There is an obvious corresponding relationship between vibration root mean square (RMS) values in different positions and the suction curve.

Furthermore, using a similar modelling approach to the one presented in Lu et al. [75], Lu et al. [77] numerically and experimentally investigated cavitation induced vibration and instabilities in a centrifugal pump during cavitation generation and development. Their results revealed that the formation, collapse and shedding of cavitation, and the rotor-stator interaction were responsible for the occurrence and intensification of flow instabilities. Vibration signals were regarded as the characteristic signals to detect the inception and development of cavitation in centrifugal pumps. Cavitation occurrence was corresponding to 0.59% head drop which is much smaller than the traditional critical cavitation points which correspond to 3% head drop.

In Zhang et al. [78], pressure pulsations under cavitating conditions, pressure amplitudes at the blade pass frequency and RMS values in the 0-500Hz frequency bands were combined to investigate cavitation induced pressure pulsations. High frequency response pressure transducers were mounted on the side wall on threaded holes located between the impeller and the volute inlet area to monitor pressure pulsations. An additional pressure transducer was mounted at the suction pipe. Cavitation was simulated experimentally by using a vacuum pump to extract air from the water storage tank and gradually reducing the pressure in the experimental setup.

The results of this work indicated that for monitor points located in the pump volute, thus further away from the cavitation region, a predominant blade passing frequency can be noted along with its harmonics. Its amplitude increases when moving from non-cavitating to cavitating conditions. A probe into the pressure energy for the suction pipe mounted transducer indicates that it initially remains unchanged and then it rapidly decreases at cavitation number range, and it finally rises when the cavitation number are dropped below the critical cavitation number. This is associated with the cavitation structure change from a vapour phase (compressible) to liquid phase (incompressible).

Zhang et al [79] studied vibration energy trends in various frequency bands with the aim of clarifying cavitation induced vibration characteristics in a centrifugal pump with slope volute. Several accelerometers were mounted on the surface of slope volute to obtain vibration data. Absolute static pressure in the storage tank was reduced gradually using a vacuum pump to lower the $NPSH_A$ of the centrifugal pump. Vibration levels were associated with the flow structure inside the pump. They showed that cavitation has a significant impact on low frequency signals. A rise in vibration levels after inception point was observed which then dropped and raised again when the cavitation number is reduced further. The 3% head drop criteria was found to be indicative of cavitation when its already in the developed phase, which make it insufficient to avoid cavitation related failures. As such analysis of high frequency signals was deemed suitable for use in the detection of inception cavitation.

Mais [80] stated that cavitation is characterized by random broadband energy between 20k and 120k CPM, which can cause excessive system wear. Ayli [81] provided a review of cavitation studies on hydro turbines both experimentally and numerically. The review covers Pelton turbines, Kaplan turbines and Francis turbines but does not cover PATs and it calls for further studies on cavitation phenomena in hydraulic machinery. In analysing the local structure of the flow in a Francis turbine, Minakov et al. [82] showed that the low frequency pressure pulsations in water turbines are mainly caused by a precessing vortex rope downstream of the runner. Like both conventional turbines and centrifugal pumps, PATs can also suffer cavitation, but this phenomenon is not as well understood as in the prior mentioned machines.

Singh [83] presented an alternate methodology to study cavitation in PATs, the Combined Suction Head Number (CSHN), and demonstrated that through this methodology PAT cavitation behaviour can be represented with a single dimensionless curve. Alatorre-Frenk [84] explored the incidence of cavitation in PATs by comparing their critical Thoma number with that of conventional turbines and showed that cavitation is slightly worse in PATs than in conventional turbines of similar specific speed.

Li and Zhang [85] studied cavitating flows and cavitation behaviour in turbine mode of a centrifugal pump using CFD techniques. They used a combination of the full cavitation model [67] and the k-ε turbulence model to represent the fluid behaviour inside the pump. A comparison of the model performance and experimental data shows that the model overpredict the head and hydraulic efficiency by 9.2% and 7.4% in maximum. Cavitation performance in turbine mode was compared with pumping mode and distinct differences were identified. The NPSHR in turbine mode was found to be around half that in pump mode with less dependency in flow rate. The cavity in turbine mode presented itself as a sheet at the blade suction side and a rope originating from the impeller cone while in pump mode is dominantly sheet cavitation.

Furthermore, Rakibuzzaman et al. [66] investigated cavitation performance of a pump in both pumping and generating modes and found that in turbine mode, cavitation propagated itself from the centre of the impeller and distributed to the trailing edge in the blade suction side as compared to propagating from the leading edge on the suction side towards the trailing edge on the pressure side of the impeller blade in pumping mode. They coupled the Rayleigh-Plesset cavitation model to the SST k-ω turbulence model to describe the fluid behaviour inside the pump. Validation of the simulation results with experimental data indicates an average deviation of 3.01% and 3.63% for the head and efficiency respectively. The obtained maximum deviations for head and efficiency are 12.67% and 8.53% respectively.

Jain et al [86] experimentally investigated cavitation in a pump-as-turbine and found out that when the non-dimensional speed defined by the ratio between the actual speed and the rated speed is between 0.79 – 0.86, the detected vibration levels remain lower. At higher speed ratio of around one vibration was found to be higher and the cavitation number below the critical cavitation number, indicating a higher risk of the inception of cavitation at rated operating speeds. As such, they recommended operation of a PAT below the rated speed for better cavitation performance. They limited their vibration analysis to the monitoring of the f_n and the BPF, which indicated a possibility of travelling bubble cavitation on blade suction side, von Karman vortex cavitation on blade trailing edge and a vortex rope cavitation near the outlet pipe inlet. Further indepth analysis of the other frequency components is necessary to gain an overall understanding of the PAT's cavitation behaviour.

The previous investigations mentioned have examined cavitation in PATs in the micro-hydropower scale while no investigations have been conducted to date on this phenomenon in the pico-hydropower scale (<5kW), despite the abundance of such hydropower potential in practice [87]. This depicts a gap in literature that will require some attention to ascertain the cavitation behaviour and performance of a PAT in the pico-hydropower scale.

Cavitation is associated with pressure pulsations and uneven load distribution that can seriously affect machine efficiency and operational stability [61, 76]. Low-level pressure pulsation presents no detrimental effect to a machine, however when pressure pulsations are excessive, they can result in severe damages [88]. Excessive pressure pulsations may cause dynamic loading of machine components, excessive vibration and noise. Even though that is the case no study exists investigating cavitation induced pressure pulsation in PATs. Duan et al [89] pointed out that for an axial-flow pump, pressure pulsations are an important excitation source for vibration. It is against this backdrop that we point out the need for a study of cavitation induced pressure pulsations leading to understanding of cavitation induced vibrations.

2.4. MAINTENANCE STRATEGIES

The process of maintenance is a very important aspect in any production or manufacturing operation including in micro-hydropower generation. It is described as the management, control, execution and quality of those activities which will reasonably ensure that design levels of availability and performance of an equipment is achieved in order to meet the business objectives. It is imperative to define availability as it appears in the maintenance definition stated. Availability is the ability of a piece of equipment to perform its required function at a stated instant of time.

For many years the way maintenance is conducted has evolved influenced by the need to cut costs and increase the effectiveness of equipment. This has seen a paradigm shift from a completely reactive maintenance approach to a proactive maintenance philosophy. There are three main types of maintenance strategies that can be utilised in taking care of machines namely, reactive, preventive and predictive maintenance.

These strategies have been described in literature under differing names but all having the same meaning as described in the following sections. Mobley [90] make use of the phrase corrective or breakdown maintenance while Mobley [91] uses the phrase run-to-failure to describe a reactive maintenance philosophy. Some authors use the phrases time-based maintenance and condition-based maintenance to describe preventive and predictive maintenance respectively. The decision on which is the optimum maintenance strategy is based on the balance between maximum possible availability and reliability[92].

2.4.1. Reactive Maintenance

This maintenance strategy is based on the philosophy that "if it ain't broke, don't fix it" or "fix it when it breaks". Mobley [91] call it a "no maintenance" approach as the only time when failure of an equipment is being investigated is when it occurs. This is usually unexpected, and it tends to present high costs as compared to other maintenance strategies. The costs associated with this maintenance strategy are tied to spare parts inventory cost, overtime labour costs and lost production costs.

2.4.2. Preventive Maintenance

Preventive maintenance entails the scheduling of maintenance activities after a predetermined period. This period is dependent upon the elapsed time in calendar months or hours of operation. The schedules are decided based on the mean-time-to-failure statistic[91], which is defined as the ratio of the cumulative operation time to the total number of failures over a stated period in the life of an equipment [52].

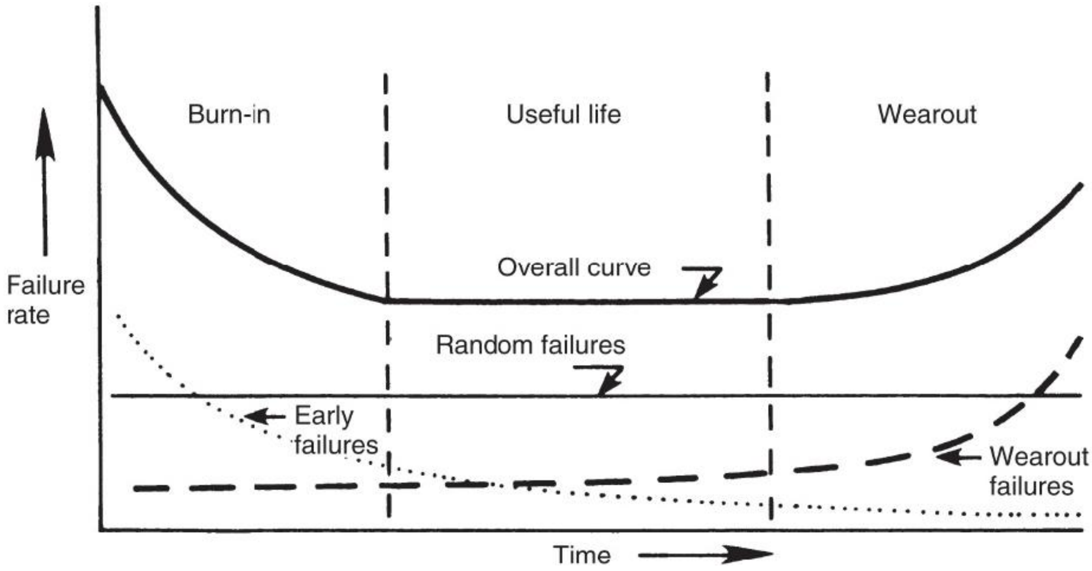

Figure 2.4-1. The bathtub curve

The bathtub curve or the MTTF curve shown in Fig. 2.4-1 [52] indicates that an equipment has a high probability of failure early on in its life, a phase termed infant mortality rate. These failures decrease until they flat out in the phase known as useful life phase where the failure is constant due to the occurrence of random failures. During the later stage of equipment life failures increase sharply because of the increase in wear out mechanisms.

The fact that maintenance activities are scheduled based on the average life of a component can be a disadvantage as different failure modes are treated as a single classification. As a result, some machines tend to fail before the arrival of the scheduled time leading to costs associated with downtime and unscheduled works. Moreover, most parts are replaced while they still have some useful life remaining that yielding waste and increasing the annual maintenance costs due to spare parts acquisition and warehousing.

2.4.3. Predictive Maintenance

Realisation of the wastage and over maintenance that result due to use of the preventive maintenance strategy has led to the development of the predictive maintenance strategy bridging most of the gaps that resulted from the prior mentioned strategies. Predictive maintenance relies on the data obtained from the operating machines to decide on what maintenance activities to perform and at what frequency.

ISO 9001:2015 [93] talks of evidence-based decision making, as decisions made based on the analysis of information and data are more likely to produce desired results. This principle is also applicable in maintenance and predictive maintenance is the strategy of choice in ensuring that this is realised. Maintenance decisions are all supported by evidence of deterioration obtained from the analysis of condition monitoring data.

Data is obtained from machines through the usage of sensors, which monitor machine operating condition, system efficiency and other machine health indicators [94] and is used to determine the actual mean-time-to-failure or performance degradation. As a result, maintenance actions are carried just in time to avoid costly downtimes hence prolonging uptime. This just-in-time approach to carrying out maintenance also reduces the costs associated with warehousing of spare parts, as spares are only ordered when they are needed.

In a recent study carried out by Deloitte Analytics Institute[95], it was found that predictive maintenance brings about material cost savings amounting to 5 to 10% on average while increasing the equipment uptime by 10 to 20%. It was also concluded that as a result maintenance costs are reduced by 5 to 10%, also reducing maintenance planning time by 20-50%. Even though Predictive Maintenance is associated with these advantages, its application also presents some negative points.

Dependency in data means that the quantity and quality of it may be a limiting factor to the implementation of a predictive maintenance programme. To adequately analyse root causes of failures and predict future failure events requires abundance of failure information, which is usually lacking especially for organisation that have no history of collecting failure data. The establishment of processes needed for Predictive maintenance also bring costs which can be high initially. In the long run the benefits of the implementation of predictive maintenance can be realised outshining the early setup costs.

PWC and MAinnovation [96] also surveyed companies from Belgium, Germany and Netherlands to get an idea of their current state and future plans regarding predictive maintenance. Four levels of maturity in predictive maintenance were identified namely, Visual Inspections (Level 1), Instrument Inspections (Level 2), Real-time Condition Monitoring (Level 3) and Predictive Maintenance with Big Data Analytics (Level 4).

Their results indicate that two thirds of the respondents are still at level 2 of maturity in predictive maintenance with only 11% at level 4. They also note the highest level of ambition from respondents about improving their maturity level and they forecast that one in three companies will be at level 4 in 5 years duration. These are quite interesting findings and can be used to dictate the maintenance strategies for the next generation of equipment.

Maintenance of this equipment will be mainly based on predicting their failures and ultimately prescribing the most effective preventive measures by applying advanced techniques on big data[96]. This will certainly lead to increased equipment life, increased uptime, reduced maintenance costs, motivated employees and reduced impact on the environment.

2.5. VIBRATION MONITORING BASED FAILURE DETECTION AND DIAGNOSIS

In predictive maintenance or condition-based maintenance, fault detection is one of the three tasks that describe the diagnosis process as outlined in the EN 13306 standard [97]. The other tasks that come after fault detection are fault isolation and fault identification, herein referred to as fault diagnosis. Fault detection refers to the determination of an abnormal operating condition of the system [98], while diagnosis means isolating the fault and identifying its cause.

Early fault detection may provide invaluable warning on emerging problems, with appropriate actions taken to avoid serious consequences [99]. Usually, an impending failure condition manifest itself in a machine way before the total failure occurs. When a fault begins to develop in a machine, some of the dynamic processes in the machine changes as well, resulting in a noticeable change in important machine condition and operating parameters such as vibration, pressure and temperature. Condition monitoring techniques such as vibration analysis, thermography, lubrication analysis, acoustic analysis etc., are used to identify such changes in dynamic processes leading to early detection and identification of developing faults.

Vibration analysis offers an upper hand in machine condition monitoring as it is capable of detecting, locating and distinguishing faults while offering the capability for application to inaccessible components. It also allows a non-destructive approach to data collection offering a massive amount of information contained in the obtained vibration signatures. According to the ISO 13373 standard [100], changes in the machine vibration behaviour can be caused by mechanical, electrical and hydraulic causes. Mechanical causes include changes in balance, alignment, wear or damage in journals or anti-friction bearings, gear or coupling defects, cracks, rubbing and mechanical looseness. Hydraulic causes relate to fluid-flow disturbances in hydraulic machines, while electrical causes are associated with transient excitations in electrical machines.

ISO 13371 [100] also outlines the following purposes for which the information obtained from using vibration analysis in a condition monitoring system can be used for; increasing equipment protection, improvement of personnel safety, improving maintenance procedures, early detection of problems, avoidance of catastrophic failures, extension of equipment life and enhancement of operations. In hydraulic machines, such as PATs, all these benefits can be realised when both mechanical sources and hydraulic sources of vibration are considered in developing predictive maintenance systems for such machines.

Vibration analysis-based fault detection is reliant on techniques such as trending and comparative analysis of obtained vibration data. Trending can be classed as either broadband or narrowband. The validity of trending of historical vibration data is reliant on accurate normalisation to remove effects of variables such as speed and load on the vibration energy levels[91]. As such, valid trending of vibration data can indicate over time a change in machine condition. Trending of broadband vibration monitors the overall machine vibration for all operating frequencies whereas narrowband also monitors overall vibration but at predetermined frequency bands. The use of narrow bands increases the usefulness of the data and provides the ability to monitor, trend and set alarms for specific machine train components hence improving the accuracy of detecting incipient faults.

On the other hand, comparative analysis is dependent on the availability of baseline data, industrial reference data or known machine condition data. For each machine train that is to be included in the predictive maintenance program, baseline data sets are captured at installation or immediately after completion of a first scheduled maintenance after the program was established. This baseline data sets will be used as a reference for comparison purposes with the machine condition data at the time of measurement. Any dissimilarity between the two can be an indication of a fault condition.

Known machine condition data can be used for comparison purposes for detection of some known failure conditions. In this scenario, data collected from a suspected failure of a machine is compared with data from a known failure condition for identifying a machine fault condition. Industrial reference standards such as the ISO 2372 (later replaced by ISO 10816 and superseded by ISO 20816) provides a reference criterion for comparison purposes with the actual machine conditions, as such they can be used as a basis for a vibration analysis-based detection system.

2.5.1. Time Domain-Based Analysis Techniques

Time-domain data consists of contributions from all vibration components in the machine train and the whole installed system. Even though time domain data can help detect an anomaly, components are difficult to isolate hence the difficulty in identifying the fault condition from time domain data. While the use of frequency spectrums obtained from transformed time waveforms is prevalent in fault detection, the adoption of time domain vibration response for fault detection has been limited. Nonetheless, methods derived from time domain vibration signals such as PeakVue®, Root Mean Square (RMS), kurtosis and some pseudo fractal-based techniques have been developed for fault detection purposes and sometimes, time-domain based methods dependent on probability density functions (PDF) have been presented.

2.5.1.1. Vibration Amplitude

Techniques such as the PeakVue® method [101] are dependent on the use of vibration amplitude in time domain to indicate the occurrence of a fault condition. The PeakVue® method involves filtering out low frequency components from the raw vibration signal via a high order high pass analog filter and sample out peak values over a specified total time. PeakVue® analysis method uses the trending of the peak-to-peak values of the time domain data for both fault detection and severity assessment.

Besides the commercialised PeakVue® method, other vibration amplitude-based techniques for time domain-based analysis of vibration signals include Peak and Peak-to-Peak values that are used to detect sudden spikes caused by impacts in the signal. The Peak value present the largest amplitude value present in the signal. It does not account for total signal energy, any fluctuations or a transient behaviour in the signal. Peak-to-Peak value is associated with the difference between the maximum peak and the minimum peak of the signal. Changes in these two parameters may be indicative of impacts in the signal. Al-Obaidi [102] described the use of vibration amplitude in both time domain and frequency domain as the threshold for cavitation detection.

2.5.1.2. Root Mean Square (RMS)

The use of vibration criteria such as the ISO 20816 standard are based on overall (RMS) vibration levels of the measured signal [103]. ISO 20816-1 [104] gives the recommended ranges of boundary values for different vibration severity zones. This allows the setting up of alerts and alarms for change of machine vibration from one severity zone to the other indicative of faults in the machine or change in operation conditions. Such standards provide broad guidelines, but real-world machines often operate under unique conditions.

The limits may be too conservative or too lenient for specific machines or operating environments leading to either unnecessary maintenance conducted or missing out early signs of failures. The other limitation of the use of the standard for predictive maintenance purposes may arise from the focus on overall levels of vibration without diagnosis of the root cause. The RMS value has proven to be a very useful parameter in fault monitoring as it tends to evolve as the fault progression occurs. However, it might be limited in the detection of incipient failures as it shows little change in the early stages of mechanical failures.

$$x_{rms} = \sqrt{\frac{1}{N}\sum_{1}^{N}|x_i|^2} \tag{2.5-1}$$

The RMS value as described in Eqn. 2.5-1 is the most common value used when a single value needs to be used to describe a dynamic signal [105]. It tells us about what the square root of the mean square of the signal is. This is useful as it is directly related to the energy content of the vibration profile, thus also describing the destructive capability of a vibration signal. In vibration analysis, the RMS value can be converted to other units of amplitude such as Peak by multiplying by a factor of $\sqrt{2}$. This assumes sinusoidal behaviour.

2.5.1.3. Crest Factor

Crest factor, *CF,* is defined as the ratio of the signal's peak amplitude value to its RMS value. It's used to indicate the quality of the signal and to show if a signal contains a great deal of peaks [106]. The latter use is most useful in condition monitoring purposes and if a signal is found to show a greater deal of peaks can indicate the existence of or development of a fault condition. Equation 2.5-2 shows how the crest factor is computed with x_p representing the peak amplitude while x_{rms} is the signal RMS value.

$$CF = \frac{x_p}{x_{rms}} \tag{2.5-2}$$

For a sinusoidal signal, the crest factor is equal to 1.414 and the deviation away from sinusoidal form of a signal leads to either a higher or lower value of the crest factor. A higher deviation of the crest factor from its normal values can be considered a sign of increased peaks in the signal indicative of a failure occurrence.

2.5.1.4. Kurtosis

Kurtosis evaluates how peaked or how flat a signal distribution is. It is widely used to identify non-periodic impacts. The idea is that a high kurtosis value indicates the high impulsive component of the signal with more sharpness in the signal intensity distribution [107]. It's a useful parameter for bearing fault analysis and its usefulness in vibration signal analysis has been demonstrated in [108-111]. The usefulness of kurtosis in vibration-based fault analysis indicates the importance of probability distributions in the detection and diagnosis of faults in machines. As such, methods utilising probability distributions have been proposed for fault detection purposes [112-114].

$$k = \frac{\frac{1}{N}\sum_1^N (x_i - \mu)^4}{\sigma^4} \tag{2.5-3}$$

The computation of the Kurtosis, *k,* is as per Eqn. 2.5-3 with x_i being the individual signal data point, μ is the mean of the signal and σ is the signal's standard deviation. N represent the total number of data points in a signal. The natural kurtosis of the normal distribution is equivalent to 3 and sometimes this is deducted from the computed value using the above equation to ensure that the excess kurtosis of a normal distribution equates to zero. In practical terms, if kurtosis is greater than zero it means that the distribution consists of high or sharp peaks about the mean and heavier tails while values lower than zero indicate a distribution with flatter peaks about the mean and thinner tails.

2.5.1.5. Skewness

Skewness is a statistical measure that describes the asymmetry of a signal' probability distribution relative to its mean [115, 116]. Boylan and Cho [117] indicated that for a skewness value greater than zero the right tail of the distribution is longer and heavier, and the preponderance of values generally lies to the left of the mean while for a skewness value less than zero implies a heavier and longer left tail with most values laying to the right of the mean. In vibration analysis, skewness quantifies how much a signal deviates from being symmetrical, indicating whether high-amplitude events are biased toward the positive or negative values [116]. It is described by Eqn. 2.5-4, and it comprises the third central moment.

$$S_k = \frac{\frac{1}{N}\sum_1^N (x_i - \mu)^3}{\sigma^3} \tag{2.5-4}$$

Healthy rotating machines tends to produce vibration signals with low or zero skewness indicating symmetric distribution of vibrations. However, once the machine health condition changes to faulty, some level of asymmetry is observed which indicates an increase in the magnitude of the skewness value.

2.5.1.6. Other Probability Distribution-based Methods

Time domain parameters such as kurtosis and skewness characterise the signal's probability distribution. Even though these parameters have demonstrated usefulness in vibration-based fault detection and diagnosis, individually they don't offer an overall description of the signals PDF. As such other techniques have been proposed in literature that attempts to provide an overall description of the signal's PDF.

Vibration signals obtained from rotating machines can be classed as either deterministic or random. Deterministic signals can be predicted through a mathematical function whereas random signals cannot be predicted at any future instant. When obtained from a cavitating machine, vibration signals can be either deterministic, characterized by a change in the vibration energy of a specific frequency band, or random in nature indicated by a change in the overall vibration levels [118-120]. It is usually convenient to utilize the concept of probability density functions to gain further understanding of signals. PDFs are defined by the value of instantaneous amplitude within a certain interval divided by the size of that interval [121].

The actual PDF of a dataset is usually unknown; therefore, an estimate of the general PDF must be obtained. This can be carried out through either a parametric or a non-parametric approach. Parametrically, the data is assumed to be sampled from a known distribution such as the Gaussian distribution whereas in a non-parametric approach PDFs are estimated by adapting the data via means such as the use of histograms and use of estimators such as naïve, kernel and nearest neighbour method [122]. Al-Hashmi [121] reported that the PDFs of vibration data captured from a cavitating pump exhibit high count around the mean amplitude, spreading out symmetrically as amplitude increases in both positive and negative direction indicating closer resemblance to the Gaussian distribution. It is as such that we assume a Gaussian PDF for our study case as the PDFs follow a similar characteristic. The Gaussian distribution is expressed as per Eqn. 2.5-5 [121]:

$$f_n(x) = \frac{1}{\sigma\sqrt{2\pi}} e^{\left(\frac{-(x-\mu)^2}{2\sigma^2}\right)} \tag{2.5-5}$$

and the true density function of the data is obtained by substituting its mean (μ) and standard deviation (σ) into the expression. Similarly, a histogram estimator can be used to obtain the signals actual PDF, which is defined by:

$$f_a(x) = \frac{1}{M} \times \frac{(number\ of\ x_1 in\ same\ bin\ as\ x)}{(width\ of\ bin\ containing\ x)} \tag{2.5-6}$$

where M represents total number of data points and x represents individual data points in the signal.

Boylan and Cho [117] presented a comprehensive demonstration and analysis of how various statistical properties within a data set can influence the shape and corresponding properties in a normal probability plot (NPP). Umesh and Ganguli [123] used the NPP of the PDF to show the difference between the dispersions of damaged and undamaged cases when studying the effect of uncertainty on the structural health monitoring of a smart composite plate with matric crack.

The normal probability plot (NPP) graphically assesses normality of a dataset. The relative cumulative frequencies of the data are demonstrated by plotting the data on a straight line and comparing the quantiles of the observed data with that of the theoretical distribution, i.e., a Gaussian distribution. The shape of the curve in the NPP and the way it deviates from the reference line provides information about the characteristics of the actual distribution in terms of the first four sample moments i.e., mean, variance, skewness and kurtosis [117].

If $[x_1, x_2, \dots, x_n]$ represents an ordered sample of data and $F(X) = (x - \mu/\sigma)$ represents its cumulative distribution function with μ being the mean and σ the standard deviation, the abscissa of the NPP is the sample ordered statistics x_i, and the ordinate is the inverse of the normal cumulative distribution function (CDF) $Z_i = F^{-1}(p_i)$ where p_i is the cumulative probability associated with each rank-ordered data. The cumulative probability can be obtained using Eqn. 2.5-7 as proposed by Blom [124], where i represents the rank order number and n represents the number of data points.

$$p_i = \frac{i - 0.375}{n + 0.25} \tag{2.5-7}$$

In Sharma and Parey [125], a fault detection method was proposed using entropy measurement and a modified PDF. Moreover, Rzeszucinski et al [114] proposed some condition indicators for gearbox fault detection and monitoring based on the amplitude of the Gaussian PDF. In order to quantify the changes observed in a PDF when the machine condition moves from healthy to faulty, Rzeszucinski et al [112] proposed the deviation from the normal distribution (DND) technique. They used this technique to compare and quantify the actual PDF of a signal with its normal PDF during heathy and faulty operation for condition monitoring purposes. Asnaashari and Sinha [113] proposed utilizing the DND of vibration signals to detect cracks on beamlike structures, modifying the DND further to make it suitable for application in recognizing discontinuities related to crack locations. With further modification the technique could be applicable in the detection of a variety of machine faults by quantifying the changes they present to the signals PDF.

2.5.2. Frequency Domain-based Analysis

Frequency domain analysis of vibration signals by means of Fourier transform is the dominant technique in vibration analysis-based fault detection and diagnosis even though it provides average information that ignores the time varying nature of fault signals. As a result of continued research and development in the sensing and data acquisition techniques, a myriad of signal processing techniques has emerged over time. These include techniques based on the Hilbert transform, time frequency methods such as short-time Fourier transform, wavelets and empirical mode decomposition, and have proved their worth in structural health monitoring applications. Nagarajaiah and Basu [126] reviewed these techniques in detail and proposed a method of identifying multi-degree of freedom linear time invariant and linear time variant systems based on such time frequency techniques.

As compared to time domain data, frequency domain data can be useful in both detecting and diagnosing failure conditions in a machine train. A comparative analysis of amplitudes of frequency components of a baseline, reference or known machine condition data and the captured frequency data of the machine can yield valuable information as to the condition of the machine hence indicating failure conditions when they exist. Frequency domain data unlike time domain data can also provide diagnostic information as different machine faults manifests themselves at distinct frequency peaks. This make it easy to isolate the fault, something that is not easy when only dealing with time domain data.

2.5.2.1. Discrete Fourier Transform

A time-domain signal is converted into frequency domain through a Discrete Fourier Transformation (DFT) process, making it possible to identify the represented frequencies in the data. In general, the Discrete Fourier Transform (DFT) takes a digitized time signal x_k, $k = 0, 1, 2, \dots, N-1$ and transforms it into an N length complex valued vector Y_m, $m = 0, 1, 2, \dots, N-1$. Practically, this is achieved through the Fast Fourier Transform (FFT) implementation. It is defined by [127, 128];

$$Y_m = \sum_{k=0}^{N-1} x_k . exp\left(-2\pi j \frac{mk}{N}\right), \qquad m = 0,1,2,\dots,N-1 \tag{2.5-8}$$

From this definition of the DFT, it is evident that the amplitude is dependent on the size of the variable N, which is undesirable. Increasing the value of N will result in more and more of the signal utilised to compute the respective amplitude for the specific frequency bin meaning there is a need for normalisation to take care of this issue. For ease of computation the above computation is divided by the value of N but since in this case a window function will be used to deal with problem of leakage in the spectrum, a window-based normalization is adopted. The normalisation factors S_1 and S_2 based on the utilised window function, w_j, are defined by Brandt [105] and Heinzel et al. [127];

$$S_1 = \sum_{j=0}^{N-1} w_j \tag{2.5-9}$$

$$S_2 = \sum_{j=0}^{N-1} {w_j}^2 \tag{2.5-10}$$

The S_1 normalisation factor considers the length N of the DFT and the gain of the window function whereas S_2 normalization factor compensates for the situation where the noise power falls into a single frequency bin hence raising its noise floor and yielding a constant noise floor that is independent of the value of N in the spectral density.

$$PS_{rms} = \frac{2.|Y_m|^2}{S_1^2};\ m = 0,1,2,\ldots,\frac{N}{2} \tag{2.5-11}$$

$$PSD_{rms} = \frac{2.|Y_m|^2}{F_s.S_2};\ m = 0,1,2,\ldots,\frac{N}{2} \tag{2.5-12}$$

The result of the DFT, Y_m, is a complex valued vector of length $N/2+1$, which can be interpreted as a power spectrum (PS_{rms}) according to Eqn. 2.5-11 or the power spectral density (PSD_{rms}) according to Eqn. 2.5-12 where F_s is the signal sampling frequency and rms indicate the unit of measurement. To present the results as a linear form, the square root of the corresponding PS_{rms} or PSD_{rms} is taken. The value 2 in these equations stems from the fact that the FFT is an efficient algorithm that doesn't compute the redundant results of negative frequencies [127].

2.5.2.2. Spectral Bandpower

Spectral bandpower computes the total energy or power of a signal within a specific frequency band of interest from the signal's PSD. This isolates the specific frequency band and analyse its energy making it possible to detect and classify the occurrence of a fault. For instance, localised damage in rolling element bearings typically generates high-frequency components due to impact and resonance effects, which can be quantified using bandpower in predefined frequency bands [129]. These bands are usually selected based on known frequency signatures of specific faults such as bearing defects, gear mesh frequencies or structural resonances.

Its implementation involves the decomposition of vibration signals using the spectral estimation methods followed by the integration over the frequency range of interest. Trending the derived bandpower features can be useful in spotting changes in machine dynamics and it can also be used as part of a machine learning feature matrix.

2.5.3. Application of Vibration Analysis in Cavitation Detection and Diagnosis

Cavitation excites both low frequency pressure oscillations and high-frequency pressure pulses [118]. The resulting low-frequency oscillations can be attributed to the dynamics of the cavity whereas the high-frequency pulses are a result of bubble collapse releasing some shock waves. These affects the vibration response of the machines as vibrations and disturbances are transmitted through the fluid and the structure.

Its detection and diagnosis are of utmost importance in condition monitoring of hydraulic equipment as it has been associated with devastating outcomes such as, damage to material surfaces, flow instabilities and excessive vibrations that can lead to machine performance degradation and even premature failures. According to Koivula et al. [130], cavitation detection can be achieved by directly verifying the existence of cavities. This is only possible if the machine has means of observing visually as the bubbles develop, which is an aspect that is mostly practical on test rig setup but not the full-scale turbine or pump systems. As a result of the complexity in construction of these hydraulic equipment indirect detection of cavitation via pressure, acceleration and acoustic instruments has taken precedence on field applications.

Many studies have been conducted in recent years proposing some means of detecting cavitation in hydraulic machinery before it enters the critical stage where it can have detrimental effects to the machine's operation and health status. These studies are mostly based on turbines and pumps with less focusing on pumps-as-turbine (PATs) [118, 131-134]. The reason being that the wide adaptation of PATs is a relatively new pump application, which researchers have been focusing more on the prediction of their performance characteristics and selection to match site conditions.

The available cavitation detection techniques can be divided into three classes namely, monitoring of the total head or efficiency of the machine, study of the frequency spectrum of the measured data and applying amplitude demodulation techniques to the high frequency pressure and vibration measurements [135]. Monitoring of total head in pumps and hydraulic efficiency in turbines and identifying cavitation when these parameters drop by 3% and 1% respectively, is not a reliable method as it has been found that cavitation incepts before these points and can cause noticeable wear on the impeller surfaces [136-139].

Cavitation bubble implosion results in the production of shockwaves that excites a wide range of frequencies in the high frequency end of the spectrum. As the cavity moves downstream of the flow it excites low frequencies [118]. The use of the frequency spectrum obtained by DFT offers a better alternative as more information can be obtained about the dynamics of the cavity. As such most of the cavitation detection techniques are based on monitoring amplitudes of discrete frequency components and comparison of the spectrum content from a cavitating condition to that of non-cavitating conditions. Some authors quantify the cavitation intensity through the calculation of the signal power content in various frequency bands while others rely on the vibration energy trends in various frequency bands [137, 140].

The application of the amplitude demodulation techniques offers an extension of the spectrum-based cavitation detection methods by filtering out low frequency components from the data and unmasking the modulating frequency components that are related to the dynamics of the developed cavity [118, 141]. This is a widely used technique in cavitation detection, but it involves rigorous computation that involves filtering, Hilbert transformation and computation of the auto power spectrum of the Hilbert transformed data [118].

Valentin et al. [142] applied the FFT, RMS and amplitude demodulation techniques to various sensor data obtained from different locations on a Francis turbine system in order to study hydraulic phenomena such as vortex rope, resonances, instabilities and cavitation. Their results shown that performing an FFT of the signal is not enough to directly obtain the information of what is happening in the machine hence the need for demodulation techniques.

On the other hand, Al-Obaidi [102] studied cavitation occurrence inside a centrifugal pump and concluded that using FFT techniques for signal processing in frequency domain to detect cavitation is an effective approach via the use of waterfall plots. Similarly, Abdulaziz and Kotb [143] suggested monitoring the sharp fluctuations in the overall vibration level for detection of cavitation inception. In the frequency domain, they suggested monitoring discrete vibration levels corresponding to both the rotational speed and the first blade passing frequency. Randal [115] suggests trending of the constant percentage bandwidth (CPB) spectrum instead of either overall vibration levels or FFT spectra.

Escaler et al. [118] pointed out that cavitation detection can be conducted via a comparison of amplitudes of a given high frequency band with a uniform and sharp increase of this band in comparison to the cavitation-free condition indicative of the presence of cavitation. In the low frequency range, they note that cavitation induced fluctuations can be detected through the analysis of the frequency content of the vibration and pressure signals.

It is evident from the analysis of literature that, even though some researchers implemented the FFT in detecting cavitation occurrence in hydraulic turbines, it can only bring about reliable detection when the cavitation status is in the fully developed state, which can be having destructive consequences on the interiors of the machine.

2.6. APPLICATION OF MACHINE LEARNING IN FAULT DIAGNOSIS

Predictive maintenance (PdM) enabled by digital technologies such as artificial intelligence, digital twins and internet of things, aims to shift the conduct of maintenance from a reactive to a proactive approach by leveraging data. Machine Learning (ML) techniques are particularly suited for this due to their ability to identify hidden patterns and anomalies. Anomaly detection is an important feature of PdM that deals with identifying deviations in data that may indicate equipment failure. Vagnoni et al. [144] outlined various anomaly detection strategies in hydropower operations, including adaptive thresholding and alarm set-point adjustment, aimed at identifying deviations from optimal performance.

Several studies have demonstrated the application of ML in hydropower. Brennmoen [145] explored the field of anomaly detection with specific emphasis on using real-world data obtained from a power transformer. The study developed a test case based on key features of winding temperature, hydrogen concentration and active power. Betti et al. [146] developed a novel Self Organizing Map (SOM) Neural Network based key performance indicators for condition monitoring of hydropower plants. The system was setup and tested as part of a condition monitoring system for two hydropower plants in Italy where over 20 anomalous cases were detected in a period of 16 months. In a similar study, Velasquez and Flores [147] proposed two techniques to enable predictive maintenance in the Pena Blanca Hydroelectric power plant namely Deep Neural Network coupled with Logistic Regression and a Recurrent Long Short-Term Memory Neural Network (LSTM) Autoencoder to classify various types of failures.

Using the MATLAB Classification Learner Application, Xayyasith et al [148] demonstrated the applicability of ML using 31-month long maintenance log data for a water-cooling system in a hydropower plant. Better results were obtained from Support Vector Machines (SVM) and Decision trees (DT) models. Lang et al [149] conducted a comprehensive analysis of a hydropower plant using an artificial neural network (ANN) model developed from over three years full scale vibration measurement data. To assess potential model performance degradation, models were developed using datasets from different periods and used to assess discrepancies in future monitoring. It was observed that when statistical distribution of the future monitoring data closely aligned with that of the training set the model performed well, while when there was a significant difference in the statistical distribution of the two sets of data the resultant was irrational predictions and unreasonable trends.

Most of the work has been conducted with focus on rotating machinery in general, not specifically limited to hydropower. Cen et al. [150] conducted an extensive analysis of the current state of ML algorithms in machinery fault diagnostics applications. They categorised ML techniques into three frameworks: shallow ML, deep learning and transfer learning. Shallow ML based diagnostic models consisting of ANNs and SVMs were found to be simple, reliable and fast to implement. Deep learning techniques were found to be capable of providing end-to-end diagnostic services in the presence of large amount of training samples and the pursuit of higher accuracies. Transfer learning-based diagnostic models were associated with the realisation of knowledge transfer across conditions, machines or even fields. It was recommended that a hybrid approach is advisable to leverage on the benefits of different learning frameworks as well as to overcome their limitations.

The performance of different ML algorithms in detecting faults in various rotating equipment components was analysed in [151]. The results indicated the inadequacy of SVM based fault detection methods over large datasets even though it was found to be consistent in diagnosing faults. Deep learning Neural Networks offered better performance while Decision Trees and Random Forest based models were found to require less computational times. Juying et al. [152] realised that to accurately adopt the use of Deep Neural Networks, the issues of imbalance of faults in the dataset, need to reconfigure network structure and the optimization of network scale need to be addressed. However, Zhang et al. [153] observed that even though fewer datasets used in devising ML based fault diagnostic methods originate from the actual machine operating conditions, the data volume for normal operations far much exceed that for anomalous operation.

Sunal et al. [154] compared the performance of different ML approaches in detecting induction motor faults limited to the use of motor current signature analysis and realised that Convolutional Neural Networks (CNNs) and Multi-Layer Perceptron based ANNs perform better than SVM or other solutions (e.g. Long-Short Term Memory Autoencoders). A method combining Mel-frequency cepstrum coefficients and extreme learning machine was proposed for the effective diagnosis of axial piston pump faults by Jiang et al. [155]. A comparison of the model's performance with that of a back propagation ANN and an SVM model shows a higher fault detection accuracy rate, shorter training and diagnosis times with better application prospect.

Saeed et al. [156] used the techniques of Principle Component Analysis (PCA), LSTM and CNN to propose a fault diagnosis model which could not only detect faults early but also has the ability to identify fault scenarios that does not fall in any of the existing groups. PCA is used for anomaly detection while the outputs from CNN and LSTM autoencoder are compared to diagnose the fault with differing results indicating a potentially new fault case. Similarly, an LSTM autoencoder was used for detection alongside a feature importance-based feature engineering and a random forest based classifier for diagnosis in a fault diagnostic system [157]. The system could be applicable to both sensor and machine-based faults.

On the other hand, Fawwaz and Chung [158] proposed a real-time fault detection method for hydraulic systems using a genetic algorithm-based feature selection in combination with LSTM autoencoder that leverages temporal information on time series sensor data. The method attains high accuracy while being robust to noisy data, maintains low detection times and reduces data packet size outperforming prior proposed methods. A combination of a Linear Discriminant Analysis (LDA) and a hybrid kernel extreme learning machine was proposed to diagnose faults in multi-component systems obtaining higher accuracies over 99.5% and errors lower than 0.20% [159]. Similarly, a combination of k-means clustering algorithm for preprocessing data, an SVM and a CNN Gated Recurrent Unit (CNN-GRU) for fault classification was proposed for the fault diagnosis of hydraulic systems in [160]. CNN-GRU model becomes advantageous under complex and diverse failure modes while the SVM performs better in diagnosing most of the failure modes.

The use of ANNs alone in machine fault diagnosis has been studied with some studies aiming to improve its applicability and performance. Sepulveda and Sinha [161] developed an ANN based ML model by optimising the vibration parameters based on the dynamics of the machine for multiple speed operation to bridge the gap existing in vibration based machine learning where models developed may not predict faults accurately if applied on other identical machines. When blindly tested on a similar machine at different operating conditions, it showed robustness and reliability significantly improving the developed model.

To improve the model further Sepulveda and Sinha [162] simulated different rotor faults to update the model and blindly tested it at a different operating speed resulting in accurate binary classification of heathy and faulty data while diagnosis of misalignment resulted in high misclassification. Similarly, Almutairi and Sinha [163] expanded on this by including anti-friction bearing faults while Almutairi et al. [164] focused on reducing the required spectrum features by integrating the poly combined coherence spectrum (pCCS) technique, preserving amplitude and phase information. Most notable was the high level of accuracy achieved independent of machine operating speed.

Similarly, there exist studies that proposed the use of DT on their own to conduct fault detection and diagnosis in machinery. For example, Sakthivel et al. [165] developed a DT model to classify impeller faults, faulty bearings, cavitation and faulty seals in a mono-block centrifugal pump. The DT was acknowledged for being able to perform both feature prioritization and fault classification. High values of overall accuracy were obtained during training and testing indicating the suitability of practical application for fault diagnosis. On a similar study [166] the performance of a DT was compared with that of rough sets in generating rules from statistical features extracted from vibration signals under good and faulty condition of a mono-block centrifugal pump. Better overall classification accuracy was obtained for the DT based model against a rough sets-based model. Similarly, Castellanos et al. [167] used a chain of two DT models to evaluate the use of DT classifiers for diffuser multistage centrifugal pump monitoring under high viscosity two phase flows. In comparison to a single DT, a chain of DT reduced the overall performance in fault detection and classification.

The use of SVMs has also garnered a wide coverage in machinery fault detection with prominent examples being the work of Panda et al. [168], who used an SVM model to classify varying levels of flow blockages at the inlet pipe and inception cavitation in a pump. Results indicated that binary fault classification offered better prediction accuracy for all flow blockage conditions whereas multiclass fault classification obtained moderately high prediction accuracies. The prediction of inception cavitation obtained high accuracies at higher rotational speeds. Goyal et al [169] deployed an SVM model to evaluate the effectiveness of a newly developed low-cost non-contact vibration sensor. It was observed that linear SVM outperforms other kernel based SVMs in classifying bearing faults using data from both the developed sensor and an accelerometer.

In [170], an SVM algorithm was used to classify engine faults into healthy and several fault classes using Hilbert Huang Transform extracted features. Engine fault diagnosis accuracies of over 90% were achieved for the several fault classes. Lin [171] studied the influence of different Gaussian kernel functions on the performance of SVM algorithm in the monitoring of motor bearing faults. Results indicate that the medium Gaussian SVM method improves reliability and accuracy of motor bearing fault detection and diagnosis. Similarly, Zhu et al. [172] proposed the optimization of the SVM classifier parameters using Quantum Genetic algorithm resulting in higher accuracies in fault diagnosis when compared to traditional SVM method. Konar & Chattopadhyay [173] coupled SVMs with a continuous wavelet analysis (CWT) and compared its performance with a discrete wavelet transform (DWT)-ANN based approach in bearing fault detection. Excellent results were obtained with the CWT-SVM approach than the DWT-ANN approach.

Table 2.6-1. Examples of intrisically interpretable ML models

Model Type	**Description**	**Interpretability Level**	**Typical Use Cases**
Linear Regression	Linear mapping of inputs to outputs	High	Forecasting, parameter sensitivity
Logistic Regression	Linear relationships between features and output	High	Binary classification, risk scoring
Decision Trees	Rule-based, hierarchical structure	High	Diagnostics, classification
Rule-based Models	If-Then logic structures	High	Rule extraction, symbolic reasoning
Naïve Bayes	Probabilistic, transparent assumptions	medium	Text classification, spam filtering

In the context of machine learning for machinery fault diagnosis, model interpretability is always overlooked. This is also the case in all the analysed papers in this section. Model interpretability considers a degree to which how predictions made by the model can be explained. Interpretability enables users to understand which features are influencing the model's conclusions reducing uncertainty and promoting adoption. Carvalho et al [174] provided a comprehensive review of research state on machine learning interpretability while focusing on the societal impact, developed models and interpretability metrics.

To assess model interpretability of the approaches found in literature, the two broad paths characterising it namely, by-design and post-hoc were considered. Molnar [175] describes interpretability by-design as intrinsically existing interpretability due to the models nature while post-hoc interpretability involves creating explanation methods which are applicable to existing black box models. Examples of intrinsically interpretable models is given in Table 2.6-1.

The assessment of interpretability of ML based diagnosis techniques in literature was limited to inherently interpretable models as post-hoc methods might provide plausible explanations but unfaithful ones that do not accurately reflect the model's internal logic. Intrinsic models leave no ambiguity in explanations. In Table 2.6-2 a comparison between recent approaches that adopted a hybrid of two or more models to the application of ML techniques to machinery fault diagnosis is presented.

Table 2.6-2. Comparison of previously conducted studies

Paper	Investigated Machine	Features Engineering	ML Techniques	Prediction Accuracy	Model Interpretability
Liu & Li [160]	Hydraulic system	K-means clustering	SVM & CNN-GRU	99.77% & 96.60%	Post-hoc
Liu et al. [159]	Hydraulic system	Statistical Time-domain based	LDA & HKELM	99.5%	Post-hoc
Mallak & Fathi [157]	Hydraulic system	Statistical Time-domain based	LSTM & Random Forest	>98%	Post-hoc
Zhu et al [172]	Centrifugal Pump	Statistical Time-domain based	SVM & QGA	92.5%	Post-hoc
Castellanos et al [167]	Multi-stage centrifugal pump	Operation parameters and their derivatives	Chain of Decision Trees (CART)	78.28% & 77.8%	By design - DT
Saeed et al [156]	Nuclear power plant	Principal Component Analysis	CNN & LSTM	-	Post-hoc

Considering the methods presented in these works, it is evident that most of the reviewed studies prioritise prediction accuracy and overlook prediction interpretability. Yet, as noted by Carvalho et al. [174], interpretability is crucial for user trust and practical deployment. It is necessary to look further into this area as to ensure that ML model predictions could be understandable to the human user for purposes of further using the information obtained to support root cause analysis.

2.7. SUMMARY

In summary, this section demonstrated the availability of different cavitation modelling approaches and their applications in centrifugal pump numerical studies. Even though there is wide coverage of the study of cavitation in centrifugal pumps, the studies are biased towards the pump mode operation with limited studies focused on turbine mode as another centrifugal pump application which has gained traction in recent years. As such there is a need for the understanding of the cavitation phenomenon in centrifugal pumps operated as turbines.

Moreover, the use of vibration analysis in the study and understanding of cavitation has been analysed and different existing vibration-based detection techniques covered. However, the wide reliance on FFT based techniques has been shown to be inadequate with reliable detection only realised when cavitation is at an advanced stage, which could be detrimental to the safe operation of hydraulic machines. In the case of PATs, it was demonstrated that not enough studies have been conducted to aid in the detection and diagnosis of cavitation as a potential destructive phenomenon that is worth designing against or ensuring its early detection for quick adoption of remedial action.

Lastly, a summary of recent works that has proposed the adoption of ML techniques for fault detection and diagnosis as a means of safeguarding against issues associated with potential late detection of machine faults were analysed. The adoption of a hybrid use of different algorithms to complement each other was highly recommended. Interpretability of these approaches was also found to be important more so that it is crucial for user trust and practical deployment. However, this was found to be a major inadequacy in recent studies with focus mostly directed towards overall prediction accuracy.

To conclude, the key gaps identified in this section are summarised as follows:

a. While a limited number of studies of cavitation in PATs have been conducted, it focused on the micro-hydropower scale, no studies have explored the pico-hydropower scale (< 5 kW). Given the abundance of such hydropower potential, further research is needed to ascertain cavitation behaviour and performance at this scale.
b. Cavitation is usually associated with pressure pulsations. Despite the understanding that excessive pulsations can lead to dynamic loading, excessive vibration and noise, none of the analysed studies investigated cavitation-induced pressure pulsations in PATs. This points out a need for the understanding of pressure pulsations under cavitation conditions and their influence on machine performance.

c. Most cavitation studies focused on the pumping mode, even though turbine mode operation has gained traction in recent years. To fully understand the turbine mode cavitation characteristics and how it differs from pump mode, more studies are required including the implications for PAT design and operation.
d. Existing PAT cavitation studies have limited vibration analysis to monitoring the fundamental frequencies i.e., f_n and BPF, and the broader description of broadband energy in a wide frequency range. A broader frequency spectrum analysis is necessary to identify the different cavitation phases the PAT goes through as this phenomenon evolve, its effects in performance and ways of monitoring it.
e. Parameters such as Kurtosis and Skewness has demonstrable usefulness in vibration-based fault analysis, but techniques that quantify the overall changes in the signal's probability distribution have not been widely adopted in cavitation detection studies.
f. Even though there is a significant progress in the adoption of machine learning techniques for the diagnosis of machine faults, gaps remain in model interpretability. It is difficult to understand how most of the proposed approaches in literature make a prediction. Therefore, there is a need to demystify this or adopt techniques whose prediction approach could be understood.

3. RESEARCH METHODOLODY

This chapter presents the methodology adopted to achieve the aims and objectives of this study, which is centred on understanding cavitation in PATs and developing a suitable predictive maintenance platform using different signal processing and machine learning techniques. The methodology is designed to ensure a comprehensive understanding of cavitation in PATs and to facilitate the development of suitable detection and diagnosis tools based on experimental data.

The chapter begins by outlining the overall research strategy including the philosophical underpinning, types of enquiries and methodological orientation adopted. This is followed by a detailed description of the research model, which serves as the conceptual and practical framework guiding the sequential and integrated components of the study ranging from computational fluid dynamics (CFD) modelling, through experimental validation to development of a predictive maintenance platform.

Recognizing the importance of using appropriate equipment for experimentation and data collection, the chapter also includes a section justifying the selection of the test PAT as the object of research. The suitability of this system is presented in terms of its scalability, experimental flexibility and technical relevance to the study objectives.

Finally, the chapter concludes with an outline of the specific methods of study, detailing how modelling, experimentation and data analysis were integrated to fulfil the research goals. The combination of these methodological components ensures that the study is grounded in rigorous engineering analysis while contributing practical insights to the field of PAT operations, monitoring and maintenance.

3.1. RESEARCH STRATEGY

Research can be looked at from three different perspectives that are mutually inclusive namely the viewpoint of the application of the research findings, the study objectives perspective and the perspective of the mode of inquiry used in conducting the study [176]. From the application of the research findings perspective, research can be classed as either applied or pure research with the current study classified under the former. From the perspective of the objectives of the study, research can be classed as descriptive, explanatory, exploratory and correlational; the current research takes the exploratory approach. Finally, in the viewpoint of the mode of enquiry used in conducting the study, research can be classed as either qualitative or quantitative with the latter representing the approach employed in the current study.

This study is classed as applied because it investigated detection and diagnosis of cavitation in PATs; therefore, the research findings were implemented in the development of a predictive maintenance platform, hence having an applied purpose. By virtue of seeking understanding of the cavitation phenomenon and devising condition monitoring criteria for the process, the research serves an exploratory purpose. Since this study was dependent on the collection and analysis of the numerical data representative of machine health conditions, it can be thought of as adopting the quantitative approach.

Research can also be categorised as either deductive or inductive based on its scientific point of view [176, 177]. In this thesis both inductive and deductive reasoning approaches were utilised. The computational fluid dynamics model utilised both approaches as the model was based on the knowledge behind the modelled system representing deductive reasoning and the collection and analysis of data and later use for knowledge generation represented an inductive approach.

The nature of this research was experimental and exploratory; it involved the development of a numerical fluid model to simulate fluid flow inside the PAT. The solution data from the fluid model was used to guide the experimental study of the process of cavitation, leading to new insights and understanding of the phenomenon. The model was developed ex novo with guidance from measurements taken of the important pump dimensions and its fluid flow parameters. A new PAT system was not developed but the research incorporates an existing design of a PAT from Novara [32], instead the installed instrumentation were altered to match the current research requirements.

3.2. RESEARCH MODEL

In earlier studies on pump-as-turbine technology, the focus has been mainly on the technology design and performance characterisation. This research added another dimension to the study of PAT technology, namely maintenance. PAT operation and maintenance requirements have been overlooked in the past and this research's aim was to concentrate on developing a condition-based maintenance system for PATs that would take into consideration different hydraulic phenomena inside the machine. Initially, the study was limited to the investigation of cavitation but other disturbances in the machine operation either hydraulic or mechanical can be added to the system so that it holistically represents all potential failure modes in a PAT. Figure 3.2-1 illustrates the research model for achieving the set research goals.

The model is divided into three major components that define how this research was conducted also representing the thesis results chapters. Each of the component represented has sub-tasks that made it possible to attain chapter objectives. The first component is the computational fluid dynamics modelling, for which its results are presented in Chapter 4 of the thesis. This component begins with the description of the numerical model and the associated validation and verification studies conducted. The model is then used to conduct cavitation studies yielding cavitation occurrence results and analysis of pressure pulsation data that inform the modification of the test rig for experimental work.

The second component presented the results of the experimental work and the associated cavitation studies conducted. This makes up Chapter 5 of the thesis whose focus is in using the obtained experimental time-domain data to propose a cavitation detection method that was implemented as part of the detection function of the predictive maintenance platform. Furthermore, the output data from this component of the research project was used in the platform development component of the model, which completes the model.

In this component, the captured data was further analysed in the frequency domain to obtain power spectral densities (PSD) for each operation state of the machine. The intention was to follow up the detection function presented in Chapter 5 with a diagnosis function which is presented in Chapter 6. The goal was to investigate the possibility of generalizing features observed in the signal PSD plots as resulting from changes in the cavitation state. Using different machine learning approaches models were then trained in Chapter 6 to automatically provide diagnosis of the PAT cavitation condition. The best performing models were selected and implemented in the predictive maintenance platform, thereby providing an automated diagnosis capability.

Finally, Chapter 7 presents a description of the predictive maintenance platform functionality. It shows how elements of this research fits in together to provide an automated predictive maintenance capability. In Chapter 8 of the thesis, we provide concluding remarks including recommendations for further studies and development of the platform.

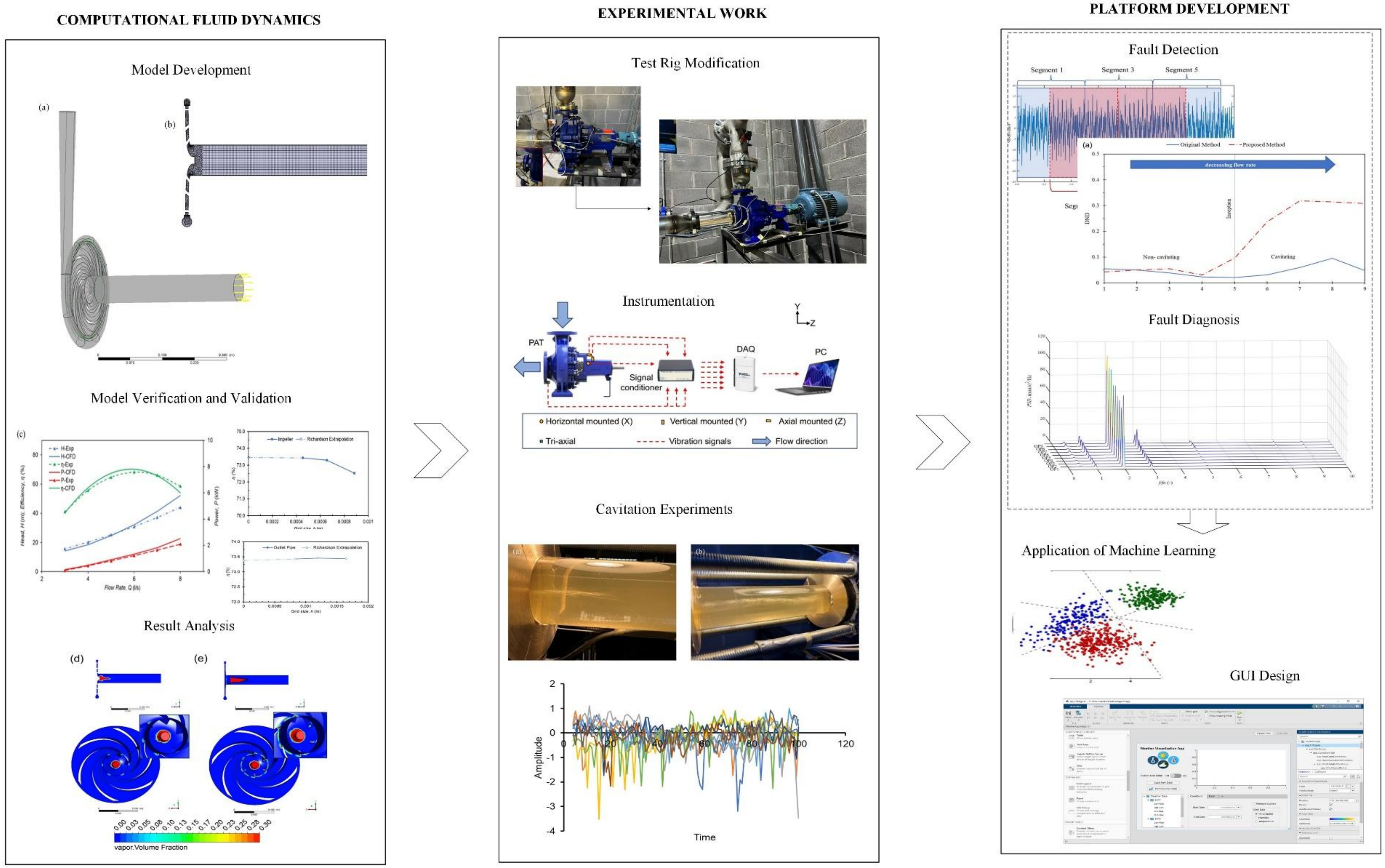

Figure 3.2-1. Research Model and Framework for the Implementation of the predictive maintenance system

3.3. THE EXPERIMENTAL PUMP-AS-TURBINE TEST RIG

3.3.1. Description of the Test Rig

This study adopted the experimental test rig designed and assembled in the work of Novara [32]. This experimental setup had been developed for the testing of PAT performance in turbine mode for micro-hydropower applications. The setup consisted of a KSB ETN 050-32-200 volute type centrifugal pump operating in reverse as a turbine and driving a standard 5.5 kW ABB 3GBA 132 210-ADD induction motor operated as a generator. This was connected to the grid via a 5.5 kW Mitsubishi Electric FR-A741-5.5K regenerative variable speed drive (VSD)/inverter. The water flowing through the system was supplied from a 2 m^3 water reservoir through a 9.2 kW Ebara 3D 50-200 centrifugal pump operating at 2900 rpm. The system was modified from its initial design by incorporating a viewing pane at the outlet of the PAT to allow observation of the machine's cavitation condition.

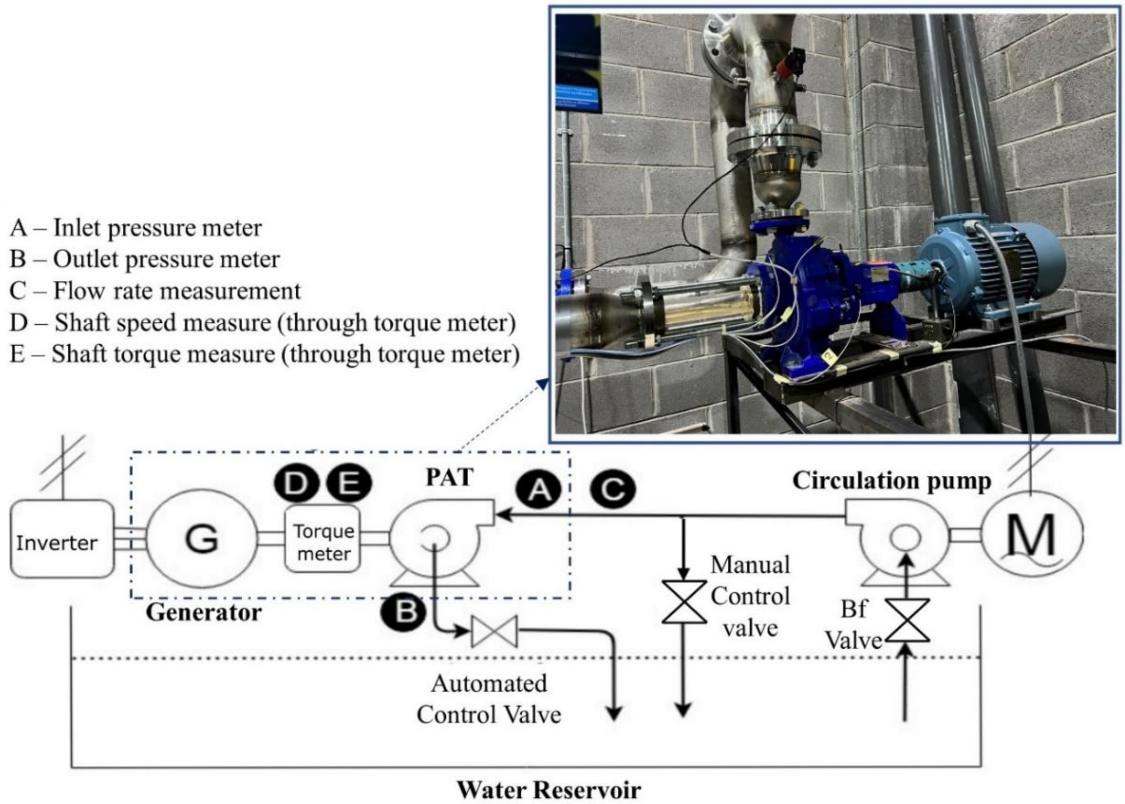

Figure 3.3-1. Schematic of the experimental test rig

Figure 3.3-1 shows the schematic of the experimental test rig with an insert photograph of the test PAT as adapted form Novara [32]. The PAT was instrumented with two pressure sensors, a Gems Sensors 3000 Series (0.025% accuracy) and a Gems Sensors 3500 series (0.01% accuracy), are installed at the PAT inlet and outlet, respectively whereas the power output was directly measured at the input side of the VSD with an uncertainty of 0.2%. The VSD also serves the purpose of setting the generator operation speed. A TUF 2000M ultrasonic flow sensor with 1% full scale accuracy was used to obtain flow measurements and flow through the system was varied by adjusting a manually operated control valve at the outlet end of the supply pump. These operation data were acquired using a 14-bit model 6009 National Instruments (NI) Data Acquisitions card connected to a personal computer using USB cable.

3.3.2. Equipment Justification

This section aims to provide justification for the suitability of the PAT as the object for the research. The basic design features of the experimental setup are a maximum pressure of 5 bar, a maximum flow rate of 20 l/s and a power output up to 5 kW [32]. These are typical of many potential micro-hydropower locations in water networks. The PAT under investigation is described by the following design features, best efficiency point (BEP) flow rate of 6 l/s, BEP head drop of 33.5 m, BEP shaft output power of 1 kW, maximum efficiency of 51.5% and 1520 rpm design speed of rotation.

This PAT is considered suitable for this research due to its balanced combination of experimental flexibility, scalability and technical relevance, making it an appropriate and justified choice as the research object for the study of cavitation. The system enables controlled production and monitoring of key phenomena associated with cavitation, which is central to both the numerical and experimental components of this research. Despite its relatively small size, the study PAT operates based on the same fundamental fluid dynamics principles as larger sized, industrial-scale PATs. It demonstrates characteristic flow patterns, head-flow relationships and susceptibility to cavitation under off-design conditions. This will allow the findings such as pressure pulsation trends, vibration signatures and the onset of cavitation to be scaled and generalised to larger systems.

The small sized nature of the PAT and the test-rig setup also allows precise manipulation of flow rates, pressures and operating conditions to reliably induce cavitation without the need for the installation of expensive apparatus that could be used to manipulate downstream pressures to initiate cavitation occurrence. This is essential as for the sake of the available time and financial assistance for the project, the same outcome could be achieved without needing extra funding and time frame extensions. Moreover, the system was already equipped with pressure and flow transducers making procurement of extra sensors limited to only vibration accelerometers and associated circuitry elements.

In addition, conducting cavitation experiments at higher power ratings could be costly and potentially damaging to larger sized PATs. A 1 kW system provides a safe, cost effective and reproducible environment for conducting destructive tests without compromising safety or equipment longevity. Lastly, small-scale PAT systems are widely used in laboratory environments for teaching and research. The findings from this study could directly benefit future academic research, training and development of low-cost condition monitoring systems, especially for small scale hydraulic systems.

3.4. METHOD OF STUDY

To accomplish the set aims and objectives and address the research questions, this project follows a three-pronged approach that incorporates modelling, experimental work and data analysis. Modelling involves such aspects as the development of numerical models, simulation of cavitation and post processing of numerical simulation results. The numerical simulation aspect is very important as the machine can be run at many different operating points at low cost yielding a large knowledge base for subsequent processes.

The experimental aspect of the research involved setup of measurement instrumentation comprising accelerometers, flow meter, pressure transducers, and torque meter on a lab scale PAT. Since the numerical simulation part of the project was mostly concentrated on the hydraulics of the flow, the experimental work ensured vibration data was collected and used to develop algorithms for the detection and diagnosis of cavitation. Cavitation experiments were conducted, vibration and pressure pulsation data obtained and used in the development of the predictive maintenance system that considers effects of hydraulic sources of failure in the machine operating performance.

Lastly, data analysis played a crucial part in ensuring that the resultant algorithms and developed models resulted in accurate performance in monitoring cavitation. Various data analysis techniques were implemented at various stages of the project. Data analysis was in the form of visualisation of flow field in the case of numerical modelling data and for experimental data various data analysis methods were used to filter out unwanted frequencies in the vibration signals, conduct feature engineering for data pre-processing for machine learning etc.

4. NUMERICAL ANALYSIS OF CAVITATION IN A CENTRIFUGAL PUMP-AS-TURBINE

4.1. INTRODUCTION

Cavitation is the formation and rapid collapse of vapour bubbles in a liquid caused by a pressure drop in a flowing fluid. It occurs when the pressure of a liquid drops below its vapour pressure resulting in the development of vapour bubbles [178]. When these bubbles are transported to locations of higher pressure they implode, releasing energy that can cause damage to the surrounding materials be it piping or impeller blades. Cavitation is ubiquitous within hydraulic machines such as pumps and turbines because of the energy conversion process taking place within them that include changes in the fluid pressure.

The widespread use of pumps-as-turbine (PAT) is a recent development that has been facilitated by the growing need for reliable, dispatchable and cheap alternate energy sources to meet changing needs of the power grid. Moreover, the emergence of new application areas for micro-hydropower such as wastewater treatment plants and water distribution networks has supported the adoption of this technology [37, 87]. However, as the adoption of PAT use has increased, its coverage in research also increased but focusing on design aspects biased towards sizing and the conversion of pump performance characteristics into turbine performance.

With this increased use of PATs to generate power, it is important that like in pumping mode the cavitation performance of centrifugal pumps in generation mode be well understood. This is particularly the case since PATs are used under conditions for which they have not been designed for and their susceptibility to cavitation need to be understood. Addressing this gap can help alleviate losses due to breakdowns and missed energy production in such applications. Even though there have been efforts in literature to understand the cavitation performance of a centrifugal pump operating in turbine mode, the extensivity of the efforts are minimal.

The purpose of this chapter is to use numerical analysis incorporating computational fluid dynamics (CFD) methods to characterize cavitation occurrence in PATs, including assessing means of detecting cavitation using conventional indicators such as changes in head and hydraulic efficiency, as well as analysing the frequency content of pressure pulsations. The study is exploratory and interpretative in nature rather than exhaustive, serving the purpose of providing qualitative insight into the evolution of cavitation on PAT systems and identifying representative flow features and operating conditions that can inform the subsequent experimental investigations and diagnostic tool development. A more detailed justification of the modelling choices and the limited parameter space considered is provided later in Section 4.4.

Simulations were conducted to investigate the flow behaviour and cavitation phenomena within a PAT system, from the volute entrance to the downstream outlet pipe. The simulation encompassed critical components including the volute, impeller and the outlet pipe. ANSYS CFX® was used as the primary simulation platform with computational model comprising approximately 7.73 million elements. Unsteady Reynolds-Averaged Navier Stokes (RANS) equations, coupled with the Shear Stress Transport (SST) $k - \omega$ turbulence model were employed. This approach enabled accurate modelling of three dimensional, transient, incompressible and viscous flows without heat transfer. To capture the detailed flow characteristics within the impeller, the entire impeller domain including six blade passages was modelled. This comprehensive approach was necessary because the flow entering from the volute is non-uniform, invalidating the assumption of axis-symmetry in the impeller.

4.2. DESCRIPTION OF THE NUMERICAL MODEL

Before conducting the study, it was necessary that several decisions be made on the type of the simulation to be conducted. This involved deciding on the following components of the design process:

- Two-dimensional (2D), Quasi-three-dimensional (quasi-3D) or full three-dimensional (3D) simulation

Whether to adopt a 2D or 3D simulation is problem specific. A 2D simulation may be necessary especially at early engineering design stages while a quasi-3D is actually a 2D simulation with extra source terms added to account for acceleration and deceleration caused by rapid changing of geometry or flow boundary layers [179]. On the other hand, a 3D simulation is necessary for complex geometries with complex 3D dynamic features of flow which complicate the simplification process to either 2D or quasi-3D. Considering the current case, a full 3D simulation was deemed necessary as both the geometry and flow were considered as being complex for a 2D or quasi-3D simplification.

- Compressible or Incompressible flow

For a compressible fluid, changes in pressure and temperature result in a change in the fluid density. The working fluid of the PAT is water and its changes in density are sufficiently small to be ignored. As such, the flow was regarded as incompressible. Moreover, water is a Newtonian fluid and has its shear stress linearly related to strain via a coefficient of viscosity.

- Viscous or Inviscid flow

For viscous fluids, fluid friction has significant impacts on fluid motion. To decide whether the flow is viscous or inviscid, the Reynolds number is used. Using the design flow rate of 0.006 m^3 s^-

[1] and the impeller diameter of 0.209 m, the flow Reynolds number was found to be 7.71×10^6, which is much higher than the 2000 value that is used to determine the transition to turbulent flow. A high Reynolds number is indicative of inertial forces being more significant than viscous forces. However, the presence of solid boundaries in the current case does require that fluid viscosity be included, which means that viscous flow was used in this study. The 'No-Slip Wall' boundary condition which equates velocities at solid walls to zero was adopted for all solid walls. The 'No-Slip Wall boundary can result in a thin layer with large strain rate, which ultimately affects the outer fully developed turbulent flow and generate eddies and losses.

- Laminar or Turbulent Flow

Random eddies with different length scales describes turbulence. For the study of turbulence, instantaneous quantities are expressed as the sum of its mean and the fluctuating term and the Navier-Stokes equation can well describe it. Considering the Reynolds number of 7.71×10^6, the flow in the current study is considered turbulent and is considered too high for the application of a Direct Numerical Simulations due to less computing power. Since the mean flow features are of interest in real-life engineering applications, the sum of the steady components and the fluctuating terms are substituted into the instantaneous Navier-Stokes equations to yield the RANS equations. The RANS equations coupled with the turbulence model present an effective way to simulate the effects of turbulence.

- Steady or Unsteady flows

Steady state flow refers to conditions where the flow properties at any point in the system are time invariant whereas unsteady flows show variation with time. Since the current study entails evaluation of cavitation inside the PAT, an unsteady flow is assumed as the formation and collapse of vapour bubbles in the fluid will lead to properties of the flow varying with time.

4.2.1. Governing Equations and Turbulence Modelling

In the PAT, during cavitation there is a flow mixture of water and vapour, which is unsteady, three dimensional, turbulent and isothermal. The flow governing equations include the continuity equation, momentum equation and vapour transport equation. Moreover, the SST $k-\omega$ two equation turbulence model is coupled with the unsteady RANS equations to account for turbulence within the flow. Equations 4.2-1 and 4.2-2 give the continuity and momentum equation for the mixture transport where α, ρ and μ are volume fraction, density and dynamic viscosity respectively whereas the subscripts *l, v* and *m* are representative of the liquid phase, vapour phase and the mixture respectively [180].

$$\frac{\partial \rho_m}{\partial t} + \frac{\partial(\rho_m u_i)}{\partial x_i} = 0 \tag{4.2-1}$$

$$\frac{\partial(\rho_m u_i)}{\partial t} + \frac{\partial(\rho_m u_i u_j)}{\partial x_j} = \rho_m g - \frac{\partial p}{\partial x_i} + \frac{\partial}{\partial x_i}\left[(\mu_m + \mu_t)\left(\frac{\partial u_i}{\partial x_j} + \frac{\partial u_j}{\partial x_i} - \frac{2}{3}\frac{\partial u_k}{\partial x_k}\delta_{ij}\right)\right], \tag{4.2-2}$$

The density and dynamic viscosity are obtained from the weighted average of each phase volume fraction as per Eq. 4.2-3 and 4.2-4, and the variables *u, p* and μ_t refers to time averaged velocity, time averaged pressure and turbulent viscosity respectively whereas subscripts *i, j* and *k* are indicative of the cartesian coordinates.

$$\rho_m = \rho_l \alpha_l + \rho_v \alpha_v \tag{4.2-3}$$

$$\mu_m = \mu_l \alpha_l + \mu_v \alpha_v \tag{4.2-4}$$

The conservation equation governing the transport of vapour volume fraction during cavitation is expressed by Eqn. 4.2-5. In this formulation, the source terms $\dot{m}^+$ and $\dot{m}^-$ represent mass transfer due to evaporation and condensation, respectively, as defined in Eqns. 2.3-14 and 2.3-15 [181]. These source terms are derived from bubble dynamics modelled using the Rayleigh-Plesset equation, which provides a physically sound, computationally efficient and widely used method for capturing the key mechanisms of cavitation.

The Raleigh-Plesset equation describes the radial dynamics of a single spherical vapour bubble subjected to the pressure difference between the local pressure and the vapour pressure p_v. For practical CFD implementation, a simplified form of the Rayleigh-Plesset equation is used to derive the interphase mass transfer rate (Eqn. 2.3-9), where second-order terms and surface tension are neglected for computational efficiency. In this context, R_B denotes the bubble radius. The nature of the phase change i.e., evaporation or condensation, determines the direction of mass transfer, with the rate depending on both the number of bubbles per unit volume and the prevailing pressure conditions. The resulting source terms provide the coupling between the vapour phase and liquid phase in multiphase cavitation simulations.

$$\frac{\partial(\rho_v \alpha_v)}{\partial t} + \frac{\partial(\rho_v \alpha_v u_j)}{\partial x_j} = \dot{m}^+ - \dot{m}^- \tag{4.2-5}$$

For more precise prediction of the flow structure inside the PAT, it is important for turbulence structures to be accurately modelled within the flow domain. The Shear Stress Transport (SST) $k - \omega$ turbulence model was selected to provide closure to the Reynolds-averaged flow governing equations. The SST $k - \omega$ turbulence model was developed by Menter [182] by taking the best available elements of the standard $k - \varepsilon$ turbulence model and the $k - \omega$ model while accounting for the important effect of the transport of principal turbulent shear stress. The model utilises the original $k-\omega$ model in the sub- and log-layer and gradually switches to the standard $k-\varepsilon$ model in the wake region of the boundary layer and free shear layers [182]. The SST $k-\omega$ includes the modification to the eddy viscosity allowing for the transport of the principal turbulent shear stress in the prediction of severe adverse pressure gradient flows.

Formulation of the SST $k-\omega$ turbulence model is described by the following equations:

Turbulent kinetic energy equation:

$$\frac{\partial(\rho k)}{\partial t}+\frac{\partial(\rho u_i k)}{\partial x_i}=\frac{\partial}{\partial x_j}\left[(\mu+\sigma_k\mu_t)\frac{\partial k}{\partial x_j}\right]+\tau_{ij}\frac{\partial u_i}{\partial x_j}-\beta^*\rho\omega k \tag{4.2-6}$$

Turbulent frequency equation:

$$\begin{aligned}\frac{\partial(\rho\omega)}{\partial t}+\frac{\partial(\rho u_i\omega)}{\partial x_i}\\ &=\frac{\partial}{\partial x_j}\left[(\mu+\sigma_\omega\mu_t)\frac{\partial\omega}{\partial x_j}\right]\\ &+2\rho(1-F_1)\sigma_{\omega 2}\frac{1}{\omega}\frac{\partial k}{\partial x_j}\frac{\partial\omega}{\partial x_j}+\frac{\gamma}{\nu_t}\tau_{ij}\frac{\partial u_i}{\partial x_j}-\beta\rho\omega^2\end{aligned} \tag{4.2-7}$$

Table 4.2-1. The equation constants for the SST $k-\omega$ turbulence model

Equation constant	Value
σ_{k1}	0.85
$\sigma_{\omega 1}$	0.5
β_1	0.0750
α_1	0.31
β^*	0.09
κ	0.41
γ_1	$\gamma_1=\frac{\beta_1}{\beta^*}-\frac{\sigma_{\omega 1}\kappa^2}{\sqrt{\beta^*}}$
σ_{k2}	1.0
$\sigma_{\omega 2}$	0.856
β_2	0.0828
γ_2	$\gamma_2=\frac{\beta_2}{\beta^*}-\frac{\sigma_{\omega 2}\kappa^2}{\sqrt{\beta^*}}$

Where the constants ϕ (β, σ_k, σ_ω, γ, …) are calculated from the constants ϕ_1 (β_1, σ_{k1}, $\sigma_{\omega 1}$, γ_2, …) and ϕ_2 (β_2, σ_{k2}, $\sigma_{\omega 2}$, γ_2, …) as $\phi=F_1\phi_1+(1-F_1)\phi_2$ and the equation constants are as given in Table 4.2-1. To properly account for the turbulent shear stress transport, a limiter is applied to the formulation of the eddy viscosity as per Eqn. 4.2-8 where Ω is the absolute value of the vorticity and F_2 is given by Eqn. 4.2-9. Variable y represents the distance to the next surface.

$$v_t = \frac{a_1 k}{\max(a_1\omega;\ \Omega F_2)} \tag{4.2-8}$$

$$F_2 = tanh\left(max\left(2\frac{\sqrt{k}}{0.09\omega y};\frac{500v}{y^2\omega}\right)\right) \tag{4.2-9}$$

4.2.2. Computational Domain, Boundary Conditions and Numerical Schemes

The computational domain consists of three sub domains, namely: the volute, impeller and the outlet extension pipe. Reference to inlet and outlet here means the machine is considered when operating as a turbine. Figure 4.2-1 presents the three sub-domains making up the computational domain. It is worth noting that both the volute inlet and the outlet pipe are extended further to ensure fully developed flow conditions at the said boundaries and eliminate reverse flows close to either the inlet or outlet hence affecting the accuracy of results.

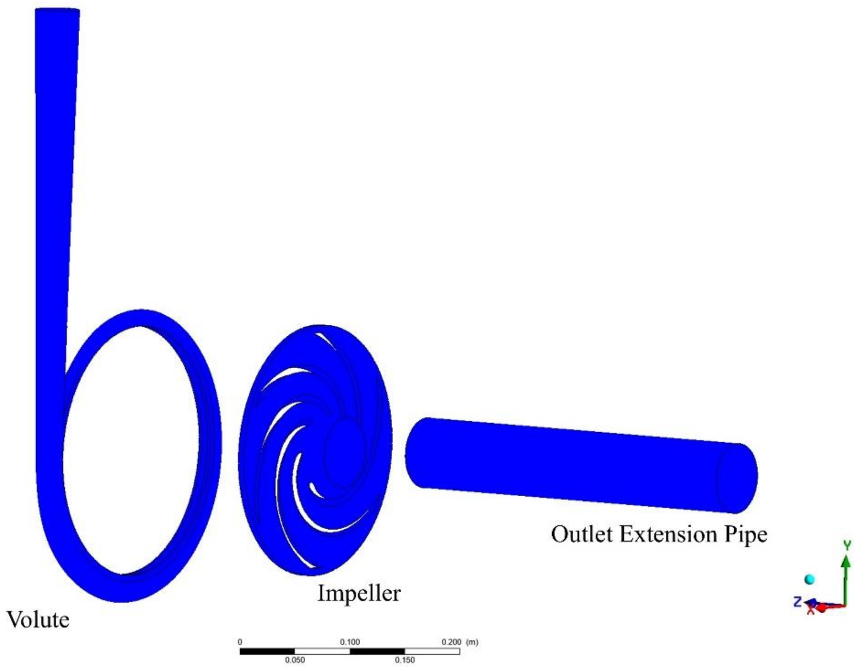

Figure 4.2-1. Computational domain of the investigated pump

In developing the computational domain, no prior engineering drawings were available for the whole pump assembly, as such the 3D geometry were developed ex-novo, hence the potential for minor differences with the actual studied pump. In the 3D modelling of the PAT, impeller clearances were not considered meaning that volumetric losses due to leakage through impeller gaps are not accounted for. Moreover, drag friction losses in the back of the impeller disks and mechanical friction losses due to shaft and bearing rotation were also not accounted for.

For both the steady state simulations, conducted to yield initial conditions, and the transient simulations, the boundary conditions were set to mass flow rate at the inlet and static pressure at the outlet. When conducting steady state simulations, the static pressure at the outlet was set to 1 atmosphere (atm.) with reference pressure set to zero and various values of the mass flow rate at the inlet were set to obtain the machine's performance curves over its operating range. The interface linkage between rotating and stationary domains was set to Stage (Mixing Plane). The Stage (Mixing Plane) model performs a circumferential averaging of the fluxes through bands on the interface. Solutions are then obtained in each reference frame. All solid boundaries were defined as no-slip walls and the turbulence intensity was set to medium turbulence (I = 5%).

When conducting transient simulations, transient rotor-stator interface was used between stationary and rotating domains allowing flow field information transfer between the said domains. A high-resolution option was selected for both turbulence numeric and advection schemes permitting a reduction of numerical diffusion. Time dependent terms of the governing equations were discretized using a second order backward Euler scheme with 10 inner loop iterations for every timestep of Δt = 0.00022s representative of a 2 degrees impeller rotation angle and the simulation was performed over a total of 16 impeller rotations as the monitored quantities remained steady with time. This also allowed capture of enough time varying pressure pulsation data for frequency analysis at a higher resolution. The outlet pressure value was varied until cavitation occurrence was evident in the setup. Moreover, convergence was determined by the RMS residuals between successive iterations dropping to 1×10^{-5}.

4.2.3. Computational Grid and Grid Independence Study

The ANSYS Mesh tool was used to discretise all the computational domains into small control volumes which the transport equations would be solved. Unstructured tetrahedral dominant elements were selected to mesh the impeller and the volute whereas for the outlet extension pipe a structured hexahedral mesh was used. The choice of the elements for each of the components was dictated by the complexity of the domain to be meshed. The extension pipe presented the simplest of the domains hence ease of obtaining a structured mesh whereas the volute and the impeller appeared to be complex geometries. To be compliant with the requirements of the chosen turbulence model the near wall boundary was refined such that it yielded a Y^+ value of approximately lower than 5.

Table 4.2-2. Grid sizes for the domains

Grid	Volute	Impeller	Outlet Pipe	Total Mesh
Fine	2,699,876	3,130,054	1,899,540	7,729,470
Medium	1,257,610	1,047,523	671,428	2,976,561
Coarse	576,108	424,030	252,495	1,252,633

To analyse and evaluate the uncertainty of discretization errors caused by different grid scales, the Grid-Convergence Index (GCI) based on the Richardson extrapolation method was computed as outlined by Celik et al. [183]. The pressure along a vertical line across the impeller centre to its periphery, head consumed by the PAT and the generated torque at the output shaft have been compared for this purpose. This is because in a PAT most of the energy conversion takes place in the impeller. Three set of grids having a similar refined node distribution in the boundary layer were generated for each sub domain by increasing the global element size. Table 4.2-2 shows the number of elements in each of the created grids for each of the three sub domains.

Figure 4.2-2 shows the pressure profile along the y-axis normalised by the impeller radius R measured on a vertical line from the impeller centre to the volute at an axial location $z = -3.5$ mm. The pressure on this line as the flow moves from the volute to the PAT outlet through the impeller for the three grids used is shown. It is evident that all the grids can capture the flow behaviour through the impeller. The accuracy of the solution increases as the grid becomes denser as indicated by both the medium and fine grid being closer to the extrapolated solution. The coarse grid shows some areas where it overpredicts the pressure indicating that it is not suitable to be used without further refinement. Considering the fine and medium mesh it is evident that their results are almost identical which means the medium mesh can predict the flow conditions as reasonably well as the fine mesh.

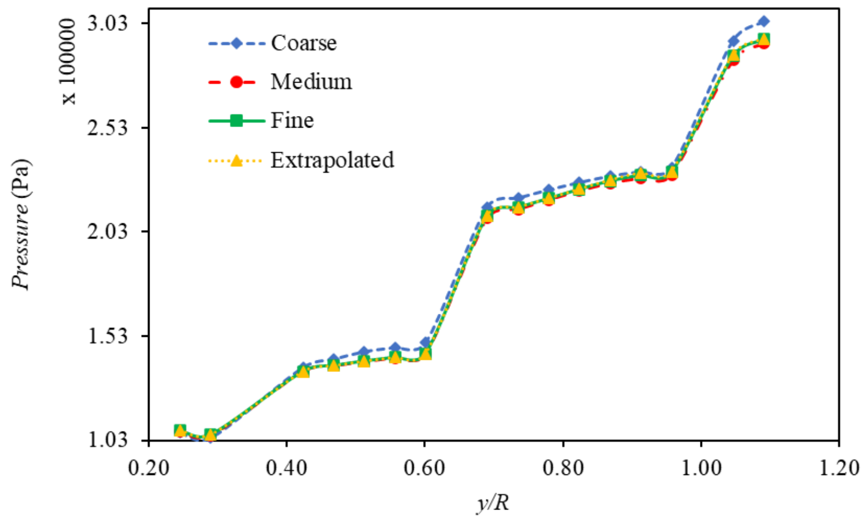

Figure 4.2-2. Verification of grid independence

For each sub domain, grid discretization errors were estimated by varying the grid size of a single sub domain while keeping the others fixed. Steady-state simulations were then performed using boundary conditions of a 6 kg/s mass flow rate at the inlet and 1 atm. static pressure at the outlet. The resulting GCI parameters for the three grid levels in each computational sub domain are presented in Table 4.2-3.

Table 4.2-3. Computed discretized errors

	Impeller		Volute		Extension Pipe	
N_1, N_2, N_3	3130054, 1047523, 424030		2699876, 1257610, 576108		1899540, 671428, 252495	
r_{21}	1.4		1.3		1.4	
r_{32}	1.4		1.3		1.4	
	ϕ = Head	ϕ = Torque	ϕ = Head	ϕ = Torque	ϕ = Head	ϕ = Torque
ϕ_1	31.3235	8.6159	31.3235	8.6159	31.3235	8.6159
ϕ_2	31.2413	8.5775	31.3504	8.6081	31.3044	8.6138
ϕ_3	31.2379	8.4863	31.733	8.6968	31.3162	8.6150
p	-9.47	2.57	10.12	9.27	-1.43	-1.66
ϕ_{ext}^{21}	31.24	8.64	31.32	8.62	31.27	8.61
e_a^{21}	0.26%	0.45%	0.09%	0.09%	0.06%	0.02%
e_{ext}^{21}	0.27%	0.32%	0.01%	0.01%	0.16%	0.06%
GCI_{fine}^{21}	-0.35%	0.029%	0.00%	0.00%	-0.52%	-0.17%

The *GCI* index, GCI_{fine}^{21}, and the extrapolated relative error, e_{ext}^{21}, are very small for the simulation results for the fine grid and this was deemed acceptable for use on the premise that no further refinement could make a significant difference in the results. The numerical uncertainty in the fine grid is reported as 0.52% for head and 0.17% for torque. As such in consideration of the computational resources available the fine mesh was selected to be used in this study. The selected computational mesh is shown in Fig. 4.2-3.

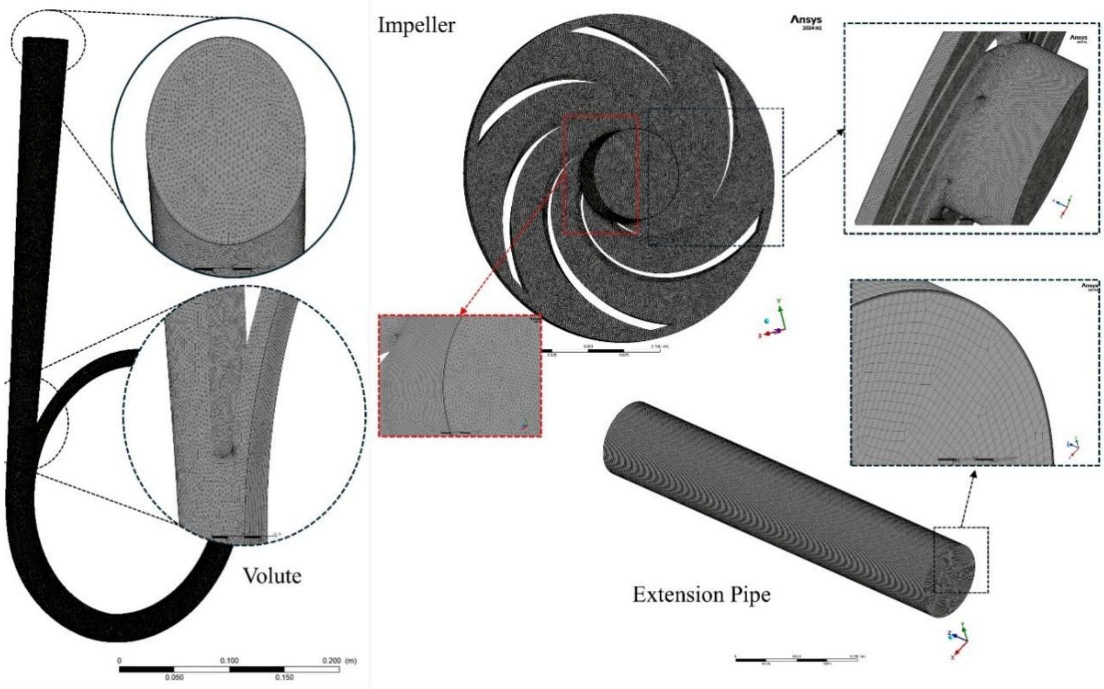

Figure 4.2-3. Final computational mesh

In line with the selected turbulence model, the non-dimensional wall distance Y^+ was examined following the initial simulations to ensure it was lower than 5 for wall bounded flows. This check helps assess whether the first grid cell near the wall is appropriately sized. A very low Y^+ value indicates that the wall flow remains laminar, allowing for accurate resolution of the velocity profile from the wall into the free stream. If average Y^+ exceeded 5, the mesh was refined in the near-wall region and simulations were repeated until the desired Y^+ target was achieved.

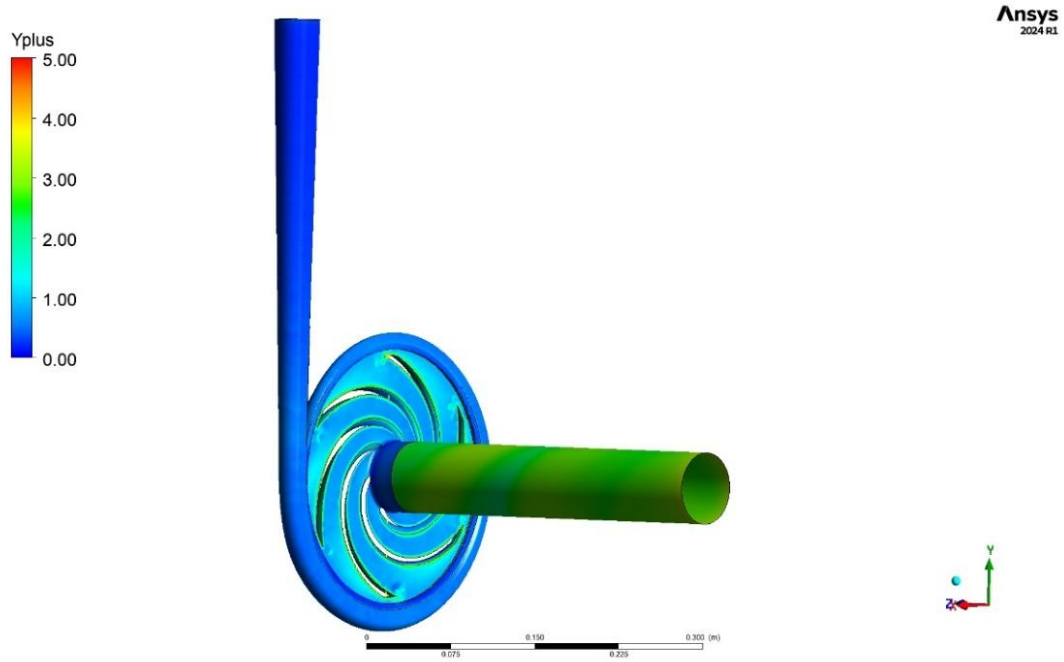

Figure 4.2-4. Contour plots of the Y+ near the wall surface

The Y^+ distribution shown in Fig. 4.2-4 evaluates the near-wall mesh resolution for the suitability of the SST *k-ω* turbulence model. The contour spans a Y^+ range of 0 to 5. Most surfaces exhibit values between 0 and 3, with low Y^+ observed along the volute outlet walls, suggesting effective viscous sublayer resolution, Moderate Y^+ values near impeller blades and the outlet pipe indicate localised regions where the mesh may benefit from further refinement, but it was deemed suitable for the current study.

Monitor points were strategically placed in various locations within the computational fluid domain as illustrated in Fig. 4.2-5. In the volute region, a monitor point, designated V_T, was positioned at the volute tongue to capture pressure variations as the flow transitions from no cavitation state to fully developed cavitation. On the impeller, five monitor points were defined, two at the leading edge of one of the blades (LE_1 and LE_2) and three at the trailing edge, located on both the suction and pressure sides (TE_1, TE_2 and TE_3). This configuration was selected to monitor local pressure fluctuations near expected cavitation inception zones and track their upstream propagation.

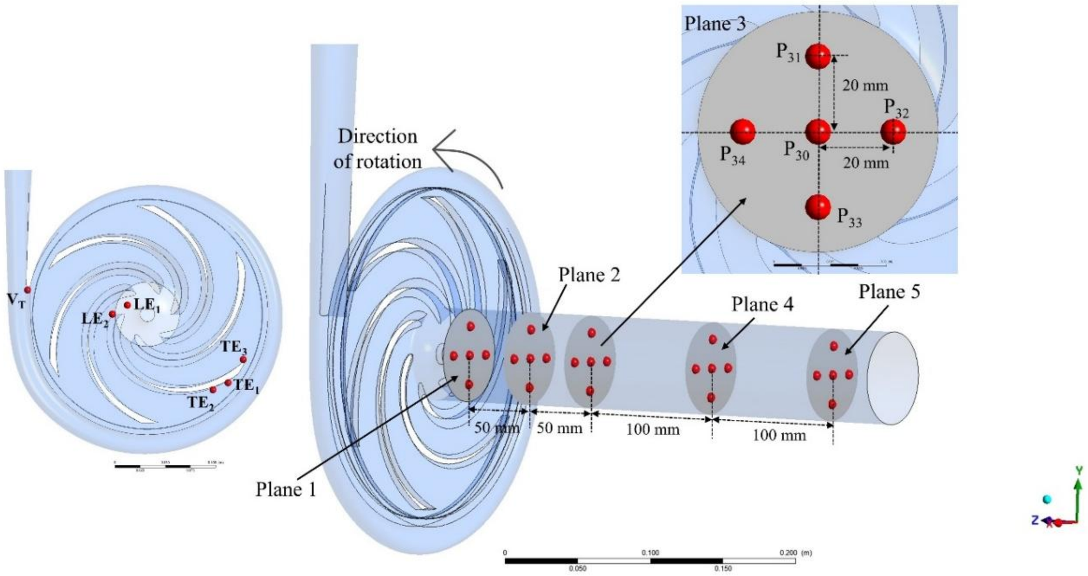

Figure 4.2-5. Location of monitoring points in the computational domain

Additional monitor points were placed along the outlet pipe, distributed across five axial planes situated at the pipe entrance and at distances of 50 mm, 100 mm, 200 mm and 300 mm downstream of the impeller exit. Each plane was assigned an index from 1 to 5. On every plane, five monitor points were placed with one at the pipe centreline and four circumferentially around it, each 20 mm radially from the centre and positioned at angular locations of 0º, 90º ,180º and 270º. The centreline monitor point were labelled P_{10}, P_{20}, P_{30}, P_{40} or P_{50} according to their respective planes. The surrounding monitor points on each plane were labelled in a clockwise direction starting from the 12 O'clock position; for example, plane 3 included monitor points P_{31}, P_{32}, P_{33} and P_{34}, respectively.

4.2.4. Model Validation

Results from the steady state simulations at various mass flow rate values were used to validate the performance of the model in comparison with experimental data. Steady state simulations at six different mass flow rates in the range 3 to 8 kg/s were conducted to obtain head, power and efficiency curves. These performance curves were compared with experimental data from Novara [32] and the results are presented in Fig. 4.2-6 with CFD referring to simulation obtained results while Exp refers to experimental results.

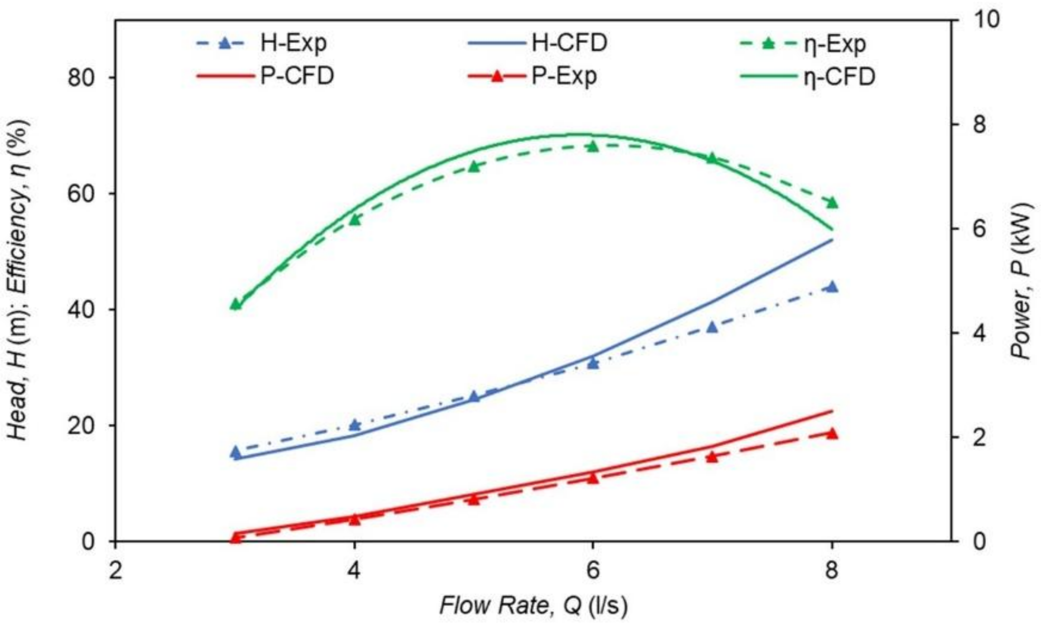

Figure 4.2-6. Comparison of numerical and experimental performance curves

The results indicate that the performance curves developed from the CFD model agrees well with the experimental curves. Both the head and power curves increase with the flow rate while the efficiency initially increases then reach the best efficiency point (BEP) where it begins to decrease with further increase in flow rate. Comparison of the curves show higher variations at the highest flow rates, indicating increased deviations as flow rate in increased. The model was adopted for use in the cavitation investigation as simulations were conducted at lower flow rates where the difference between the simulation and experimental data was low.

4.3. CAVITATION SIMULATION METHODOLOGY

Cavitation simulations were systematically conducted to investigate the onset and progression of cavitation within a PAT operating under varying outlet pressure conditions. All simulations were conducted at 1500 rpm operating speed with two distinct flow rate values selected for analysis, Q_{bep} = 6.0 l/s representing the design best efficiency point (BEP) and at Q_{off} = 4.0 l/s, representing an off-design condition. The BEP flow rate was chosen to provide a baseline under nominal hydraulic performance and investigate cavitation vulnerability at design flow, while the reduced flow rate of 4 l/s was intentionally selected to heighten cavitation occurrence.

At lower flow conditions, the dynamic head decreases resulting in an increased likelihood of local pressure dropping below vapour pressure, thereby promoting the onset of cavitation. These two conditions also mirrored the experimental scenarios ensuring consistency between simulation and laboratory validation. For each flow rate, steady-state simulations were initially performed across twelve distinct operating points, each defined by a different static pressure value imposed at the PAT outlet boundary.

The selected outlet static pressures were 1.000 (operating point 1), 0.750 (operating point 2), 0.500 (operating point 3), 0.250 (operating point 4), 0.200 (operating point 5), 0.175 (operating point 6), 0.150 (operating point 7), 0.125 (operating point 8), 0.100 (operating point 9), 0.090 (operating point 10), 0.080 (operating point 11) and 0.070 atm. (operating point 12). These values were chosen to incrementally reduce outlet static pressure, thereby promoting vaporization of the fluid and capturing the threshold conditions for cavitation inception.

The steady state simulation results, which established the pressure and velocity fields at each operating point, were used as initial conditions for the subsequent transient flow simulations. These transient analyses were essential for resolving the dynamic characteristics of cavitation and its associated pressure fluctuations, which are not captured in steady-state models. Cavitation within the PAT was assessed through both qualitative and quantitative metrics. Firstly, the vapour volume fraction was visualised throughout the flow domain to identify regions of vapour formation, accumulation and collapse, particularly around the blades and in the outlet pipe. This visualization provided insight into the spatial evolution and intensity of cavitation pockets as outlet static pressure was lowered. Moreover, this qualitative assessment was carried to compare similarity with laboratory experimental observations.

Secondly, time series of pressure data were extracted from the monitoring points within the PAT computational domain. The data was analysed to evaluate the pressure pulsations associated with cavitation events. Spectral analyses of the extracted pressure data were conducted to examine frequency domain characteristics enabling identification of specific frequency ranges associated with incipient and fully developed cavitation.

In conducting the spectral analyses, time domain pressure data for the last 11 impeller revolutions from the simulation data were used to compute the spectrums for each operating point with number of samples used equal to 2048. To reduce leakage of spectral energy into closer frequency bins a Hanning window was used and data samples were zero padded to improve the smoothness of the plots.

4.4. SCOPE AND LIMITATIONS OF ADOPTED THE NUMERICAL APPROACH

The numerical approach adopted in this thesis, presented in Sections 4.2 and 4.3, is justified by the specific role assigned to the numerical simulations within the overall research framework. The CFD analysis was not intended to provide an exhaustive parametric optimisation of the PAT hydrodynamics, nor to reproduce cavitation behaviour with full quantitative accuracy across all operating conditions. Instead, its primary purpose was to offer a physically consistent and qualitative overview of the cavitation process and its evolution as the operating conditions transition from standard '*no cavitation*' regime to '*full cavitation*' regime.

Given this objective, a limited and carefully selected set of operating parameters were considered sufficient based on previous studies. The numerical simulations were designed to capture the dominant flow features, cavitation inception, growth and collapse mechanisms as well as describing the associated pressure pulsations that characterise cavitating flows in PATs. These phenomena are governed primarily by global operating conditions such as flow rate, rotational speed and pressure drops, rather than by fine-scale parametric variations. As such, extending the parameter space would have significantly increased computational cost without providing proportional additional insight relevant to the aims of the overall study.

Furthermore, the numerical results were not used in isolation, but as a qualitative and interpretative foundation for the subsequent experimental and signal processing work. The CFD analysis was employed to identify cavitation-prone regions, distinguish between different stages of cavitation development and highlight frequency and pressure trends that could reasonably be expected to manifest in vibration measurements. This role does not require extensive parametric studies, but rather a robust representation of the underlying physics across representative operating points.

In this context, the choice of a limited number of numerical test cases ensured a balance between physical fidelity and computational efficiency, while maintaining consistency with the broader multi-stage methodology of the thesis. The numerical model therefore serves as a guiding tool for understanding cavitation behaviour in PATs and for informing experimental design, rather than as a standalone predictive model. This approach is aligned with the overarching goal of the research, which is the development of a practical predictive maintenance tool rather than hydrodynamic optimisation of the machine.

4.5. RESULTS AND DISCUSSIONS

4.5.1. Cavitation Performance

The available Net Positive Suction Head ($NPSH_a$) is an essential parameter for evaluation the onset of cavitation in hydraulic machines. In pumps, it quantifies the pressure margin between pressure at the pump inlet and the minimum pressure inside the pump. It is defined as the difference between the local absolute pressure head and the vapour pressure head, also considering the fluid's kinetic energy as given in Eqn. 4.4-1, where p_1 is the mean local static pressure at the pump inlet, p_v is the vapour pressure of the fluid, v_1 is the absolute velocity at the impeller entrance, ρ is the fluid density and g is the acceleration due to gravity.

$$NPSH_a{}^P = \frac{p_1 - p_v}{\rho g} + \frac{v_1^2}{2g} \qquad (4.5\text{-}1)$$

Conversely, the required Net Positive Suction Head ($NPSH_r$) represents the minimum value of the $NPSH_a$ necessary at the pump inlet to avoid cavitation affected operation. For pumps, this is commonly determined using the 3% head drop criterion, which identifies the $NPSH_a$ at the point where the developed head has declined by 3% from its nominal value. This marks the conditions where cavitation has a noticeable impact on pump performance, beyond which prolonged operation can result in physical damage.

$$NPSH_a{}^T = \frac{p_2 - p_v}{\rho g} + \frac{v_2^2}{2g} \qquad (4.5\text{-}2)$$

In turbines, a similar form of the $NPSH_a$ is relevant but evaluated at the outlet. $NPSH_a$ in turbines is given in Eqn. 4.4-2 where p_2 and v_2 refer to the mean static pressure and the absolute fluid velocity at the turbine outlet, respectively. According to IEC 60193 [184] the cavitation limit in turbines is typically defined using the 1% hydraulic efficiency drop criterion, which marks the point where the efficiency reduces by 1% due to cavitation.

In the context of PATs, there are no alterations made to the pump geometry to allow for operation as a turbine. Although some researchers have explored geometric modifications to enhance turbine performance, there is no consensus on the appropriate cavitation criterion for PATs mainly due to limited coverage in literature. It remains unclear whether to apply the 3% head drop used for pumps or the 1% efficiency loss used for turbines. To quantify the machine's susceptibility to cavitation under varying conditions, the cavitation number is employed as defined in Eqn. 4.4-3, where H is the total dynamic head across the machine.

$$\sigma = \frac{NPSH_a}{H} \qquad (4.5\text{-}3)$$

Figure 4.4-1 illustrates the variation in the head and hydraulic efficiency of the PAT as the cavitation number (σ) is varied at Q_{off} = 4 l/s. Both the hydraulic head and the efficiency remain relatively constant at 20.63 m and 71.06%, respectively, as σ decreases until a critical threshold is reached at σ = 0.0595 (indicated by the orange -- line). Beyond this point, the head begins to slightly drop until σ = 0.0344 (indicated by the red -- line), where the rate of decrease accelerates with further reductions in σ, while the efficiency curve rises steadily until the end of the simulated range. The drop in head is attributable to cavitation occurring in the PAT, while the rise in the efficiency is consistent with expected trends before a decline at lower cavitation numbers, as observed by Li and Zhang [185].

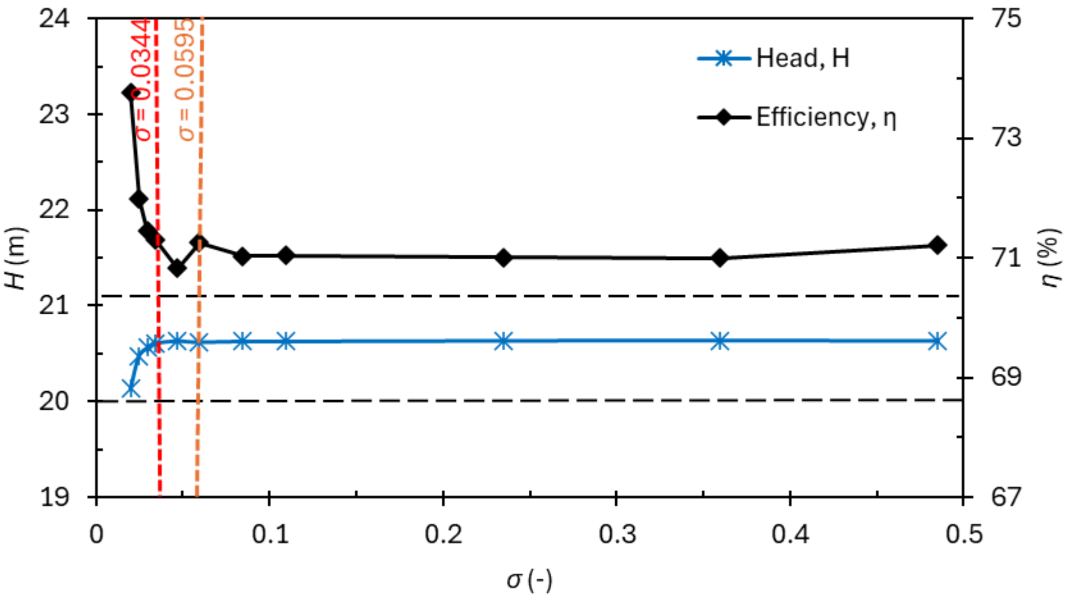

Figure 4.5-1. Variation of Head and the Hydraulic efficiency with cavitation number at the investigated off-design flow rate value of Q_{off} = 4 l/s

The results of the efficiency curve may be indicating that the simulated range is insufficient to capture the expected drop in efficiency, however, the PAT is already cavitating meaning that the 1% hydraulic efficiency reduction criterion is inadequate as a cavitation detection measure in PATs. Similarly, although the PAT is already operating under cavitating conditions, the observed drop in head does not reach the 3% threshold. This implies that relying solely on the 3% head drop criterion may falsely classify the PAT as safe operation, potentially leading to an inaccurate assessment of cavitation susceptibility.

On the other hand, Fig. 4.4-2 presents the variation of both the head and the hydraulic efficiency with respect to cavitation number at the best efficiency point (Q_{bep} = 6 l/s). The efficiency remains constant at 73.04% until σ = 0.0595, beyond which it slightly increases through the remainder of the simulated range. However, unlike the case at off-design flow rate (Q_{off} = 4 l/s), the head curve does not exhibit a decline. The head remains constant at 33.28 m, indicating that cavitation has not yet progressed to a level that impacts PAT performance. Changes in both head and efficiency remain below the 3% and 1% thresholds, respectively, further demonstrating the inadequacy of using these criteria alone to assess cavitation at this flow rate.

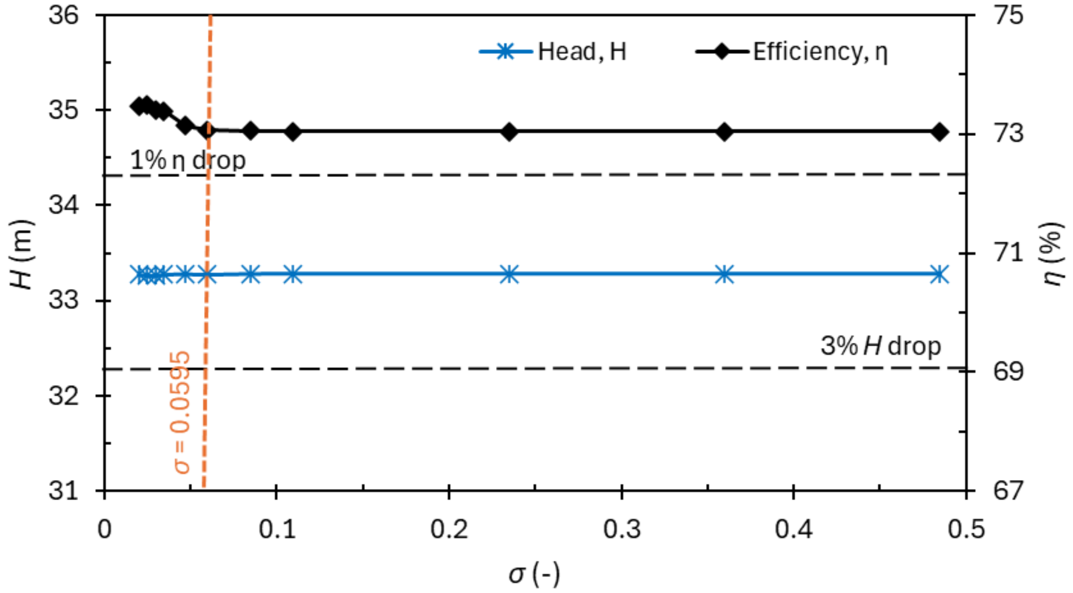

Figure 4.5-2. Variation of Head and the Hydraulic efficiency with cavitation number at the investigated off-design flow rate value of Q_{bep} = 6 l/s

Comparing the two flow rates, it is found that cavitation occurs at a higher cavitation number under off-design flow conditions than at the design flow rate. This is indicated by the drop in head observed at Q_{off}, which does not appear at Q_{bep} within the simulated range. Additionally, cavitation onset in PATs appears to be preceded by an increase in shaft power, reflected in the observed rise in efficiency. A potential explanation for this phenomenon is the reduction in skin friction caused by the formation of a thin vapour layer on the impeller surface, as noted by Alatorre-Frenk [186]. With regard to the applicability of both the 3% head drop and the 1% hydraulic efficiency drop criteria for defining cavitation limits in PATs, the results suggest that changes in efficiency are more sensitive indicators of cavitation onset. This is demonstrated by the rise in the hydraulic efficiency curve, although the suitability of the 1% efficiency drop is inadequate. At design flow rate a maximum increase of 0.58% in efficiency was observed, while at off-design flow rate the efficiency increased by up to 3.89%, based on the peak value achieved in the simulation. Therefore, monitoring efficiency changes offers a greater potential for early detection of cavitating conditions compared to monitoring head loss.

4.5.2. Flow Field Characteristics

The variation of the pressure distribution inside the PAT with the cavitation number (σ) is presented in Fig. 4.4-3 under off-design flow rate (Q_{off}). At a higher cavitation number, σ = 0.4850, the pressure inside the impeller is observed to be high with values above 50 kPa. Pressure distribution in the PAT impeller remains suitably high for all cavitation numbers until at σ = 0.0719 where low-pressure zones with values less than the vapour pressure (3169 Pa at 25 ^{0}C) begin to develop at blade leading edges in the suction side (assuming pump mode configuration) and some areas of the impeller locking nut edges. This is regarded as the σ value at which cavitation begins to occur and its observed on two of the six blades.

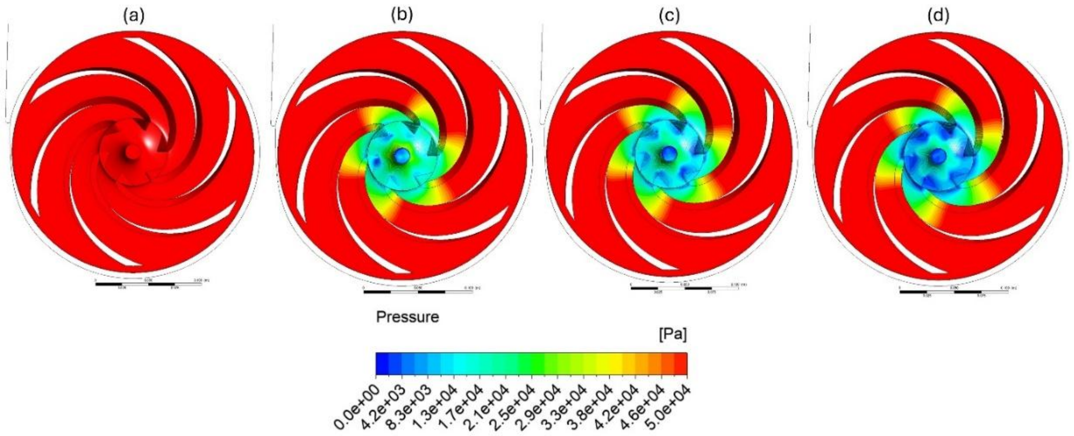

Figure 4.5-3. Pressure distribution under off design flow conditions at (a) σ = 0.4850, (b) σ = 0.0719, (c) σ = 0.0469 and (d) σ = 0.0295.

Further reduction of the cavitation number to σ = 0.0469 leads to an increase in low-pressure regions falling below the vapour pressure. These zones are observed on all blades, specifically at the suction side near the leading -edge hub attachment points. Additionally, the entire impeller lock nut area becomes enveloped by low-pressure zones indicating a deterioration in cavitation conditions compared to previous cases. When the cavitation number is decreased further to σ = 0.0295, the low-pressure coverage intensifies across the impeller eye, with most regions registering pressures below vapour pressure. Notably, the blade shroud attachment areas are now entirely within this low-pressure domain and the low-pressure region has shifted to the pressure side. These observations collectively signify a further worsening of the cavitation state.

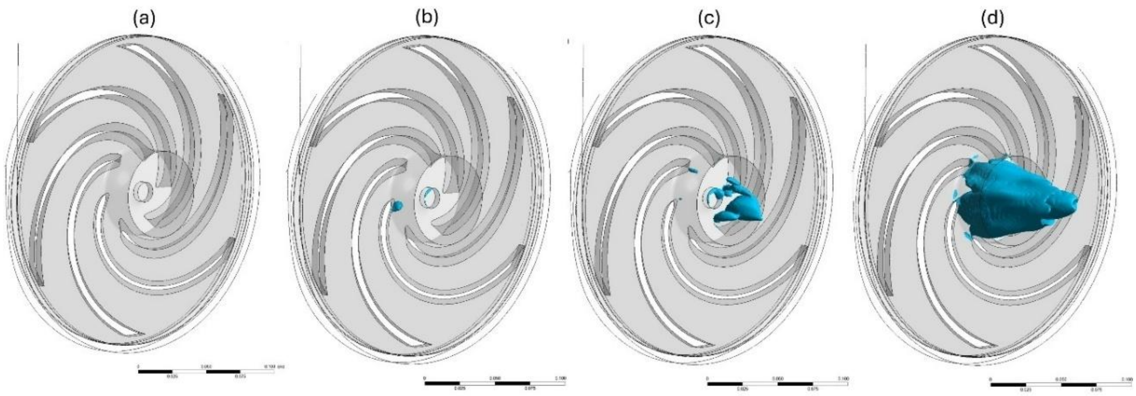

Figure 4.5-4. Evolution of the cavitation structure under off design flow conditions at (a) σ = 0.4850, (b) σ = 0.0719, (c) σ = 0.0469 and (d) σ = 0.0295.

Figure 4.4-4 shows the visualization of the growth of the developed cavitation structure inside the PAT impeller as σ is varied, using iso-surfaces of vapour volume fraction (α = 0.1). At σ = 0.0719, a small vapour cavity develops at blade leading edge due to the reported low-pressure zone. A similar structure develops at the impeller locking nut area coincident with the observed area of pressures lower than vapour pressure. As σ reduces to 0.0469, the cavity is observed at the blade suction side at leading edge hub area for all the blades which shows further development of the cavity. Moreover, some cavities are observed moving from the locking nut area into the outlet pipe. Further reduction in cavitation number to σ = 0.0295 reveals a torch-like cavity covering most of the impeller eye region, with some smaller cavities developing at the blade pressure side near the leading edge.

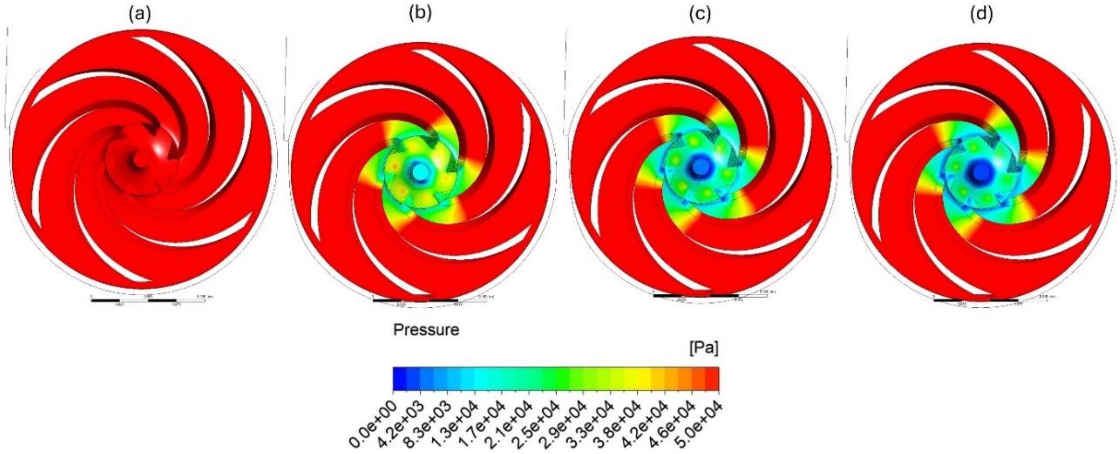

Figure 4.5-5. Pressure distribution under best efficiency flow conditions at (a) σ = 0.4850, (b) σ = 0.1095, (c) σ = 0.0595 and (d) σ = 0.0469.

Under best efficiency flow conditions (Q_{bep}), the pressure distribution across various cavitation numbers is presented in Fig. 4.4-5. At σ = 0.4850, the pressure distribution closely resembles that of the off-design condition (Q_{off}), characterised predominantly by high pressures exceeding 50 kPa. However, unlike the Q_{off} case, cavitation begins to develop when σ = 0.1095. This is evidenced by the formation of sub-vapour pressure zones around the impeller lock nut area. Despite this onset of cavitation, the pressure at the blade leading edge remains above the vapour pressure, indicating a localized rather than widespread cavitation condition.

Reducing the cavitation number to σ = 0.0595 reveals that the entire impeller locking nut area becomes enveloped by a vapour cavity. Additionally, small cavities begin to form on the pressure side of the blade leading edge, near the blade-shroud attachment points. A further reduction to σ = 0.0469 results in a slight expansion of the cavitating region around the impeller locking nut. Moreover, sub-vapour pressure zones appear circumferentially along the radial edge of the shroud, indicating continued growth of the cavity.

Figure 4.4-6 presents visualization of the evolving cavity structures using iso-surfaces of vapour volume fraction (α = 0.1). Cavitation initiates at σ = 0.1095, with a small cavity forming along the outer edges of the impeller locking nut. As the cavitation number is reduced to σ = 0.0595, the cavity expands, fully housing the impeller locking nut's periphery. At this stage, cavity shedding becomes evident, with vapour structures detaching and being transported downstream into the outlet pipe.

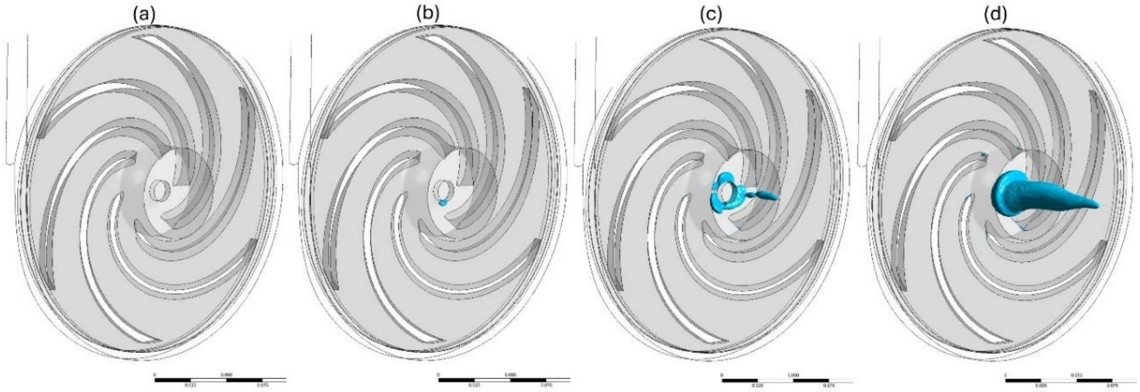

Figure 4.5-6. Visualization of the cavitation structure under best efficiency flow conditions at (a) σ = 0.4850, (b) σ = 0.1095, (c) σ = 0.0595 and (d) σ = 0.0469.

With a further reduction of the cavitation number to $\sigma = 0.0469$, the cavity evolves into a precessing vortex core (PVC) around the impeller axis. This PVC is accompanied by minor cavities forming at the pressure side of the blade leading edges near the impeller shroud across all blades. As the cavitation number continues to decrease, PVC lengthens and becomes more pronounced, maintaining attachment to the impeller in the region around the locking nut.

4.5.3. Temporal Analysis of Cavitation Post-Inception

To investigate the events immediately following cavitation inception and to relate them to experimental observations, the evolution of the cavity at $\sigma = 0.0595$ was analysed using a time-resolved animation of the flow field. This visualization was constructed from transient simulation results spanning from the 2790th timestep onward, capturing the dynamics of the vapour volume fraction iso-surface over time. Here, the variable T denotes the period of one full impeller rotation.

Figure 4.4-7 illustrates the temporal evolution of the cavity structure at $\sigma = 0.0595$ under best-efficiency flow conditions. If t_0 and t_4 represent equivalent phases in the cavity development life cycle, the cavity is observed to detach from its origin and be advected downstream by the flow. Upon reaching regions of higher pressure, the cavity collapses almost instantaneously. This cycle of detachment, advection and collapse repeats continuously, manifesting as a train of fast-moving vapour bubbles.

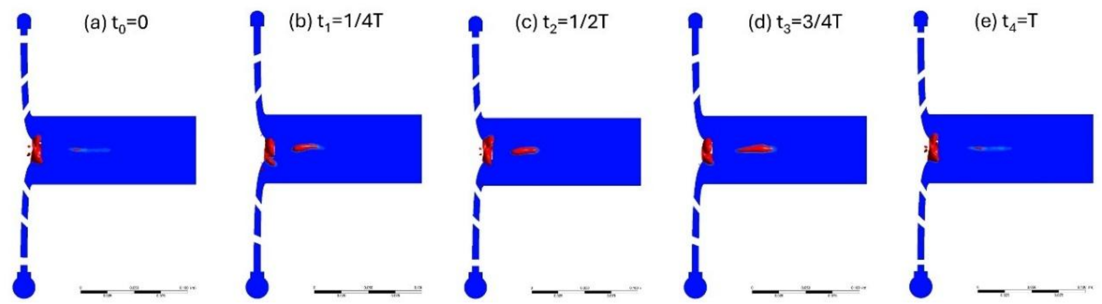

Figure 4.5-7. Temporal variation of developed cavity under best efficiency flow conditions at σ = 0.0595.

Similarly, the temporal evolution of cavitation at σ = 0.0595 under off design flow condition is presented in Fig. 4.4-8. The cavity initially forms near the blade leading edge, then migrates toward the impeller centre, where it detaches and is carried downstream by the flow. Upon entering the regions of elevated pressure, the cavity rapidly collapses. This cycle repeats, generating cavitation structures of varying sizes that are continually transported downstream and subsequently implode. This behaviour closely mirrors experimental observations, where clusters of vapour bubbles are seen moving from within the impeller toward the outlet pipe.

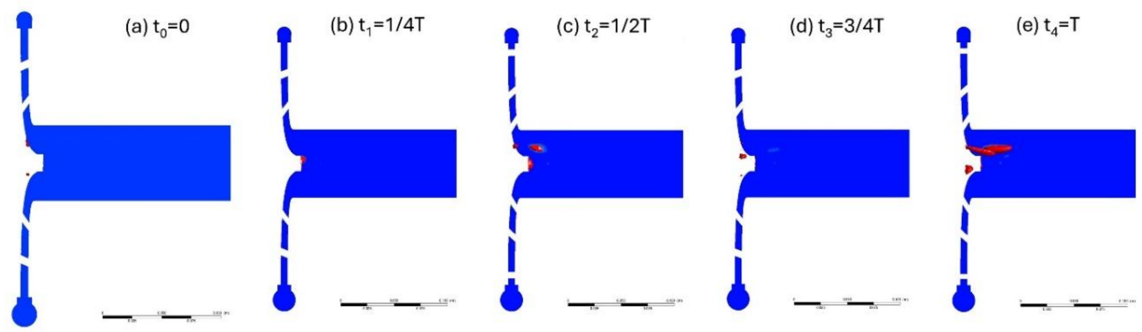

Figure 4.5-8. Temporal variation of the developed cavity under off-design flow condition at σ = 0.0595.

Figure 4.4-9 shows the various cavitation structures observed during experimentation as the flow rate was varied to induce cavitation within the PAT. The cavitation process evolved through three distinct stages: fast travelling vapour bubbles, a sheet-like cavity and a precessing vortex (PVC). Initially, short-lived bursts of fast-moving vapour bubbles appeared, though they were difficult to capture on camera due to their brief duration. Typically visible in only two or three pulses, these bubbles were soon followed by the formation of a stable sheet-like cavity, clearly visible in the viewing pane as shown in Fig. 4.4-9(b).

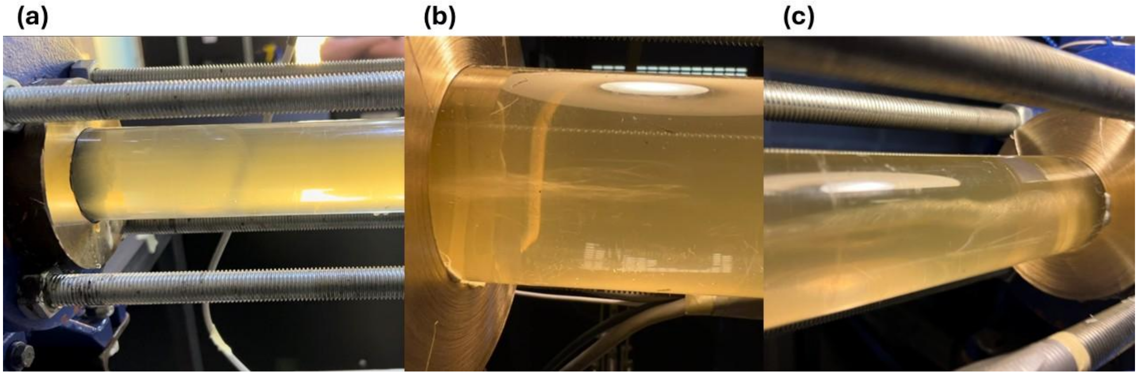

Figure 4.5-9. Observed cavitation structures from the experimental work (a) showing 'no cavitation' (b) sheet-like cavitation structure and (c) a precessing vortex core (PVC).

Comparing this to the simulation results, the fast-travelling bubble exhibited behaviour consistent with the early-stage cavitation seen in Figs. 4.4-7 and 4.4-8. Their transient nature reflects rapid cavitation inception and collapse, occurring within a short time frame. As pressure conditions deteriorate slightly inside the impeller, these initial bubbles evolve into a more persistent sheet-like cavity.

The appearance and development of the sheet-like cavity are highly dependent on the local pressure field. With further changes, the cavitation progresses into the formation of a PVC, which may develop into a torch-like structure if conditions worsen. The PVC rotates in the same direction as the impeller. Notably, unlike in pumping mode, the occurrence of cavitation in this configuration is not audible, suggesting a less violent and more stable cavitation behaviour.

4.5.4. Frequency Analysis of Pressure Pulsations

Pressure pulsations are generated when a rotating blade passes the volute tongue or stationary diffuser blades. They reach their maximum value when the tip of the blade passes this point directing maximum energy in the form of flowing fluid towards the machine discharge point. At any point between the blades, the space between the blades and the volute tongue is large, and hence some of the fluid goes through this space and is recirculated.

The variation in the transfer of energy to the discharge point leads to a change in the discharge pressure, constituting a pressure pulsation. In a PAT this variation from minimum to maximum energy transfer occurs at the impeller inlet point, hence the reason behind the selection of the monitoring points TE_1, TE_2, TE_3 and V_T in Fig. 4.2-5. Below the frequency content of the obtained pressure pulsations at various monitoring points were analysed.

Impeller Region

Figure 4.4-10 shows the waterfall plot for the pressure pulsation data captured at LE_1 and LE_2 at Q_{off} conditions across all operating points. In both plots, the dominant frequency component is consistently observed at 15 Hz, corresponding to 60% of the impeller's rotational speed ($0.6f_n$). At

LE_2, the fundamental frequency, f_n = 25 Hz, remains clearly identifiable and maintains a consistent amplitude across all operating points. In contrast, the amplitude of the 0.6f_n sub-harmonic component remains constant initially but diminishes and eventually disappears after the nineth operating point. As shown in the LE_2 plot, highlighted by the red arrow, there is a noticeable shift in pulsation energy, beginning at the sixth operating point, from the 3rd harmonic toward lower frequencies near 0 Hz, coinciding with a further reduction in outlet pressure.

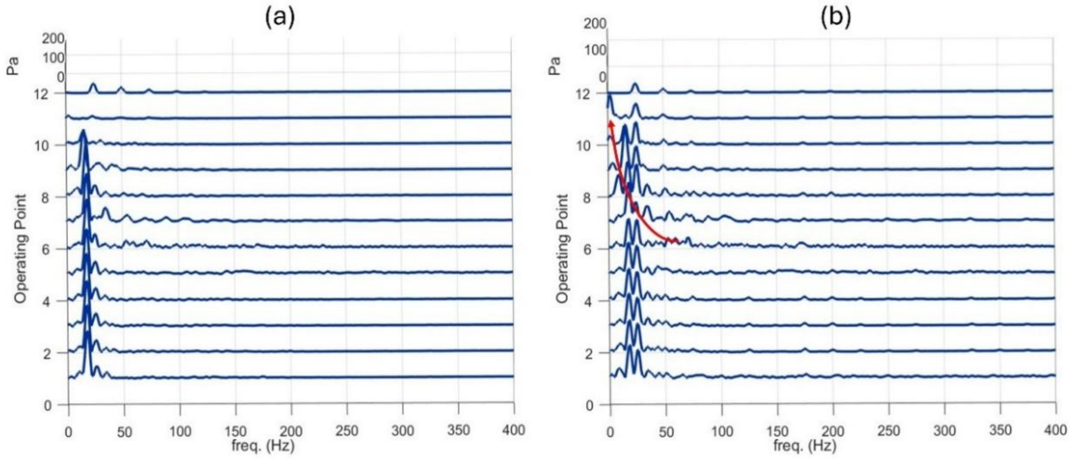

Figure 4.5-10. Waterfall plots showing the evolution of pressure pulsation spectra under off design flow condition at locations (a) LE1 and (b) LE2.

In Fig. 4.4-11, the waterfall plots of pressure pulsation data at Q_{bep} are presented. At LE_1, the fundamental frequency (f_n) dominates the pressure pulsation spectrum, while at LE_2 the second harmonic of f_n is more prominent. At both measurement locations, the blade pass frequency (f_b) is evident during the first four operating points but disappears thereafter. Notably, the ninth harmonic of f_n increases in amplitude up to the sixth operating point before diminishing to very low levels. At LE_1, the f_n component is accompanied by the second and the third harmonics. At LE_2, the f_n component is also present with a slight increase in amplitude, along with its third harmonic.

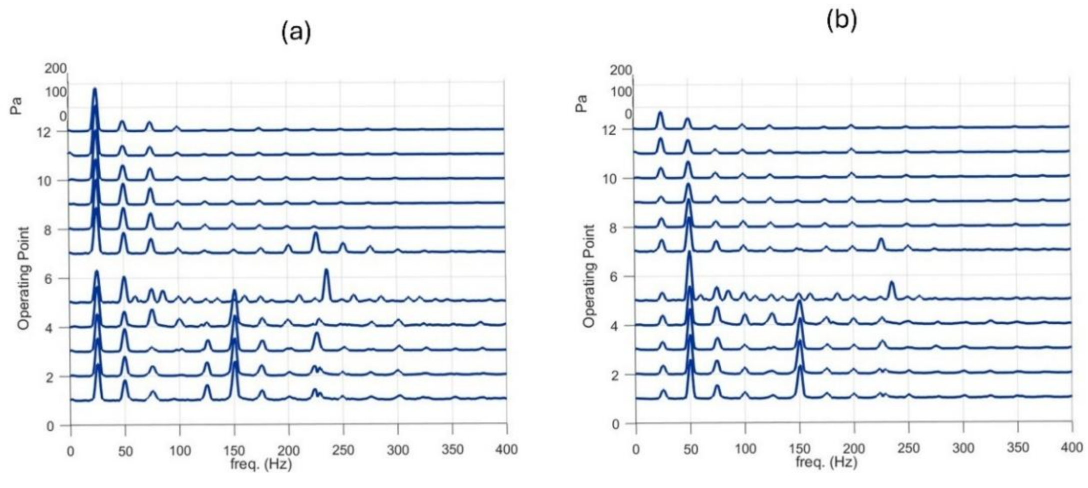

Figure 4.5-11. Waterfall plots showing the evolution of pressure pulsation under design flow conditions at locations (a) LE1 and (b) LE2.

Figure 4.4-12 displays side-by-side waterfall plots of pressure pulsations at TE_1, TE_2 and TE_3 under both Q_{off} and Q_{bep} conditions. At TE_1, the dominant frequency component is the fundamental frequency (f_n), followed by the blade pass frequency (f_b). These are accompanied by several harmonics of f_n. Under Q_{off} conditions, the harmonic amplitudes initially decrease from f_n to the third harmonic, then gradually increase, peaking near the f_b component. Beyond this point, the amplitudes of the higher-order harmonics decrease steadily until the nineth harmonic, after which they remain relatively constant. A similar pattern is observed under Q_{bep} conditions, although the third harmonic retains a noticeable amplitude instead of nearly disappearing.

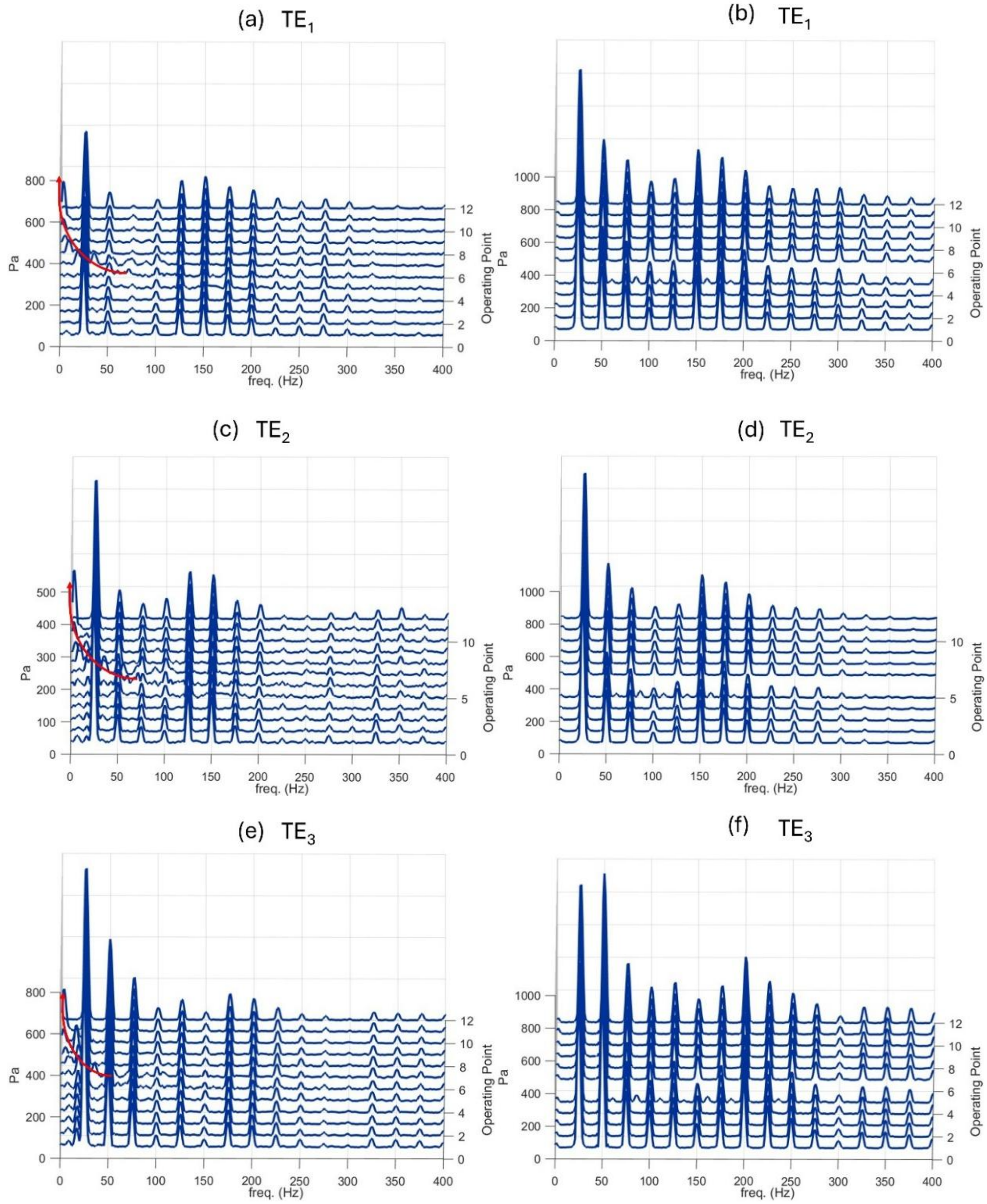

Figure 4.5-12. Waterfall plots showing the evolution of pressure pulsation as the flow condition are varied as measured at the blade trailing edge (a), (c) and (e) for Q_{off} and (b), (d) and (e) for Q_{bep}.

A notable feature under Q_{off} conditions is the shift in spectral energy from the third harmonic toward lower frequencies near 0 Hz, beginning at the sixth operating point and continuing through the last operating point. This trend is highlighted by the red arrow in Fig. 4.4-12. This energy shift is consistently observed across all three monitoring points namely TE_1, TE_2 and TE_3. While the waterfall plots for TE_2 and TE_3 exhibit similar behaviour to those at TE_1, a key distinction at TE_3 is that the second harmonic becomes the dominant frequency component, exhibiting a slightly higher amplitude than the fundamental frequency, f_n.

Volute Tongue Region

At the volute tongue, the dominant pressure pulsation frequency under Q_{off} conditions is the blade pass frequency along with its second harmonic, whereas under Q_{bep} conditions only the f_b component dominates the spectrum. The amplitudes of these components remain consistent across all operating points. However, like the observations at LE_2, TE_1, TE_2 and TE_3, a shift in pulsation energy is noted at Q_{off}, from the third harmonic towards low frequencies near 0 Hz. This begins at the sixth operating point and continues to the final one. This shift, highlighted by the red arrow in Fig. 4.4-13(a), corresponds to a subtle increase in the amplitude of low-frequency components as the system progresses further into the cavitation zone.

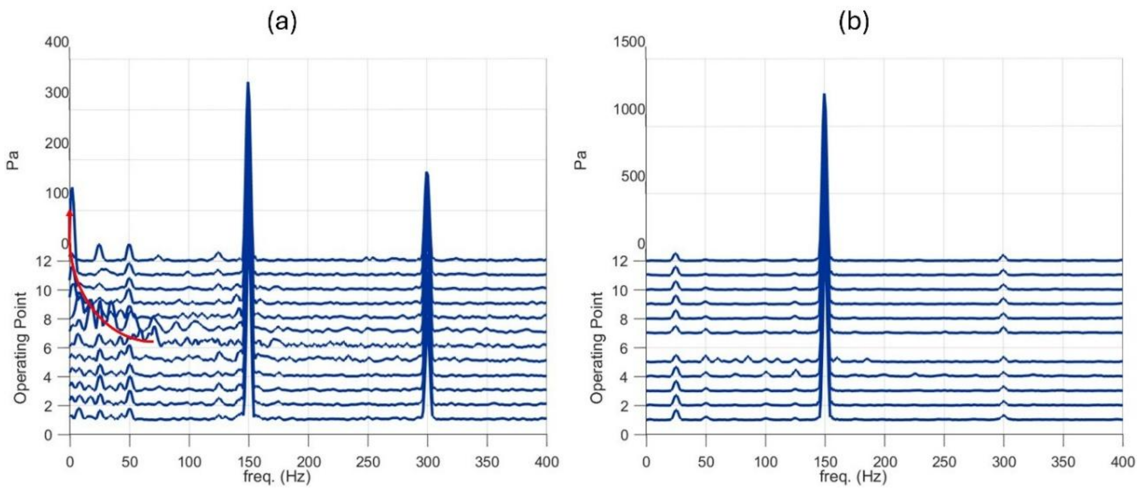

Figure 4.5-13. Waterfall plots showing the evolution of pressure pulsations as the flow condition worsened as monitored at the volute tongue for (a) Q_{off} and (b) Q_{bep}.

Outlet Pipe

In contrast to the pressure pulsations observed in the impeller and volute regions, the outlet pipe exhibits minimal influence from rotational speed-related frequencies. Figure 4.4-14 presents the variation of pressure pulsations measured at Plane 1 under Q_{off} conditions. At monitoring point P_{10}, an elevated noise floor and increased low frequency content are evident across all operating points up to the tenth point. However, at the final two operating points the spectral energy drops significantly, indicating a substantial reduction in pulsation activity.

At monitoring points P_{11}, P_{12}, P_{13} and P_{14}, the waterfall plots reveal a consistent pattern in which a dominant frequency at approximately $0.31f_n$ appears with an amplitude largely unaffected by changes in operating point, persisting until the nineth operating point after which it decreases and eventually disappears. This frequency component does not correlate with cavitation behaviour, as it remains independent of the PAT's operating conditions, suggesting it may be a flow rate dependent characteristic within the PAT. Similar spectral behaviour is observed across the other four monitoring planes. Additionally, the circumferential pressure monitors show an elevated noise flow around the blade passing frequency up to the tenth operating point.

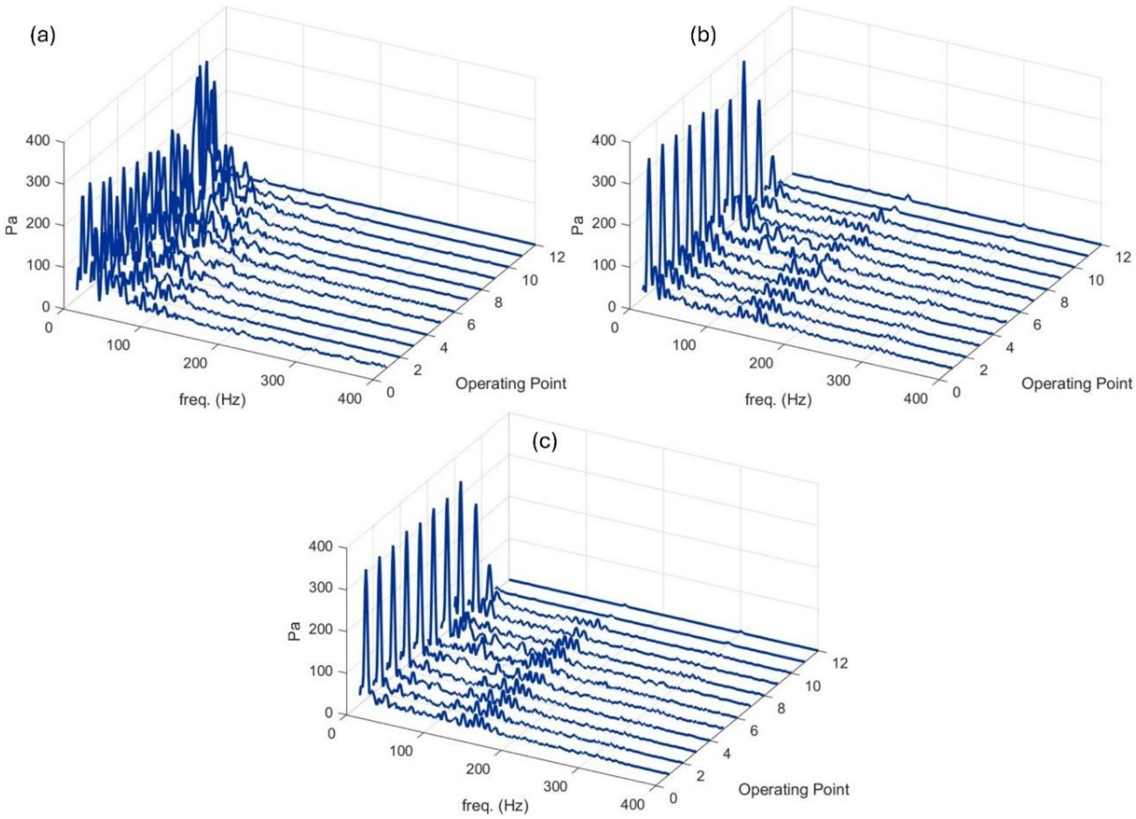

Figure 4.5-14. Waterfall plots showing the evolution of pressure pulsations under Q_{off} as monitored at Plane 1 (a) monitoring point P_{10}, (b) monitoring point P_{11} and (c) P_{12}

In contrast, the pressure pulsations spectra under Q_{bep}, shown in Fig. 4.4-15 are more stable and lack the chaotic characteristics seen under Q_{off} conditions. At P_{10}, the fundamental frequency dominates up to the seventh operation point, beyond which no clear dominant frequency is observed and the spectra appear relatively flat through to the final operating point. A similar trend is observed at the other monitoring locations. Notably, the fourth harmonic of f_n is the dominant frequency component up to the fifth operating point, accompanied by observable peaks at f_n, second harmonic, fifth harmonic, and f_b. At P_{11}, the amplitudes of these components diminish significantly after the nineth operating point, while at P_{12} the spectral peaks persist through the tenth operating point, with an additional prominent peak at the eighth harmonic.

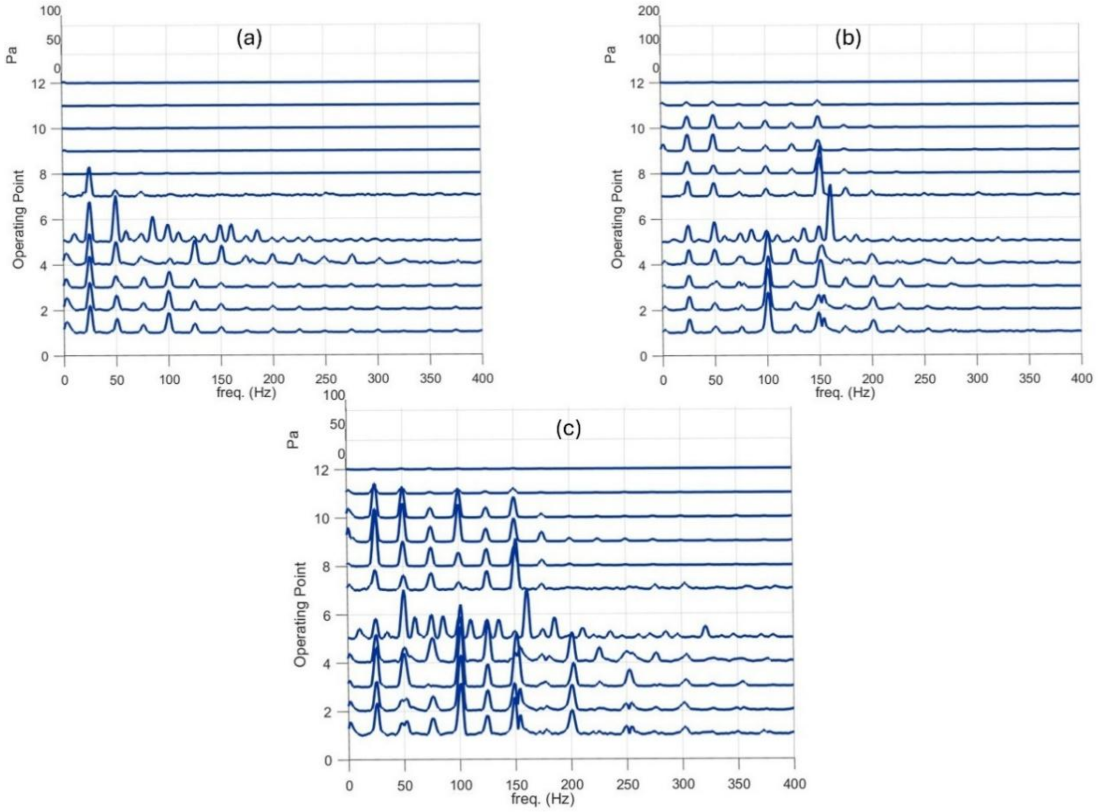

Figure 4.5-15. Waterfall plots showing the evolution of pressure pulsations under Q_{bep} as monitored at Plane 1 (a) monitoring point P10, (b) monitoring point P11 and (c) P12

4.5.5. Discussion of Results

The presented results provide a characterization of cavitation behaviour in PATs, focusing on two flow conditions namely off-design (Q_{off} = 4 l/s) and design flow condition (Q_{bep} = 6 l/s). The analysis employed both cavitation performance curves, flow visualization and the frequency domain analysis of cavitation-induced pressure pulsations.

From the cavitation performance curves, it was observed that under design flow conditions, cavitation incepts earlier than under off-design flow conditions but has a limited impact on PAT performance. Minor rise appears in the hydraulic efficiency curve, while the head remains largely unchanged, indicating that efficiency is more sensitive to cavitation-induced changes. In contrast, at off-design flow conditions, cavitation onset occurs slightly later, but its impact is more pronounced as evidenced by a steep decline in head. Interestingly, hydraulic efficiency shows an increase as the cavitation regime changes, a trend also observed by Li and Zhang [185]. However, their findings suggest that this increase is temporary and ultimately reverses as the cavitation number continues to decrease, highlighting the need for further simulations at lower cavitation numbers.

An evaluation of conventional criteria for defining cavitation onset in both pumps and turbines i.e., 3% drop in head and the 1% drop in hydraulic efficiency, respectively, showed that neither criterion alone adequately captures cavitation onset in PATs. However, the data indicate that variations in hydraulic efficiency in general offer greater sensitivity to the onset and progression of cavitation in a PAT. Notably, even when the efficiency does not decrease by the full 1%, positive changes in efficiency may still signal cavitation activity, suggesting they could serve as a viable early indicator.

Flow visualization yielded critical insights into the spatial development of cavitation within PATs. At the design flow rate, cavitation initiates near the impeller lock nut region, while under off-design conditions, it begins at the suction side of the blade leading edge. This suggests that at lower flow rates, insufficient water flow through the impeller prevents proper adherence to the blade profile, leading to localised low-pressure zones. When pressure in the impeller drops further, these zones quickly reach vapour pressure, resulting in vapour bubble formation that is then transported downstream by the flow.

Although cavitation initiates early at the design flow rate, it has little impact on PAT performance until cavity shedding begins, which may temporarily increase hydraulic efficiency. Under off-design conditions, performance degradation becomes more pronounced as the cavity extends from the suction side of the blade leading edge into the pressure side. This transition diminishes the lift generation capability of the blades, resulting in a marked drop in head and a corresponding decrease in the generated power, evidenced by the steep head drop observed on the cavitation performance curve.

Cavitation development at both design and off-design flow rates follows a similar sequence; initial cavity formation in low-pressure zones within the impeller, growth of the cavity and eventual shedding driven by the incoming fluid flow. The shed cavities are advected into the outlet pipe, where they collapse under higher pressure. This process manifest itself as bursts of rapidly travelling bubbles. As cavitation becomes more severe, these bubbles evolve into thin sheet-like structures attached to the impeller lock nut, which then transform into a precessing vortex core. With further deterioration in operating conditions, this structure finally evolves into a torch-like formation.

The analysis of pressure pulsations at various locations within the flow domain reveals that, although cavitation induces pressure pulsations at off design flow conditions, their magnitude remain consistently lower than the dominant frequency components in the spectrum. These cavitation-induced pulsations exhibit rotational behaviour at frequencies influenced by the prevailing outlet pressure conditions. At the onset of cavitation, the pulsations occur at a frequency approximately corresponding to the third harmonic of the impeller’s rotational speed. As cavitation progresses toward fully developed conditions, this frequency gradually shifts toward the lower end of the spectrum, approaching 0 Hz. Notably, these pulsations are detectable only within the impeller region, suggesting that their detection via pressure sensors positioned downstream of the impeller may be impractical.

Additionally, under off-design flow conditions, a distinct low-frequency component appears in the spectral data, which is independent of the cavitation regime. This component is presumed to be flow-related, as it is absent under design flow conditions, indicating that the specific flow characteristics at that point do not support the formation of this spectral feature.

4.6. SUMMARY

This chapter employed CFD simulations to characterize cavitation behaviour in pump-as-turbines (PATs), focusing on two operating conditions, design flow rate of 6 l/s and the off-design flow rate of 4 l/s. Through the use of cavitation performance curves, flow visualization and frequency domain analysis of pressure pulsations, the chapter provided detailed insights into the onset, development and effects of cavitation within PATs.

Key finding reveals that cavitation incepts earlier under design conditions but has minimal impact on performance, while off-design conditions lead to delayed cavitation onset with more severe consequences, notable as a steep decline in head. Hydraulic efficiency proved to be a more sensitive indicator of cavitation than conventional thresholds, showing meaningful variations even before meeting the 1% drop criterion. This suggests the need for reconsidering standard cavitation indicators when applied to PATs.

Flow visualizations highlighted different initiation zones between operating conditions and emphasized how cavity evolution affects PAT performance. The movement of the cavitating zone to the pressure side of the blade was found to be accompanied by performance degradation. Under worsening conditions, cavities progressed from small vapour bubbles that subsequently changed into sheet-like cavities to precessing vortices and eventually into torch-like structures, marking stages of increasing performance deterioration.

Frequency domain analysis of pressure pulsations further underlined the complexity of cavitation in PATs. Their frequency varied from half of the blade pass frequency towards frequencies nearer to 0 Hz as cavitation conditions deteriorated. While cavitation-induced pulsations existed, their amplitudes were lower than impeller-speed related frequency components and confined to the impeller region, indicating possible limitations in detection through downstream sensors. However, the coincidence of this component with the system's natural frequencies might present a challenge to the safe operation of the PAT. A flow-dependent, low frequency component was also observed under off design conditions, unrelated to cavitation but potentially valuable for understanding flow dynamics.

In conclusion, this chapter highlights the need for cavitation characterization methods tailored specifically for PATs. It calls for further investigation at lower cavitation numbers and more comprehensive monitoring strategies to support reliable operation and improved performance prediction.

5. EXPERIMENTAL INVESTIGATION AND DETECTION OF CAVITATION IN PATS

5.1. INTRODUCTION

The purpose of this chapter is to present the test procedures that were followed when investigating cavitation in the PAT test rig in a laboratory setup and document the observed test results. The experiment was conducted in as close as possible condition to PAT installations in the field, as such there was no additional suction or vacuum creation systems that are typical of laboratory studies but a rarity in real applications. The PAT Test Rig was described in Chapter 3 and is further shown in figure Fig 5.1-1.

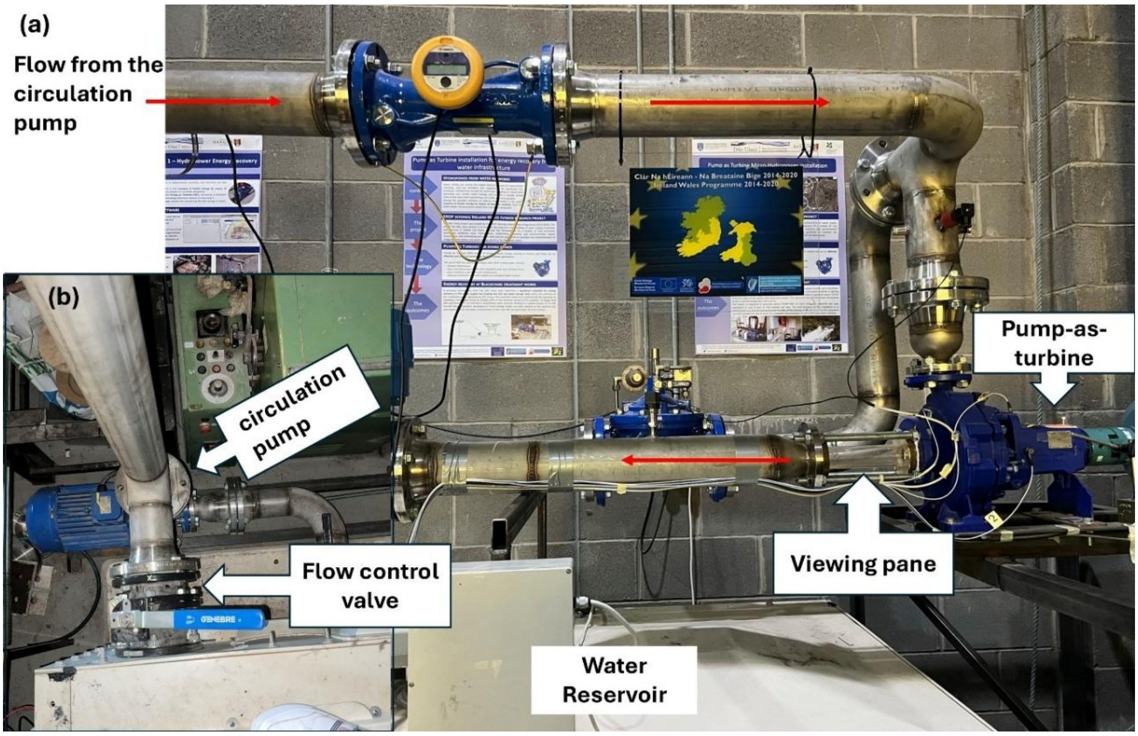

Figure 5.1-1. The experimental test rig used in the study:(a) side view of the PAT and the inlet pipe; (b) plan view (insert) of the circulation pump and the flow control valve.

A 9.2 kW centrifugal pump, Ebara 3D-200, operating at 2900 rpm is used to circulate water through the system from a 2 m^3 water storage tank. The water flows through a KSB-ETN 050-32 200 volute type centrifugal pump in reverse, which in turn drives a 5.5 kW induction motor operated as a generator. By throttling a flow control valve downstream of the circulation pump outlet, some flow can be diverted through back to the storage tank, thus controlling the flow rate through the PAT. A viewing pane is installed immediately downstream of the PAT outlet to ensure flow out of the impeller can be viewed. Pressure sensors installed upstream and downstream of the PAT are used to measure the pressure drop across the PAT while a flow meter is installed in a straight pipe upstream of the PAT to monitor flow measurements.

This chapter begins by extending that by describing the vibration acquisition sensor system design. The designed sensor system was then coupled with the already existing flow rate and pressure data acquisition system to capture both vibration and operational parameters of the PAT. Captured operation data was used in the analysis of the PAT performance under cavitating conditions whereas vibration data was used to propose techniques for the detection of cavitation in a centrifugal PAT. The proposed cavitation detection technique is dependent on the time domain analysis of vibration data. Experiments were conducted at various PAT operating speeds to ensure the wide applicability of the proposed techniques over the whole operation range of the machine.

The contents of this chapter have been partly published as:

Stephen C.; Basu B.; McNabola A. Performance Analysis of a Pump-as-Turbine Under Cavitating Conditions. In Proceedings of the Advances in Hydraulic Research: 40th International School of Hydraulics, Katy Rybarkie, Poland, 23-26 May 2023. Springer Nature: Cham, Switzerland, 2024

Stephen C.; Basu B.; McNabola A. Detection of Cavitation in a Centrifugal Pump-as-Turbine Using Time-Domain-Based Analysis of Vibration Signals. *Energies*, Vol. 17(11), p. 2598, 2024.

5.2. VIBRATION SENSOR SYSTEM DESIGN

5.2.1. Measurement Parameters

Condition monitoring involves tracking and analysing various condition parameters to assess the health and performance of machine components. Some of the key parameters that are worth monitoring include vibration, temperature, pressures, acoustic emissions and electrical signals. Vibration analysis has been utilized for decades in damage detection, making it the most reliable technique, particularly when coupled with a diagnostic decision-making system [187]. It is extensively used in industrial applications for diagnosing different types of machine faults, meaning that the same principles and signal processing techniques can be extended to detect cavitation providing smooth integration into existing condition monitoring frameworks.

While other condition monitoring parameters such as acoustic emissions and pressure fluctuations can provide useful insights, vibration analysis offers several distinct advantages in the context of cavitation monitoring in hydraulic machinery like PATs. Cavitation in hydraulic machines leads to the formation, growth and collapse of vapour bubbles, particularly near the impeller blade surfaces. When these vapour bubbles collapse violently, they produce localized pressure shocks and mechanical vibrations. These rapid changes are directly transmitted to the structure of the machine, making vibration sensors particularly accelerometers highly suitable in capturing these phenomena in real-time.

Unlike acoustic emissions, which may be affected by fluid properties or boundary reflections, vibration signals reflect the actual structural response of the system to excitations [134]. This makes vibration a more reliable indicator of the health and integrity of mechanical components under stressing conditions. Moreover, vibration measurements are non-intrusive and does not require modification of the fluid flow path. Accelerometers are relatively low-cost, easy to install and suitable for long-term operation, which aligns well with the goals of a real-time predictive maintenance system.

Vibration signals also offer the possibility of probing both its time-domain and frequency domain characteristics, which can be leveraged using advanced signal processing techniques. This rich source of information is ideal for developing automatic detection and diagnostic models suitable for monitoring modern critical equipment. Lastly, while parameters like pressure pulsations are also affected by the occurrence of cavitation, they often require more intrusive transducers with need for careful calibration to avoid being affected by noise. Their use could be primarily to supplement the capabilities of vibration measurements to offer a more complete picture of the machine health.

5.2.2. Sensor Selection

In this study, 100mV/g piezoelectric accelerometers were selected for vibration measurements due to their high sensitivity and suitability for detecting low-amplitude vibrations typically associated with incipient faults. The chosen sensors offer a broad frequency response ranging from 0.5 Hz to 10 kHz, which encompass most of machine fault frequencies. The high sensitivity also ensures that even slight vibrations are captured with a good signal to noise ratio, a critical factor when dealing with moderate vibration levels expected in a lab-scale experimental setup. This eliminates the need for complex signal amplification and enhance the quality of data during signal processing.

Furthermore, the 100mV/g accelerometers are commonly used in experimental cavitation studies, offering a practical and validated option for condition monitoring research in turbomachinery [134, 188]. Their compatibility with standard data acquisition systems and cost effectiveness also makes them ideal for academic and applied research contexts. Its selection balances between technical accuracy with practical feasibility ensuring reliable signal acquisition for PAT cavitation.

The schematic for the vibration data acquisition is displayed in Fig. 5.2-1 while the technical specification of the measurement instrumentation is presented in Table 5.2-1. Three single axis accelerometers were stud mounted at the non-drive end (NDE) bearing housing of the PAT in mutually perpendicular directions to capture the full picture of the vibration experienced by the machine because of its cavitation state. The bearing housing serves as a critical structural component that transmits dynamic loads from the rotating shaft to the foundation, making the NDE bearing an ideal location for monitoring the PAT’s response. Vibrations from occurrences within the impeller propagates through the shaft and are transmitted to the bearing assemblies. By installing sensors in all orthogonal directions, it becomes possible to detect directionally dependent vibration modes that might be missed if only a single axis was monitored.

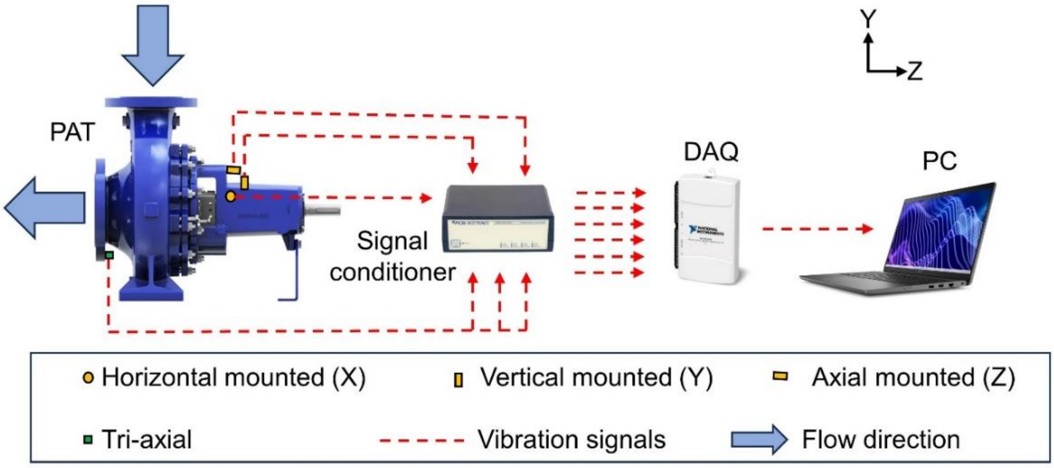

Figure 5.2-1. The schematic of the vibration acquisition instrumentation and software

A single triaxial accelerometer was adhesively mounted at the PAT outlet flange to enable simultaneous capture of vibration signals in three orthogonal directions providing a comprehensive measurement of the dynamic behaviour of the system in response to cavitation. The outlet flange was selected as a strategic location because its directly downstream of the impeller and closer to the expected cavitation occurrence region, which means signals don't need to be transmitted longer paths before they can be captured. Moreover, the selection of a triaxial sensor took into consideration the shortage of a suitable installation location at the flange which could accommodate three sensors each for a specific direction.

Accelerometers were connected via a signal conditioner unit to a 16-bit NI 6210 analogue to digital data acquisition system (DAQ). A signal conditioner unit ensures supply of the required electrical power to accelerometers while also serving the function of preparing the output signals by amplifying the signals and filtering out potential noise. The selection of the DAQ device was based on its portability, ruggedness and compatibility with common programming languages used in development of software platforms. An NI DAQExpress Ver. 5.0.0 data logging software was used to store the digitized vibration signal on a personal computer for further analysis. The software provided a user-friendly interface for setting input channels and parameters.

Table 5.2-1. The Technical Specification of the Measurement Instrumentation

Instrument	Performance	Electrical	Physical
Single Axis Accelerometer Make: ICP® Accelerometer Model: 352C33 ECN: 28610 Qty: 3	Sensitivity (±10%): 100mV/g Measurement Range: ± 50g pk Frequency Rage (±5%): 0.5 – 10,000Hz Resonant Frequency: ≥ 50kHz Broadband Resolution: 0.00015g rms Non-linearity: ≤ 1%	Excitation Voltage: 18 – 30 VDC Constant Current Excitation: 2 – 20mA Output Impedance: ≤ 200 Ohm Output Bias Voltage: 7 – 12 VDC Settling time: 1.0 – 2.5 sec	Sensing element: Ceramic Sealing: Hermetic Electrical Connector: 10 – 32 Coaxial Jack Mounting Thread: 10 – 32 Female Mounting Torque: 10 – 20 in-lb
Triaxial Accelerometer Make: ICP® Accelerometer Model: 356A45 ECN: 49997 Qty: 1	Sensitivity (±10%): 100mV/g Measurement Range: ± 50g pk Frequency Rage (±5%): 0.7 – 7,000Hz Resonant Frequency: ≥ 30kHz Broadband Resolution: 0.0005g rms Non-linearity: ≤ 1%	Excitation Voltage: 20 – 30 VDC Constant Current Excitation: 2 – 20mA Output Impedance: ≤ 200 Ohm Output Bias Voltage: 8 – 12 VDC Settling time: ≤ 5 sec	Sensing element: Ceramic Sealing: Hermetic Electrical Connector: ¼ -28 4-Pin Mounting: Adhesive
Signal Conditioner Unit Make: ICP® Sensor Signal Conditioner Model: 482C05 ECN: 43617 Qty: 1	Channels: 4 Output Range: ± 10 V Low Frequency Response (- 5%): < 0.1 Hz High Frequency Response (-5%): >1000kHz Phase Response (at 1 kHz): ± 1^0 Cross Talk (maximum): -72dB	AC Power: 100 – 240 VDC Excitation Voltage (to Sensor): +26 VDC Constant Current Excitation (to sensor): 2 – 20 mA Discharge Time Constant: > 5 sec Broadband Electrical Noise: 3.5µV rms	Electrical Connector (to sensor): BNC Jack Electrical Connector (to DAQ): BNC Jack
Upstream Pressure Sensor Make: Huba Control Model:501.930002141 Qty: 1	Pressure Mode: Relative Pressure range: 0 – 10 bar Output: 0 – 10 V Accuracy: 0.1% FS	Power Supply: 10 – 33 VDC Load: >10kOhm/<100nF	Electrical Connector: DIN EN 175301-803-A Outside Thread: G1/4, Sealed at the back, DIN 3852-E
Downstream Pressure Sensor Make: Gems Sensors	Pressure Mode: Absolute Pressure Range: 0 – 4 bar Output: 4 – 20 mA	Supply Voltage: 10 – 30 VDC Maximum Load Resistance: (Supply Voltage -10) X 50 Ohms	Electrical Connection: DIN 43650A Pressure Port: G1/4 External

Model: 3500B0004A01G000RS Qty: 1	Accuracy: 0.25% FS		
Ultrasonic Flow Meter Make: TUF Model: 2000M Qty: 1	3 Analog Inputs Output: 4 – 20 mA Accuracy: 1% FS	Power Supply: 8 – 36 VDC	Electrical Connection: 3-pin plug
Data Acquisition Device Make: NI Model: 6009 Qty: 1	Inputs: 4 Differential or 8 SE Input Resolution: 14 bits (Differential) or 13 bits (SE) Maximum Sample Rate: 48 kS/s (aggregate) Converter Type: Successive Approximation AI FIFO: 512 bytes Input Range: ± 10 V Software: DAQExpress / NI LABVIEW	Power Supply: USB, 4.10 – 5.25 VDC	USB Connector: USB Series B Receptacle I/O Connectors: 16 Position Terminal Plugs Screw Terminal Wiring: 16 – 28AWG
Data Acquisition Device Make: NI Model: 6210 Qty: 1	Inputs: 8 Differential or 16 SE Input Resolution: 16 bits Maximum Sample Rate: 250 kS/s (aggregate) Converter Type: Successive Approximation Input FIFO: 4095 Samples Input Range: ± 10 V CMRR (DC to 60Hz): 100 dB Software: DAQExpress/ NI LABVIEW	Power Supply: USB, 4.5 – 5.25 VDC Maximum inrush current: 500 mA Maximum Load (Typical Current): 400 mA at 4.5V	I/O Connectors: Two 16-position combicon USB Connector: Series B Receptacle Screw Terminal Wiring: 16 – 28 AWG

Note that the images of the different instruments are presented in **Appendix A** along with calibration certificates for the accelerometers used in vibration data acquisition.

5.3. METHODOLODY

This study employed a combination of experimental, observational and signal processing techniques to investigate the cavitation phenomena in a PAT system, ultimately developing a reliable cavitation detection method suited for condition monitoring. Experimentation involved controlling the water flow through the system to find the suitable conditions for cavitation to occur. This was coupled with observations to judge the condition of the flow out of the impeller as the flow through the system was being controlled to obtain cavitation friendly conditions.

To assess the normality of obtained vibration data indicative of various cavitation states, a normal probability plot (NPP) and the Gaussian probability distribution of measurement data were computed. These techniques were the basis of the proposed time-domain cavitation detection technique in this chapter. The rationale for choosing these signal processing techniques was based on the premise that system faults lead to changes in the signal's probability distribution. Therefore, by quantifying the differences between probability distributions under various machine fault conditions, it may be possible to detect the presence of such faults.

5.3.1. Identification of Cavitation Condition

Cavitation occurrence inside the PAT was qualitatively monitored via observations through a transparent Perspex viewing pane integrated into the system downstream of the PAT impeller. Three distinct cavitation regimes were identified during the conduct of the experiments, which agreed with the obtained CFD simulations conducted in Chapter 4,

- **No Cavitation** – clear, undisturbed flow with no visible vapour structures
- **Inception Cavitation** - thin clear sheet-like structure originating from the centre of the impeller and extending into the outlet pipe, occasionally accompanied by fast travelling bubbles.
- **Full Cavitation** – development of a dense, whitish vapour-filled vortex core spanning the entire length of the viewing pane, attributed to localised pressures falling below the vapour pressure due to swirling flow components under off-design conditions.

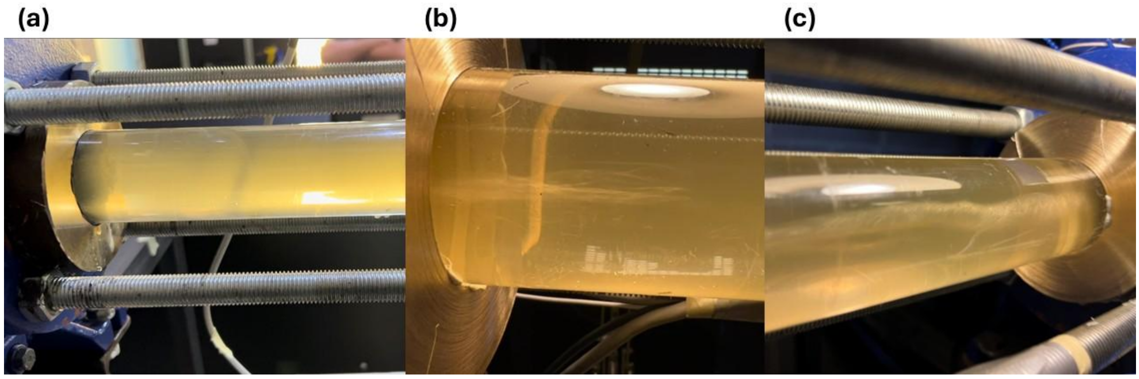

Figure 5.3-1. The observed flow through the viewing pane under (a) 'no cavitation' (b) 'inception cavitation' and (c) 'full cavitation' conditions.

Figure 5.3-1 illustrates the visual characteristics of the flow under the three cavitation regimes as observed through the viewing pane. It is worth noting that before the occurrence of a thin clear sheet-like structure, a burst of fast travelling vapour bubbles was observed that was almost impossible to capture on camera. Therefore, there were no pictures taken that clearly portrayed this phase of cavitation development inside the PAT. Nonetheless, the duration of these fast-travelling bubbles was short-lived, quickly changing into a thin sheet-like structure. As such, the thin clear sheet-like structure was taken to be representing the 'inception cavitation' phase.

5.3.1.1. Potential for Subjectivity

The above-described cavitation classification method is heavily reliant on visual observation of the flow within the PAT. While visual observation is widely used in experimental cavitation studies due to its direct and intuitive nature, it inherently introduces an element of subjectivity that must be critically acknowledged. One source of subjectivity arises from the qualitative interpretation of cavitation appearance. The visual transition between *'no cavitation'*, '*inception cavitation'* and '*full cavitation'* is often gradual rather than abrupt. This can lead to ambiguity, particularly near threshold conditions where small vapour structures intermittently appear and collapse. The precise point at which such behaviour is classified as '*inception cavitation'* or it transitions into '*full cavitation'* may vary between observers or even for the same observer at different times.

Another source of subjectivity is related to observer dependence and human perception. Visual classification depends on the observer's experience, judgement and expectations. Lighting conditions, viewing angles and flow transparency can also influence what is perceived as cavitation. In addition, the dynamic nature of cavitation that is characterised by rapid growth and collapse of vapour structures, means that short-lived vapour structures may be missed or overemphasized depending on observation duration. Temporal variability also contributes to subjectivity. Cavitation can fluctuate over time at a given operating point, particularly near inception point. A classification based on brief observation may therefore not fully capture the representative cavitation state. This introduces uncertainty when defining discrete cavitation classes from inherently unsteady phenomena.

Despite these limitations, visual observations remain a necessary and pragmatic reference method in the context of this study due to budgetary constraints in relation to procurement of advanced high speed photography equipment. Most importantly, visual classification was not used as an end in itself, but as a ground-truth labelling mechanism to support vibration-based analysis and machine learning model development. To mitigate subjectivity, visual observations were conducted consistently under controlled lighting and operating conditions while classification was based on cavitation behaviour sustained over significant time periods rather than isolated events.

In addition, the study did not rely on subtle distinctions between visually similar cavitation states. Instead, cavitation was grouped into clearly distinguishable stages i.e., '*no cavitation*', '*inception cavitation*' and *'full cavitation',* where visual differences are clearer and more reproducible. These broad categories align with common practice in experimental cavitation research and are appropriate for the objectives of detection and diagnosis rather than in-depth cavitation modelling. The validity of the visual classification was further reinforced by the strong correlation observed in the probability density functions presented in section 5.5.1. The consistency in probability density functions of the same classification stage for a specific operating speed suggests that, while subjectivity exists, it did not dominate or invalidate the results.

5.3.2. Cavitation Experimentation

Experimentation commenced with the activation of the supply pump to establish water flow through the hydraulic circuit, placing the PAT in an unloaded, free spinning state. After two minutes of continuous circulation, the flow rate was manually reduced to facilitate safe connection of the electrical load without triggering system protection mechanisms. Subsequently, the Variable Speed Drive (VSD) was configured to operate the generator at a constant speed of 1500 rpm, representing nominal grid -synchronous loading conditions.

The PAT-generator system was then allowed to operate for an additional ten minutes to ensure synchronization between mechanical and hydraulic conditions. Once synchronization was confirmed, the flow was manually adjusted via a control valve to the optimal operating point and allowed to stabilize for three minutes to achieve steady state conditions. Measurements of both vibration and process data were taken while observing the flow regime for qualitative description of the cavitation state. The control valve was incrementally adjusted to achieve nine operating conditions ranging from a high flow rate value to a low flow rate value. These were determined by dividing the full stroke of the valve lever arm into ten equally spaced positions, ranging from fully closed position to fully open. At each new valve setting, the system was allowed to stabilise for approximately three minutes prior to data collection. The observed cavitation status was noted for each of the measurement point.

These experiments were conducted in duplicate to evaluate repeatability and assess result variability. Observations across repeated trials revealed no significant variations, confirming reproducibility of the measurements (See **Appendix B**). In addition to the baseline speed of 1500 rpm, the PAT was tested at five other rotational speeds i.e., 900, 1200, 1350, 1650 and 1800 rpm, to evaluate the machine behaviour across a wide operational range. For each speed, extra measurements were recorded under the following conditions, locked rotor and runaway conditions. During locked rotor operation the impeller shaft is mechanically restrained using a self-locking wrench, preventing rotation while water continued to flow through the impeller passages. This configuration simulated hydraulic loading without mechanical power generation. During runaway condition the PAT was operated in an unloaded, free spinning state by disconnecting the generator from the VSD, thereby eliminating shaft toque and electrical load.

Table 5.3-1. Summary of the investigated operating points at various operating speeds

Operating Point	Flow rate (l/s) at different operating speeds					
	900 rpm	**1200 rpm**	**1350 rpm**	**1500 rpm**	**1650 rpm**	**1800 rpm**
OP1	8.41	7.48	8.14	7.69	7.14	7.15
OP2 †	8.79	7.73	6.91	6.79	7.17	6.52
OP3	6.92	7.15	7.01	6.91	6.76	6.56
OP4	7.28	7.08	6.76	6.67	6.21	6.00
OP5	6.85	6.58	6.18	6.13	5.89	5.50
OP6	6.28	5.99	5.60	5.48	5.09	4.71
OP7	5.90	5.60	5.17	5.03	4.45	4.00
OP8	5.19	5.03	4.51	4.18	3.49	3.02
OP9	4.26	3.91	3.11	2.94	1.78	1.28

Colour code: No Cavitation; Inception Cavitation; Full Cavitation

† Baseline operating condition

Table 5.3-1 provides a summary of the flow rates observed at each of the nine operating points across the six tested rotational speeds. Cavitation states were categorised and colour coded as follows, green represented the 'no cavitation' state, orange represented the 'inception cavitation' state while red represented 'full cavitation' state. The baseline operating condition corresponding to the optimal design conditions at each rotational speed, is marked with the Greek Obelisk symbol † symbol and is referenced consistently throughout the subsequent chapters.

5.3.3. Measurement Data Acquisition

All vibration measurements were acquired at a sampling frequency of 12.8 kHz over a duration of 60 seconds. This high sampling frequency was selected to enable detailed analysis of frequency content across a broad spectrum, capturing potential cavitation signatures in both the low and high-frequency ranges. The dataset recorded at the machine's best operating flow rate was designated as the baseline condition. This baseline represented the optimal, cavitation-free operating point of the PAT and served as the reference for identifying deviations linked to cavitation onset and progression.

To reduce low-frequency noise, the vibration data was processed using a third-order high-pass Butterworth filter with a cut-off frequency of 10 Hz. Frequencies below this threshold were excluded to eliminate background noise typically associated with environmental disturbances.

Figure 5.3.2 shows the signals for the three cavitation states before and after the high pass filtering process for the 1500 rpm operating speed. The third-order Butterworth design was selected for its balance between steep attenuation and minimal phase distortion, making it well-suited for distinguishing relevant dynamic features in the vibration signal. The filter implementation was carried out in MATLAB.

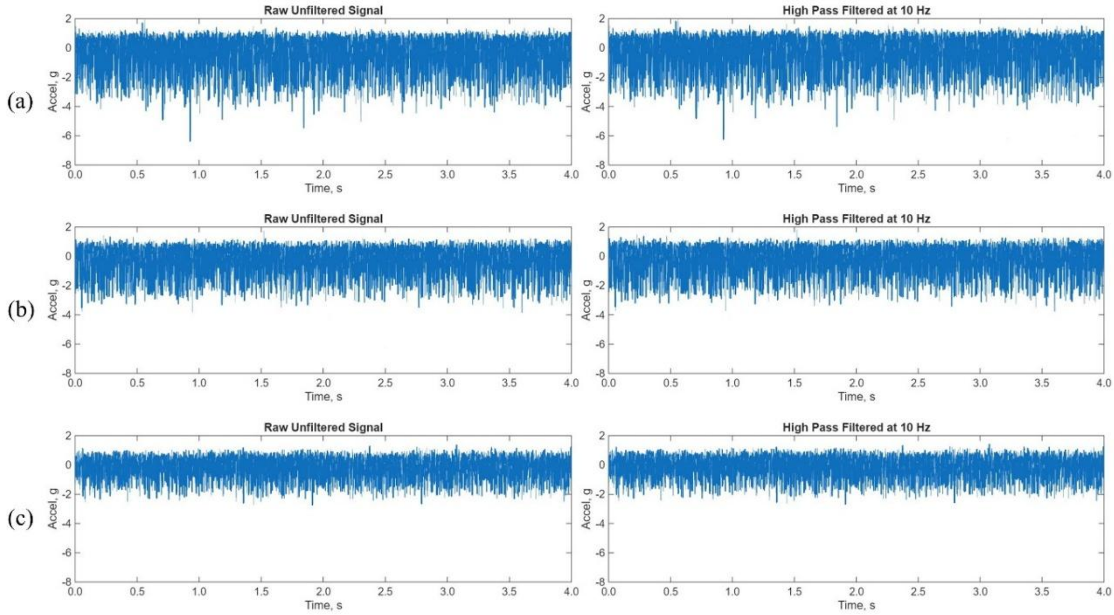

Figure 5.3-2. Vibration signals before and after high pass filtering at 10 Hz for the a) "no cavitation" case, b) inception cavitation" case and c) "full cavitation" case

In parallel, process data in the form of flow rate, power output, upstream and downstream pressure data were sampled at 1 kHz over a 60 second period. Given the relatively slow variation of these parameters, the data was averaged to obtain one value per second per parameter. These averaged values were used to characterise PAT performance under varying operating conditions.

5.4. PAT PERFORMANCE ANALYSIS UNDER CAVITATING CONDITIONS

The performance of PATs under cavitating conditions remains an area which has received limited attention in the literature. Most PAT-focused research efforts have been towards selecting the right PAT size for a specific application and understanding the PAT performance characteristics. Most cavitation-focused research has not considered PATs in turbine mode considering its relatively recent widespread use. As a result, even though cavitation is ubiquitous with hydraulic machines, its occurrence in PATs has been greatly overlooked. Understanding cavitation performance is essential as it guides in deciding the safe operation zone of these kind of machines, and this is particularly important considering that PATs are operating in modes for which the original pumps were never designed to operate in. As such it is the purpose of this section to provide the initial steps in including the PAT cavitation performance in the design of PAT systems by studying how the occurrence of cavitation affects its performance.

5.4.1. PAT Performance Curves

When designing PAT systems, it is standard practice to place its operating range within the two common design curves, which are the locked rotor curve and the runaway speed curve. These two curves are representative of the flow head relationship when the impeller is not spinning and when the impeller is spinning freely without producing any torque, respectively. Outside of this operating range the PAT performance is unsatisfactory. However, operating the PAT in this zone does not necessarily mean the machine is safe from cavitating flows.

Figure 5.4-1 shows the characteristic curves obtained when measurements were taken at various operating speeds, *N*. In Fig. 5.4-1(a) the head curve is shown with the locked rotor and runaway condition curves overlayed to depict the areas at which the operation of the PAT is limited. This is the shaded region of the plot which represents the performance envelope of the PAT. It is evident from this figure that the limit of operation of the PAT is very narrow for each rotational speed.

Keeping the flow rate through the machine constant and increasing the operating speed, the head required increases. The power output and the overall efficiency of the system follows a similar trend. Many techniques have been proposed that can be used to predict the nominal point of the PAT from pump mode characteristics. This helps designers select a pump unit to be used as a PAT without having to perform some experimental work. However, a grey area exists when it comes to cavitation as most studies that claim to have investigated PAT cavitation behaviour have mainly focused on pump mode operation with little efforts aimed towards the turbine mode.

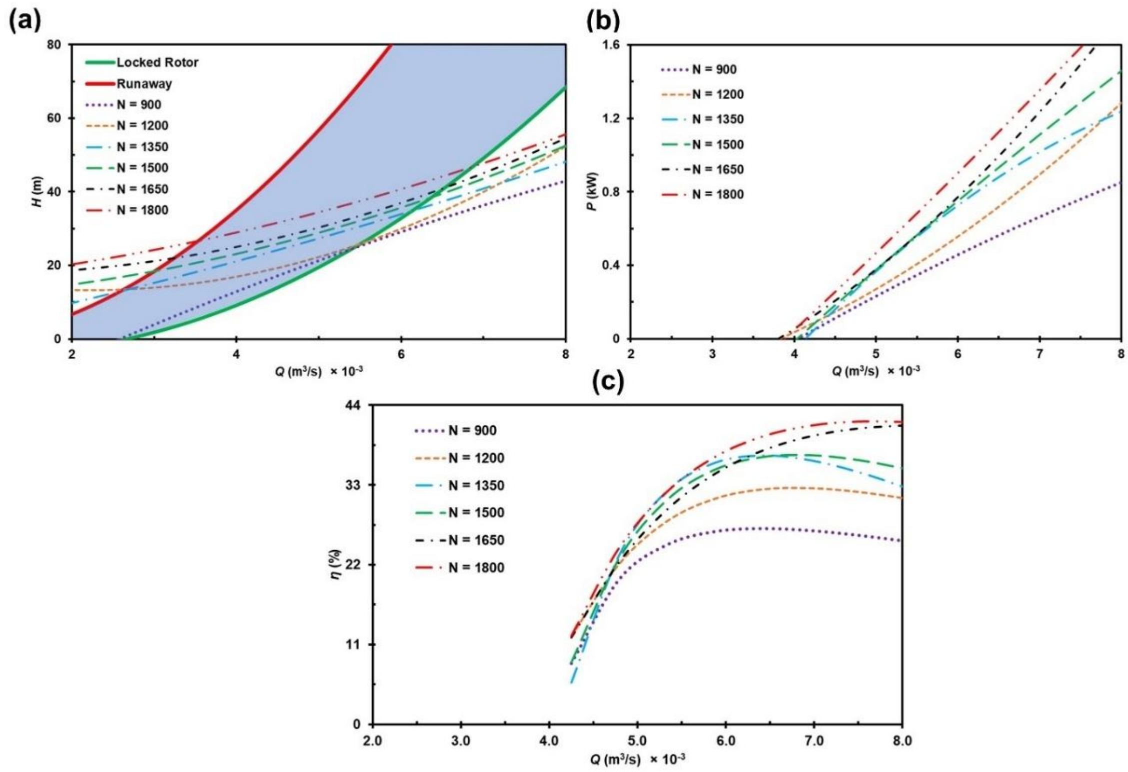

Figure 5.4-1. PAT characteristic curve under varying operation speed (a) head (b) power (c) efficiency

It remains unclear what the limits for cavitation free operation in PATs are, even though it is a well-known fact that cavitation is a significant risk to hydraulic machines. To investigate the possibilities of considering cavitation performance of PATs during design, cavitation occurrence inside the PAT was observed as the flow conditions were being varied for each rotational speed. When the PAT was deemed to be undergoing full cavitation as described in section 5.3, the performance characteristics were observed and analysed. In Fig. 5.4-2, the flow conditions at which inception cavitation and full cavitation starts where noted and plotted on the head curves. The region between these points means that the machine is in the transition state between 'inception cavitation' and 'full cavitation'.

Observation of both zones indicate that the occurrence of inception cavitation initiates at a constant head value which is equivalent to 29.65m when individual values are averaged. Similarly, the values for the full cavitation zone averages to a flow rate value of 4.03×10^{3} m^3/s. Further observation of the power curves indicate that the full cavitation zone coincides with the zero-output power point of the PAT.

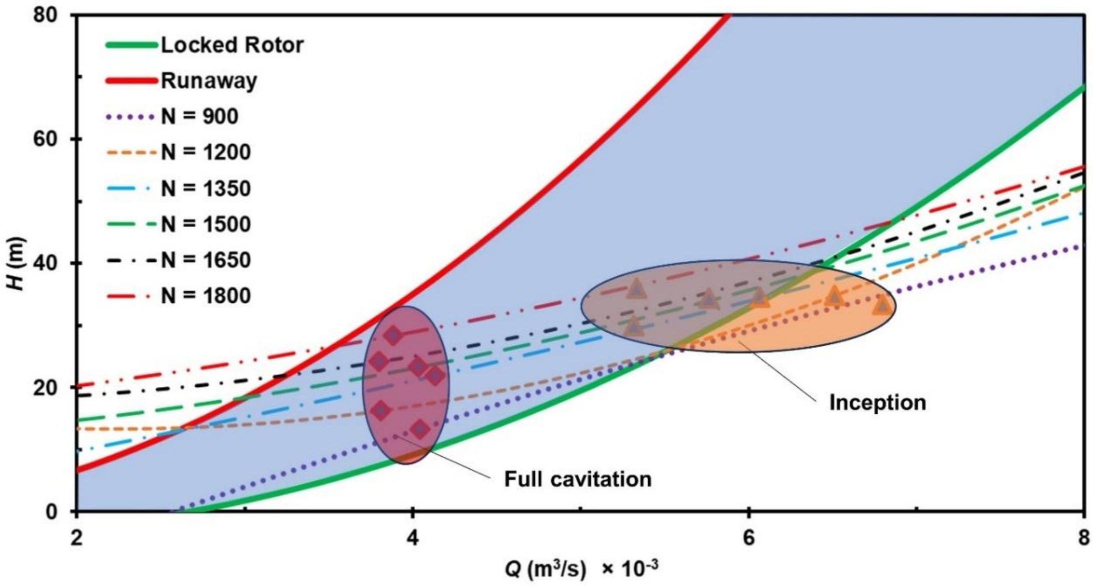

Figure 5.4-2. Cavitation occurrence zones in a PAT at various operating speeds

In order to generalize the prediction of the occurrence of both inception and full cavitation in PATs, the characteristic curve generalization for head and power suggested by Novara and McNabola [189] were used. They used a database of 113 PATs of different sizes, manufacturers and types to approximate the best fit of two second order polynomials as shown in Eqns. 5.4-1 and 5.4-2, respectively.

$$\frac{H_t}{H_{bep}} = a\left(\frac{Q_t}{Q_{bep}}\right)^2 + b\left(\frac{Q_t}{Q_{bep}}\right) + c \quad (5.4\text{-}1)$$

$$\frac{P_t}{P_{bep}} = d\left(\frac{Q_t}{Q_{bep}}\right)^2 + e\left(\frac{Q_t}{Q_{bep}}\right) + f \quad (5.4\text{-}2)$$

where H_t, H_{bep}, Q_t, Q_{bep}, P_t, and P_{bep} represent the head through the PAT, head at BEP, flow rate through the turbine, flow rate at BEP, output power generated by the PAT and the output power at BEP, respectively. The variables a, b, c, d, e and f are regression coefficients defined as per Table 5.4-1.

Table 5.4-1. Coefficients for Eqns. 5.4-1 and 5.4-2

Non-dimensional head curve		Non-dimensional power curve	
a	1.160	d	1.248
b	(0.0099 N_s + 1.2573) – 2d	e	(0.0108 N_s + 2.2243) – 2d
c	1 – a – b	f	1 – d – e

Equation 5.4-1 defines the estimation of the relative head curve based on the known BEPs and PAT specific speed. At onset of cavitation, this equation consistently converges to H_t = 29.65m for all

values of rotational speeds, N, allowing for the derivation of Eqn. 5.4-3. This equation provides the corresponding flow rate value, $Q_{t,ic}$, at which cavitation is expected to initiate within a PAT

$$Q_{t,ic} = Q_{bep} \times \frac{-\mathrm{b} \pm \sqrt{b^2 - 4\mathrm{a}\left(c - \frac{29.65}{H_{bep}}\right)}}{2\mathrm{a}} \tag{5.4-3}$$

$$Q_{t,fc} = Q_{bep} \times \frac{-e \pm \sqrt{e^2 - 4df}}{2d} \tag{5.4-4}$$

Similarly, Eqn. 5.4-2 describes the relative power outputs as a function of BEP flow rate and specific speed. Under full cavitation conditions, the relative power approaches zero, enabling Eqn. 5.4-4 to be derived. This equation represents the flow rate, $Q_{t,fc}$, at which full cavitation is predicted to occur. The coefficients a, b, c, d, e and f used in these equations are as detailed in Table 5.4-1.

These formulations provide a basis for incorporating cavitation susceptibility into the design of PAT systems. Specifically, they define a recommended operating range bounded by the two flow rate thresholds, $Q_{t,ic}$, which represent the inception of cavitation. Operating within this narrow region minimizes the risk of cavitation-induced damage and helps maintain optimal system performance. Operation outside this range should be avoided, as it increases the likelihood of destructive cavitation effects and leads to reduced hydraulic efficiency.

It is important to note that the derived equations are preliminary and require further validation using a broader dataset encompassing PATs of varying sizes and capacities to confirm their general applicability. This forms a key area for future research, once additional cavitation data across diverse PAT configurations becomes available.

In conclusion, this section presented a conceptual framework for integrating cavitation limits into PAT design. With further development and validation, this approach could serve as a valuable tool for enhancing system reliability and performance by proactively accounting for cavitation during the design phase.

5.5. CAVITATION DETECTION IN A CENTRIFUGAL PAT

Cavitation detection in hydraulic machinery is of utmost importance as it safeguards their integrity as well as ensures that they are always operated at conditions that offer performance at desirable efficiency. In conventional turbines and pumps, this phenomenon is well understood and there are available techniques that make its detection a routine task in modern powerplant systems. However, these techniques have never been investigated in PATs. Moreover, the advent of automated algorithms for predictive maintenance of machinery, especially machine learning based classification algorithms, requires computation of signal features that can describe the machine condition. For the optimal performance of this classification algorithms the signal features need to be computed from parameters that are can be deemed as machine condition indicators.

$$PSD = |X(f)|^2 \tag{5.5-1}$$

The use of overall vibration measurement in the form of RMS values of measured signals is one such technique. RMS represents the overall level of energy in the measured signal, and it is defined as per Eqn. 2.5-1. The power of frequency components in the spectrum of the measured signal is sometimes used to detect cavitation in the form of a Power Spectral Density (PSD). Equation 5.5-1 gives a mathematical representation of the signal power in the frequency domain with $|X(f)|$ being the FFT Transformed vibration signal.

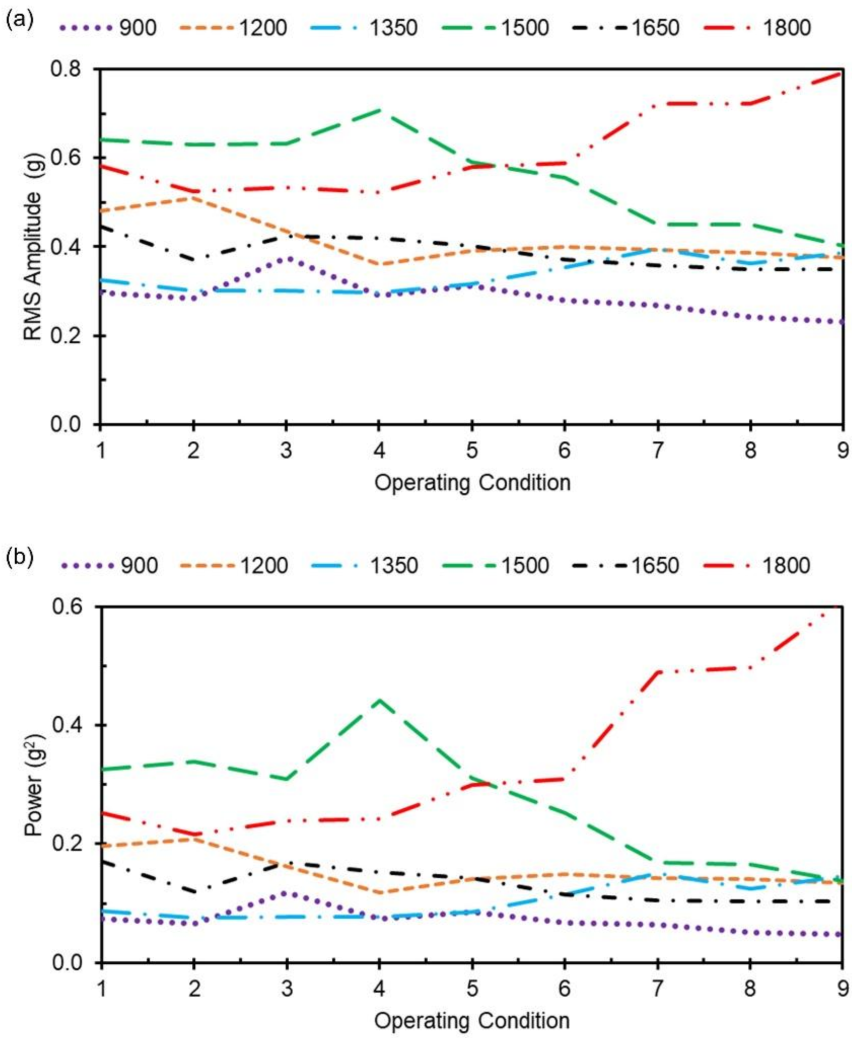

Figure 5.5-1. Trend plots of both RMS and power values as operating condition is being varied

The measured vibration signals were used to compute the RMS and Power values of the measured vibration signals. These were trended as operating conditions were varied as indicated in the earlier tables. Figure 5.5-1 shows the trend plots of each of the two parameters, (a) RMS and (b) Power, as operating conditions were being varied for each of the studied rotating speeds. The values of both RMS and Power follows a similar trend.

From the plots, higher changes in the trend lines are observed in two of the operating speeds namely, 1500 rpm and 1800rpm, with all other studied operating speeds depicting close to a flat trend line as the operating conditions varied from no cavitation to cavitation. At 1500 rpm there is an observed increase in both RMS and Power values when the operating point is being varied from OP3 to OP4. The two parameters then reduce in magnitude to their initial levels at OP5. This reduces further as the machine condition goes further into cavitating conditions.

Similarly at 1800 rpm, both parameters remain almost constant from OP1 to OP4, where it then begins to rise when operating conditions changes to OP5. The uptrend continues further into fully cavitating conditions. Overall, when the PAT is under cavitating conditions the observed variations appear to be speed dependent as at some operating speeds the overall RMS and Power values trend downwards whereas at other speeds it trends upwards.

The use of both RMS and Power to monitor and detect cavitation in PATs does not appear to present an effective solution for field implementation in this case, as for most of the operating speeds investigated their trend lines are almost flat creating a difficulty in setting alarm levels. This could be a main cause of false positives in a condition monitoring setup. As such, it is imperative to investigate other means that could facilitate easy and accurate detection of cavitation in PATs.

5.5.1. Modified Deviation from Normal Distribution Technique for Cavitation Detection

The Deviation from Normal Distribution (DND) technique as proposed by Rzeszucinski et al. [112] is based on the comparison of the deviation of vibration responses from their corresponding normal distributions. The idea here is that these deviations are different between varying structural health conditions, thus being able to differentiate between healthy and faulty conditions. If the reviewed dataset follows a Gaussian distribution, most of the data points will fall along a straight line in a Normal Probability Plot (NPP). However, non-linearity is indicated by deviations from the straight line, and these can be quantified as the DND. The DND represented by the area between the actual and Gaussian distribution was computed according to Eqn. 5.5-2 [113]:

$$DND = \sum_{i=1}^{n} \left(\frac{|Z_{a,i} - Z_{n,i}| + |Z_{a,i+1} - Z_{n,i+1}|}{2} \right) (\Delta x) \tag{5.5-2}$$

where n represents the number of data points in a signal, $Z_{(a,i)}$ and $Z_{(n,i)}$ represent values for the actual and Gaussian distribution, respectively, at i^{th} data point, and Δx is the spacing between data points.

When calculating the original DND, the values of $Z_{(n,i)}$ and $Z_{(n,i+1)}$) are drawn from the same dataset used to compute the actual distribution, thus comparing it to its theoretical Gaussian distribution, which may diverge from the Gaussian distribution of vibration data for healthy operating conditions. To ensure that the DND reflects the machine's healthy condition, we generate the Gaussian distribution from the baseline data and employ it to compute the DND for subsequent operational conditions, clearly delineating the machine's healthy condition from other operating points. In this context, the baseline data pertain to the data collected when the machine is operated at its optimal efficiency point for the designated operating speed. The underlying concept is that the actual distribution for each operational condition varies depending on the machine's cavitation status, leading to fluctuations in the DND. Under the conditions of 'no cavitation', DND values are expected to align with or approximate those of the baseline condition, while cavitating conditions are anticipated to yield distinctly different values from the baseline.

Probability Density Functions

The probability density functions (PDFs) of the captured vibration data were computed to qualitatively describe existing variations as the machine condition is being varied. The Gaussian PDFs were computed using Eqn. 5.5-3 whereas the actual PDF was computed using the histogram estimator defined by Eqn. 5.5-4, where the variables μ and σ in Eqn. 5.5-3 represent the mean and standard deviation of the signal under investigation whereas M and x in Eqn. 5.5-4 represents total number of data points and individual data points in the signal, respectively.

$$f_n(x) = \frac{1}{\sigma\sqrt{2\pi}} e^{\left(\frac{-(x-\mu)^2}{2\sigma^2}\right)} \tag{5.5-3}$$

$$f_a(x) = \frac{1}{M} \times \frac{(number\ of\, x_1 in\ same\ bin\ as\ x)}{(width\ of\ bin\ containing\ x)} \tag{5.5-4}$$

Figure 5.5-2(a) shows the Gaussian PDF of all studied operating conditions at N = 1500 rpm, whereas Fig. 5.5-2(b) shows their actual PDFs. An in-depth observation of the PDFs indicates that the studied operating conditions can be grouped into three categories. The PDFs for operating conditions OP1 to OP4 form the first group, OP5 and OP6 form the second group, and OP7 to OP9 form the third group. These groups are clearly visible in the tails of the Gaussian PDF plot.

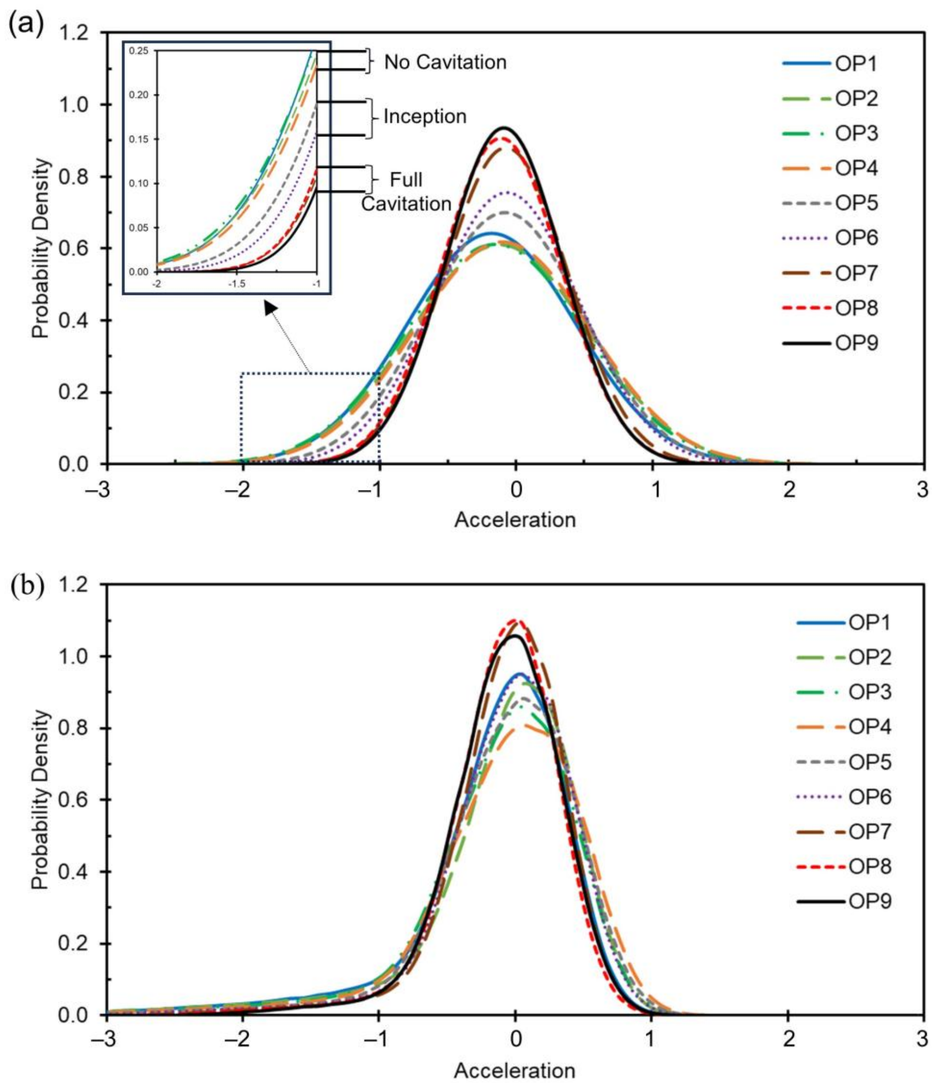

Figure 5.5-2. Computed PDFs for the studied operating points (a) normal PDF and (b) actual PDF.

Operating point OP5 falls under the inception cavitation conditions, contrary to the observed flow regime through the viewing pane. It is likely that inception cavitation occurs before it can be visible in the viewing pane, especially since the viewing pane is a little downstream of the impeller centre where the cavitation process initiates. This presents a possible source of error in the experiment, as there is over reliance on the observer's judgement to confirm the cavitation status of the machine. The same applies to operating condition OP7, which, according to the data, falls under the full cavitation regime as opposed to inception cavitation per Table 5.3-1. The boundary between observed flow under 'inception cavitation' and 'fully developed cavitation' can be difficult to judge, which might have resulted in the machine operating conditions being incorrectly described based on the experimenter's judgement. Nonetheless, the groupings observed in the PDF plots provide an immediate correction of this potential experimental error.

The first group is characterized by broader PDFs with low peaks. This coincides with the non-cavitating condition of the PAT. In the second group of PDFs, the peaks increase and the PDF narrows, as compared to the first group. This matches with the inception cavitation condition. When fully cavitated, the PDFs becomes narrower with higher peaks. In Fig. 5.5-2(b), the actual PDF for all operating conditions consists of longer left tails of the distribution, which is indicative of negative skewness with the preponderance of values lying on the right of the mean.

From this analysis, it is evident that the magnitude of the vibration acceleration is decreasing as the cavitation status worsens. This can imply less vibration and reduced chances of wear and tear with cavitation, consequently meaning cavitation detection in this case is counterintuitive. However, analysis of PDFs of vibration data captured at other PAT operating speeds and varying cavitation status showed different trends (indicated later).

At varying operating speeds, both above and below the design speed, a combination of increasing and decreasing trends of vibration amplitudes was observed, hence, invalidating the inference that monitoring cavitation in PATs defies logic. As such, this prompts for a cavitation detection technique that is resistant to the speed dependency of vibration amplitudes but sensitive to changes in the PAT cavitation state. The prior described variation between the three groups of investigated PDFs might be useful for condition monitoring purposes, but it becomes difficult to quantitatively evaluate the differences in a PDF plot. As such, there exists a need for a more quantifiable means of segregation between the different operating conditions for fault detection.

Normal Probability Plot

To facilitate understanding of how the data deviate from the normal distribution, the normal probability plot was used. Two approaches were adopted in creating the NPP, (a) the reflection of distribution of the data relative to their own Gaussian distribution i.e., the original DND method, and (2) the reflection of the distribution of the data relative to the Gaussian distribution of the baseline data i.e., the proposed modified method.

Figure 5.5-3 shows the NPPs obtained by comparing the actual distribution of data for each operating condition with its own Gaussian distribution. Comparing the plots for each operating condition does not show any significant differences that can be the basis for condition monitoring. This indicates that comparing the actual distribution of data with its normal distribution in an NPP will not yield reasonable differences suitable for monitoring in a condition monitoring setup, hence, proving the need for alter-native approaches.

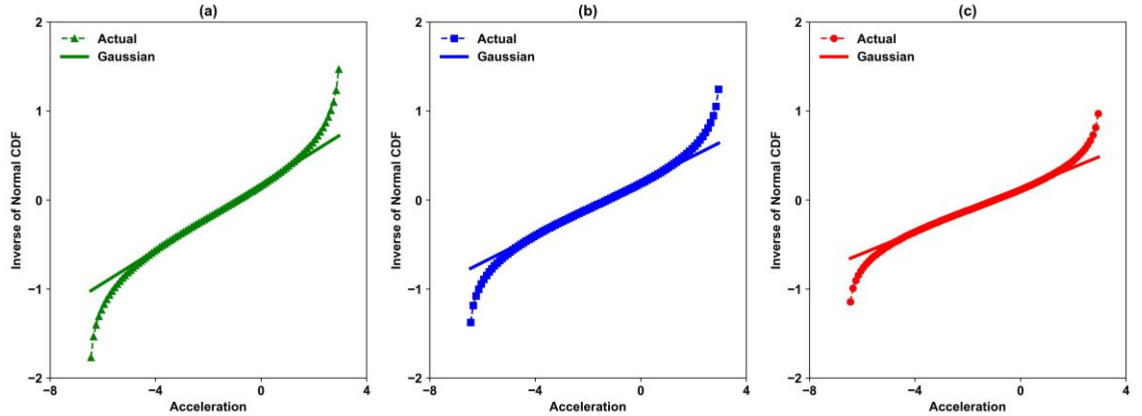

Figure 5.5-3. NPP for actual distribution against its own normal distribution, (a) non-cavitating, (b) inception cavitation, and (c) full cavitation.

In Fig. 5.5-4, the NPP was obtained by comparing the actual distribution of data with the normal distribution of the baseline data. When the PAT is not under cavitating conditions (Fig. 5.5-4a), the data mostly lie on the normal distribution line, diverting only at the extreme ends. The actual distributions of the 'no cavitation' operating conditions match exactly. When cavitation initiates, see Fig. 5.5-4b, there is an evident variation in the data, as indicated by the actual distribution line visibly crossing the normal distribution line three times, creating a larger area between the two curves. The extreme ends of the actual distribution show that the vibration acceleration tends to increase beyond that of the baseline, which is indicative of the increased effects of outliers in the data.

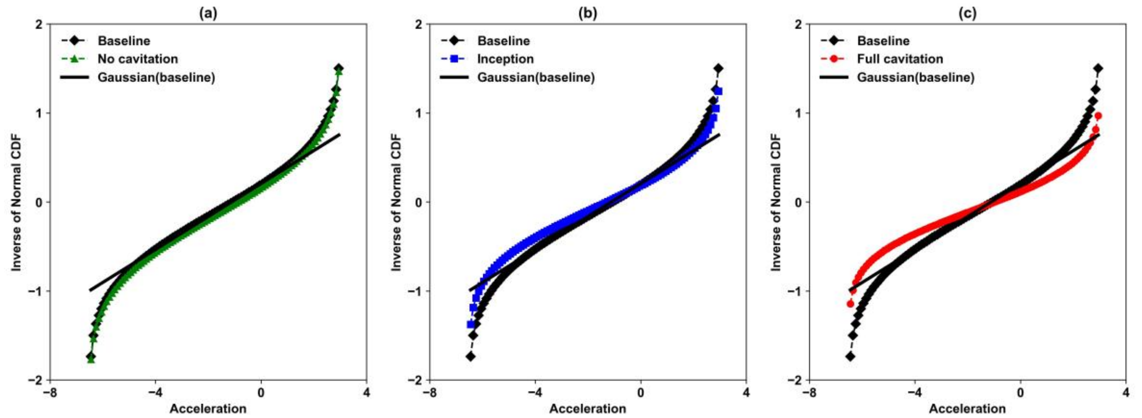

Figure 5.5-4. NPP for actual distribution against the normal distribution of the baseline, (a) non-cavitating, (b) inception cavitation, and (c) full cavitation.

Under fully cavitating conditions (see Fig. 5.5-4c), the NPP resembles that of inception cavitation, with the area between the baseline normal and the actual distribution of the full cavitation data significantly increasing. Further comparison of the actual distributions shows that the full cavitation condition curve further crosses the baseline data curve at extreme ends, signalling a reduction in vibration acceleration amplitude. This reduction in amplitude must be because of the effects of the developed vortex rope in the dynamics of the machine. Alatorre-Frenk [186] noted that when a PAT goes through inception cavitation, the effects of the vortex rope in the dynamics of the machine increases, which then normalizes because of the reduction in the skin friction due to the formation of vapour at the structural surface.

These observed differences in distributions from various operating conditions also provide a qualitative differentiation of cavitation and it is important to quantify this for condition monitoring purposes. The quantification of the areas observed between the actual distribution and the normal distribution of the baseline data provides the basis of the proposed time-based detection method for cavitation.

Deviation from Normal Distribution

The concept of DND was utilized to quantify the observed differences in the NPP obtained by comparing the actual distributions of various operating conditions with the Gaussian of the baseline data. In the prior sections, it was demonstrated that the NPP obtained by computing the actual distributions of each operating condition with its own Gaussian distribution provides little variation between the operating conditions. As such, the DND was computed using the two methods, the original method proposed by Rzeszucinski et al. [112] of using actual distribution with its Gaussian PDF and the proposed method of comparing the actual PDF to the Gaussian PDF of the baseline data. It should be noted that applying the original method of Rzeszucinski et al. [112] previously developed for detection of failures in gearboxes is novel in terms of its application to PAT failure data, while the modified method applies a further developmental step in tailoring the technique toward the PAT application.

In this study, instead of applying the DND method for detection of structural defects, we investigate the application of the DND technique in detecting fluid disturbances in the form of cavitation in a PAT. Unlike structural defects, fluid-induced disturbances are inherently non-linear, which means their characteristics vary highly with time. It is assumed that since measurements are taken on structural elements of the machine, the changes in the captured vibration data are indicative of the changes taking place within the flowing fluid that is transmitted to the structure. This is deemed adequate to characterize cavitation occurrence inside the PAT.

Figure 5.5-5 shows a trend plot of the DND as the operating condition is being varied from non-cavitating to fully cavitating conditions. The solid line across the figure indicates the separation between observation of cavitating and non-cavitating conditions. The DND value obtained from the proposed method increases to higher values after inception cavitation into fully cavitating conditions. The gradual increase in the plot from non-cavitating to cavitating conditions depicts the capability of trending the DND obtained from the comparison with the normal distribution of a baseline data in detecting changes in the fluid flow regime. As such, this is an indication of strong detection capabilities for cavitation in a PAT.

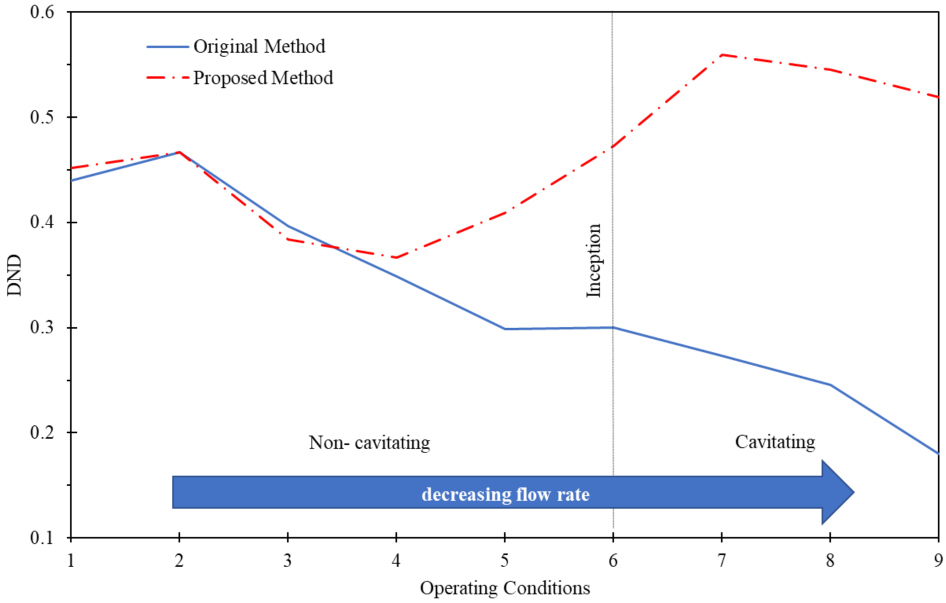

Figure 5.5-5. Trend plot of the DND with varying operating conditions

For the original method, the DND plot decreases continuously from operating point OP2. This consistent drop in the value of the DND would make it difficult to use for condition monitoring purposes. It is evident in the plot that the original method fails to provide a consistent variation between the PAT's cavitation status. There is variation in the DND values for the same condition, i.e., no-cavitation condition consistently increases when using this approach, indicating some possible unreliability issues associated with this method when used in detecting cavitation in PATs. Moreover, this consistent increase in the magnitude changes from one operating point to the next has no respect for the change in operating condition, as its also observed into full cavitating condition.

5.5.2. Validation of Detection Capabilities of the Modified DND Technique

Further experimental tests were conducted to show the effectiveness of the proposed method in detecting cavitation in a PAT. Tables 5.3-1 indicates the investigated test conditions for the operating speeds of 900, 1200, 1350, 1650 and 1800 rpm, respectively. The observed operating regime is also indicated for each operating point.

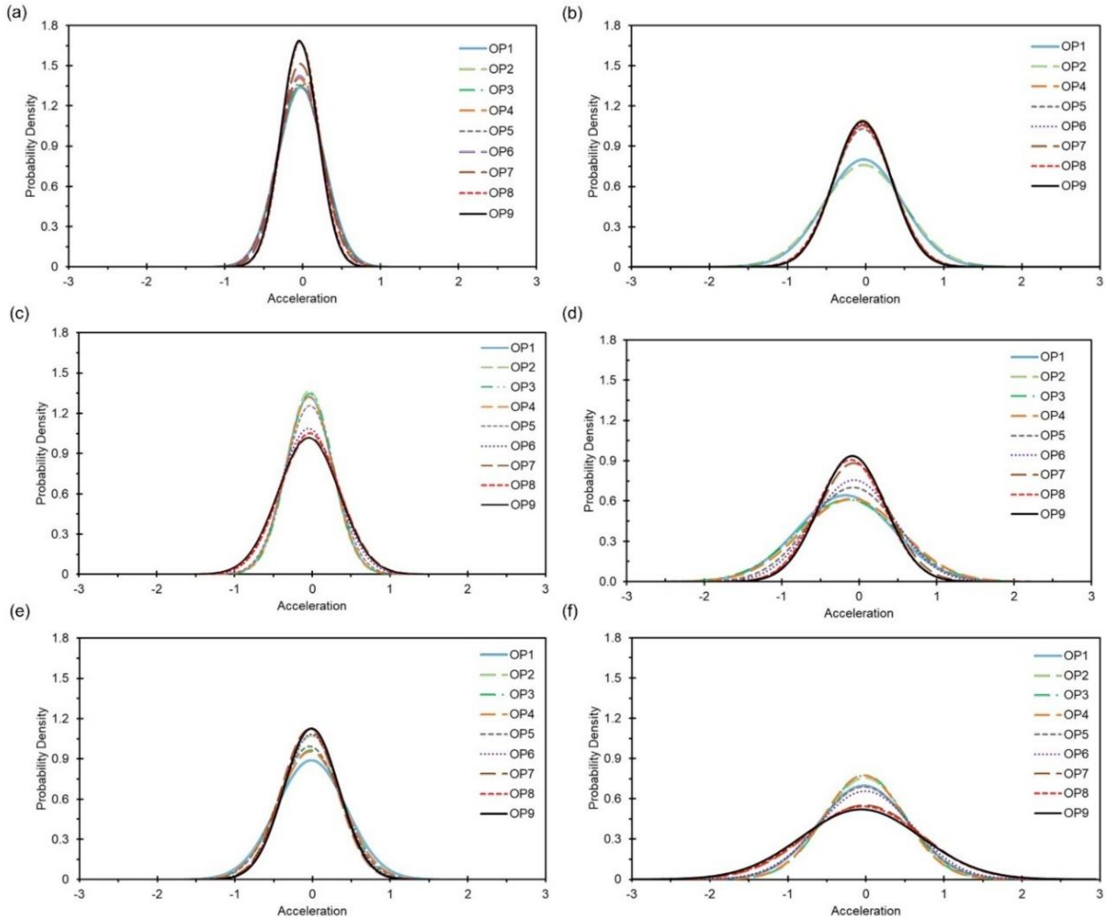

Figure 5.5-6. Gaussian PDFs for the investigated operating speeds, (a) 900 rpm (b) 1200 rpm (c) 1350 rpm (d) 1500 rpm (e)1650 rpm and (f) 1800 rpm.

Gaussian PDFs for these operating speeds were computed and the results are shown in Fig. 5.5-6. As discussed in Section 5.5-1, these PDFs show a varying trend of vibration acceleration, with some speeds showing an increasing vibration behaviour and some showing a decreasing vibration behaviour. For the values of N = 900, 1200, 1350 and 1800 rpm, vibration acceleration for cavitating conditions depict a wider range, thus, wider PDF plots with lower PDF peaks in comparison to narrower plots with higher PDF peaks for non-cavitating conditions, indicative of narrow acceleration ranges with majority of points lying close to the mean acceleration value. Furthermore, it is evident from PDF plots that it is difficult to describe the relationship between rotational speed and vibration acceleration. This is indicated by acceleration amplitude's peak-to-peak values for non-cavitating conditions increasing from 2 g at 900 rpm to 5 g at 1500 rpm followed by 4 g at 1800 rpm. A similar characteristic is observed for cavitating conditions.

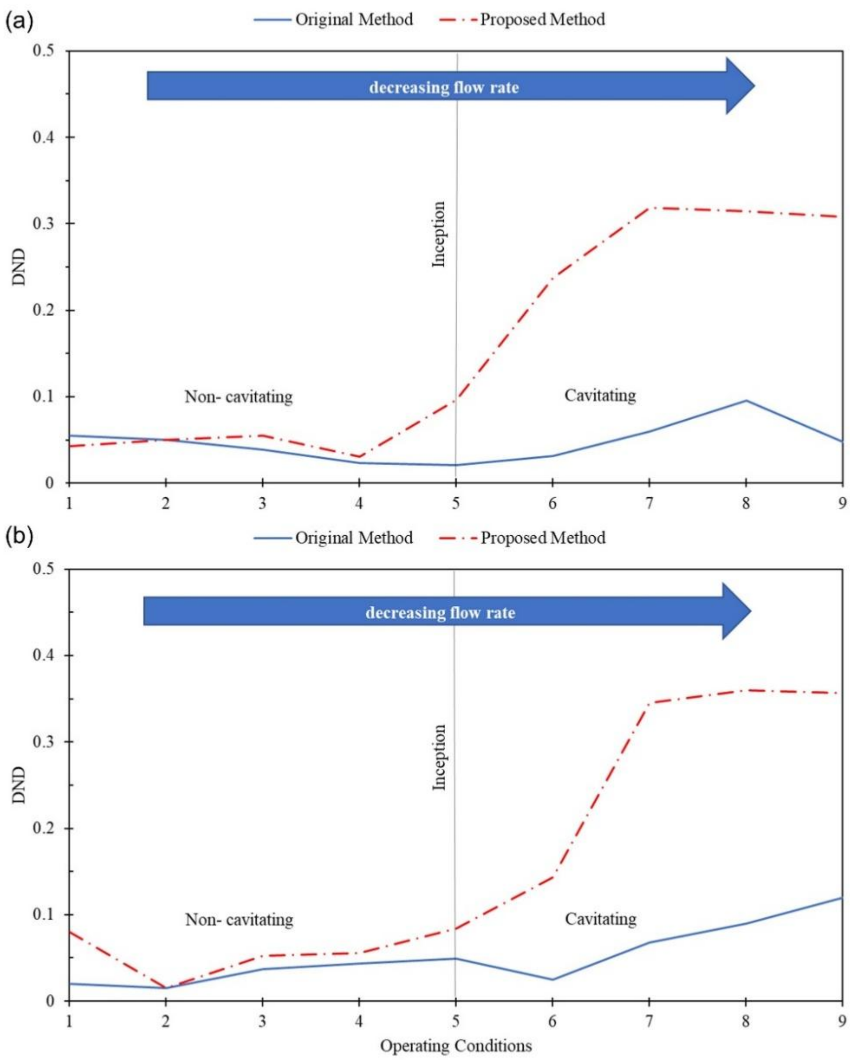

Figure 5.5-7. DND trend for data obtained when the machine was operated at (a) 1350 rpm and (b) 1800 rpm

Based on this analysis and the observed trend of data captured at various speeds, cavitation occurrence alters vibration response differently at various operating speeds. At some operating speeds, there is a resultant increase in vibration levels, whereas at other speeds, vibration levels of the PAT decrease. This is also evidenced in the trending of the overall vibration values and power presented in earlier sections. This variable response at various speeds can be considered evidence for a requirement of a cavitation detection system in PATs that is robust and independent from operational speed.

Like the analysis conducted in the prior section, the DND value changed trends as the machine cavitation status varied from 'no cavitation' to 'full cavitation'. Figure 5.5-7 shows the obtained trend plot when the machine was operated at 1350 rpm and 1800 rpm. Similarly, the plot compares the proposed method of computing the DND to its original version. It is evident from the plot that the proposed method shows a higher magnitude change when the cavitation state changes from no cavitation to full cavitation. There is an observed magnitude increment in the value of DND during cavitation as compared to the no cavitations state. Moreover, the comparison of the proposed method with the original version indicates that the magnitude of the change observed when using the original version is very small and difficult to discern when compared with the proposed new method, especially when the cavitation state changes from no cavitation to full cavitation. This can be a very important factor when the modified DND is being trended for condition monitoring purposes, which could yield false negatives.

5.5.3. Setting Limits for Monitoring Purposes

To ensure effective monitoring and early fault detection thresholds were established to distinguish between normal operating conditions, and progressive stages of cavitation occurrence. These limits were derived from the statistical analysis of the modified DND data under the cavitation states categorised as ‘no cavitation’, ‘inception cavitation and ‘full cavitation’, respectively.

Table 5.5-1. Monitoring Limits for the modified DND at all investigates operating speed

Rotation Speed, N	Threshold Level	Bearing Xdir	Bearing Ydir	Outlet Flange Xdir	Outlet Flange Ydir	Outlet Flange Zdir
1800	Warning	7.9530	4.2713	5.1986	4.5144	5.9270
	Critical	7.1206	5.9173	4.4540	3.8491	5.1594
1650	Warning	12.1948	9.5393	12.6474	13.2726	15.4962
	Critical	12.3253	8.0866	15.0359	16.8210	17.3751
1500	Warning	10.0136	7.4801	5.0018	4.9943	5.5705
	Critical	12.2098	9.9715	5.2942	5.3656	6.1801
1350	Warning	6.7268	10.3104	6.1387	8.1247	15.7990
	Critical	7.7658	10.8815	7.5048	13.8647	21.3712
1200	Warning	23.1468	17.6317	17.0895	13.8882	18.4490
	Critical	5.3414	6.2450	4.7903	3.1290	5.7134
900	Warning	11.3594	23.7322	17.6758	15.7894	17.0763
	Critical	7.1409	17.4220	12.3882	9.7166	12.0867

The mean values of the obtained modified DND corresponding to each PAT cavitation state were computed. Based on these, two threshold levels were set and Table 5.5-1 presents the values of the obtained limits for all the operation speed at all vibration measurement location. *Xdir*, *Ydir* and *Zdir* refers to measurements collected in the horizontal, vertical and axial direction, respectively.

- Warning Limit: This threshold was defined as the midpoint between the ‘no cavitation’ and ‘inception cavitation’ average values. It serves as an early indication of deviation from optimal performance, prompting further inspection or alteration of process parameters.

- Critical Limit: This threshold was calculated as the midpoint between the 'inception cavitation' and 'full cavitation' average values. Exceeding this limit suggests a transition into a significantly cavitating condition, potentially requiring immediate corrective action.

These limits provide a data-driven, condition-specific basis for real-time monitoring and automated alert systems. The accuracy of limit placement is enhanced by the use of historical data whose condition has been confirmed during experimentation, as such it reflect realistic operational variability. Visualizations of incorporating these thresholds are presented in **Appendix C**. The performance of the proposed method in detecting the occurrence of cavitation inside a PAT is quite promising and with further fine tuning of limits by incorporating machine learning models, the method can be of valuable importance in avoiding failures caused by cavitation.

5.5.4. Implications and Practical Applicability of the Proposed Technique

The experiments were conducted in as close as possible conditions to PAT installations in the field. No additional suction or vacuum systems were included that are typical of laboratory studies of this nature but are not 100% representative of real-world applications. As such, it is evident that in real world operational settings, PATs will be exposed to cavitating conditions that can be detrimental to their operation, especially in cases where there is a wide variation in flow conditions and/or frequent start-up or shut-down operations. Application of the proposed DND approach to detect cavitation occurrence can be helpful in averting such effects, particularly where there is lack of expert understanding of the cavitation phenomenon in the generation mode of PATs [190].

Deployment of the technique in a typical industrial scenario would entail computation of the DND from captured vibration data and trending the value over time. This can be accomplished at the data capture point via edge computing as it does not require complex lines of codes to compute the DND and large data storage space. The potential limitations associated with field deployment include the reliance on baseline data and the possibility of baseline drift due to varying operating conditions. The effects of the changes in operating speed have been investigated here and the robustness of the technique was demonstrated under varying speed conditions. Variation in operating conditions could also be a result of changes in head–flow conditions and maybe the accumulation of material on rotating parts of the impeller due to the type of application such as wastewater treatment. Since the technique was proven efficient in detecting cavitation when flow rate was varied, it is, therefore, assumed that similar changes will not result in many performance problems. However, it has not been demonstrated how the technique will perform under constant flow but varying pressure conditions. This can be investigated in future works.

The proposed technique is highly dependent on the use of baseline data, which might be difficult to ascertain in the field. Even though that is the case, the use of baseline data is widely acceptable in condition monitoring systems. Most predictive maintenance programs use baseline data captured at installation or immediately after the completion of the first scheduled maintenance post the establishment of the program. The baseline data will then be used as a reference for comparison purposes with the machine condition at any future instant. Any variations observed can be an indication of a developing fault condition. Thus, baseline data provide historical context needed to identify subtle changes or trends indicative of impending failures.

From the practical applicability point of view due to operation in resource-constrained environments including embedded systems and edge devices, depending on baseline data can ensure that machine condition can be determined without the need for storing large amounts of machine condition data. In the proposed technique, only a single machine dataset is stored and used to compare against future collected data to decide the machine condition. It is envisaged that the amount of storage space required will be minimum, hence lowering the cost of the predictive maintenance program. From this baseline data, a selection of parameters could then be computed, including the DND, that could be used to monitor the machine fault condition. The technique would also allow implementation on edge devices, as the baseline data will only occupy a small storage space and future data will be used just to compute the DND that will be trended and monitored over time.

Moreover, the use of baseline data is important in condition monitoring, as it helps to reduce cases of false positives due to variations in operating conditions. Since baseline data will also be used as a reference for differentiating between faulty and healthy machine conditions, eliminating cases of healthy condition identified as faulty becomes an easy task of comparing with it, hence hastening the whole process. Also, with the existence of historical baseline data, there would be a benchmark to use when deciding whether to update the baseline with the current machine condition data. Even though the machine would not be faulty, updating the baseline could be necessary more so because some machine applications involve the accumulation of material on machine components and normal wear, which cannot be categorized as faulty.

Updating baseline data periodically should safeguard against baseline drift that could result in an increase in either false negatives or false positives. To ensure the robustness of baseline data, incremental learning algorithms can be applied to continually update the baseline data as machine operating conditions vary over time. Baseline data can also be computed from a set of data that represent the anomaly-free condition of the machine. In this study, four or five data sets were classified as without cavitation and represent ranges of operating conditions. Taking an average value of these datasets to be representative of the baseline data would help to guard against baseline drift in the system in the short term.

In comparison with the statistical approaches of proper orthogonal decomposition (POD) and dynamic mode decomposition (DMD) that have garnered wide coverage in fluid dynamics problems, the DND technique is applicable to systems that can be characterized by a known statistical distribution that experience subtle changes in the system behaviour. The DND method produces data that are relatively simple to interpret and is particularly useful when understanding the underlying physics is not as important. In contrast, the POD and the DMD are well-suited to situations where spatial correlations are critical [191-194]. POD and DMD are data-intensive techniques and the proposed DND technique could be used to yield input data to these techniques in a machine learning application.

5.6. SUMMARY

In this chapter, experiments were conducted to induce cavitation within a pump-as-turbine (PAT) and vibration data collected coinciding with ‘no cavitation’, ‘inception cavitation’, and ‘full cavitation’ operating conditions. These conditions were differentiated by the observed cavitation structure as seen through the viewing pane at the PAT outlet. PAT Performance curves were computed, assessed and used to propose a mathematical relationship for considering cavitation behaviour when designing PAT hydropower systems. Result of performance assessments under cavitating conditions indicated that for all operating speeds, the inception of cavitation converges to a constant head value of 29.65m indicating that the PAT is mostly operating under cavitating conditions, while ‘full cavitation’ occurrence coincides with a constant flow rate value of 4.03 l/s.

Moreover, the acquired vibration signals were used to propose an improved time-domain approach for detecting cavitation in PATs. The proposal of this approach is necessitated by the increasing adoption of machine learning algorithms in predictive maintenance that requires to be fed with sensitive condition parameters as inputs. The proposed detection approach involves modifying the computation algorithm for the deviation from normal distribution (DND) method. Instead of comparing the captured data’s actual distribution with their own Gaussian distribution estimate, we use the Gaussian distribution values derived from selected baseline data at the designated operating speed.

Subsequently, the computed DND values were trended to illustrate the changes in the signals corresponding to variations in cavitation detection status. This modification of the original DND method relies on comparing the current machine state with its known healthy state, represented by baseline data at the best efficiency point. Our results indicate that a significant change in the magnitude of DND is detected when the PAT transitions into a cavitating state using the proposed method. Conversely, minimal changes in DND were observed when employing the original method, highlighting potential challenges in setting alarm thresholds for effective condition monitoring purposes.

The proposed approach was further validated by analysing data collected during PAT operation at different rotational speeds, including speeds exceeding and lower than the design speed. Consistently, our findings demonstrate the capability of the proposed approach to accurately detect cavitation states within the PAT, thereby enhancing condition monitoring effectiveness compared with the original method. Conversely, the minor DND value changes observed using the original method could make cavitation detection difficult, and with weaker detection capabilities.

This study also doubles up as the first application of the DND method to fluid-based machinery failures. With no prior evidence of the DND method applied in the detection of fluid-based failures, our study underscores the responsiveness and reliability of the proposed approach in cavitation detection within PAT hydropower systems. Furthermore, the simplicity and ease of implementation of the DND method make it suitable for monitoring by either domain experts or operators in a total productive maintenance framework. However, potential limitations such as the requirement for baseline data availability and the possibility of baseline drifts under varying operation conditions should be noted. Nonetheless, these do not invalidate the benefits of implementing this technique in a real-world application, as it also allows for real-time application.

While this chapter focused on detecting cavitation under stationary conditions, future research should explore the application of our proposed method under non-stationary conditions involving simultaneous changes in rotational speed and flow conditions. Overall, our findings suggest that the proposed approach offers a responsive and reliable technique for cavitation detection in PAT systems, with promising real-time application for condition monitoring in fluid-based systems.

6. FAULT DIAGNOSIS AND APPLICATION OF MACHINE LEARNING APPROACHES

6.1. INTRODUCTION

To be certain of the real cause of the detected changes in the vibration data it is important for a predictive maintenance system to be able to differentiate between various potential causes of the changes. Vibration signals from rotating machines can experience deviation from their normal levels due to many varying causes such as rotor related faults, coupling misalignment, bearing related failures, cavitation occurrence in the case of hydraulic machinery and structural looseness to mention but a few. Most of these faults result in similar diagnosis for the majority of rotating machinery as they result in comparable vibration response regardless of the rotating machine under investigation.

Hydraulic faults, unlike mechanical failures, are machine dependent meaning that there is a possibility that different machines will portray different responses when under such failure conditions. Therefore, this necessitates an in-depth understanding of how to confidently diagnose their occurrence. As it has been well explained in previous chapters, cavitation in PATs has not been deeply investigated prior to this study and hence the existence of a gap in literature that this chapter aims to fill about its diagnosis after change detection.

This chapter approaches the process of diagnosis from the perspective of root cause finding after change detection using such parameters as the ones described in Chapter 5. The aim is to provide further information on the cause of the realised changes in the acquired and trended DND as the changes might be due to a variety of causes. How can we decide that the observed increased DND change is a result of cavitation occurrence in a PAT? We start by manually examining the frequency spectrums of the acquired vibration signals to see if we can leverage on existing heuristics for diagnosing cavitation in pumps and/or turbines. We then assess for the existence of possible generalizations of spectrum interpretations and associate that to the diagnosis of cavitation in PATs. Finally, we probe the possibility of automating the diagnosis process by implementing machine learning algorithms to enable fast, reliable and accurate predictive capabilities for effective decision making.

The contents of this chapter have been partly published as:

Maheshwari, B.; Paudel, B.; **Stephen, C**.; Crespo-Chacon, M.; McNabola, A. Developing an Advanced Machine Learning Framework for Cavitation Detection in Hydropower Plants. *Hydro 2024,* Graz, Austria, 18-20 November 2024.

Stephen C.; Basu B.; McNabola A. Evaluation of Supervised Machine Learning Techniques for Cavitation Detection and Diagnosis in a Pump-as-Turbine System. *Expert Systems with Applications,* vol. 296, p. 129167, 2026.

6.2. FREQUENCY-DOMAIN BASED DIAGNOSIS OF CAVITATION IN PATS

This section extends the work explained in the previous chapter where vibration signals were used to compute and monitor DND values in the time domain for the purposes of detecting any potential changes in the signals that may be deemed significant with potential detrimental effects to the safe operation and reliability of a PAT system. We continue with the segregation of our data according to the three observed cavitation statuses of the PAT, i.e., 'No cavitation', 'Inception Cavitation' and 'Full Cavitation'. The spectrums of each of the investigated operating condition are compared with that of the baseline data, which is representative of the obtained spectrum when the PAT is operated at optimum conditions with the objective of identifying the frequency components that get excited because of a changing cavitation status.

6.2.1. Frequency Spectrum Computation

The time domain vibration signals obtained at various operating conditions indicative of either of the observed cavitation status were used in the computation of the frequency spectrums presented in this chapter. For the purposes of maximizing meaningful information from the frequency spectrums, frequencies below 1000Hz were analysed for vibration velocity whereas frequencies above 1000Hz were analysed for vibration acceleration. The reason behind this subdivision of the frequency spectrum into two is because it is well known in vibration analysis and monitoring field that the velocity spectrum is accurate up to frequencies equal to 1000Hz with the acceleration spectrum being sensitive to frequencies north of this value. Thus, changes in the spectrum at lower frequencies will be accurately obtained in the velocity spectrum and those occurring at higher frequencies can be suitably detected in the acceleration spectrum.

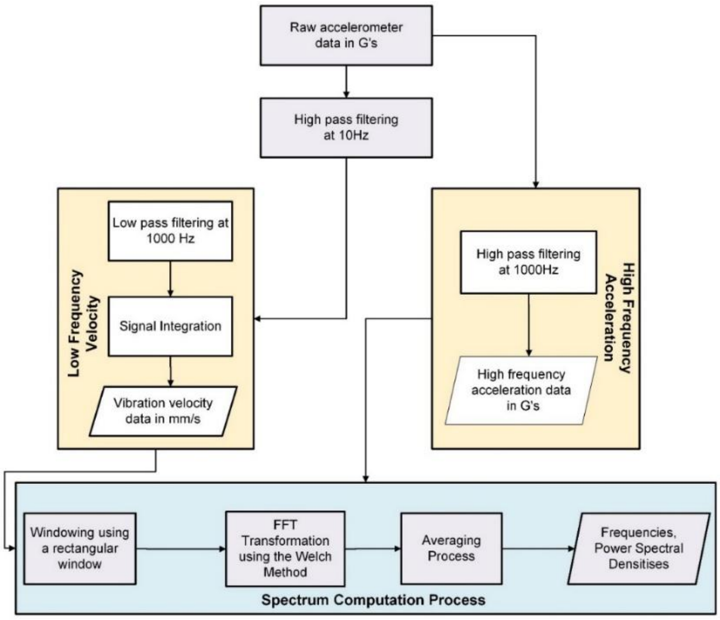

Figure 6.2-1. The flow chart for the spectrum computation process

Figure 6.2-1 presents the information flow diagram showing how the signal was converted from accelerometer time domain signals into the two frequency spectrums indicative of lower and higher frequencies. The vibration signals were first passed through a high pass filter at 10Hz to eliminate low frequency noise that could distort the spectrum and affect accuracy. A 3rd order Butterworth filter with a cutoff frequency of 10Hz was used for this purpose. The reason behind the selection of this type of filters is a maximally flat response in the passband in comparison to other types i.e., Chebyshev and Bessel. It offers the best compromise between attenuation and phase response as it has no ripple in the passband or stopband [195].

The high pass filtered signal was then passed through a signal divider where it is divided into either a high frequency acceleration signal containing frequencies between 1,000 – 5,000 Hz or low frequency velocity signals covering the frequency range 10 - 1,000 Hz. To convert the accelerometer acquired vibration data into velocity signals, a high-performance Infinite Impulse Response (IIR) filter-based integrator was used. The resultant velocity signals are shown in Fig. 6.2.2 for an operating speed of 1500 rpm at a) *"no cavitation, b) "inception cavitation"* and c) "*full cavitation"*. This IIR was presented by Pintelon and Schoukens [196] and was coupled with a linear-phase Finite Impulse Response (FIR) high pass filter to improve its stability as per Brandt [105]. Brandt [105] demonstrated the superiority of this integrator in comparison to the common integrators such as the simple integrator, trapezoidal rule integrator and the low pass filter based integrator.

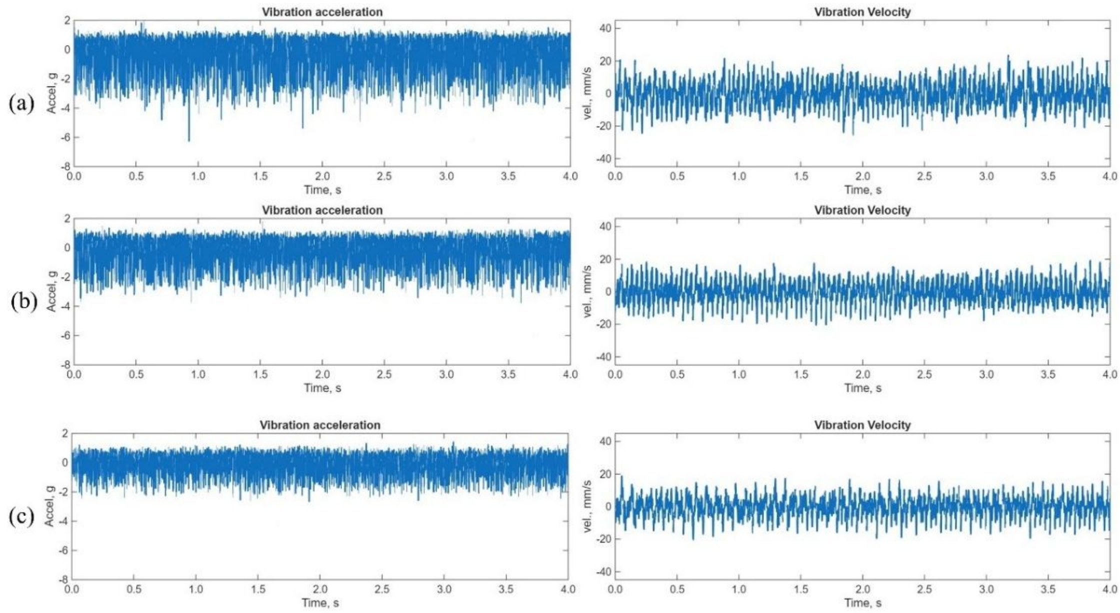

Figure 6.2-2. The results of the integration process from acceleration signals to velocity signals for (a) "no cavitation", (b) "inception cavitation" and "full cavitation" at 1500 rpm

Each of the two signals i.e., high frequency acceleration and low frequency velocity signals, were then passed through the spectrum computation process. The signals were first windowed using a Hanning window of length $N = 2^{14}$. The choice of the Hanning window was to balance between amplitude accuracy and the rate of decrease of the spectral leakage into other frequency bins. The Hanning window results in a maximum amplitude error of -1.42dB with the sidelobes dropping at f^{-3} where f is the frequency bin [127].

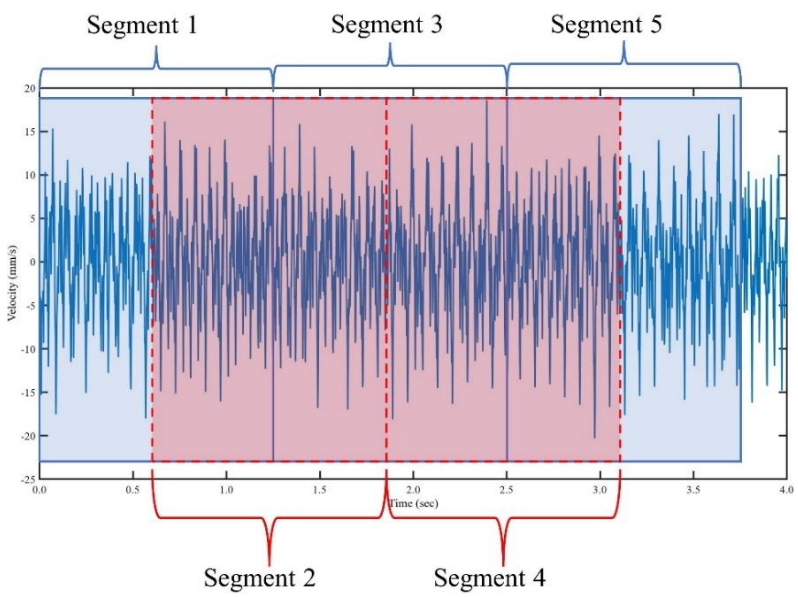

Figure 6.2-3. The signal segmentation process showing the 50% overlap used

The windowed signal was then transformed into the frequency domain through the implementation of the Welch Method of estimating the Power Spectral Density. The input signal is segmented into five different segments of length N = 2^{14} and a 50% overlap, as depicted in Fig. 6.2-3. The spectrum of each segment is computed and then they are averaged out resulting in a Power Spectral Density vector and the associated frequencies.

6.2.2. Velocity Spectrums for Lower Frequencies

In presenting the results each sensor installation direction was considered separately as well as the installation location. This was to ensure that the existence of changes in the spectrum are not overlooked because of being biased towards a single sensor which might have presented more recognisable changes. The data is presented as waterfall plots to aggregate them in a single plot for easy comparison and identification of changes because of changing flow conditions. Data collected at the bearing housing consists of only the vertical and horizontal direction, excluding the axial direction as the sensor was found to be faulty. The data obtained at the PAT outlet flange consisted of all three directions.

Non-drive end (NDE) bearing housing

Figures 6.2-4 and 6.2-5 shows the waterfall plots of the low frequency parts of the power spectral density (PSD) for horizontal and vertical direction vibration at 1500 rpm, respectively. It is evident that for the horizontal vibration the spectrum resembles each other at various operating conditions consisting of mostly three components namely 1X, 2X and 3X, i.e., the use of X means it is a multiple of the operating speed.

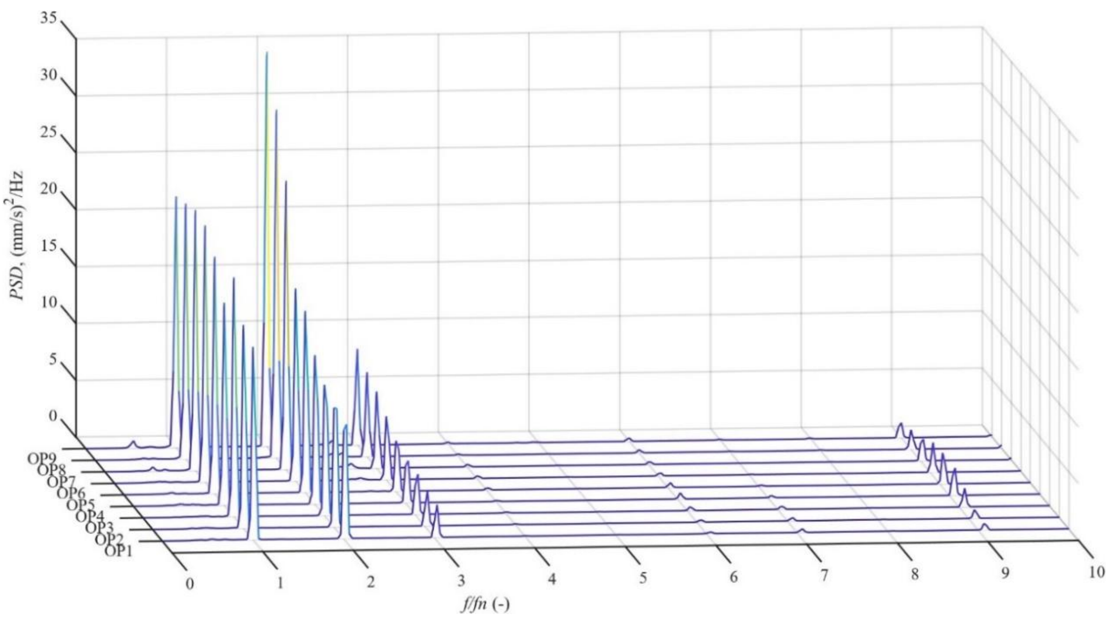

Figure 6.2-4. Horizontal vibration velocity waterfall plot for NDE bearing measurements at 1500 rpm

The peaks of 1X components are the highest followed by the peaks of 2X and 3X respectively at higher flow conditions. This trend continues for both non-cavitating and inception cavitating operating condition, OP1 – OP6. As the condition changes into fully cavitating condition, i.e., OP7

– OP9, the dominant frequency component shifts to the 2X component. This could be an indication of how cavitation occurrence in a PAT affects the vibration frequency spectrum or PSD but the magnitude change is low.

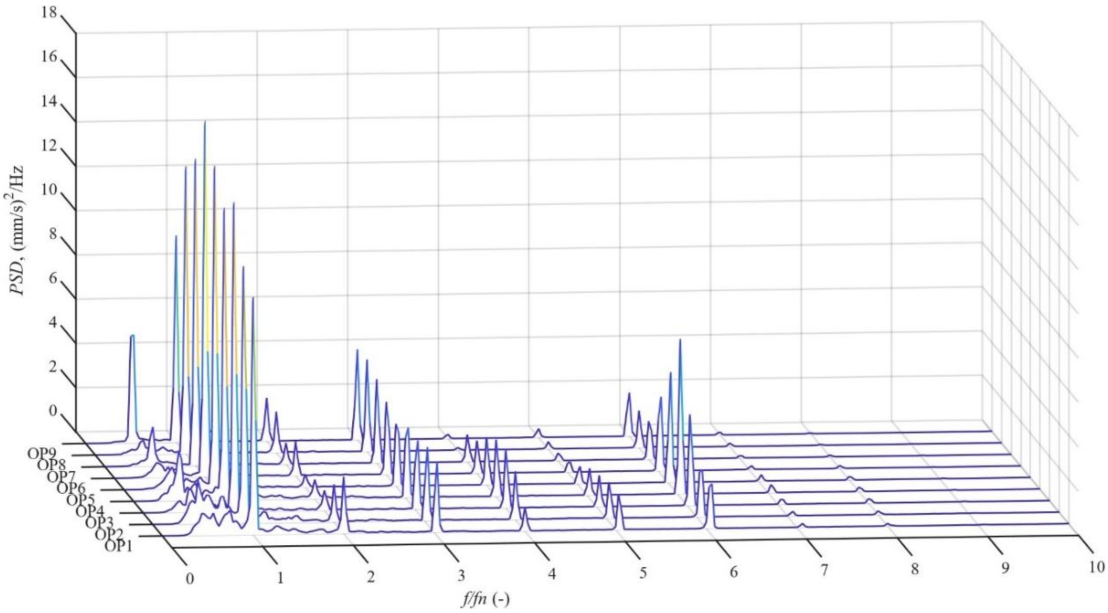

Figure 6.2-5. Vertical vibration velocity waterfall plot for NDE bearing measurements at 1500 rpm

In the case of the vertical vibration, the frequency peaks are observed at the harmonics of the rotating speed up to 6X. The 1X component is dominant at all operating conditions. Also, there is a visible sub harmonic around 0.5X which increases the noise flow at OP1 – OP6. At OP9 the 0.5X frequency peak is well defined with an increased amplitude. The general trend of the dominant frequency peak is that the amplitude increases until it reaches the maximum at OP6 then it begins to drop at a similar rate.

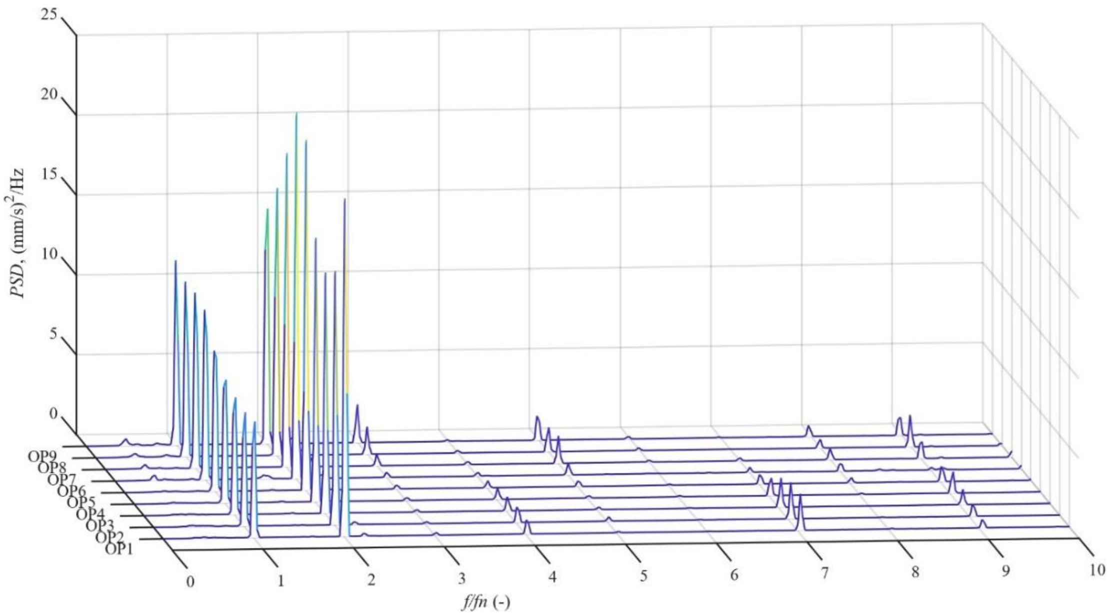

Figure 6.2-6. Horizontal vibration velocity waterfall plot for NDE bearing measurements at 1800 rpm

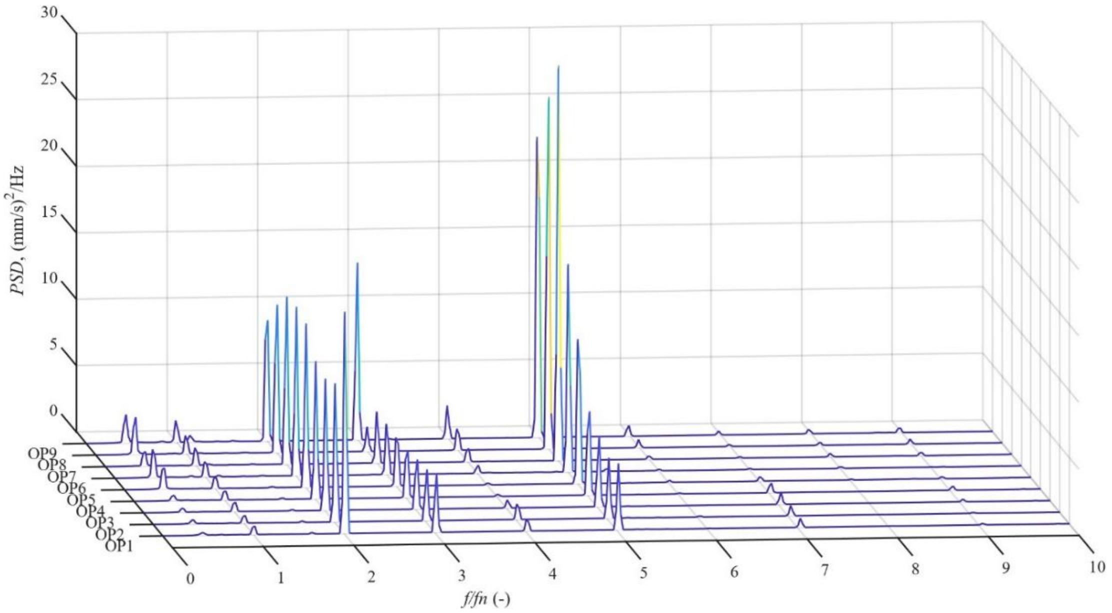

Figure 6.2-7. Vertical vibration velocity waterfall plot for NDE bearing measurements at 1800 rpm

Similarly, Figs. 6.2-6 and 6.2-7 shows the power spectral densities for low frequency vibration obtained in the horizontal and vertical directions with the PAT operating at 1800 rpm. Unlike Fig. 6.2-4, Fig. 6.2-6 depicts an increased number of running speed harmonics with each showing a different response to changes in operating conditions. For example, when comparing the magnitudes of frequency peaks, 2X is the most dominant followed by 1X and all other harmonics up to 9X have lower amplitudes. Some frequency components' magnitude increases with worsening of the cavitation condition from non-cavitation to full cavitation, i.e., 0.5X, 1X, 3X, 5X and 8X, whereas the magnitude of 4X and 7X reduces with the worsening of the cavitation operating condition.

In Fig. 6.2-7 the dominant frequency peaks are the 5X followed by 2X then 3X. Other harmonics up to 9X portray a similar occurrence to that explained for the horizontal vibration. The amplitude of the dominant frequency component increases as the cavitation condition worsens. The increase in the amplitude of the 0.5X frequency component is more defined than at 1500 rpm as it increases more uniformly from the no cavitation operation condition to fully cavitating conditions.

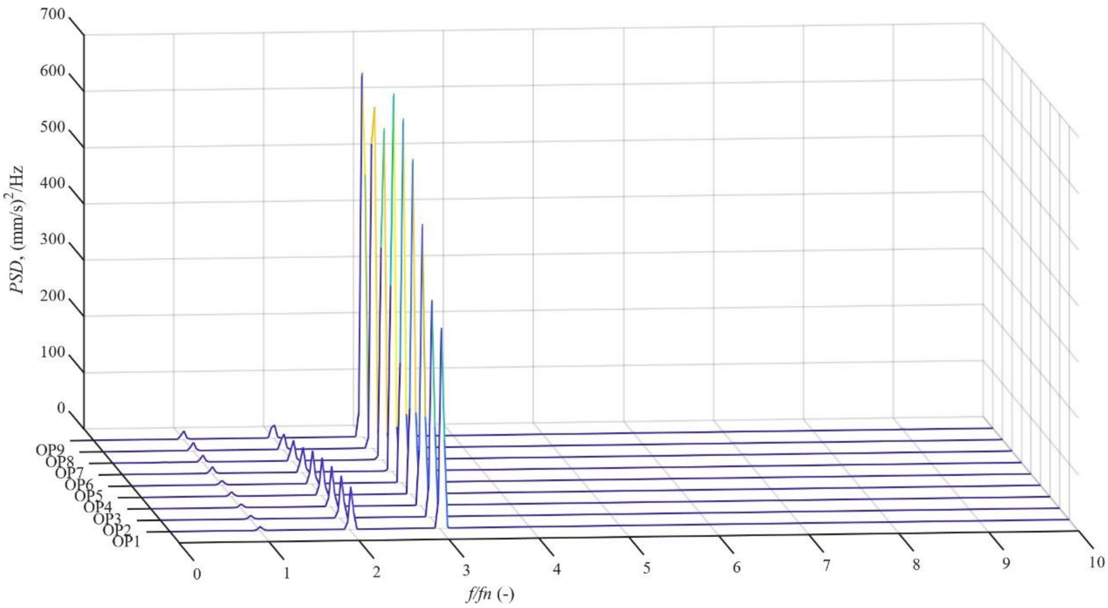

Figure 6.2-8. Horizontal vibration velocity waterfall plot for NDE bearing measurements at 1350 rpm

Figures 6.2-8 and 6.2-9 present the waterfall plots for the low frequency PSDs for data obtained with the PAT operating at 1350 rpm in the horizontal and vertical directions respectively. The horizontal axis vibration shows elevated magnitudes of the PSD at 3X with other peaks visible at 1X and 2X. The amplitude of the 3X components appears to be flow rate dependent as it increases with a change of operating conditions towards lower flow rates of OP9. There is no evident relationship between the increase in the PSD amplitude with the change in cavitation status as the amplitude increase is also observed at the same cavitation status but different operating point.

On the other hand, the PSD of the vibration obtained in the vertical direction shows a chaotic waterfall plot with frequency peaks observed spanning from 1X to 9X and some sub-synchronous frequency components at 0.6X and 1.5X. For this measurement direction, the most dominant frequency peak is observed at 7X which shows higher amplitudes at OP7. There is an observed increasing PSD magnitude at 0.6X, 1.5X, 2X, 3X, 5X, 6X, 7X and 9X with higher amplitudes observed at fully cavitating conditions. The amplitude of 1X peaks don't seem to be increasing with worsening cavitation condition while 4X peaks have an inverse relationship with the cavitation operating condition, the amplitude decreases when the cavitation condition worsens.

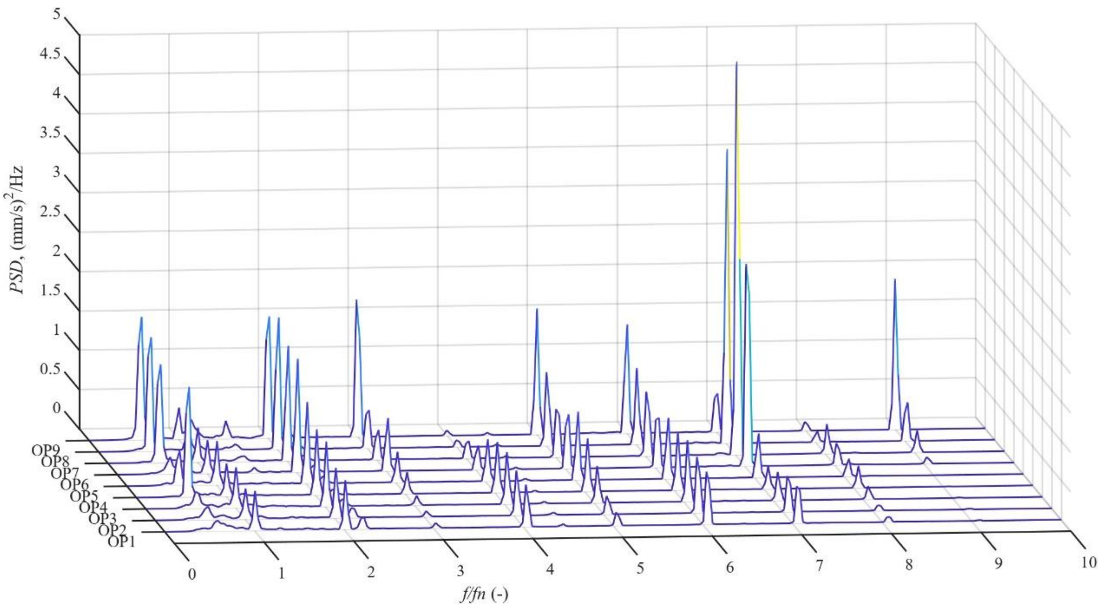

Figure 6.2-9. Vertical vibration velocity waterfall plot for NDE bearing measurements at 1350 rpm

PAT outlet flange

A similar analysis was conducted for vibration data captured at the PAT outlet flange using an adhesively mounted tri-axial accelerometer and the results are presented here. It is worth noting that this sensor installation location is close to the actual cavitation occurrence location when compared to the NDE bearing housing location. As such we should pay particular attention to these data as due to its location the effects of a potential signal attenuation during propagation might be minimised.

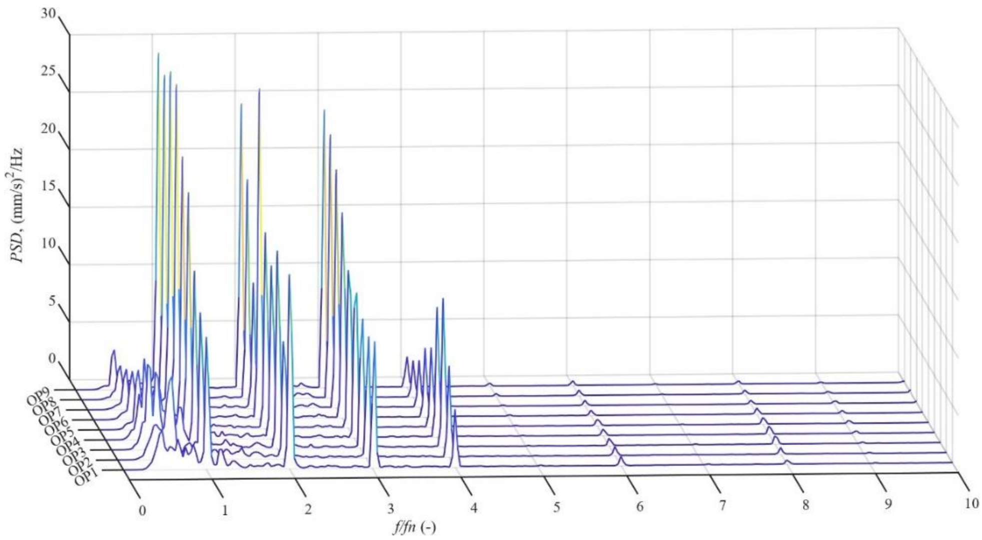

Figure 6.2-10. Horizontal vibration velocity Waterfall plot for PAT outlet flange measurements at 1500 rpm

Figure 6.2-10 shows the horizontal velocity waterfall plot obtained from the data captured with the PAT operating at 1500 rpm. Well-defined 1X, 2X, 3X and 4X frequency peaks are observed in the plot with the dominance reducing with the increasing harmonic number. For each of the components, the magnitude increases with changing flow rate condition with high amplitudes observed at fully cavitating conditions. Moreover, below 1X there is an increased noise floor with a 0.5X frequency peak protruding for all operating points. The variation in the amplitudes of this 0.5X component is minimum meaning that this component might not be related to the changing cavitation status of the machine.

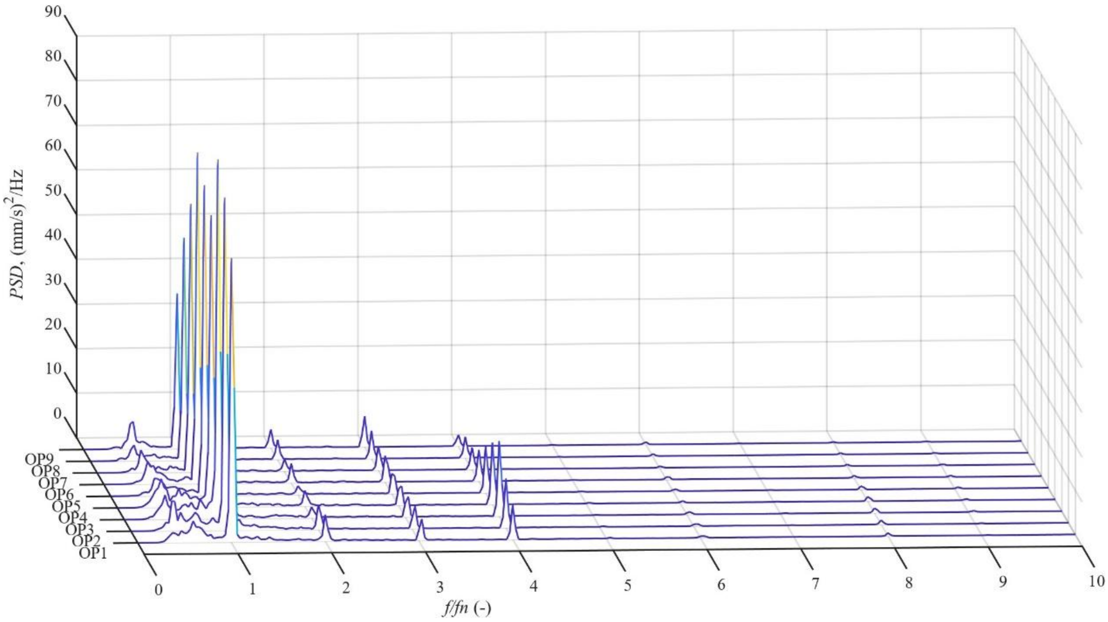

Figure 6.2-11. Vertical vibration velocity Waterfall plot for PAT outlet flange measurements at 1500 rpm

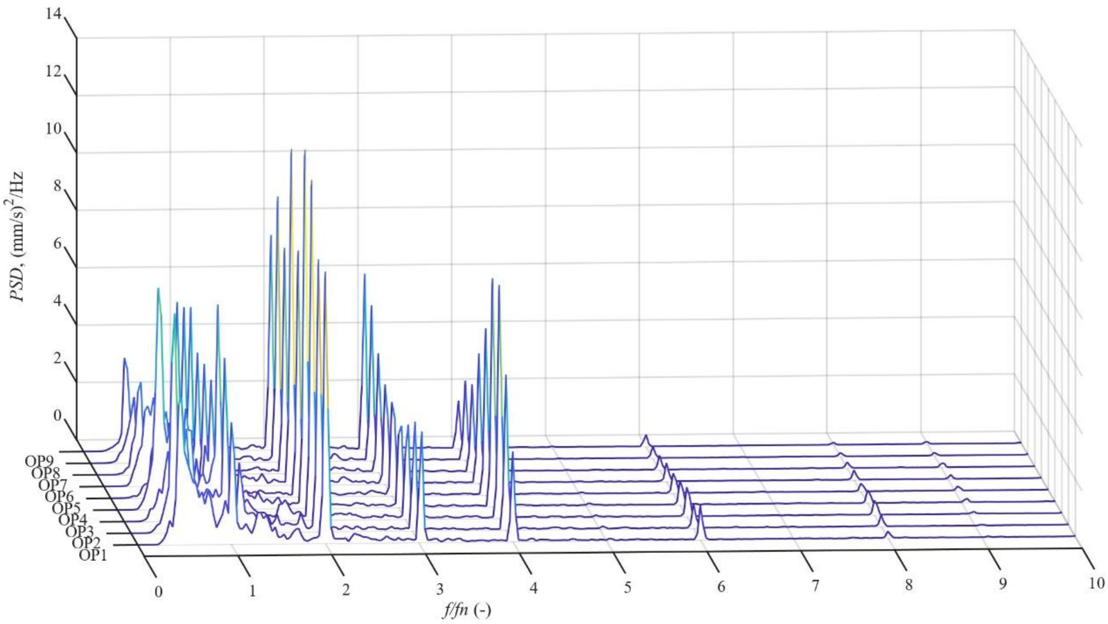

Figure 6.2-12. Axial vibration velocity Waterfall plot for PAT outlet flange measurements at 1500 rpm

The vertical velocity waterfall plot for the vibration measured at the same location is shown in Fig. 6.2-11 while Fig. 6.2-12 depicts the same plot for vibration measured in the axial direction. Like the horizontal direction plot, the vertical direction plot shows the occurrence of 1X, 2X, 3X and 4X frequency components with 1X being dominant. The existence of the 0.5X frequency component is also evident though with a constant amplitude level for all operating points. Worsening the cavitation status of the machine does not seem to have a major effect on the amplitude of the frequency peaks as it is observable that the highest peaks are at OP3 and OP6, which represent the "no cavitation" and "inception cavitation", respectively. The 4X components show a direct dependency in flow conditions with higher flow rates giving higher amplitudes and lower flow rates yielding lower PSD amplitudes.

The plot of the axial vibration waterfall on the contrary show the existence of frequency peaks up to 9X apart from 5X. The 2X component is the most dominant one and consists of peaks that constantly increase from OP1 to OP6 and then gradually decreases. The 4X component displays a similar behaviour to 2X while the 3X component slowly increases until the maximum amplitude is observed at OP9. The plot shows an increased noise floor from 0-1.5X with frequency peaks protruding at 0.5X and 1X.

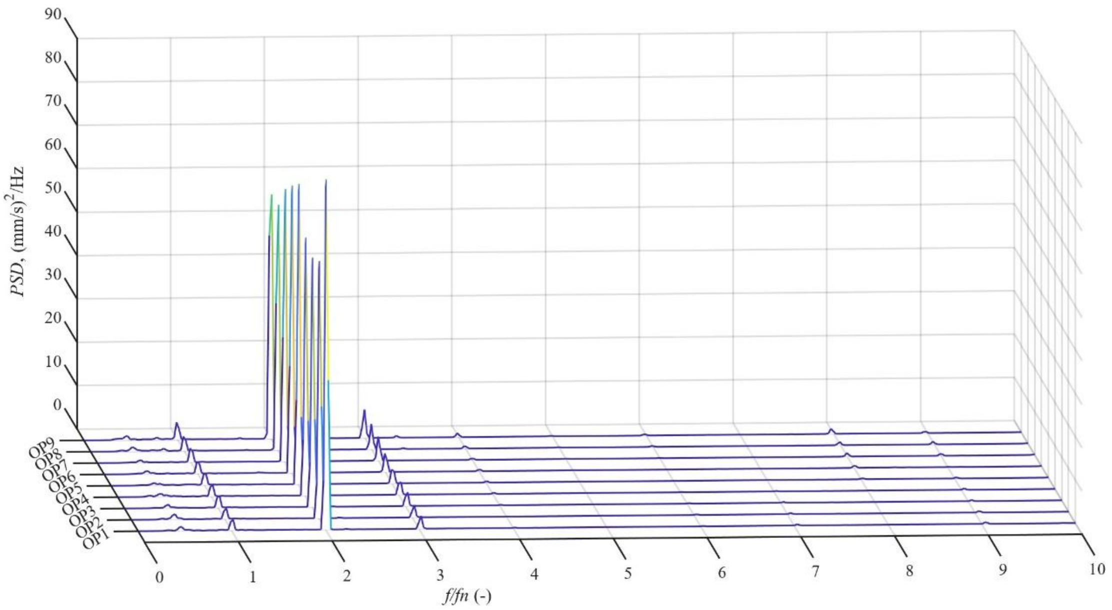

Figure 6.2-13. Horizontal vibration velocity Waterfall plot for PAT outlet flange measurements at 1800 rpm

The waterfall plot of horizontal vibration obtained at the PAT outlet flange with the machine operating at 1800 rpm is shown in Fig. 6.2-13. The peaks in the plot are well defined with the dominant observed frequency component being 2X. The magnitudes of 1X and 3X are lower than at the dominant frequency. For the dominant frequency component, the magnitudes increase up to inception cavitation point then slightly reduces into full cavitation condition.

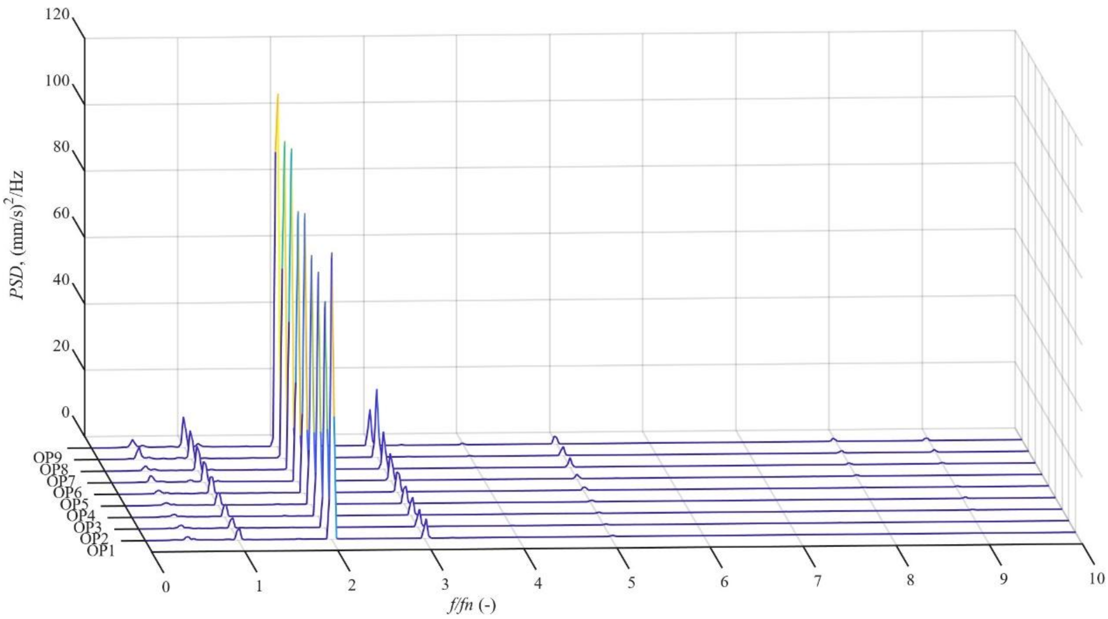

Figure 6.2-14. Vertical vibration velocity Waterfall plot for PAT outlet flange measurements at 1800 rpm

Figure 6.2-14 similarly shows the waterfall plot of the vibration obtained in the vertical direction at the PAT outlet flange. Like the plot for the horizontal direction, the 2X component is the most dominant with other observable frequency peaks at 0.5X, 1X and 3X. The amplitude of dominant frequency component uniformly increases with the worsening of the cavitation status into full cavitation. The same trend is observable for the 0.5X frequency component though at lower magnitudes.

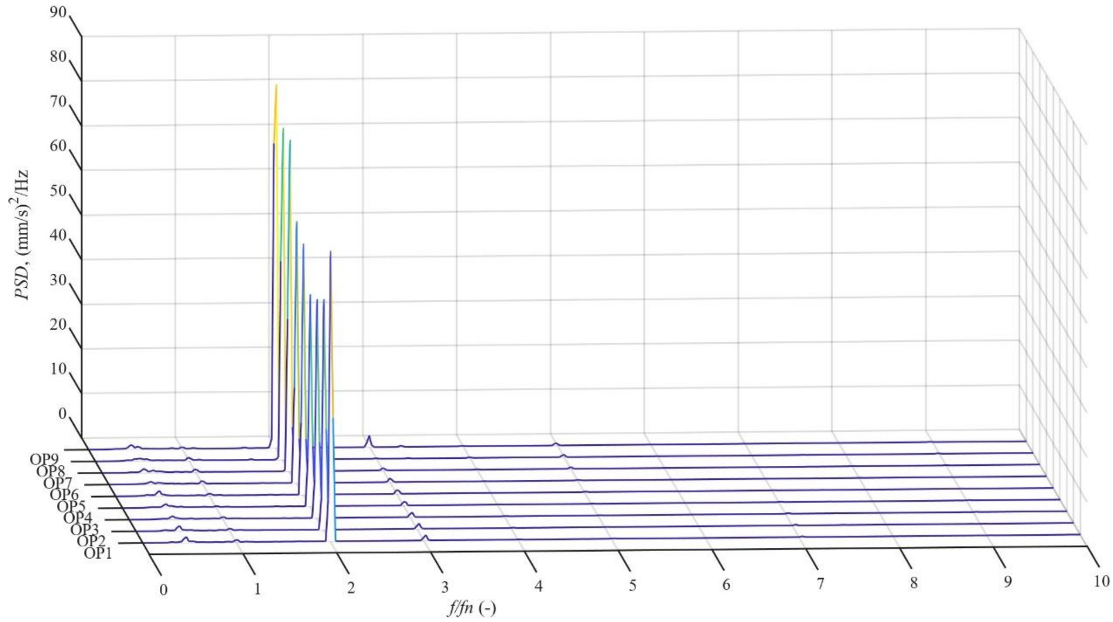

Figure 6.2-15. Axial vibration velocity Waterfall plot for PAT outlet flange measurements at 1800 rpm

In the axial direction, the waterfall plot shown in Fig. 6.2-15 only shows the existence of the 2X component which increases in magnitude as cavitation status of the PAT worsens into full cavitation at OP9. The peaks at 0.5X, 1X and 3X are comparatively small as compared to the 2X component. Its also observable that at OP1 the magnitude of the PSD at 2X shows a higher value as compared to subsequent operating points at lower flow rate. The probable reason for this increase in amplitude is the shift towards cavitating conditions at higher flow rates which couldn't be confirmed in the current study.

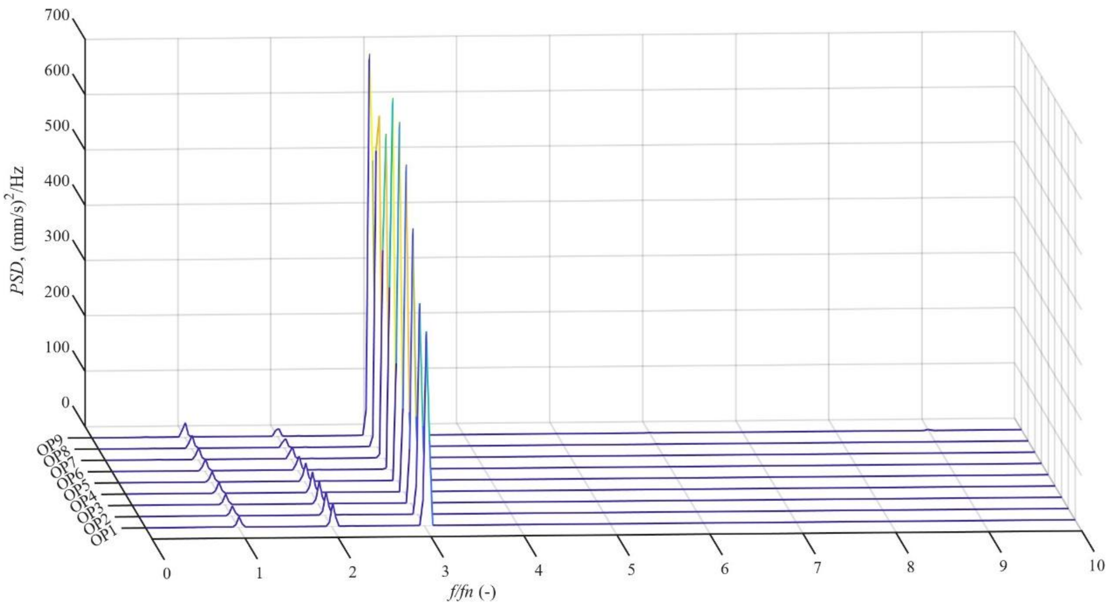

Figure 6.2-16. Horizontal vibration velocity waterfall plot for PAT outlet flange measurements at 1350 rpm

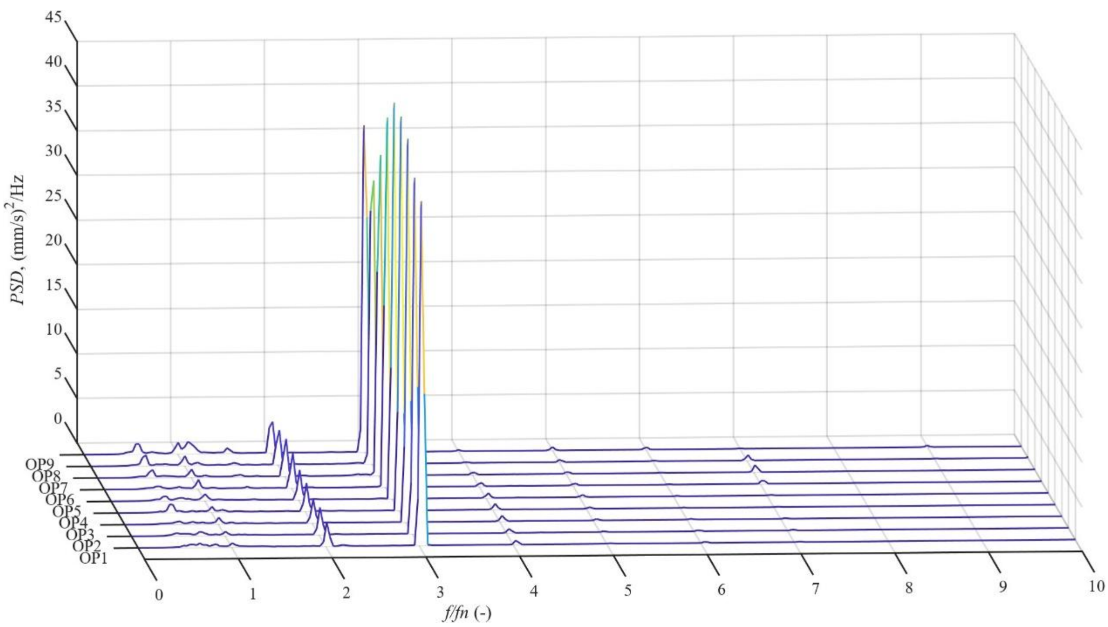

Figure 6.2-17. Vertical vibration velocity waterfall plot for PAT outlet flange measurements at 1350 rpm

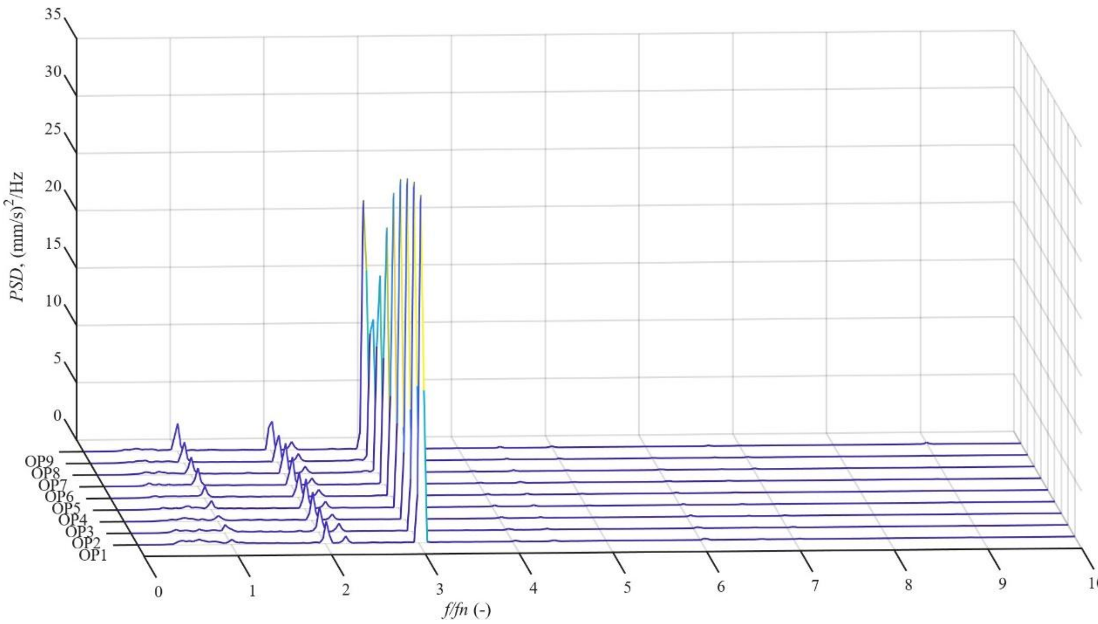

Figure 6.2-18. Axial vibration velocity waterfall plot for PAT outlet flange measurements at 1350 rpm

Figures 6.2-16 to 6.2-18 shows the vibration velocity waterfall plots for data captured at the PAT outlet flange with the PAT operating at 1350 rpm in the horizontal, vertical and axial directions respectively. All the plots show the dominant 3X component with other components at 1X and 2X. A 0.6X component is observed for the vertical velocity plot while the axial velocity plot also shows a 2.22X component which coincides with 50Hz line frequency. The 3X component for the horizontal direction vibration velocity constantly increases with the worsening of the cavitation condition in the PAT. For the vertical direction the 3X component increases until inception cavitation status is reached then it begins to drop while for the axial direction the amplitude of the 3X component remains constant until inception cavitation where it then begins to reduce with cavitation status moving into full cavitation. Plots for operational speeds not presented in this subsection can be found in **Appendix D**.

6.2.3. Acceleration Spectrums for Higher Frequencies

In order to get a full picture of the vibration changes brought about by the changing cavitation status from “no cavitation” to “full cavitation”, the higher frequency part of the PSD was investigated separately in this section using vibration acceleration instead. Vibration acceleration can accurately show changes in the machine vibration response at higher frequencies, making it the suitable parameter to use in this case. The obtained waterfall plots in this section are limited between a frequency range of 1000Hz to the maximum frequency of 5000Hz in accordance with the Nyquist sampling theorem. The theorem limits the sampling rate of a signal to at least twice the highest frequency component in the signal for accurate digitization [197]. In the current study we used a factor of 2.56 that is widely used in vibration measurement systems, therefore limiting our maximum frequency to 5000 Hz.

Non-drive end (NDE) bearing housing

Figure 6.2-19 shows the waterfall plot of the obtained high frequency components of the PSD for all the investigated operation conditions when the PAT was operated at 1500 rpm. The plot shows three distinct areas where there is higher energy content that can be attributed to either the changes in the machine condition or the natural frequency of the system. At frequencies between 60-80X there is an increasing energy content observable at OP1 – OP6, which then reduces in magnitude from OP7 – OP9. Also there exist increased energy content at around 119X and at 188X. The magnitude of this frequency components does not seem to be dependent on the changing cavitation condition as it randomly changes

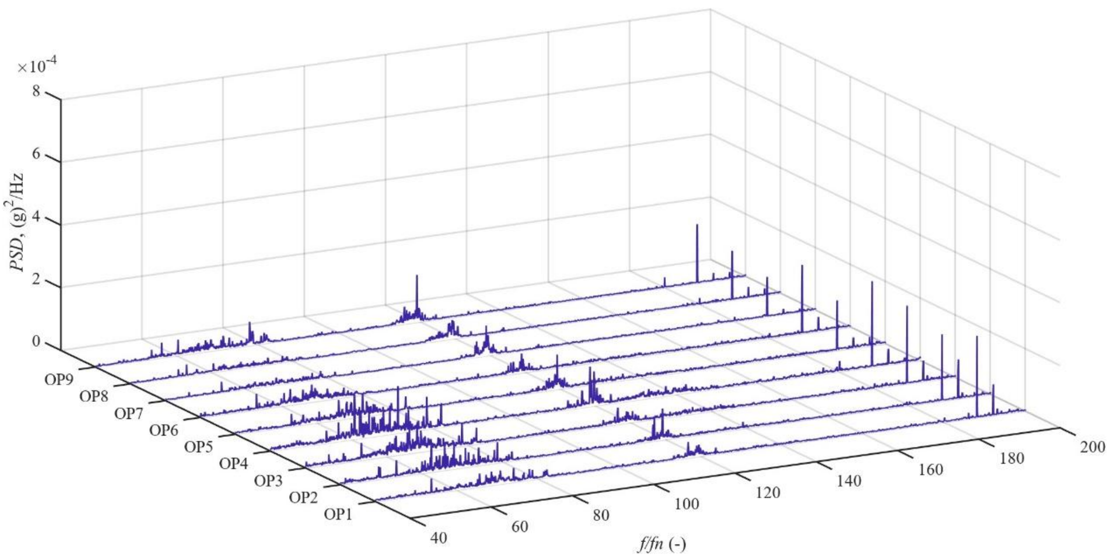

Figure 6.2-19. Horizontal vibration acceleration waterfall plot for NDE bearing housing measurements at 1500 rpm

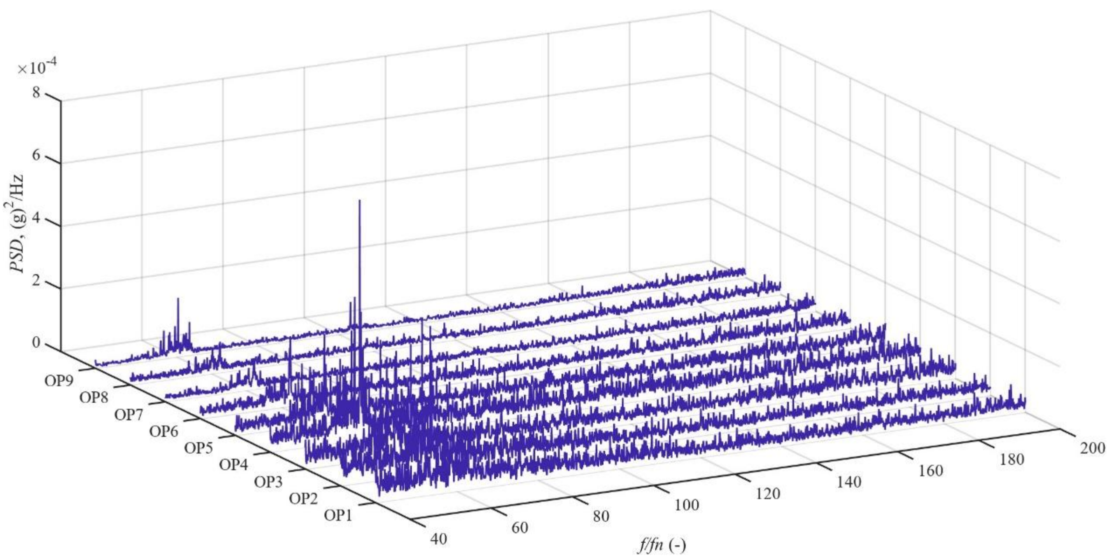

Figure 6.2-20. Vertical vibration acceleration waterfall plot for NDE bearing housing measurements at 1500 rpm

The vertical vibration acceleration at the same operation speed is shown in Fig. 6.2-20. Unlike in the horizontal direction, this plot only shows a single area of the plot where there is an observed change in the energy content in the signals. This is around 60X, and the amplitude is high at OP2, OP3 and OP4. The amplitude then reduces at OP5 – OP8 followed by a slight increase at OP9. Just like the horizontal vibration acceleration data, there seem to be no dependency on the cavitation operation condition.

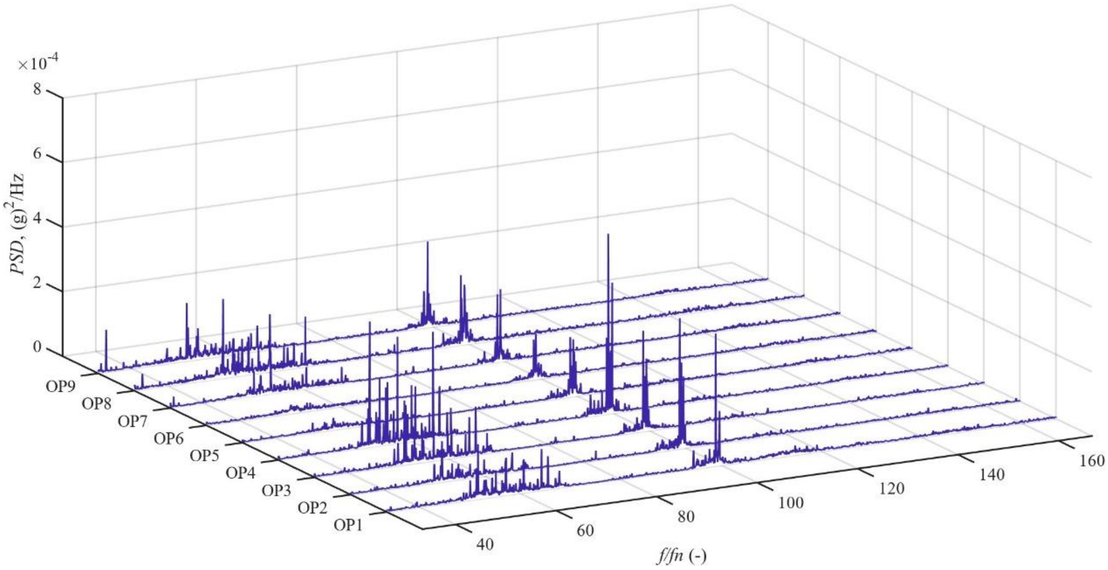

Figure 6.2-21. Horizontal vibration acceleration waterfall plot for NDE bearing housing measurements at 1800 rpm

When the operation speed is increased to 1800 rpm, the horizontal acceleration waterfall depicts two areas in the plot that contains higher energy content as shown in Fig. 6.2-21. The first area has its energy spread between 50X – 70X and the second area is around 99X. The first area shows the amplitudes increasing from OP1 – OP4 then it reduces at OP5 and OP6. The amplitude then increases from OP7 – OP9. This area of increased energy content seems to disappear when the PAT is under inception cavitation conditions. Similarly, the 99X component shows two distinct amplitudes with no cavitation operating conditions having higher amplitudes and cavitating conditions showing lower amplitudes.

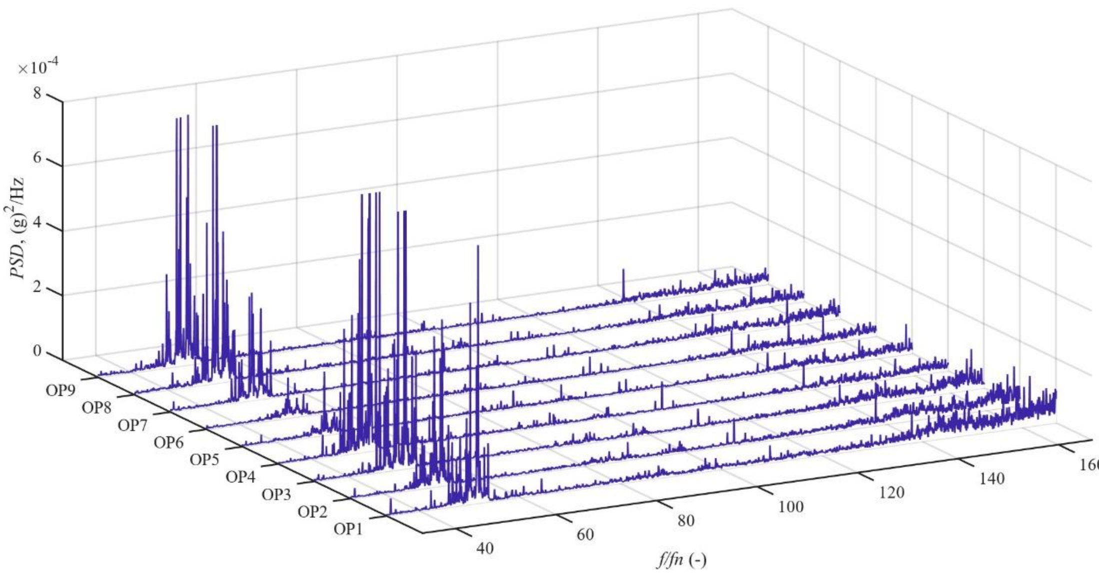

Figure 6.2-22. Vertical vibration acceleration waterfall plot for NDE bearing housing measurements at 1800 rpm

The vertical acceleration PSD waterfall for 1800 rpm shows much energy concentrated in the 40-60X range centred around 50X. This amplitude seems to be equal for most of the operating points except for OP5 – OP7. At OP7, however, it is evident that the amplitude is about to increase heading into the full cavitation condition. Overall, it can be seen that at no cavitation zone the amplitude is higher, and it reduces as the machine goes into inception cavitation zone. It then increases as it moves from inception cavitation into full cavitation.

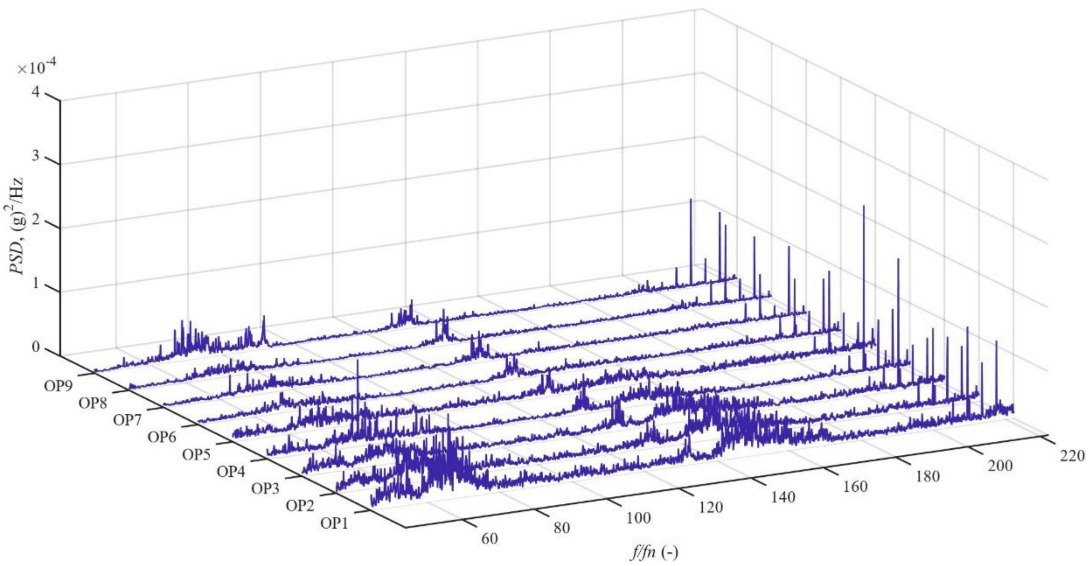

Figure 6.2-23. Horizontal vibration acceleration waterfall plot for NDE bearing housing measurements at 1350 rpm

At 1350 rpm the horizontal acceleration PSD waterfall plot (shown in Fig. 6.2-23) shows energy concentrated between 60-80X centred at 69X. Another area of the plot showing higher energy content is centred about 132X with further broadband energy between 140 – 170X. This broadband energy content disappears when the operation regime moves into cavitation conditions. Moreover, in the frequency range 200-220X there exists four frequency peaks that are separated by a spacing of 4X (equivalent to 100Hz, twice the line frequency) with the dominant peak at 209X.

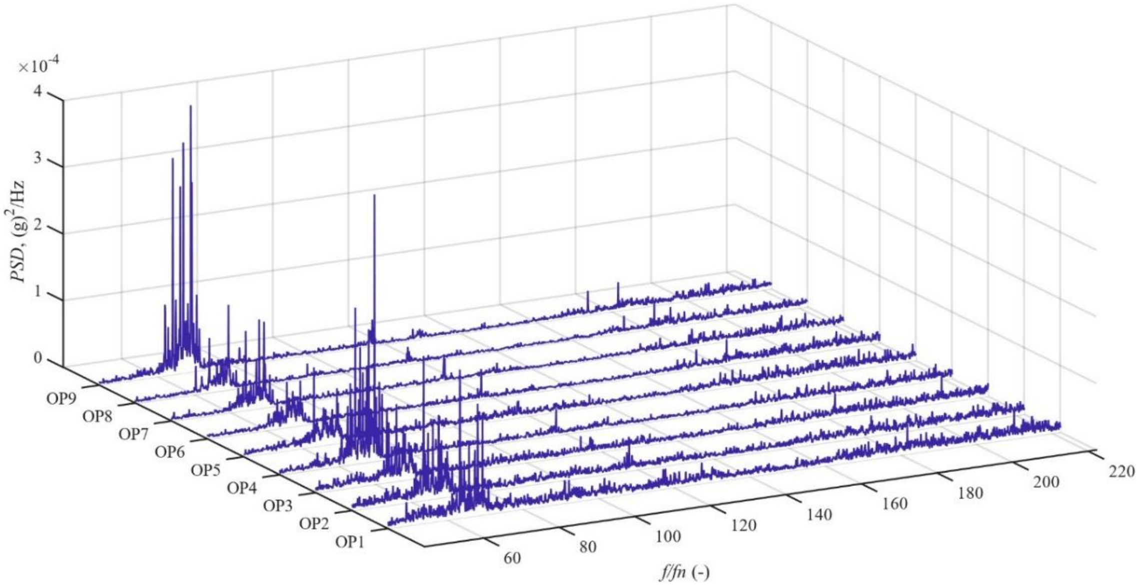

Figure 6.2-24. Vertical vibration acceleration waterfall plot for NDE bearing housing measurements at 1350 rpm

In the vertical direction however, the PSD waterfall plot only shows a single area of signal energy content concentration. This area is between the 60-80X range with higher amplitude observed at OP4 and OP9 with the other operating points having similar amplitudes.

PAT outlet flange

In this section, only the plots showing areas of higher signal energy content in the PSD waterfall plots will be presented due to the difficulty in interpreting the plots if it shows equal energy content throughout the whole investigated frequency range. Other plots will be presented in **Appendix E**. This approach will be adopted for all the three sensor installation directions for the PAT outlet flange location. Figure 6.2-25 shows the vertical direction acceleration waterfall plot obtained at 1350 rpm. It is observed in the plots that there exist two areas of higher energy content with one area in the range 160-180X and another around 198X.

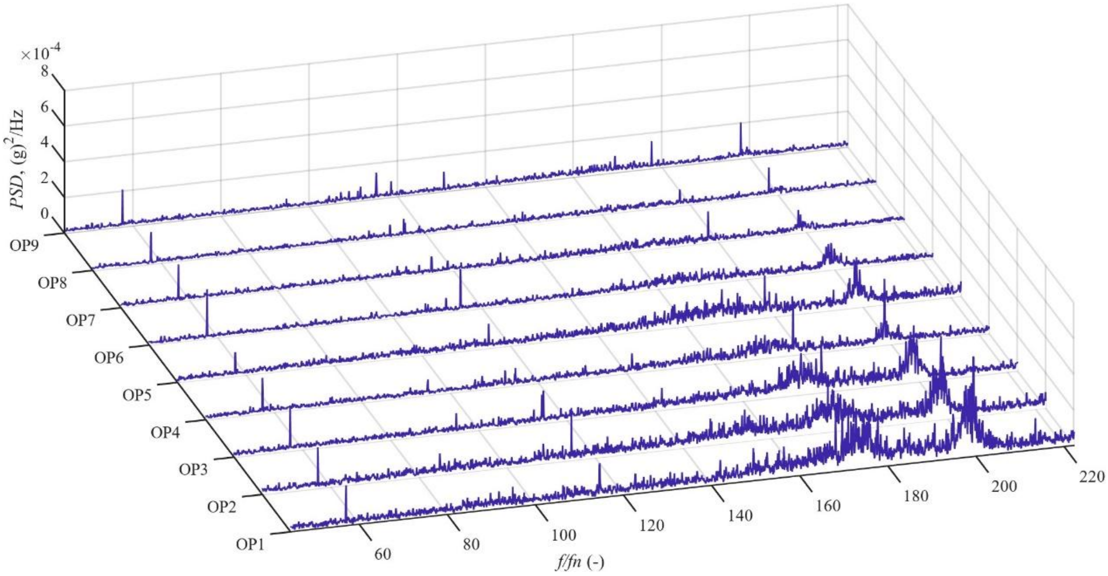

Figure 6.2-25. Vertical vibration acceleration waterfall plot for PAT outlet flange measurements at 1350 rpm

In the range 160-180X, peaks protrude at about 178X. The PSD amplitude at the two existing areas of high energy content decreases when the machine operating condition moves towards cavitating condition. From OP6 towards OP9 the amplitudes remain constant with little variation. Since for the sensor installed at the PAT outlet flange, the only plot with varying energy content was the vertical acceleration for 1350 rpm, Fig. 6.2-26 showing the vertical acceleration PSD waterfall for 1500 rpm was presented to show the almost equal energy content over the entire frequency range.

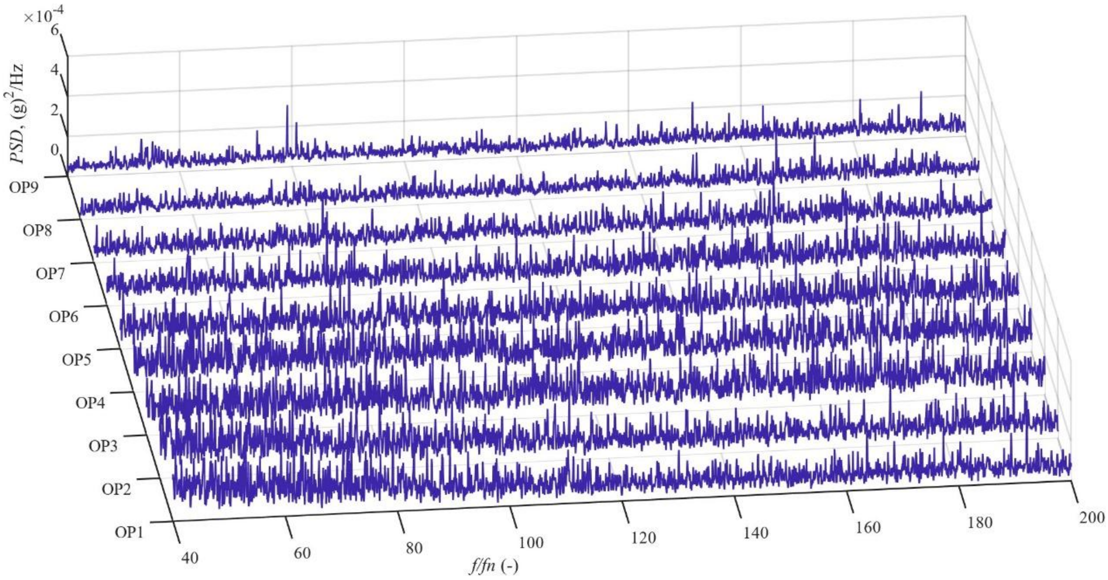

Figure 6.2-26. Vertical vibration acceleration waterfall plot for PAT outlet flange measurements at 1500 rpm

6.2.4. Section Discussions

From the results presented in this sub-section, there is no dominant feature observed that could fully be attributed to cavitation occurrence in the PAT. Initially, focusing on the horizontal vibration at the bearing housing in the vibration velocity range, it seems like the 2X component is a clear indicator, but its amplitude variation disqualifies it as so. Furthermore, concentrating on the measurements obtained at 1350 rpm, the absence of the 2X component invalidates this claim.

However, the 0.5X component is present in all waterfall plots for the vertical direction measurements and could be an indicator of the occurrence of cavitation inside the PAT. This component is observed at all presented operating speeds in measurements obtained at both NDE bearing housing and at the PAT outlet flange in the vertical direction. Even though its magnitude does not surpass that of other existing components in the plots, in most cases its either noticeable at cavitating conditions or its magnitude increases as the operating condition moves towards cavitating.

From the analysis of the PSD waterfall plots in the vibration acceleration range, it is evident that most of the observed high energy areas are due to the excitation of the machine's natural frequencies. This claim is supported by the fact that the frequencies at which these high energy content areas of the PSD plots remain the same even if changing the operating speed, i.e., the components are not operating speed dependent. As an example, at 1500 rpm the high energy content exists at 60-80X and 119X frequencies, at 1800 rpm it is at 50-70X and 99X respectively whereas at 1350 rpm it is at 60-80X and 132X respectively. These components describe components frequencies 1350-2100Hz and around 2970Hz respectively.

Overall, from the insights gained from this analysis it is difficult to generalise the findings for wider application to cavitation diagnosis in PATs. As a preliminary generalisation, it is worth mentioning that the 0.5X frequency component could be regarded as a diagnostic feature for the occurrence of cavitation in PATs and it is recommended that this feature be monitored over time and its changes could be a cavitation occurrence indicator. Moreover, since the observed changes of the investigated features in this section were minimal, to improve the accuracy of diagnosis we will investigate implementing a machine learning based algorithm as described in the following sections.

6.3. APPLICATION OF MACHINE LEARNING ALGORITHMS TO DIAGNOSIS OF CAVITATION IN PATS

In this section, the possibility of automating the diagnosis process by implementing machine learning algorithms was initiated. The intention was to leverage on machine learning algorithms' powerful capabilities of recognising patterns in data sets, their abilities to handle large amounts of data and to recognise existing relationships between inputs and outputs and make predictions on new inputs. Using the same vibration data that was described in the previous chapter, we extracted some condition features, ranked them in order of importance, developed predictive models, both supervised and unsupervised, using high importance features and tested the predictive accuracy of the developed models.

6.3.1. Feature Extraction and Selection

The dataset contains vibration and pressure signals, flow measurements, output power readings and machine operating speed values. All of the available signals are indicative of either of the three operating conditions of 'no cavitation', 'inception cavitation' and 'full cavitation'. In order to generate the much-needed big data for the implementation of machine learning, each of the vibration data measurement files were divided into 18 segments of duration 3.2s.

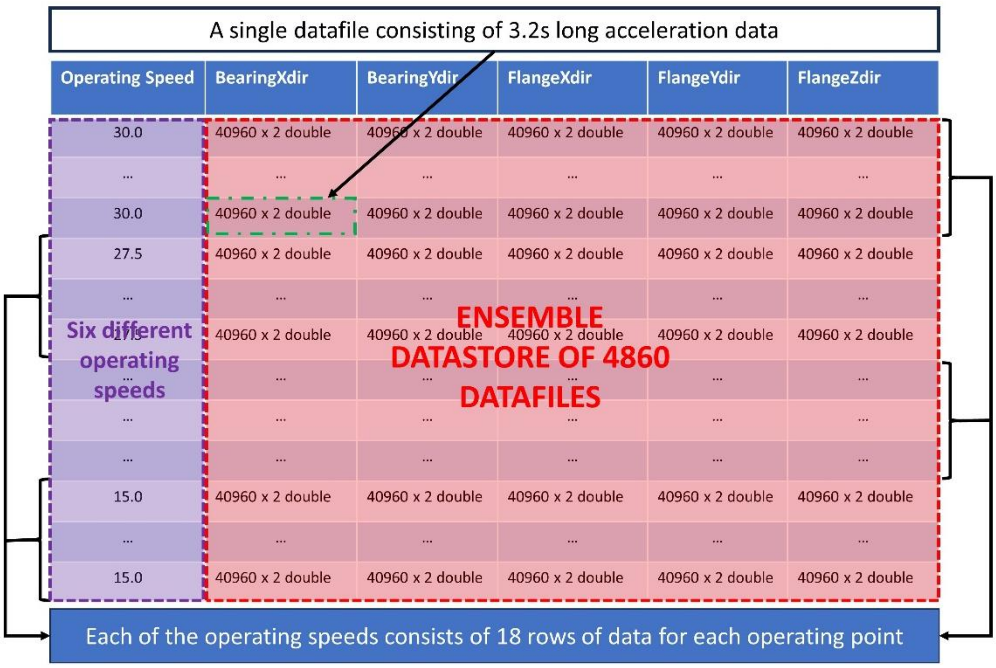

Figure 6.3-1. The summary of the Ensemble data store created

Figure 6.3-1 shows the description of the ensemble datastore with rows indicating individual data sets obtained while the columns indicate the location and direction of measurement i.e., BearingXdir – sensor is installed at bearing housing measuring in the x- direction. Each data set is stored as a cell of two columns of time and acceleration, respectively. The resultant was an ensemble datastore of 972 datasets for each of the five accelerometer locations. This data store was then used in computation of condition features for the creation of the feature matrix.

Feature Extraction

It is evident from Figure 6.3-1 that the resultant ensemble datastore is a high dimension machine condition data which requires some preprocessing before it can be fed to the machine learning (ML) model development process. Feature extraction is an important step in the development of machine learning based predictive maintenance models. A machine condition data dimensionality reduction process is required which converts a high dimensional input data into a feature set/matrix of lower dimensionality containing only the information necessary for the characterisation of machine condition. The strength of the resultant machine learning model is highly dependent on the quality of the extracted feature set hence dictating the overall reliability of the dependent monitoring system.

In the current study, both time domain and frequency domain-based features were extracted. In the time domain, fourteen features of the input signal were computed for each of the datafiles to create a feature set. These features are described in Table 6.3-1. In the frequency domain, the top ten frequency peaks and their associated amplitudes were extracted from the computed PSD for each of the datafiles to populate the feature matrix. Also, the spectrum band power was computed and used as one of the frequency domain features.

Table 6.3-1. Description of Extracted Time Domain Features

FEATURE	DESCRIPTION	COMPUTATION
Peak Amplitude, x_p	The maximum positive amplitude of the vibration signal	$x_p = \max \lvert x_i \rvert$
Root Mean Square (x_{rms})	The variance of the signal magnitude	$x_{rms} = \sqrt{\frac{1}{N}\sum_{1}^{N} \lvert x_i \rvert^2}$
Mean Amplitude, μ	The average value of the vibration signal over a sampled interval	$\mu = \frac{\sum_1^N x_i}{N}$
Standard Deviation, σ	A measure of the amount of variation in the signal about its mean	$\sigma = \sqrt{\frac{\sum_1^N \lvert x_i - \mu \rvert^2}{N-1}}$

Clearance factor, X_{CF}	The ratio of the peak value and the squared mean value of the square roots of the absolute amplitudes	$X_{CF} = \frac{x_p}{\left(\frac{1}{N}\sum_1^N \sqrt{\lvert x_i \rvert}\right)^2}$
Crest factor, *CF*	The ratio of the peak amplitude to the Root Mean Square value of the signal	$CF = \frac{x_p}{x_{rms}}$ $CF = 1.414$ for a pure sinusoid
Impulse factor, X_{IF}	A comparison of the height of the peak value to the mean level of the signal	$X_{IF} = \frac{x_p}{\frac{1}{N}\sum_1^N \lvert x_i \rvert}$
Kurtosis, *k*	A measure that describes how the tails of a distribution differ from the tails of a normal distribution	$k = \frac{\frac{1}{N}\sum_1^N (x_i - \mu)^4}{\sigma^4}$ μ – means, σ – standard deviation $k = 3$ for a normal distribution
Signal-to-Noise Ratio (*SNR*)	A measure of the signal strength relative to the background noise	$SNR = \frac{\mu}{\sigma}$
Signal-to-Noise & Distorsion Ratio, *SINAD*	The ratio of the total signal to the sum of all distortion and noise components	$SINAD = 10log_{10}\left(\frac{P_{overall}}{P_{noise} + P_{distortion}}\right)$
Shape factor, X_{SF}	A dimensionless quantity used in describing the shape of the signal independent of its size	$X_{SF} = \frac{x_{rms}}{\frac{1}{N}\sum_1^N \lvert x_i \rvert}$
Skewness, S_k	The measure of the asymmetric behaviour of a signal through its probability function	$S_k = \frac{\frac{1}{N}\sum_1^N (x_i - \mu)^3}{\sigma^3}$
Total Harmonic Distortion (THD)	A measure of how accurately the measured signal reproduces the output signal	$THD = \frac{\sqrt{V_2^2 + V_2^2 + \cdots + V_n^2}}{V_1}$ V_n is the RMS value of the n^{th} harmonic
DND	Described in Section 5.5.1	Equation 5.5.3

Additional features describing the operating conditions were added to the feature matrix to obtain a full descriptive result. These operational features are operating speed, head consumed, operating flow rate and the turbine output power. All of these parameters were normalised with respect to the best efficiency point for each operating speed. In total, 39 features were obtained for each of the data files to create a feature matrix suitable for the training of machine learning models.

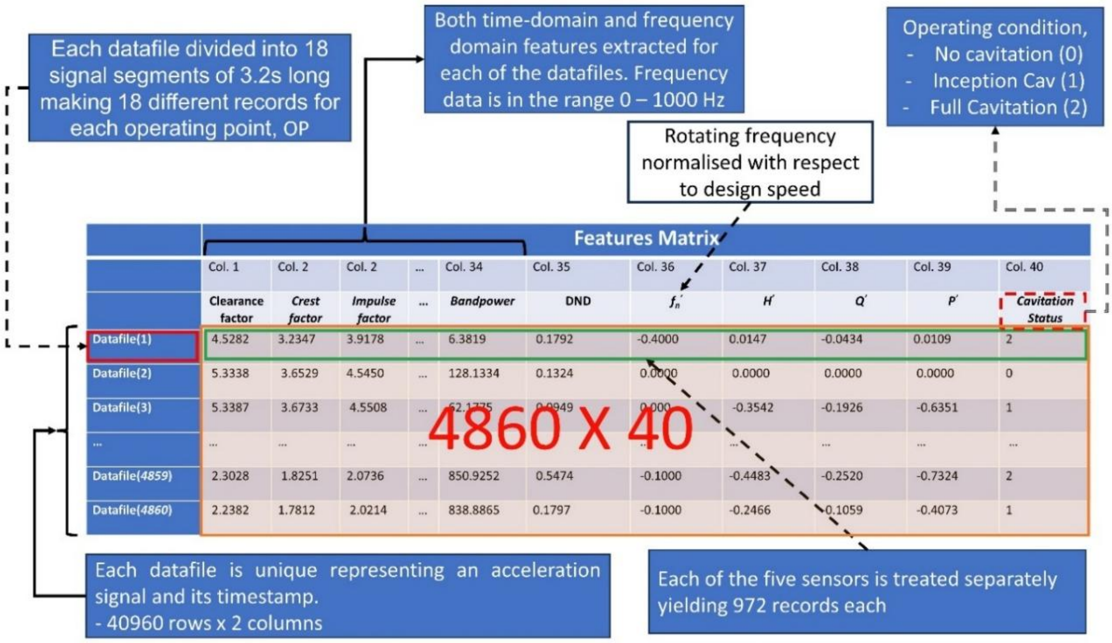

	Col. 1	Col. 2	Col. 2	...	Col. 34	Col. 35	Col. 36	Col. 37	Col. 38	Col. 39	Col. 40
	Clearance factor	Crest factor	Impulse factor	...	Bandpower	DND	f_n'	H'	Q'	P'	Cavitation Status
Datafile(1)	4.5282	3.2347	3.9178	...	6.3819	0.1792	-0.4000	0.0147	-0.0434	0.0109	2
Datafile(2)	5.3338	3.6529	4.5450	...	128.1334	0.1324	0.0000	0.0000	0.0000	0.0000	0
Datafile(3)	5.3387	3.6733	4.5508	...	62.1775	0.0949	0.000	-0.3542	-0.1926	-0.6351	1
...	...	...	...	...				...	...	...	...
Datafile(4859)	2.3028	1.8251	2.0736	...	850.9252	0.5474	-0.1000	-0.4483	-0.2520	-0.7324	2
Datafile(4860)	2.2382	1.7812	2.0214	...	838.8865	0.1797	-0.1000	-0.2466	-0.1059	-0.4073	1

Figure 6.3-2. Summary of the resultant feature matrix

Figure 6.3-2 shows a summary of the resultant feature matrix. The last column in the feature matrix shows the cavitation status which the machine was operating at when the data used to compute the features was being captured. The feature matrix is made up of 4860 records consisting of 39 features. After this feature table was computed, the data was now ready to be used in the development of various machine learning models for the prediction of the PAT's cavitation status.

Feature Selection

The extracted features from the above section consists of 39 features which could possess various levels of importance in the classification and prediction of fault classes. It is imperative that this feature matrix be scrutinised further to identify features that are of little significance when it comes to possessing high variability in information that could simplify the classification and prediction process. Surucu et al. [198] states that filtering out redundant features from the feature matrix is associated with advantages of requiring less computational and memory resources as a large dataset introduces inefficient complexity to the machine learning model, which could consequently lead to overfitting and less accurate results.

Overfitting in machine learning models especially supervised machine learning refers to the model's failure to generalise well from observed data to unseen data resulting in a perfect performance on training set and poor performance on test data [199]. As a first step in avoiding creation of classification and prediction models that will be overfitting, feature selection allows for the identification of the most important features in the feature matrix and eliminate redundant ones.

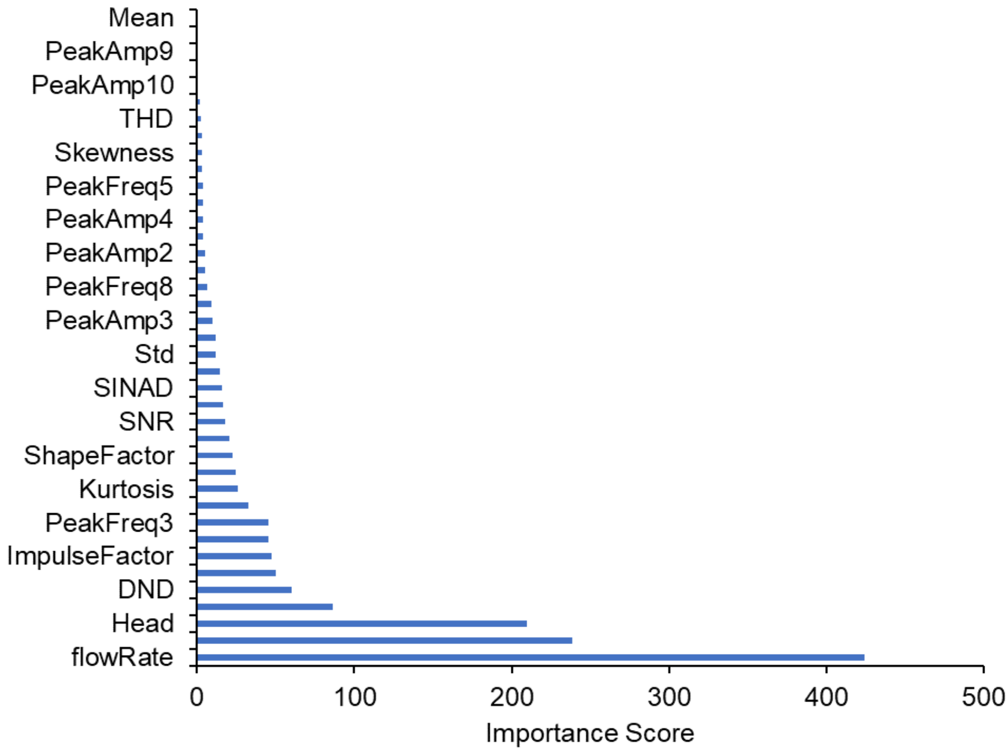

Figure 6.3-3. Features sorted in order of increasing importance score

In this study, a one-way Analysis of Variance (ANOVA) was used to rank all the features in increasing importance scores. ANOVA is a statistical method for comparing means of several data groups to determine whether the observed variations are genuine or are a result of some errors [200-202]. A one-way ANOVA considers each feature individually and tests the hypothesis that its values grouped by the response classes are drawn from a population with the same mean (Null Hypothesis) against the alternate hypothesis that the means of the populations are not all the same. Importance scores are computed by taking the negative logarithm of the *p*-values for each feature. Features are then sorted in order of decreasing importance scores and the results are presented in Fig. 6.3-3.

It is evident that much variability in the values of features is recognised mostly from the operational features with the flow rate, output power and head consumed displaying higher importance scores. From vibration data the most important feature is the second dominant frequency in the PSD followed by the DND. It is worth noting the significance of the DND in this exercise as the most dominant time domain parameter in the feature matrix.

The selection of the optimal set of features is a crucial step in building efficient and interpretable ML models. One of the challenges is determining the appropriate number of features to use as redundant features can lead to overfitting, reducing the model's robustness and reliability while also increasing computational complexity. To conduct this optimization task, a decision tree model consisting of 100 splits based on the Gini's Diversity Index (GDI) was employed to evaluate performance while systematically varying the number of top features included in the model. The use of a decision tree model was based on its inherent feature of prioritising inputs as the tree is being grown.

Table 6.3-2. Description of training and testing datasets

Purpose	**Cavitation State**	**Label**	**Number of Observations**
Training	No cavitation	0	1576
	Inception Cavitation	1	570
	Full cavitation	2	1256
Testing	No Cavitation	0	674
	Inception Cavitation	1	240
	Full cavitation	2	544

The feature matrix was then divided into two groups representing a ratio of 70:30 of the total feature matrix, resulting in 3402 instances for the training data and 1458 instances for the testing data. These data sets were then used to develop and test all the models presented in this thesis. Table 6.3-2 shows a summary of both the training and testing datasets including the labelling and the number of samples for each cavitation state. All developed models utilise a five-fold cross validation scheme where the training data is further partitioned into five separate data groups and model training is conducted with four of the five groups consecutively five times with the remaining data set used for testing until all the groups have been used to test the accuracy of the developed model. The validation accuracy is therefore given by the average test results of all the five tests.

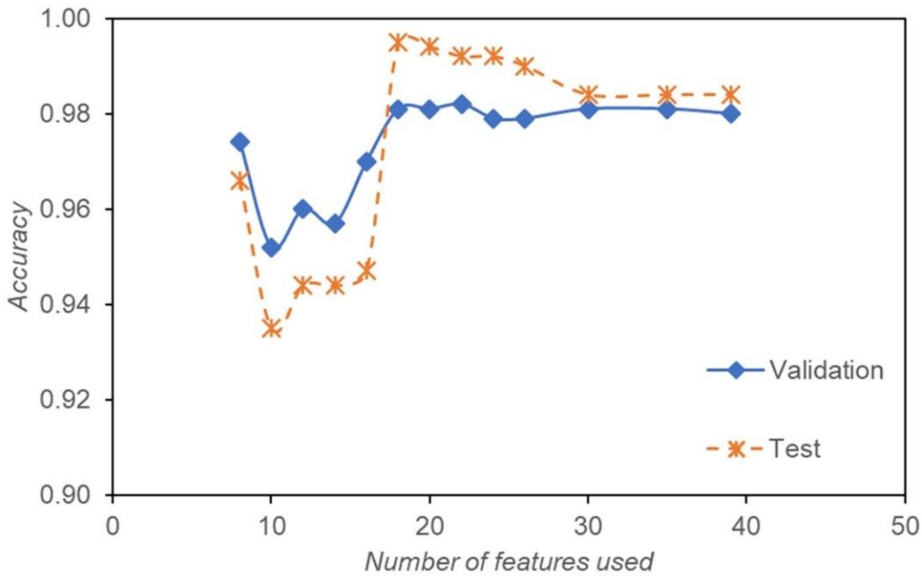

Figure 6.3-4. Feature optimisation results

Figure 6.3-4 presents the results of the optimisation study. The comparison of the accuracies, both validation and test, of the developed model with varying number of higher importance features is used to decide on the optimal number of features for adoption. It is evident that when number of higher importance features used in developing the decision tree is below 18, there is a higher instability in the obtained model accuracies. The accuracy values are observed to be fluctuating and begins to stabilise as the number approaches 18 features. This is followed by a stable performance as the accuracy obtained with even higher number of features remains around 98%. This means that the improvement in model accuracies as the number of features used is increased beyond 18 remains minimum, meaning that the use of 18 features can be selected as the optimum number of features to use in the development of machine learning models in the following sections.

6.3.2. Supervised Machine Learning

6.3.2.1. Decision Trees

A decision tree is a supervised machine learning model that recursively partitions the data based on the values of features to create distinct subsets, ultimately leading to a prediction at the leaf nodes. A standard tree consists of a single root and numerous branches, nodes and leaves. Each internal node of the tree represents a decision rule based on a specific feature, and the tree itself represents the learned model. Each leaf of the tree represents the group which classifies the datapoint while branches represent possible values of the node from which they originate. A decision tree algorithm invokes an entropy-based information gain selection criteria to select the most useful feature in the input matrix for selection at the decision node.

Once a tree has been constructed it does not retain the same level of accuracy because of possible overfitting and underfitting resulting in some branches yielding less reliable accuracies. These, therefore, create a need for pruning, removal of these low accuracy branches, to obtain better classification results. This is achieved through computation of the aggregate misclassification error for each node.

Model development – The decision tree was developed using MATLAB's '*fitctree*' function, which automatically handles tree construction, pruning and splitting using a known number of classes. The tree was constructed basing the selection of the important feature for classification at the nodes on the Gini's Diversity Index (GDI) criterion. The GDI measures the degree of the impurity in a node with the goal of minimizing this impurity at each split to pure leaf nodes, meaning that a GDI of zero implies a pure node otherwise it implies existence of impurities. The decision tree recursively splits the data into subsets that maximise class separation improving classification accuracy while doing so.

By adjusting the '*MaxNumSplits*' parameter, which dictates the maximum number of branches that are permissible at each layer, the size of the tree can be controlled. A layer here refers to all nodes that are equidistant from the root. If the number of branches exceed this amount, the tree will be pruned to limit their number. This parameter was experimentally varied to create three decision tree models of varying complexity and selected the one with the highest classification accuracy as the best choice. For each choice of the '*MaxNumSplits*' parameter, the obtained model was tested using the test dataset.

Results – Table 6.3-3 present the results of this experiment. The presented cases are representative of varying complexity of the decision tree with a '*MaxNumSplits*' = 4 indicating a course decision tree, a '*MaxNumSplits*' = 20 indicating a medium decision tree whereas a '*MaxNumSplits*' = 100 represent a fine decision tree. The time taken to train each model is also presented as the value of '*MaxNumSplits*' is varied. It is observed that increasing the '*MaxNumSplits*' parameter does not have a direct and linear influence on the time taken to train the model as a '*MaxNumSplits*' = 4 yields a longer training time than a '*MaxNumSplits*' = 20. However, increasing the '*MaxNumSplits*' parameter to 100 yields a longer training time in comparison to the other two cases.

Table 6.3-3. Model performance when varying 'MaxNumSplits' parameter

MaxNumSplits	**Accuracy**		**Training Time (seconds)**
	Validation (%)	**Testing (%)**	
4	74.5	77.2	7.6307
20	95.5	95.9	6.498
100	98.1	99.5	9.1592

Nonetheless, varying the '*MaxNumSplits*' parameter has a direct relationship to the observed accuracies of the obtained model. During model training, the '*MaxNumSplits*' of 100 results in a higher validation accuracy of 98.1% in comparison to validation accuracies of 95.5% and 74.5% at '*MaxNumSplits*' = 20 and 4, respectively. Testing of each of the trained models yielded similar results with testing accuracies of 99.5%, 95.9% and 77.2% at '*MaxNumSplits*' = 100, 20 and 4, respectively.

Overall, these results indicate a better accuracy for the fine decision tree which could be attributable to more information used in the development of the model, hence more information used in segregation of classes. Figure 6.3-5 shows a visualisation of the optimum decision tree obtained with '*MaxNumSplits*' of 100. Each of the paths from root to leaf can be regarded as a classification rule that the tree utilises to predict the class of the new data. As an example, when considering the far-right path in Fig. 6.3-5, the algorithm checks whether the flowrate parameter is equal to or exceeds -0.02711, then it checks the operating frequency parameter. When this parameter is equal to or exceeds -0.15 the data is classified as 'no cavitation' else its indicative of 'full cavitation'.

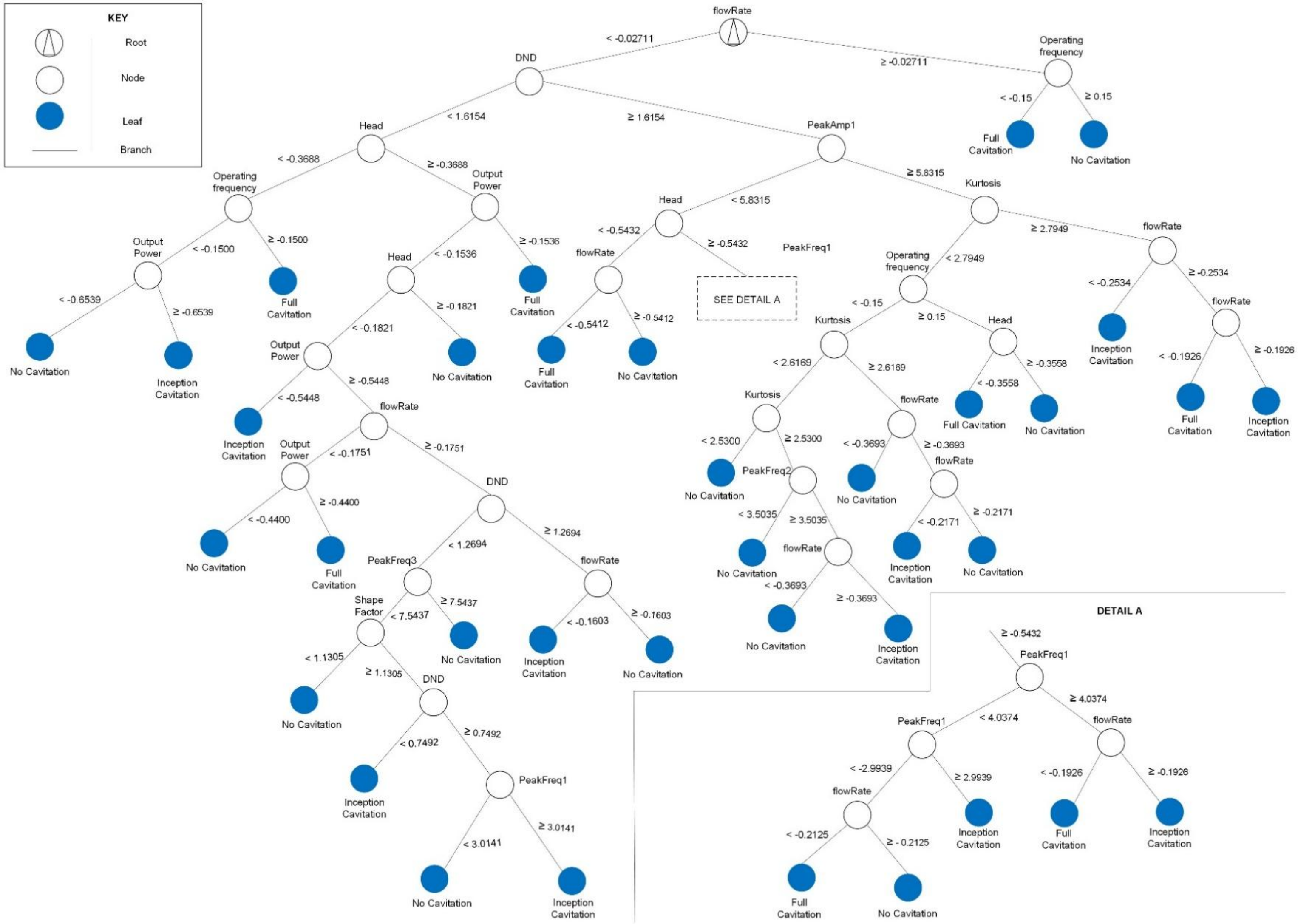

Figure 6.3-5. The final decision tree structure

To understand how the model performs in classifying data according to each of the three classes i.e., 'no cavitation', 'inception cavitation' and 'full cavitation', a confusion matrix was used as presented in Figs. 6.3-6 and 6.3-7. Figure 6.3-6 indicates the misclassification details of the training phase of the model with Fig. 6.3-7 indicating the test phase. During training phase, the model achieved True Positive Rates (TPR) of 97.7%, 96.7% and 99.3% in classifying 'no cavitation', 'inception cavitation' and 'full cavitation' datasets, respectively. This means that from the training data the model obtained higher errors in classifying 'inception cavitation' in comparison to the other two cavitation states.

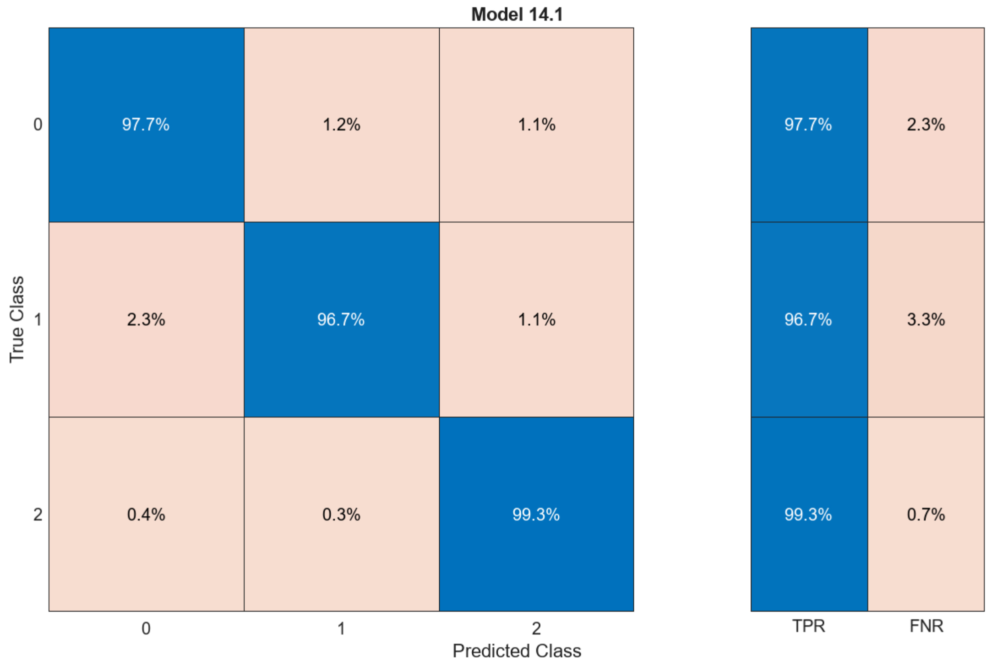

Figure 6.3-6. Confusion matric of the five-fold cross-validation (training dataset). 0 - 'No Cavitation', 1 – 'Inception Cavitation' and 2 – 'Full Cavitation'. TPR – True Positive Rate, FNR – False Negative Rate

Figure 6.3-6 shows that 0.4% and 0.3% of 'full cavitation' data is erroneously classified as a 'no cavitation' and 'inception cavitation' conditions respectively while 2.3% and 1.1% of 'inception cavitation' state data are misclassified as 'no cavitation' and 'full cavitation' states respectively. In the case of 'no cavitation' data 1.2% and 1.1% of data instances are misclassified as 'inception cavitation' and 'full cavitation' respectively.

Since there is an inadequacy in the experimental procedure associated with deciding when the machine in undergoing 'inception cavitation', the observed misclassifications are somewhat expected. This is because there was an over reliance on the experimenter's observation of the cavitation inception point which could have led to results skewed either towards a 'no cavitation' state or a 'full cavitation' state. The misclassification of both 'no cavitation' and 'full cavitation' can have serious consequences to the maintenance function. Misclassification of 'no cavitation' state could result in more false negatives leading to increased and costly maintenance activities whereas misclassification of the ‘full cavitation’ states can result in the machine’s prolonged exposure to cavitating conditions with detrimental consequences in the long run.

However, the obtained confusion matrix with the test data has resulted in better performance with zero misclassifications of either ‘no cavitation’ as ‘full cavitation’ or vice versa as shown in Fig. 6.3-7. The TPR and FNR for the testing dataset also improved yielding 99.6% and 0.4% respectively for ‘No Cavitation’, 98.3% and 1.7% for ‘inception cavitation’ respectively, and 99.8% and 0.2% respectively for ‘full cavitation’ state respectively. These results are encouraging and present a decision tree as a viable classification type that could be implemented with the current failure mode and machine combination.

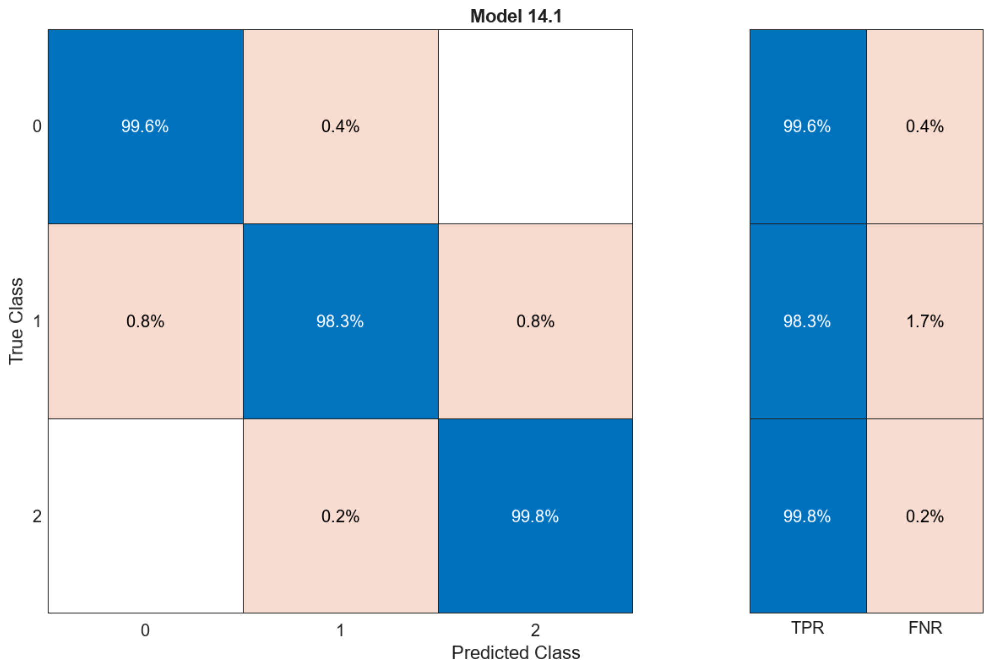

Figure 6.3-7. Confusion matrix of the testing dataset. 0 - ‘No Cavitation’, 1 – ‘Inception Cavitation’ and 2 – ‘Full Cavitation’. TPR – True Positive Rate, FNR – False Negative Rate

6.3.2.2. Artificial Neural Networks

Artificial Neural Networks (ANNs) are deep learning-based machine learning algorithms that mimic the working principles of the human brain [153, 198]. Their structure is composed of several neurons divided into three layers namely, the input layer, the hidden layer and the output layer, weight, biases and activation functions. The purpose of neurons is to receive inputs, process them by assigning weights and biases, apply activation functions and transmit results as output to the next layer. They function in a similar way to synapses in a human brain. The input layer receives the data while the hidden layer performs most of the intermediate processing of the data, transforming inputs into more abstract representations whereas the output layer produces the results depending on whether it’s for classification or regression purposes [203].

Layers make use of activation functions at the output of neurons to describe how inputs are transformed before are passed to the next layer. They determine whether outputs should be passed to the next layer or whether they require some modifications in a specific way. Activation functions introduce some non-linearity on the process to model complex patterns. As such, ANNs are particularly effective in reproducing non-linear patterns and complex relationships in data. Some commonly used functions include the *Sigmoid* function, Rectified Linear Unit (*ReLU*) function, hyperbolic tangent (*tanh*) function and the Softmax function. The Softmax is used to produce the model output, being the classification scores and labels. Weights are assigned to denote the strength of connections between neurons while biases allow adjustment of outputs independent of the inputs for greater flexibility. Weights are updated during the training process as per the error in the output layer, to fit for the correct classification results [204].

There are various types of ANNs such as Feedforward Neural Networks (FNNs) which only permits the flow of data in a single direction from the input layer to the output layer with use cases ranging from basic classification to regression problems. Convolutional Neural Networks (CNNs) are another type that specialise in the analysis of grid like data using convolutional layers mostly used in image recognition and object detection. Autoencoders represent the unsupervised type of ANNs with special application on anomaly detection and denoising applications.

Model Development – Using the '*fitcnet'* MATLAB function, various ANN models were developed by varying their structure for optimization to obtain the best architecture suitable for the input data. The '*fitcnet'* MATLAB function is used to train a feedforward, fully connected ANN for classification purposes. The first connected layer of the network has a connection with the input data and each subsequent layer is characterised by a connection to the previous layer. Each fully connected layer assigns weights to the input then add a bias vector.

In this study, the number of fully connected layers, number of neurons and the activation functions are varied while the weights and biases are automatically adjusted through iterating up to a limit of 1000 based on the characteristic of the input data. We use the same input data used in the previous section to develop the decision tree model. The number of fully connected layers is varied to obtain single layered, bi-layered and tri-layered models.

Firstly, three single layered ANN models are developed based on the *ReLU* activation function consisting of 10, 25 and 100 neurons which represent a narrow, medium and wide structured model respectively. The number of neurons of the best performing model from these three is taken as the optimum. It is then used to test for the best activation function to use by creating models using both the *tanh* function and the *sigmoid* function. A combination of the obtained best number of neurons and the best performing activation function are used to develop both a bi-layered and a tri-layered model. Performance is evaluated based on both the validation accuracy and model training times.

Results –Table 6.3-4 presents the performance of each of the developed models. The best performing activation function at the hidden layer was found to be the *ReLU* function. The *ReLU* activation function performs a threshold operation on each element of the input matrix by setting any value less than zero equal to zero. It was found out that for a single layered ANN, a model with 10 neurons results in the same validation accuracy as a model with 25 neurons. As a way of minimising complexity, a layer size of 10 neurons was selected to be the optimum size for the first layer.

In optimising for the second layer of a bi-layered ANN, the first layer was set to 10 neurons and the second layer varied between 10, 25 and 100. The results show a higher validation accuracy when the second layer has 25 neurons. Similarly, when optimising for the tri-layered ANN model, the first and second layers were set to 10 and 25 respectively, and the third layer varied between 10, 25 and 100 neurons. Results show that the highest validation accuracy obtained with a tri-layered ANN is 99.5% which was obtained with the third layer consisting of 10 neurons.

Table 6.3-4. Parameter tuning for ANN model development

Number of Layers	**Activation Function**	**1st Layer Size**	**2nd Layer Size**	**3rd Layer Size**	**Performance**	
					Accuracy (%)	**Training Time (s)**
1	*ReLU*	10	-	-	99.4	34.649
1	*ReLU*	25	-	-	99.4	34.431
1	*ReLU*	100	-	-	99.2	36.901
1	*tanh*	10	-	-	98.9	3.9295
1	*Sigmoid*	10	-	-	98.6	6.8378
2	*ReLU*	10	10	-	99.6	35.739
2	*ReLU*	10	25	-	99.8	16.914
2	*ReLU*	10	100	-	99.7	11.453
3	*ReLU*	10	25	10	99.5	4.7685
3	*ReLU*	10	25	25	99.2	5.3107
3	*ReLU*	10	25	100	99.4	11.643

Comparing the best of each of the three layouts i.e., single layered, bi-layered and tri-layered, it is observed that the highest validation accuracy was obtained with a bi-layered model. It utilises the *ReLu* activation function. There is an observed wide variation of the training times for each of the models with a single layered model taking 34.6s, while the bi-layered and tri-layered models taking 16.9s and 4.77s respectively. Reducing the number of layers in the model results in a longer training time. There is a 0.4% difference in accuracy between the bi-layered model performance and the single layered model. In the case of the tri-layered model, its difference against bi-layered model is

0.3%. As such, the bi-layered model was adopted as the optimum for the current case and will be used for further analysis.

The resultant ANN model is a feedforward network with two hidden layers, each of them with a different number of neurons. This model consists of 10 neurons in the first layer and 25 neurons in the second layer. The structure of this network is presented in Fig. 6.3-8. The model utilises the *ReLU* activation function in the hidden layers and *Softmax* as a transfer function at the output neurons. This function takes the inputs x_i and returns k classes representative of the fault condition in the current setup. During training model the *'fitcnet' MATLAB* function uses a limited memory Broyden-Fletcher-Goldfarb-Shanno quasi-Newtonian algorithm (LBFGS) [205] as its function minimization technique for the cross-entropy loss.

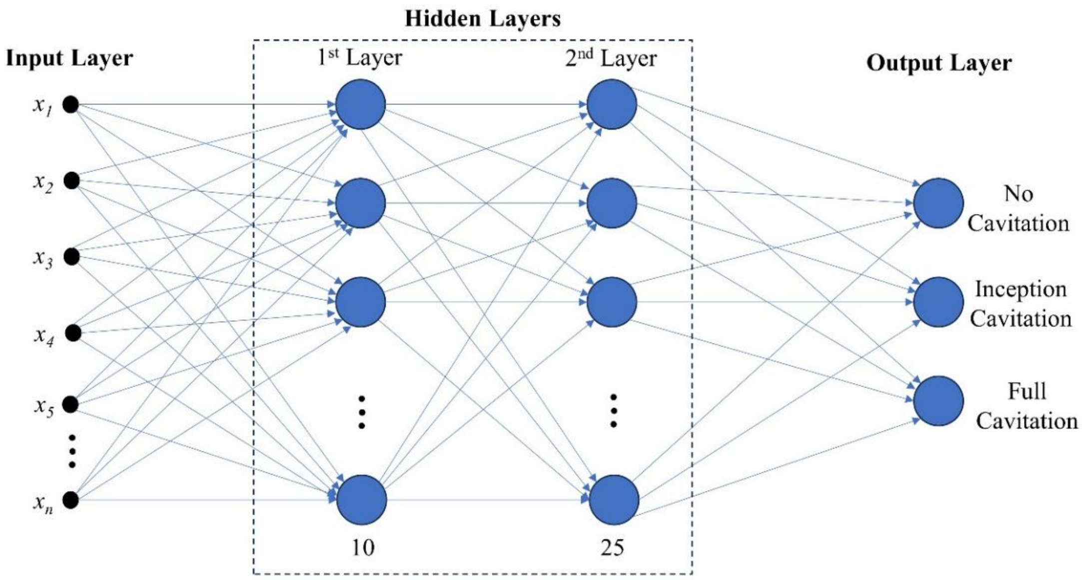

Figure 6.3-8. Structure of the developed ANN model

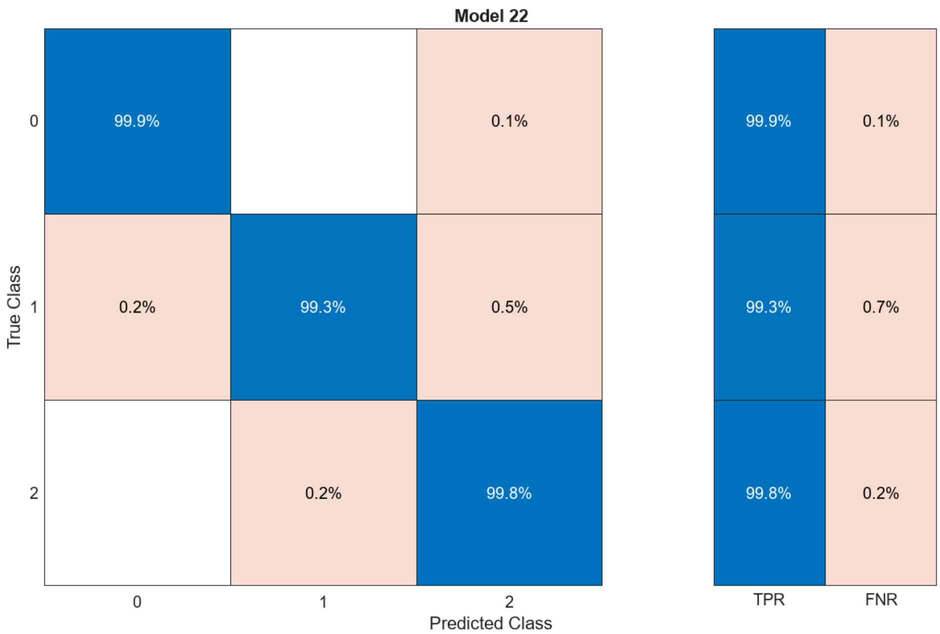

Figure 6.3-9. Five-fold cross-validation accuracy confusion matrix for the ANN Model. 0 - 'No Cavitation', 1 – 'Inception Cavitation' and 2 – 'Full Cavitation'. TPR – True Positive Rate, FNR – False Negative Rate

Figure 6.3-9 presents a confusion matrix for the five-fold cross-validation of the developed model. The model misclassifies the 'no cavitation' condition as 'full cavitation at a rate of 0.1%. Inception cavitation is misclassified as 'no cavitation' and 'full cavitation' at rates of 0.2% and 0.5% respectively. Similarly, 'full cavitation' condition is misclassified as 'inception cavitation' at a rate of 0.2%. The model does not either misclassify the 'no cavitation' condition as 'inception cavitation' or 'full cavitation' as 'no cavitation' conditions. This result in an overall validation accuracy of 99.8% which is a very good model performance.

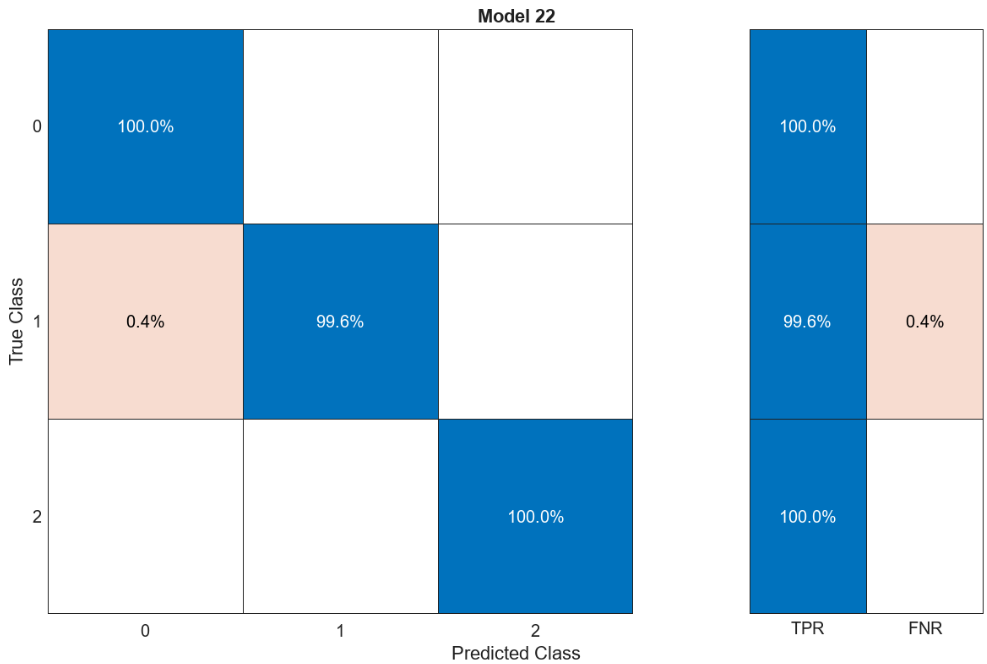

Figure 6.3-10. Test accuracy confusion matrix for the ANN model. 0 - 'No Cavitation', 1 – 'Inception Cavitation' and 2 – 'Full Cavitation'. TPR – True Positive Rate, FNR – False Negative Rate

Results of the testing phase of the model are shown as a confusion matrix in Fig. 6.3-10. It is noticed that the model correctly classifies both the 'no cavitation' and 'full cavitation' conditions with a rate of 100%. The only observed misclassification is with the 'inception cavitation' condition where 0.4% of the 'inception cavitation' data was classified as 'no cavitation' condition. This yields an overall testing accuracy of 99.9% which is a very good classification accuracy. The observed misclassification, as already discussed in the decision tree section, was expected due to the reasons of more reliance in human judgement in the collection of data to classify the machine condition especially the 'inception cavitation' condition.

6.3.2.3. Support Vector Machines

Support Vector Machines (SVMs) are categorised under a group of supervised machine learning algorithms called kernel methods. To understand the reason behind this classification we will describe the idea behind this machine learning algorithm. They are used to solve binary classification and regression problems in which data either exist in one side of a hyperplane or another i.e., whether the data represent healthy condition or a faulty condition [206]. A hyperplane represents a decision boundary defined by the number of support vectors that differentiates between classes, as shown in Fig. 6.3-11. Support vectors are a subset of the data that is used to identify the location of the separating hyperplane.

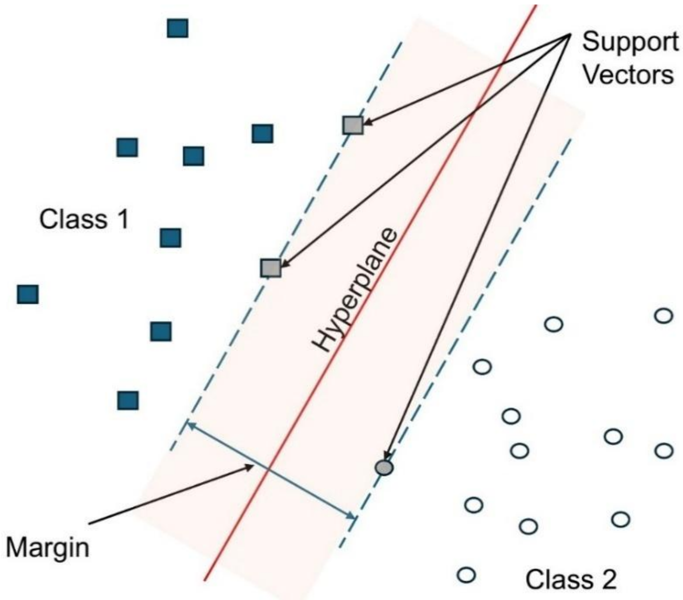

Figure 6.3-11. Binary classification of classes using SVM

The main aim of SVMs is to find the best hyperplane that separates data points of one class from those of the other to the best degree possible. This is achieved by maximizing the margin, the width representing the parallel distance between the set of support vectors. This hyperplane can only be found accurately for linearly separable problems, but most practical problems are non-linear meaning that there always a small number of misclassifications.

The above explanation was based on a binary classification problem. In the case of a multiclass problem similar to the one that we ought to solve in this thesis, the classes are reduced to a series of binary problems via the adoption of either of the three distinct strategies for multiclass classification, namely one-against-one (OAO), one-against-all (OAA) or directed acyclic graph (DAG) [198, 207].

The OAO multiclass coding strategy considers one class as positive and another one as negative while ignoring the rest. It repeats this approach for all the class pair assignments to develop a total of $k\ (k-1)/2$ binary classifiers. k in this case refers to the number of classes that the data contains.

On the other hand, the OAA strategy develop *k* binary learners with one class of data taken to be positive and the rest of classes as negative. This creates all combinations with each class considered individually as positive.

Where the classes may not be separable using a linear boundary, a kernel function is used to transform the data into a higher dimensional space making it possible to create a hyperplane that will allow linear separation. A kernel function performs this transformation as well as the required dot product in a single step hence simplifying a complex non-linear decision boundary to a linear one in the high dimensional mapped feature space. Some of the existing kernel functions that have found application in machine condition monitoring applications include the Gaussian (Radial Belief Function), linear and polynomials of various orders [198, 207].

Model Development – SVM models were developed using the MATLAB '*fitcecoc'* function, which fits error-correcting output codes classifiers for multiclass learning consisting of multiple binary learners. The trained model stores training data, parameter values, prior probabilities and coding matrices. To develop the most optimal model for the input data, two main parameters were varied to obtain a combination that offers the best performance in terms of validation accuracy.

First, the kernel function that is used to make the mapping from feature space to a higher dimensional space was varied making it possible to approximate linear relationship between classes of input feature matrix. Using a one-against-one multiclass coding strategy, four kernel functions namely Gaussian, Linear, Quadratic and Cubic kernels, were used to develop SVM models using the same training data used in previous sections. The kernel function obtaining the best performance in terms of validation accuracy was used to develop another model that implemented the one-against-all multiclass coding strategy. The combination of Kernel function and multiclass coding strategy that resulted in the best performance was chosen as the most optimal SVM.

Results - Table 6.3-5 presents the results of this parameter tuning exercise for the development of SVM models. The best performance in terms of model validation accuracy was obtained with the Cubic Kernel Function at 98.6%. The second-best option was the Gaussian Kernel function yielding 98.0% followed by the Quadratic function at 96.5%. The Linear Kernel functions resulted in the lowest performance obtaining a validation accuracy of 81.1%. Looking at the time it takes to train the model, the Gaussian kernel resulted in a shorter time of 1.8823s followed by the Linear Kernel function at 12.613s. The Quadratic and Cubic Kernels took 14.105s and 15.56 s respectively. Since the most important parameter considered in this analysis was the validation accuracy the use of Cubic Kernel was selected as the most optimal for the input data.

Table 6.3-5. Parameter tuning for SVM model development

Kernel Function	Multiclass Coding Strategy	Performance	
		Accuracy (%)	Training Time (s)
Gaussian	one-against-one	98.0	1.882
Linear	one-against-one	81.1	12.613
Quadratic	one-against-one	96.5	14.105
Cubic	one-against-one	98.6	15.560
Cubic	one-against-all	98.1	14.630

To select the best multiclass coding strategy another model was developed using the one-against-all strategy alongside the cubic kernel function. The results indicated a slight decrease in the validation accuracy from 98.6% to 98.1% when compared with the one-against-one model. The training time decreased to 14.63s in comparison to the 15.56s for the one-against-one multiclass coding strategy. In conclusion, the adopted model for further use was characterised by a Cubic Kernel function implementing a one-against-one multiclass coding strategy.

Figure 6.3-12 presents a confusion matrix for the cross-validation of the developed SVM model. The model misclassified 0.3% of the 'no cavitation' condition data into 'inception cavitation' and 0.1% into 'full cavitation'. In comparison, 0.5% of the 'inception cavitation' data was misclassified as 'no cavitation' condition while 2.3% was misclassified as 'full cavitation'. Considering the 'full cavitation' condition data, 0.2% was misclassified as 'no cavitation' while 1.8% was misclassified as 'inception cavitation'. On average the model achieves 98.6% accuracy in classifying the input data into its respective conditions with the major misclassification of input data coming from the inception cavitation class. This is a similar observation to the ANN and Decision Tree models developed in the prior sections.

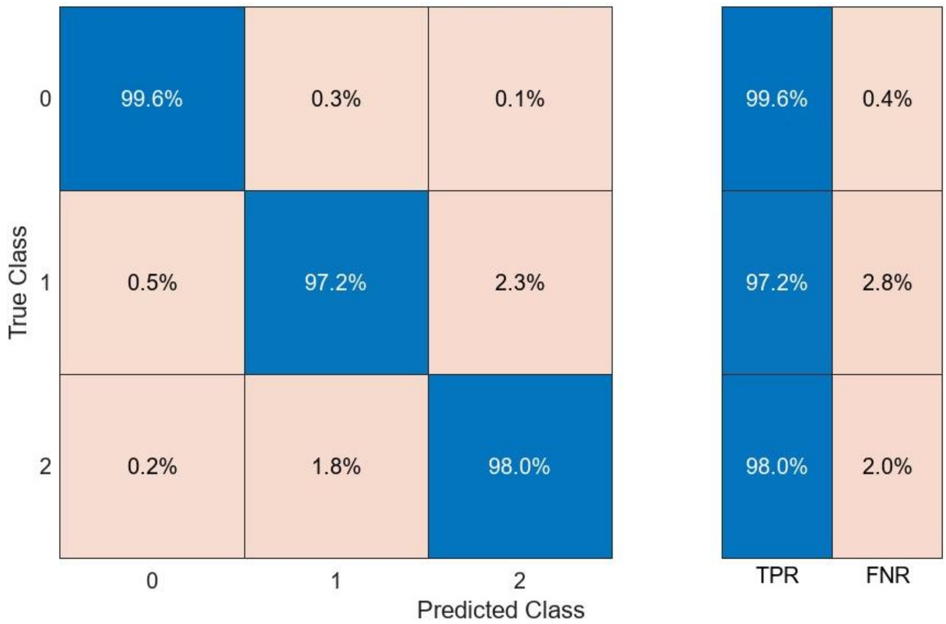

Figure 6.3-12. Five-fold cross-validation accuracy confusion matrix for the SVM Model. 0 - 'No Cavitation', 1 – 'Inception Cavitation' and 2 – 'Full Cavitation'. TPR – True Positive Rate, FNR – False Negative Rate

The result of the testing phase of the model are presented in Fig. 6.3-13 in the form of a confusion matrix. The model accurately classified all the 'no cavitation' condition data, 5% of the inception cavitation data was misclassified as 'no cavitation' (at 0.4%) and 'full cavitation' (at 4.6%) while 1.5% of the 'full cavitation data was misclassified as either 'no cavitation' (at 0.2%) or 'inception cavitation' (at 1.3%). The overall testing accuracy for the model was equal to the overall model validation accuracy of 98.6% indicating a 1.4% chance of incorrectly classifying the machine condition, which represent a good performance of the model.

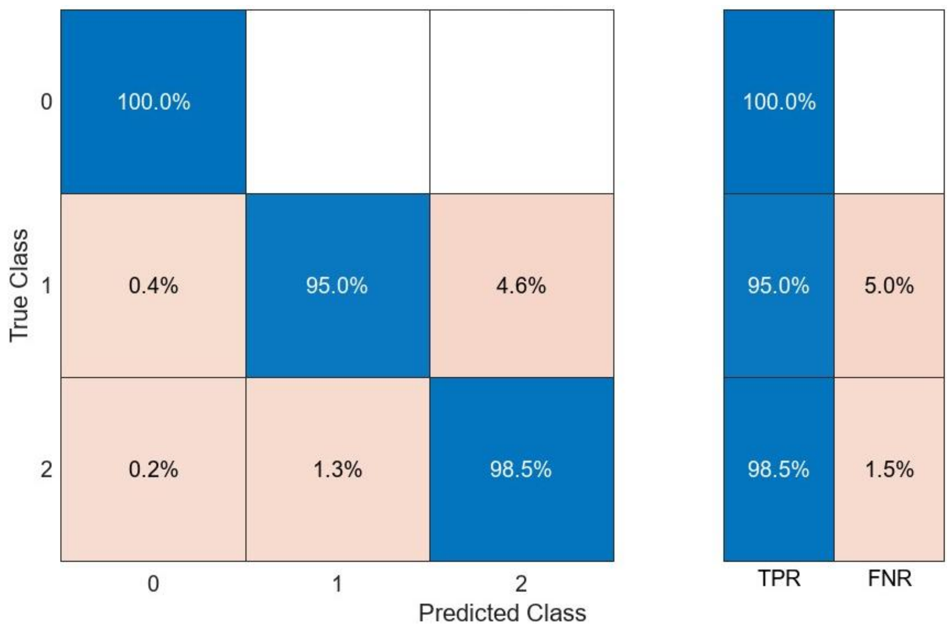

Figure 6.3-13. Testing accuracy confusion matrix for the SVM Model. 0 - 'No Cavitation', 1 – 'Inception Cavitation' and 2 – 'Full Cavitation'. TPR – True Positive Rate, FNR – False Negative Rate

As already explained under sections 6.3.2 (a) and (b), most of these misclassifications are associated with the 'inception cavitation' condition which portrays a thin line separating it from either of the two classes, 'no cavitation' and 'full cavitation'. As such, we are of the view that all the three developed models developed in this section performed well in classifying the various machine condition.

6.3.2.4. Model Interpretability Assessment

The interpretability of ML models is increasingly recognised as a critical requirement in safety-critical and industrial applications such as predictive maintenance in hydropower systems. As Molnar [175] and Carvalho et al. [174] outlined, interpretability of a ML model refers to the degree to which a human can understand the ML systems' logic to reaching a conclusion.

Interpretability could exist via two broad paths of intrinsic interpretability and post-hoc interpretability. Intrinsic interpretability exists in models whose structure is inherently understandable while post-hoc interpretability involves creating explanation methods which are applicable to existing black box models. Table 2.6-1 on page 53 presents examples of intrinsically interpretable models adapted from Molnar [175] and Carvalho et al. [174]. From the developed models only the Decision Tree offers interpretability by-design with ANN and SVM models requiring post-hoc explanation methods.

While intrinsically interpretable models offer direct insight into decision logic, approaches to interpretability such as Local Interpretable Model-agnostic Explanations (LIME) and Shapley Additive Explanations (SHAP) are post-hoc techniques for black box models. However, in this study we limited the assessment of interpretability to inherently interpretable models because post-hoc methods might provide plausible explanations but unfaithful ones that do not accurately reflect the internal logic of the model [208]. Intrinsic models leave no ambiguity.

6.3.3. Unsupervised Machine Learning

6.3.3.1. K-means Clustering

K-means clustering is a method for finding subsets of data with similar attributes and their centroids in a set of unlabelled data [209]. This is useful for modelling complex data for which prior knowledge is hard to obtain. The main aim is to learn from the existing dataset to obtain representations that could be used to predict future deviations from known machine conditions.

The K-means algorithm learns these representations by first dividing a set of n observations into k groups such that the similarity between observations in a group and the dissimilarity between observations from different groups are high [210]. Thus, the objective of the K-means algorithm is to minimize the squared distance of observations in a group.

The algorithm starts by randomly selecting k datapoints as cluster centres and iteratively moves these centres to minimise the within group variance by identifying observations that are close to it than other centres. The new subset of observations is then utilised to compute the new means and the procedure repeated iteratively until there is little change in the group centres [209-211]. The downside to this algorithm remains with the selection of the variable k which defines the number of groups the data is to be clustered at. It's often unknown in real-world applications the likely number of clusters and a decision is made by trying different numbers.

In the context of the current study, the value of $k = 3$ which is representative of the three cavitation conditions observed during data acquisition. This means the training of the model only comprises the iterative minimisation of squared distance between data points and their respective cluster means. The model was trained with the same training dataset defined in Section 6.3.1.

In contrast to the feature optimisation/prioritisation approach adopted for the supervised learning techniques, a Principal Component Analysis (PCA) based dimensionality reduction approach was used to also aid in visualising the generated clusters [212]. PCA is an orthogonal feature projection algorithm that aims to find all the components in descending order of significance where the first few principal components possess most of the variance of the original data [213]. To reduce the dimensionality of data, the least significant principal components are ignored.

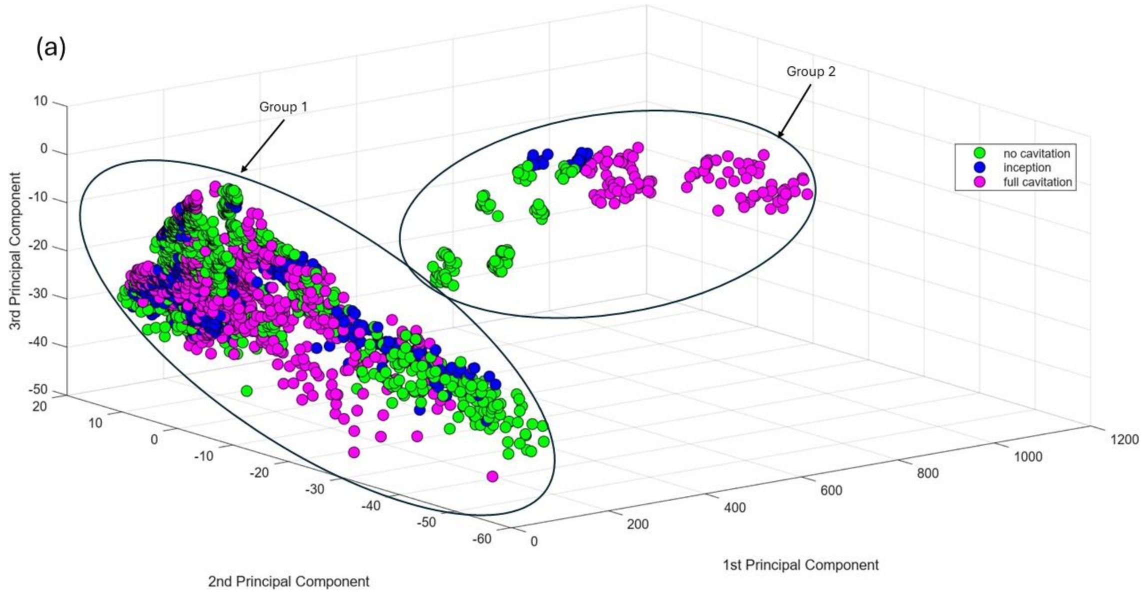

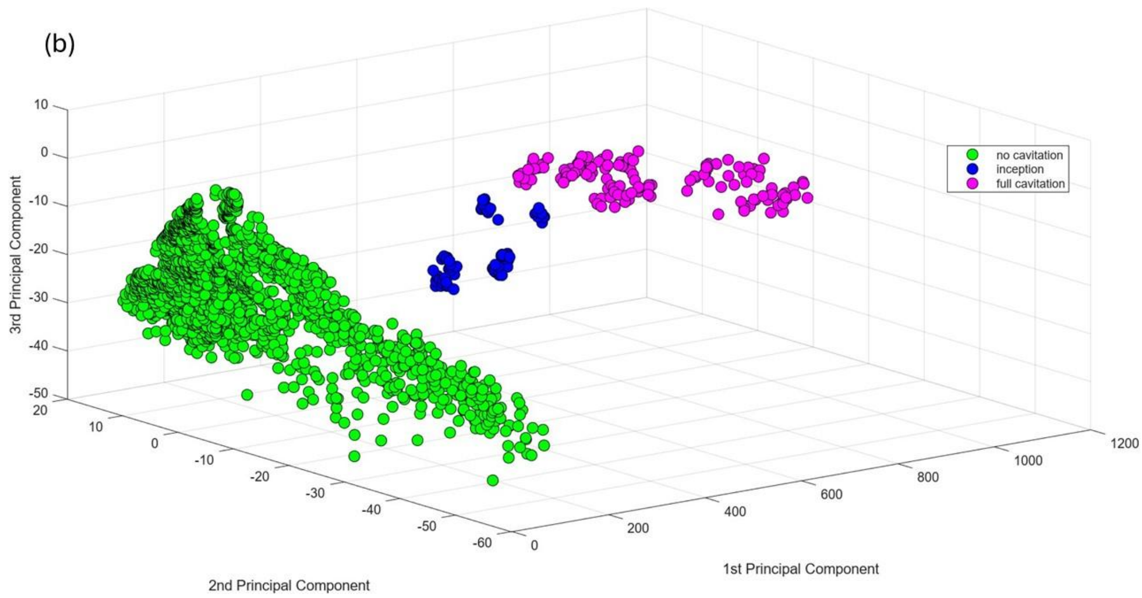

Figure 6.3-14. PCA representation of the original training data set (a) without clustering (b) with K-means clustering implemented

The result of the application of the PCA algorithm indicated that 99% of the variance in training dataset could be represented with three principal components (PCs). These principal components were used to represent the original dataset. Figure 6.3-14(a) shows the scatter plot of the original dataset after PCA projection over three dimensions defined by PC1, PC2 and PC3 before clustering using the K-means algorithm. It is evident that there exist two major groups in the dataset with individual observations representing each of the cavitation states belonging to either of the groups at random.

Running the K-means algorithm on this data set yielded a similar grouping but with the second group divided into two clusters representing 'inception cavitation' and 'full cavitation'. The first group was dominantly assigned to 'no cavitation' state as indicated in Fig. 6.3-14(b). Measuring performance of the K-means clustering algorithm does not follow the same procedure used for supervised classification algorithms. Cluster validity indices used for the measurement of cluster performance are classified into internal and external indices [214].

Internal indices usually assess the cluster performance based on information intrinsic to the data used while external indices are based on the prior knowledge about the data. As a result of this varied knowledge of the dataset used in training such clusters, internal indices can be used to dictate the best clustering algorithm suitable for the data as well as deciding on the optimal number of clusters while external indices are useful for deciding the best clustering method to employ for the dataset.

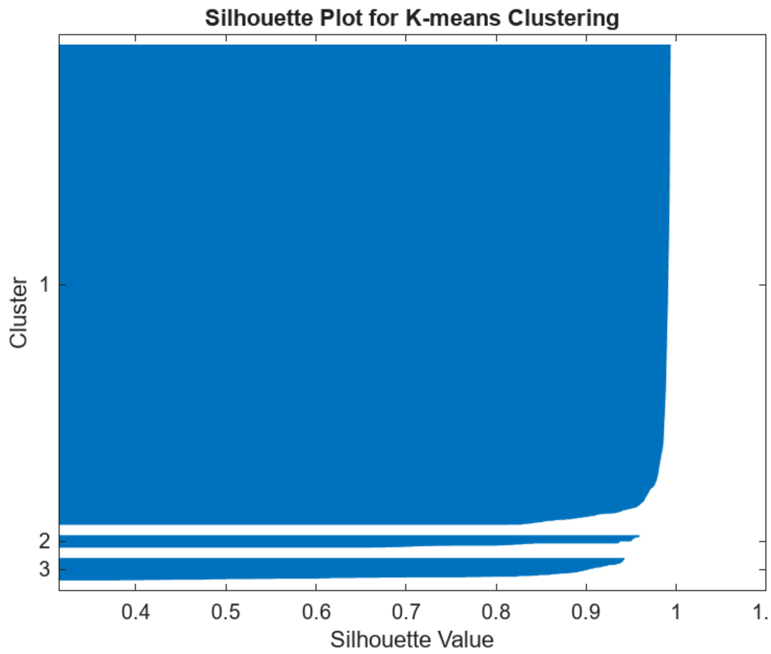

Figure 6.3-15. Silhouette score analysis of the K-means clustering with k = 3. Cluster 1 represent 'no cavitation', cluster 2 represent 'Inception cavitation' and cluster 3 represent 'full cavitation'.

To assess the performance of the clustering conducted in this study, the Silhouette Score was used. Silhouette scores are used to study the separation distance between the resulting groups of data after clustering. It ranges between [-1,1] where a score closest to -1 indicate a potential case of misclassification whereas a score of 1 indicate maximum distance between groups. A value of zero may indicate observations that lie in the separation boundary. Figure 6.3-15 shows a plot of the obtained silhouette score for the training of the model. The average Silhouette score of 97.8% was obtained indicating highly separated clusters which were visible prior to clustering.

This metric does not clearly indicate if the obtained clusters accurately portrayed the existing grouping in the data that was being investigated. Do the obtained clusters represent the failure cases under investigation? To answer this question further analysis was necessary. An accuracy score was computed as per Eqn. 6.3-1 to obtain the overall prediction accuracy of the model. This accuracy score compares better to the accuracies obtained from the supervised classification algorithms.

A validation accuracy of 43.92% was obtained which shows that, even though the clusters are well segregated, the clusters does not represent the failure condition that is under investigation in the current investigation. The data might inherently contain the observed clusters because of other pre-existing conditions which couldn't be associated with the cavitation states being investigated. Consequently, the application of this approach as part of predictive maintenance system would result in higher rates of false positives and false negatives leading to inability to reap the benefits that the system could potentially present to its benefactors.

6.3.4. Comparative Analysis of the Performance of the Developed Models

To compare the performance of the three developed supervised ML models an in-depth analysis featuring three more model performance metrics was conducted, alongside overall accuracy. These metrics include precision, recall and f1-scores. Precision measures the accuracy of positive predictions, while recall measures the model's ability to find all positive instances. These two metrics are aggregated into an F1-score, which makes it useful in cases of a trade-off between precision and recall.

Accuracy, $$Acc. = \frac{TP + TN}{TP + TN + FP + FN} \in [0,1] \quad (6.3\text{-}1)$$

Recall, $$Rec. = \frac{TP}{TP + FN} \in [0,1] \quad (6.3\text{-}2)$$

Precision, $$Pre. = \frac{TP}{TP + FP} \in [0,1] \quad (6.3\text{-}3)$$

F1-score, $$F1 = \frac{2\ \times P \times R}{P + R} \in [0,1] \quad (6.3\text{-}4)$$

Equations 6.3-1 to 6.3-4 describe the computation of Accuracy, Recall, Precision and F1-score respectively, for a binary classification problem. The variables TP, TN, FN and FP represent correctly predicted positive outcomes, correctly predicted negative outcomes, positive instances predicted as negatives and negative instances predicted as positives, respectively. In a multi-classification problem, a process of macro averaging is used to compute the values of this metrics, which is the mean of the values obtained when each class is considered individually as a binary classification problem.

Classification using decision trees demonstrated a strong capability with accuracy improving as tree complexity increases. The highest achieved accuracy was 99.66% for a fine decision tree with *'MaxNumSplits'* set to 100. While this complexity leads to improved classification, it also increases the training time. Misclassification was primarily observed in 'inception cavitation' due to what could be associated with errors in the methodology during experimental data collection, leading to indistinct separation criteria of 'inception cavitation' from either 'no cavitation' or 'full cavitation' conditions. However, the approach remains robust, particularly due to its interpretability and relatively efficient computation time compared to other methods.

On the other hand, the ANN based classification achieved highest overall performance with an accuracy of 99.86% with a bi-layered structure utilising the *ReLU* activation function. Misclassification rate remained low and slightly better than the decision tree model. The observed errors were attributed to possible overlap of classes during experimental observation. ANN offered a significant predictive power with no misclassification of 'full cavitation' cases as 'no cavitation', which could be detrimental to the reliability of a predictive maintenance system. The complexity of the ANN and its computational demands remains its disadvantage for adoption where there are resource limitations.

The SVM model demonstrated competitive performance with the best configuration using a Cubic Kernel function and a one-against-one multiclass coding strategy yielding a 98.6% accuracy. It showed robust classification performance but had notable misclassifications for the 'full cavitation' (0.2% as 'no cavitation) and 'inception cavitation' (4.6% as 'full cavitation'). While the SVM model provided competitive overall performance, the misclassification of 'full cavitation' condition as 'no cavitation' is a serious one especially when implemented as part of a predictive maintenance system. This could mean potential operation of the PAT in cavitating conditions for prolonged periods with no detection resulting in detrimental effects to hydraulic components.

Lastly, the unsupervised learning technique of K-means revealed the highest level of prediction inaccuracies of cavitation states in a PAT. Even though the cluster segregation abilities of the K-means method yielded higher performance scores, it failed to accurately group the individual observation according to their cavitation status. This means that the model could group the data as per other unknown intrinsic groupings in the dataset. With an overall prediction accuracy of 44.4% the model was deemed not suitable for application in a predictive maintenance system, as it won't provide the required safeguarding against unexpected failures.

Table 6.3-6. Summary of the performance parameters of the investigated approaches on Test Data

Metrics	Decision Tree	ANN	SVM	k-means
Accuracy (%)	99.66	99.86	98.60	44.44
Precision (%)	99.56	99.80	98.17	34.66
Recall (%)	99.47	99.89	97.70	33.68
F1-score (%)	99.52	99.84	97.93	24.87
Training Time (s)	9.16	16.91	15.56	0.026
Misclassification Cost	'Inception cavitation'	'Inception cavitation'	'Full cavitation'	'Full cavitation'
Interpretability	By-design	Post-hoc	Post-hoc	By-design

Table 6.3-6 presents a summary of the conducted performance evaluation of the investigated approaches with misclassification cost and interpretability referring to the obtained worst-case misclassification and the ease of understanding how classifications were made, respectively. The ANN model was the most accurate approach, but it requires more computational resources, making it suitable for scenarios where precision is key. On the other hand, the decision tree model offers an optimal balance between accuracy and efficiency, making it an attractive option for real-time applications.

The misclassification cost for the SVM is very high as it misclassifies the most destructive of the conditions that could be detrimental to machine operation. This is evidenced by the lowest F1-score between the supervised machine learning models. However, focusing on the unsupervised technique of k-means, the low predictive accuracy is also characterised by very low F1-score indicating the inability of the k-means model to classify observations accurately. As such it is recommended that a complementary adoption of both ANN and decision trees in a predictive maintenance system would be more beneficial with the ANN offering reliability in predictions while the decision tree used to validate its findings while also offering the potential of understanding how predictions were made.

6.3.5. Proposed Hybrid Machine Learning-based Diagnostic Framework

While predictive performance is critical in a maintenance system, model interpretability plays an equally important role in supporting transparent decision making and enabling root cause analysis. Among the models assessed, the DT offers intrinsic interpretability by producing a set of hierarchical rules that map input features to cavitation states. These rules can be visualised and traced back, providing clarity on which features triggered a classification, making the DT particularly valuable in diagnostic context.

In contrast the ANN model, although highly accurate, behaves as a 'black box' model with complex non-linear transformations that obscure the decision path. This lack of transparency can limit its utility in failure investigations or regulatory audits, even if superior in performance. To address the trade-off between accuracy and interpretability a hybrid framework, presented in Fig. 6.3-16, is proposed that integrates a DT for model interpretability and ANN for reliability.

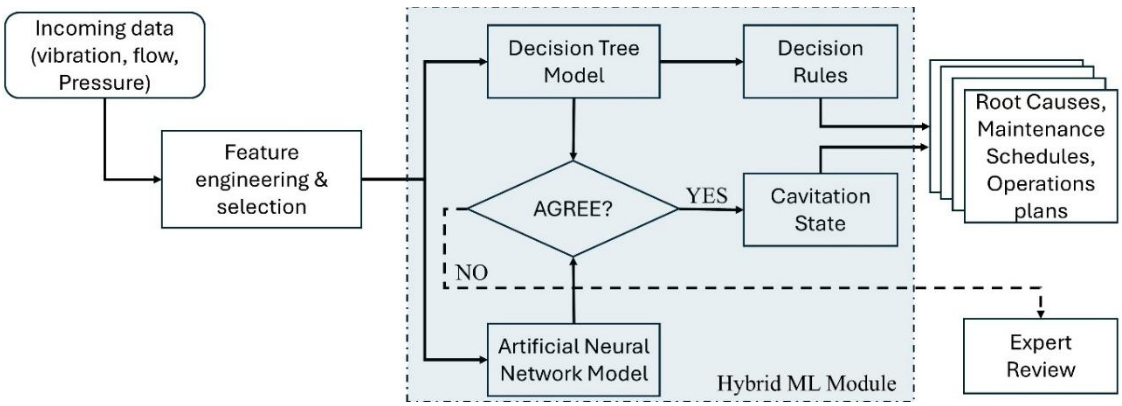

Figure 6.3-16. Flowchart of the proposed hybrid ML framework combining Decision Tree and ANN models for cavitation diagnosis

In this framework, the incoming raw vibration data from accelerometers coupled with operational data undergoes feature engineering in the feature extraction module. This is where useful features are extracted, normalised and organised into a desirable format for ML. The feature vector will then be routed through both models simultaneously for classification. The output from the models will then be compared and if in agreement, the prediction is accepted and the DT's decision path is used to generate rules for interpretability, otherwise the case is flagged for further expert analysis as this might indicate a boundary condition or previously unseen occurrence in the machine.

This hybrid approach enhances confidence in predictions, supports post prediction activities and enables traceable and auditable diagnostics that is essential for predictive maintenance deployment. A key benefit is that the DT model's decision logic can help maintenance teams understand the rationale behind failure classification and identify contributing operational patterns for long-term improvement strategies.

6.3.6. Limitations of developed ML models

The developed ML models presented in the prior sections were trained and validated using vibration data obtained from a single PAT operating under controlled laboratory conditions. While the resulting classification performance is strong within this domain, this training context introduces important limitations around model generalisation and robustness when applied to different geometries or noisier environments. It's important for these limitations to be explicitly recognised when interpreting predictive performance and considering real-world deployment.

A principal concern is domain shift, meaning the statistical properties of vibration signals may change when the model is applied to a different machine or environment from the one used for training. PATs vary widely in impeller geometry, blade count, volute design, operational speeds, mounting configuration and hydraulic operating ranges. These differences influence flow structures, cavitation dynamics and vibration transmission paths. As a result, the feature patterns learned by the ML models in this study may not remain invariant across machines. Features that are highly discriminative in the laboratory PAT setup may lose separability or shift in scale in another setup, leading to degraded classification accuracy.

In addition to machine variability, environmental and operational noise in industrial settings can significantly affect model performance. Laboratory measurements benefit from controlled conditions, minimal background noise, stable operating conditions and high-quality sensor mounting. In contrast, field installations often include multiple concurrent vibration sources, hydraulic transients, electrical noise and other disturbances. These factors can contaminate feature measurements, reduce signal-to-noise ratio and increase class overlap thereby reducing model performance and increasing misclassification cases.

There is also a potential issue of overfitting to machine specific signatures. Even when cross-validation performance was high, models may potentially learn characteristics unique to the specific test rig rather than purely cavitation related features. Such characteristics include structural resonances, sensor mounting discrepancies and drive system harmonics. This can inflate apparent performance while reducing transferability.

6.3.7. Requirements for successful field deployment

To improve robustness and generalisation capability, several key steps would be required for future development and deployment. First, a multi-conditions dataset obtained from various PATs should be developed. Collecting labelled data from multiple PAT sizes, geometries and installations would allow models to learn invariant cavitation features rather than machine specific patterns. Dataset diversity is the single most important factor in improving generalization. This could be initiated using a demonstration site where models would be updated continuously as new dataset that is not from controlled setup comes in.

Another step would be to ensure that feature normalisation and physics-informed features are prioritised. Non-dimensional or speed normalised features, frequency ratios relative to shaft speed and energy ratios across bands are more transferable than raw amplitude features. Features grounded in physical behaviour are more likely to remain stable across machines. Alternatively, domain adaptation and transfer learning techniques should be applied. Rather than training each model from scratch, pretrained models can be adapted to new PAT installations using smaller labelled datasets. This could reduce data requirements while preserving learned structure.

Moreover, online or continual learning frameworks could be implemented. Gradually updating ML models using confirmed field data can make them adaptable to machine ageing, sensor drift and changing operating conditions. This alongside standardization of sensor used, mounting methods, sampling rates and preprocessing pipelines would reduce variability and improve model compactness.

Further robustness could be obtained from combining physics-based indicators with ML outputs. If ML predictions are constrained or crosschecked by physically interpretable indicators such as cavitation numbers, pressure fluctuation thresholds or statistical deviation metrics such as the modified DND proposed in the previous chapter of this thesis, the overall diagnostic reliability increases.

6.4. DISCUSSIONS

6.4.1. Impact of Visual Observation-based Classification of Cavitation States

The machine learning (ML) models developed in this chapter rely on labelled datasets in which cavitation states were defined based on visual observations as described in Section 5.3. While this approach is common in experimental studies of cavitation, it introduces potential sources of error that can directly influence model training, validation and performance interpretation. Visual classification is inherently subjective, particularly near the thresholds of '*inception cavitation*' and '*full cavitation*', where vapour structures appear intermittently and with low intensity.

In such cases, data segments labelled as '*no cavitation'* may contain '*inception cavitation'* cases, while segments labelled '*inception cavitation*' may still largely reflect '*no cavitation'.* In the case of later stages of cavitation, the boundary between *'inception cavitation'* and '*full cavitation'* may be blurred. This uncertainty may introduce noise in the ground truth, thus limiting the maximum achievable accuracy of supervised ML models regardless of model complexity. It can also lead to increased overlap in feature space between adjacent classes and reduce classification confidence, especially for simpler or more interpretable models such as Decision Trees.

Another effect of relying on visual observations for classification of cavitation stages is potential bias in validation results. If the same observer is responsible for both classification and interpretation of results, there is a risk of a confirmation bias, where model performance appears strong because it aligns with subjective classes rather than objective physical states. In addition, standard performance metrics such as accuracy or F1-score may overestimate model reliability if ambiguous cases are consistently classed in a particular way.

Temporal variability in cavitation further complicates model training. Cavitation may fluctuate over time at a fixed operating point, meaning that vibration data segments collected under nominally identical conditions may correspond to different physical states. If visual classification does not fully capture this variability, the ML model may learn inconsistent mappings between features and classes, potentially reducing generalisation capability.

Despite these limitations, several aspects of the study mitigate the impact of subjectivity on the ML results. First, cavitation was classified into broad well-separated categories with each class covering a wide range flow rates, rather than finely graded states. This reduces sensitivity to marginal classification errors and aligns with the practical objective of fault detection rather than precise cavitation quantification. The consistency of ML results across multiple models also provides indirect validation of the classes. The fact that different algorithms converged to similar classification trends suggests that the vibration features captured genuine physical differences over artefacts of subjective classification groups.

Moreover, the use of ML itself can be viewed as a robustness test of the classes. High classification accuracies, particularly for '*full cavitation'*, indicates that these classification groups are strongly and consistently represented in the vibration data. The reduced performance typically observed near *'inception cavitation'* is therefore not a failure of the ML models, but a reflection of the inherent ambiguity in the physical phenomenon and its visual identification.

Nevertheless, the reliance on visual observations to label cavitation stages remains a limitation, particularly for model generalisation beyond the laboratory environment. Models trained on visually determined classes may implicitly encode observer specific criteria, which could limit transferability to other test rigs or field installations. This highlights the need for more objective cavitation state classification strategies in future work, such as high-speed photography-based cavitation quantification, pressure-based indices or unsupervised approaches that reduce dependency on subjective cavitation classes.

6.4.2. Comparison with Traditional Approaches

While traditional signal processing or threshold-based methods have been used for decades in the detection and diagnosis of machine defects, they seem to possess some shortcomings that can be resolved through the adoption of ML based solutions such as the approach proposed in this work. Thresholding techniques typically rely on predefined limits applied to features such as overall vibration or Root Mean Square value, Peak amplitude or spectral content. Though these methods are computationally efficient and straight forward to implement, they present limitations in terms of adaptability, sensitivity to early-stage faults and scalability.

In contrast the proposed framework aggregates several of these condition features and create models that are responsive to even slight changes of each of the variables that the models deem important. This means that instead of creating separate models for each monitored variable, which could be the approach of traditional signal processing-based techniques, the proposed framework could be adopted ensuring that all variables are taken into consideration. Traditional signal processing-based techniques create a segregation between detection and diagnosis functions, which they are unable to conduct simultaneously. The monitored variable would be compared against set thresholds which when exceeded an alarm is triggered. This prompts experts to conduct further analysis, requiring more and more use of traditional signal processing techniques. This whole process can be time consuming and costly in cases where the equipment operator is dependent on external contractors for such services.

In comparison, the proposed framework combines the detection and diagnosis functions into a single task thus ensuring that whenever an anomaly is detected, the possible causes of the observed change are provided thus eliminating time wastage. Practically, this means that for an equipment operator who does not have an inhouse maintenance expertise with proven knowhow of conducting in-depth analysis of machine condition data, focus can switch to carrying out or scheduling the required maintenance task immediately.

Furthermore, the hybrid nature of the proposed framework ensures both reliability and interpretability of predictions made. Agreement between the two approaches implies confidence in classification whereas disagreement prompts further investigation. The capability of obtaining further insights from the devised decision rules from the DT model quickens the troubleshooting and root cause analysis exercises if activated. Moreover, as more data becomes available the system can be retrained keeping tabs with changing machine dynamics while enabling continuous improvement.

In the development of the proposed approach, sensor data from all installed sensors in the machine are aggregated together to build robust models that comprehensively describe the machine overall dynamics. This strengthens the model's prediction ability as predictions are not based on the response from a single sensor fixed at a single measurement location. Utilizing both time-domain and frequency -domain signals enable the developed models to leverage the diagnostic strengths of these signals, thereby improving their overall predictive performance.

6.4.3. Implications for Hydropower

The presented framework highlights the benefits that machine learning algorithms can present as part of predictive maintenance systems in digitalization of hydropower. By leveraging the data manipulation and learning abilities of various machine learning algorithms, high accuracy models can ensure early detection of cavitation related issues, reducing operational risks and enhancing hydropower system reliability. With less requirement for high performance computational resources, algorithms such as decision trees can provide rapid insights that could help in improving efficiency and benefitting fully from real-time monitoring.

For superior performance and applications that require precision, application of approaches such as ANN is advisable as part of deep learning-based digitalization efforts while facilitating automated fault detection and diagnosis. Since a machine learning approach is usually accompanied by its own advantages and disadvantages, the integrated approach where two or more models are adopted to complement each other is plausible. In the current case, combining ANN and decision trees could optimise the predictive maintenance function while ensuring scalability. ANNs can be focused on obtaining precise predictions while the use of decision trees could be about bringing transparency and explainability of predictions.

Furthermore, the proposed hybrid approach provides a practical template for integrating interpretable machine learning models into hydropower operations, enabling not only real-time fault detection but also informed intervention, auditability and trust in digitalized systems. Interpretability enables users to understand which signals or features are influencing the model's conclusions reducing scepticism and promoting adoption. Maintenance engineers and operators need to trust that the diagnostic system is making accurate and reliable predictions about equipment health. Thus, a black box model that flags 'fault detected' isn't enough, what is important is why it happened and what component or parameter is affected.

6.4.4. Future needs in Hydropower Digitalization

Although this study focused on the application of supervised machine learning models for cavitation in PAT systems, it represents only an initial step toward the broader vision of fully digitalized hydropower infrastructure. Future research and system development should increasingly consider the integration of Artificial Intelligence (AI), Digital Twins and Industrial Internet of things (IIoT) to realise intelligent autonomous and adaptive hydropower systems.

A digital twin is a virtual representation of a physical asset, continuously updated through real-time sensor data. By integrating operational data with physics based or data-driven models, digital twins enable continuous monitoring, simulation and optimization of system performance. This enables more accurate and timely diagnosis of equipment health issues including cavitation and other degradation phenomena across the asset's lifecycle. The IIoT serves as the backbone of this architecture by enabling scalable and seamless data acquisition from distributed sensors, actuators and control systems within a hydropower facility. IIoT technologies support real-time connectivity, secure data exchange and remote access, enhancing responsiveness and intelligence of digital twin ecosystems.

The integration of AI with digital twins and IIoT represents a significant evolution in predictive maintenance, from scheduled inspections to continuous, self-optimizing monitoring systems. These systems cannot only detect anomalies but can also learn from operational data to recommend or automate corrective actions. This integration holds immense potential for both large-scale hydropower plants and decentralized micro-and pico-hydropower installations, addressing the increasingly dynamic nature of modern power systems. Looking ahead, current ML-based condition monitoring systems will need to be embedded within digital twin and IIoT frameworks. This will unlock the next generation of predictive, adaptive and self-aware smart hydropower systems.

6.5. SUMMARY

This chapter analysed the frequency content of the acquired vibration signals to assess the spectral features that are a result of the occurrence of cavitation in a PAT. Spectral analysis of the acquired vibration signals was divided into low and high-frequency range to allow use of the most suitable signal type for each of the ranges. To analyse low frequency range of 0 to 1 kHz, the vibration signal was converted into velocity due to its sensitivity to changes in the signal on this range, while vibration acceleration was used to analyse frequency content in the range above 1kHz up to the Nyquist frequency.

The results for the low-frequency analysis of the vibration signal revealed a frequency component at half the fundamental frequency at all operating speeds. The magnitude of this component showed a slight increase as the system approached 'full cavitation'. However, this component remained lower in magnitude than several other dominant rotating speed related harmonics, displaying a similar characteristic to the one observed for numerically obtained pressure pulsations in Chapter 4. In the high frequency, the observed high energy frequency regions are associated with system resonances.

These observations highlighted both the potential and limitations of frequency-based approaches for universal cavitation diagnosis in PATs, reinforcing the need for complementary approaches to cavitation detection and diagnosis. Without a clear generalizable frequency component from the spectral analysis, the use of machine learning methods was adopted as a complementary alternative for diagnosis of cavitation in PATs utilising the data acquired under various cavitation states.

Three Machine Learning (ML) algorithms of Decision Trees (DT), Artificial Neural Networks (ANN) and Support Vector Machines were investigated for their applicability in a predictive maintenance framework aimed at the detection and diagnosis of cavitation in PATs. Among these, the ANN model demonstrated the highest predictive accuracy, making it particularly well-suited for high precision maintenance applications where early fault detection is critical. The DT model, while slightly less accurate, offered strong interpretability of its predictions, making it a valuable complementary model to ANN for explainability purposes. In contrast, the SVM model also produced competitive accuracy, however, it incurred a higher misclassification cost, which poses a risk to the safe and reliable operation of hydropower equipment.

To maximize the strengths of each model, a hybrid diagnostic framework was proposed. The approach combines the predictive power of ANNs with the interpretability of DT's, enabling both accurate and explainable cavitation diagnosis. The hybrid model was designed to enhance reliability in fault prediction while ensuring that operators can understand and trust the system outputs.

The implications of these findings extend to the modernization of hydropower plants, where digitalization is key to improving efficiency and sustainability. By implementing machine learning driven predictive maintenance strategies, operators can proactively address failures, thereby enhancing system performance while supporting the global transition towards a resilient and sustainable energy infrastructure. Future research should explore real time deployment of these models and the integration of additional operational parameters.

While the proposed approaches achieved high performance for cavitation diagnosis in a Pump-as-Turbine system, several limitations exist. The models were developed using data from a single system and have not yet been validated in real-time or across different machine installations. Additionally, despite the ANN model's superior accuracy, it lacks interpretability without post-hoc explanation. Moreover, the assumed static operating conditions could limit adoption in dynamic environments. Addressing these limitations in the future would help enhance model robustness, trustworthiness and scalability in practical hydropower applications.

7. DEVELOPMENT OF A SOFTWARE PLATFORM FOR PREDICTIVE MAINTENANCE

7.1. INTRODUCTION

The growing need for reliable and efficient small-scale hydropower systems alongside the emergence of a highly dynamic electric grid, driven by variable output renewable energy sources, has amplified the adoption of Pump-as-Turbine (PAT) systems. These systems are favoured for their cost-effectiveness, adaptability and applicability to new application areas that make new hydropower projects feasible. However, the increasing variability in energy demand has led to frequent operation at off-design conditions, exposing the equipment to mechanical and hydraulic phenomena such as cavitation. Cavitation, if undetected, not only degrades performance but also threatens the structural integrity of equipment, thereby raising operation and maintenance challenges.

As digitalization continues to influence asset management practices, the integration of intelligent condition monitoring and predictive maintenance solutions has gained significant research attention. Various system architectures for predictive maintenance have been proposed in the literature, often comprising modular designs that enable data acquisition, analysis and decision-making. For instance, Gupta et al. [215] conducted a comprehensive review of intelligent Predictive Maintenance 4.0 architectures, highlighting a critical gap in the explainability of the applied analytical techniques.

Similarly, Cachada et al. [216] presented a layered architecture consisting of data collection, data analysis, dynamic monitoring and intelligent decision support modules. Syafrudin et al. [217] developed a real-time monitoring system for manufacturing processes using IoT sensors, big data platforms (Apache Kafka, Apache Storm and MongoDB) and a hybrid prediction framework integrating DBSCAN for anomaly detection and Random Forest for fault classification. Other notable contributions include Bouabdallaoui et al. [218], who introduced a machine learning-base predictive maintenance framework comprising five blocks, data collection, processing, model development and continuous model development. This framework leveraged IoT-enabled data collection from HVAC systems and deployed deep learning for predictive diagnostics.

Likewise, Lee et al. [219] designed an architecture for cyber-physical production systems structured around big data analytics, real-time detection and KPI-driven simulation, each handling storage, monitoring and performance analysis, respectively. Within the hydropower domain, Selak et al. [220] proposed a condition monitoring system for hydropower plants based on an industrial product-service system approach, emphasizing stakeholder accessibility to diagnostic information. More recently, Jad et al. [221] introduced a machine learning-based methodology for detecting and characterising long-term degradation in hydro generators. Their system, structured in alignment with ISO 13374:2003, organises data flow into sequential modules for observation, analysis and action.

In-depth examination of these contributions reveals that the most effective predictive maintenance architectures are those grounded in standards like the ISO 13374:2003, which define a structured flow of information from raw data acquisition through to actionable decision support. The same principle has guided the development described in this chapter.

Previous chapters have explored cavitation in the context of PATs and developed approaches for its detection and diagnosis using both time domain vibration signals and machine learning techniques for real-time application. Building upon these findings, this chapter focuses on the development of a dedicated software platform that integrates both the experimental insights and ML-based diagnostic capabilities into a unified framework for predictive maintenance. The platform is intended to serve as a practical decision-support tool, offering real-time monitoring, automated cavitation detection and be used for post anomaly detection data analysis. It bridges the gap between laboratory-scale analysis and field-deployable solutions by embedding trained models into a user-accessible interface.

The chapter outlines the platform architecture, key functionalities and the implementation workflow of various methods presented in this thesis. In doing so, this chapter addresses the fourth and final research objective, laying the groundwork for digitalised condition monitoring solutions tailored to the unique operational context of PATs in micro- and pico-hydropower systems.

The codes and the associated files for the developed software platform can be accessed at: https://drive.google.com/drive/folders/1K0b_hsCwZ8AeOyGJOOLuQrYuXVGTYNiS?usp=drive_link

7.2. SOFTWARE ARCHITECTURE

The software platform is organised into four main functional layers i.e., the Data Acquisition layer, Data Processing Layer, Machine Learning & Diagnostic layer and the Health Monitoring layer. These layers are supported by a centralised database and storage system to ensure seamless data handling across the platform. The architecture has been developed in alignment with the data processing and information flow requirements outlined in ISO 13374:2003. This standard defines the data flow process from sensor-level data acquisition through to advanced prognostic analysis and the generation of actionable advisories.

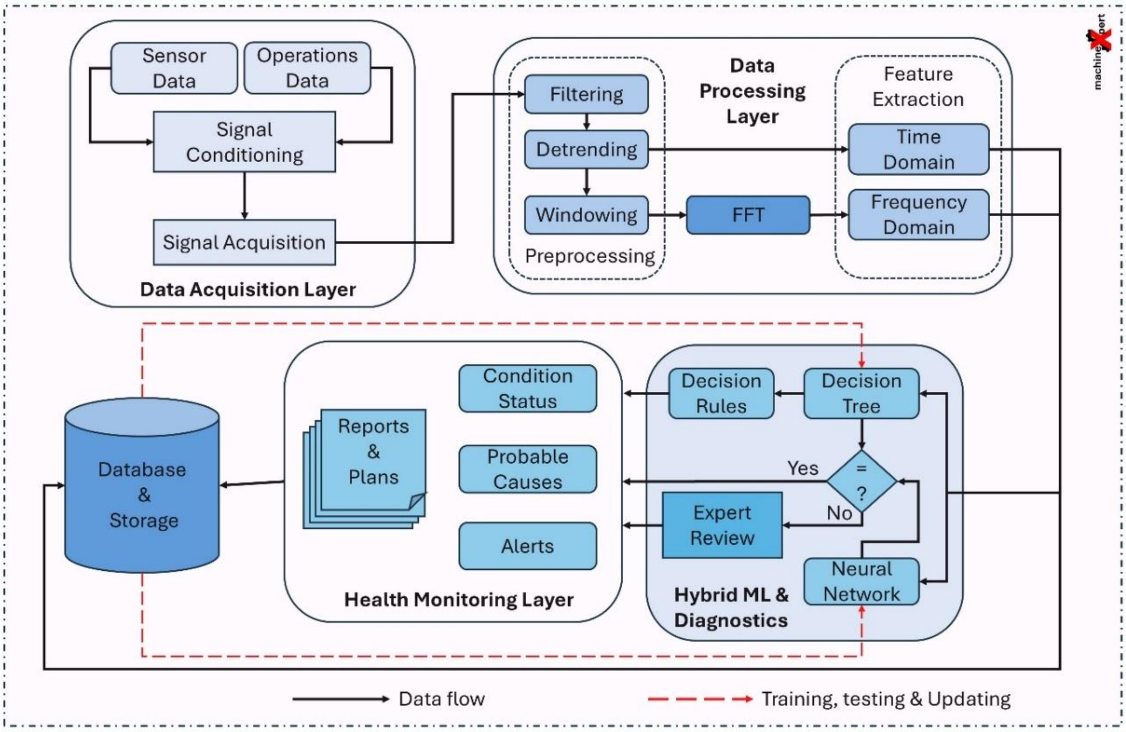

Figure 7.2-1. Overall system architecture and data flow between layers

Figure 7.2-1 illustrates the overall system architecture and the data flow between the various layers. A detailed explanation of each layer's function is provided in the subsequent sections. The software platform was implemented using MATLAB App Designer, selected for its effective integration capabilities and compatibility with the models and techniques developed throughout this thesis. MATLAB served as the primary programming and numerical computing environment during development.

7.2.1. Data Acquisition Layer

This layer is responsible for collecting and conditioning raw input data from the PAT system and consists of the following functional blocks:

- Sensor Data – This primarily covers vibration signals acquired through wired accelerometers
- Operational Data – Pressure and flow measurements obtained from the transducers installed in the PAT. These parameters are important in understanding the amount of energy the machine is receiving and its conversion efficiencies.
- Vibration sensors need to be powered and their output signals typically require amplification and conditioning. This functionality is provided by the signal conditioning units to which the accelerometers are connected. Similarly, operation data also undergoes necessary conditioning to ensure signal integrity.

The Data Acquisition function is responsible for capturing these conditioned signals at appropriate sampling frequencies and collecting enough samples to support subsequent processing and analysis stages.

7.2.2. Data Processing Layer

Incoming data from the Data Acquisition functional block is sent into the Data Processing Layer where it undergoes the following preprocessing steps that readies the data for data analysis:

- Filtering – this involves removing frequency content below or above certain thresholds that might not be of interest in the analysis or might be considered as noise to the signal.
- Detrending – removes the DC offsets and slow drifts in the signal
- Windowing – incoming signal is divided into temporal segments and window functions are applied to each segment to reduce discontinuities at the boundaries. This process helps minimize spectral leakage by tapering the signal smoothly to zero at the edges, thereby limiting the spread of energy into adjacent frequency bins in the frequency spectrum.

The FFT functional block computes the spectrums that ensures the frequency content of the signal is identifiable. This helps extract spectral features and in the manual diagnosis of the signals. The frequency domain data in the form of spectrums will then be transferred into the feature extraction module where spectrum features are extracted that are of importance in machine learning. Moreover, the detrended signal is also used to compute time domain features including the DND to create a complete feature matrix for the condition under investigation.

7.2.3. Machine Learning and Diagnostics Layer

This layer serves as the core analytical component, responsible for predicting the condition of the PAT system using a hybrid machine learning framework that combines a Decision Tree model and an Artificial Neural Network (ANN). This combination aims to balance model accuracy with interpretability. In addition to real-time predictions, this layer handles the training and updating of models when required. Retraining becomes necessary when system dynamics evolve over time due to factors such as changing operating conditions, material accumulation or material degradation, all of which can affect machine behaviour and failure patterns.

The Decision Tree functional block is responsible for the training, updating and testing of the Decision Tree classification model. It also derives interpretable decision rules based on the tree structure, which are useful in supporting root cause analysis. Similarly, the ANN functional block is also responsible for the training, updating and testing of the ANN classification model. While the ANN provides high classification accuracy, the Decision Tree model offers competitive classification accuracy along with transparent, rule-based predictions for interpretability. The outputs from both models are evaluated using the decision logic, any discrepancies between the predictions are flagged for expert review, ensuring robust and reliable decision making.

7.2.4. Health Monitoring Layer

This layer is responsible for interpreting classification results and delivering actionable insights for both operators and maintenance personnel. Predictions are visually presented, enabling easy comparison against predefined thresholds. The Condition Status functional block indicates the current severity of cavitation, while the Probable Causes functional block identifies the likely underlying cause based on decision rules extracted from the decision tree model.

Within this layer, parameters for automated data acquisition are configured, enabling continuous monitoring even without operator supervision. Once the acquisition frequency is set, the platform autonomously collects, analyses and evaluates incoming data against preset thresholds. It also determines whether each data sample should be stored based on its relevance. If any monitored condition parameter exceeds its defined limit, alerts are automatically triggered. Additionally, users can export selected analysis images directly into formal reports to support the conclusion of an analysis task.

7.2.5. Databases & Storage

All raw signals selected by the user for storage, along with extracted features, models' predictions and expert review outcomes are stored in a centralised database. This component supports several key functions:

- Trend analysis of historical machine health
- Tracking of the machine learning models
- Continuously learning and retraining workflows

Currently, the centralised database is implemented using a Microsoft Office Excel workbook, with different worksheets designated for specific data types. The 'conditionData' worksheet stores information related to the monitored machines such as vibration sensor details, installation locations and acquisition devices. Similarly, operational parameters and sensor details are documented in the 'OpsData' worksheet.

To maintain a balanced dataset within the feature matrix, confirmed instances of faulty conditions are added to the 'featureMatrix' worksheet, replacing a portion of the 'no cavitation' entries. This approach ensures the feature matrix remains current and representative of the system's true operating conditions. The matrix size is kept constantly updated, with older entries being replaced by newer ones, allowing the most recent data to be used for updating and retraining the machine learning models.

7.3. ANALYSIS WORKFLOW

The graphical user interface of the software consists of four tabs each implementing a single or multiple of the functional layers presented in the earlier section. These tabs are described in full in this section with an overview of the steps a user would take to conduct an analysis.

7.3.1. Acquisition Setup Tab

This tab ensures implementation of the Data acquisition layer of the software. At startup of the software platform this is the first tab that the software opens, presenting the user with an opportunity to setup parameters for a data acquisition task and later analysis. Figure 7.3-1 illustrates the interface of the Acquisition Setup Tab.

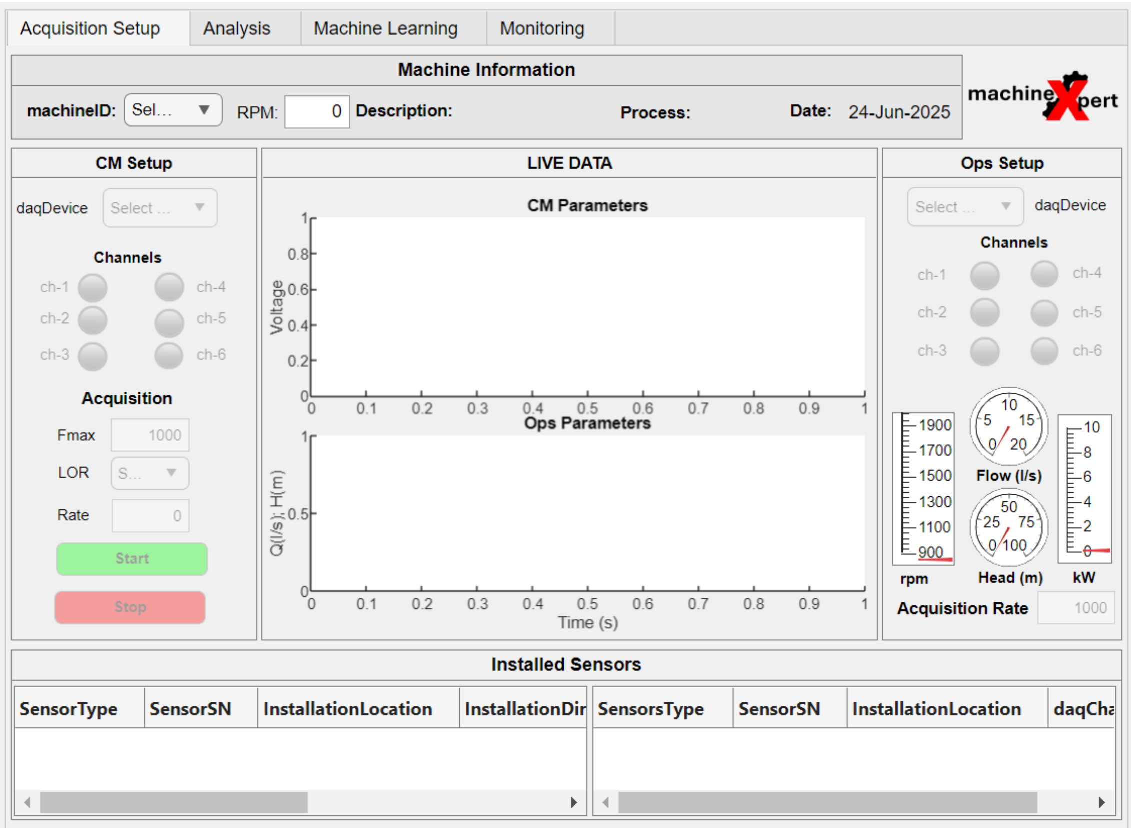

Figure 7.3-1. Graphical User Interface of the Acquisition Setup Tab of the Software

Machine Information Panel

Once vibration sensors are installed on key piece of equipment the 'ConditionData' worksheet is updated with information such as machineID, description, Process, DAQ Device connected, Sensors used and their serial numbers, their installation location, installation orientation, what channel each sensor is connected to, the output range for the channel and the terminal configuration. The first information required when the software platform is used is the machine ID, which is a unique number assigned to all equipment that are monitored in a plant setup.

This is presented as a dropdown menu, which gets automatically populated with the unique machineID's from the 'ConditionData' worksheet. When a machineID is selected, the machine operating speed (rpm), its description, the process it is connected to, and the current date, are automatically populated. A summary of installed sensors, both condition monitoring and process monitoring, is also presented at the 'Installed Sensors' section in a table format. This will then enable the DAQ Device Setup panels in the software.

Data Acquisition (DAQ) Device Setup Panels

The DAQ Device Setup panels allows the user to select the correct data acquisition device for each parameter being monitored. It is divided into two functions namely, condition data monitoring and process data monitoring. The two functions are separated because in most cases acquisition of process data is already available in the machine control system [220] and the acquisition of condition data requires high sampling frequencies which might be unnecessary for operations data monitoring. The setup section for the condition data monitoring is on the left DAQ Device setup panel while the operation data monitoring panel is on the right-hand side. Once the correct DAQ device for each is selected it is followed by the illumination of LEDs signalling the number of signal channels connected for each of the two functions.

The panel for setting acquisition parameters will then be activated where the user will input the 'Fmax' parameter, select the 'LOR' parameter and input the operational data 'Acquisition Rate' parameter. The 'Fmax' parameter allows the user to set the maximum frequency while 'LOR' dictates the number of lines of resolution required in the spectrum plots in the Analysis Tab. The 'Fmax' parameter is used to compute the acquisition 'Rate' parameter for condition data. Once these parameters are selected, the start and stop button will be enabled allowing it to be pushed to start and stop broadcasting of data, respectively.

Live Data Panels

Once the 'Start' button is pushed, live sensor data from the condition data monitoring function is plotted in real-time in the 'CM Parameter' plot area while the live sensor data from the operations data monitoring function is plotted in the 'Ops Parameters' plot area. This provides an indication that sensors are connected and are acquiring data as required. The instrument panel on the right will also provide an indication of machine speed (rpm), the head, flow rate and power its generating. Pushing the 'Stop' button cancels and resets all the current setup meaning that a restart of the whole process is necessary to acquire data.

7.3.2. Analysis Tab

Once the 'Acquisition Setup Tab' is completed and an acquisition session running the 'Analysis Tab' is enabled to allow user interaction allowing various frequency domain data analyses for understanding the signal's frequency content and probing for any potential causes of detected anomalies in the system. The graphical user interface of the 'Analysis Tab' is presented in Fig. 7.3-2 indicating the various panels it consists of. The Analysis Tab implements the functionality of the data processing layer of the software.

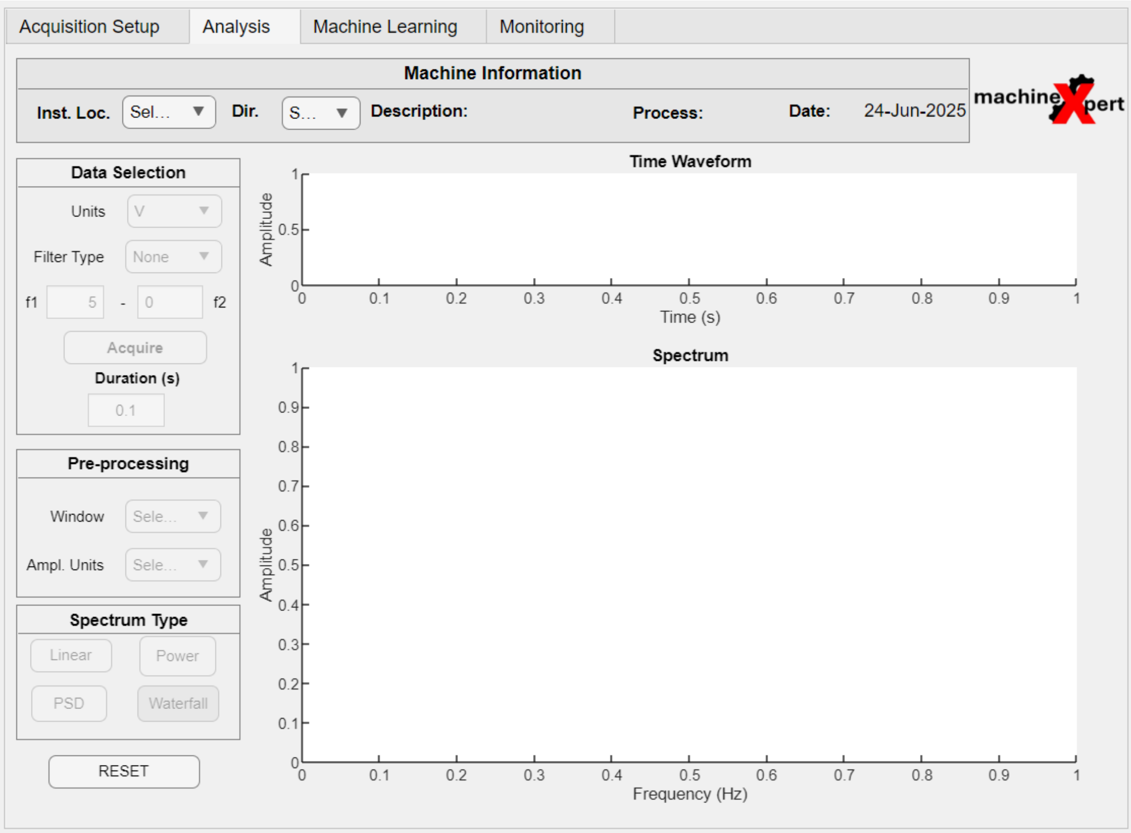

Figure 7.3-2. Analysis Tab of the Developed Platform's Graphical User Interface

Machine Information Panel

The machine information panel presents similar information from the one in the 'Acquisition Setup Tab' except for the 'Inst. Loc.' and the 'Dir.' dropdown menu. This allows the user to limit the analysis to specific sensors installed at a specific location i.e., outlet flange, non-drive end bearing, machine housing etc., allowing a more directed analysis. If no option is selected, data for all condition monitoring sensors installed in the machine is presented.

Data Selection Panel

The 'Data Selection Panel' allows for selection of the preferred units of measurement used between volts, g's, m/s^2 and mm/s. Acceleration data from accelerometers is acquired in the units of Volts (V) and are then converted to the preferred units as per the dropdown menu. This is followed by the selection of the type of filtering process dictated by the cut-off frequencies 'f_1' and 'f_2'. The available options are low-pass, high-pass and band-pass filters where the former two uses only the value of 'f_1' and the latter uses both 'f_1' and 'f_2' for the lower and upper cutoff frequencies, respectively. Pushing the 'Acquire' button captures data samples equivalent to the time value given in the 'Duration' field for analysis. The 'Duration' value is computed from the 'LOR' and the

‘Fmax’ parameters set in the ‘Acquisition Setup Tab’. The filtered data will then be plotted in the ‘Time Waveform’ plot area.

Preprocessing Panel

The acquired data from the ‘Data Selection’ panels is then used in the ‘Pre-processing’ panel where it is windowed using the selected ‘Window’. The available window options are the ‘Hanning’, ‘Hamming’, ‘Rectangular’ and ‘Flat Top’. Different window functions offer trade-off between main lobe width (frequency resolution) and side lobe suppression (leakage reduction). Therefore, allowing users to select from various window types enables the system to be optimised for different diagnostic scenarios, whether the goal is detecting closely spaced frequencies, minimizing leakage or preserving amplitude accuracy.

This flexibility is particularly important in vibration analysis for cavitation detection, where subtle frequency changes may indicate early fault conditions. Selection of any of these window functions ensures that each of the data segment used in the FFT computation of an averaged spectrum is tapered smoothly at the edges to reduce discontinuities at the boundaries, hence minimizing spectral leakage and limiting the spread of energy into adjacent frequency bins in the frequency spectrum. The ‘Amplitude Units’ selection helps the user decide whether the amplitude is presented as ‘Peak Amplitude’ or ‘RMS Amplitude’ depending on the analysis being conducted.

Spectrum Type Panel

Finally, the spectrum type group allows the user to select the type of frequency plot to display in the ‘Spectrum’ plot area. Each of the spectrum types of ‘Linear’, ‘Power’ and ‘PSD’ implements the windowed Fast Fourier Transform (FFT) with five averages to eliminate potential spurious frequency peaks. The ‘Waterfall’ presents a variation of the observed ‘Linear’ spectrum with similar spectrums obtained over time to allow identification of potential initiation and progression of faults. The ‘RESET’ button resets all the changes conducted in this tab including deleting the data temporarily stored for testing in ‘Machine Learning’ Tab.

7.3.3. Machine Learning Tab

Figure 7.3-3 presents the graphical user interface (GUI) for the ‘Machine Learning’ Tab of the developed software platform. The main function of this tab is the implementation of the Machine Learning (ML) & Diagnostics layer of the software architecture. Machine Learning models are developed and used for classification to analyse machine health status. Most importantly this is where the hybrid machine learning framework proposed on this thesis is implemented allowing both the precision in accuracy and interpretability of fault predictions. Just like the previous tabs the ‘Machine Information’ Panel of this tab populates when the ‘machineID’ is selected at the ‘Acquisition Setup’ Tab.

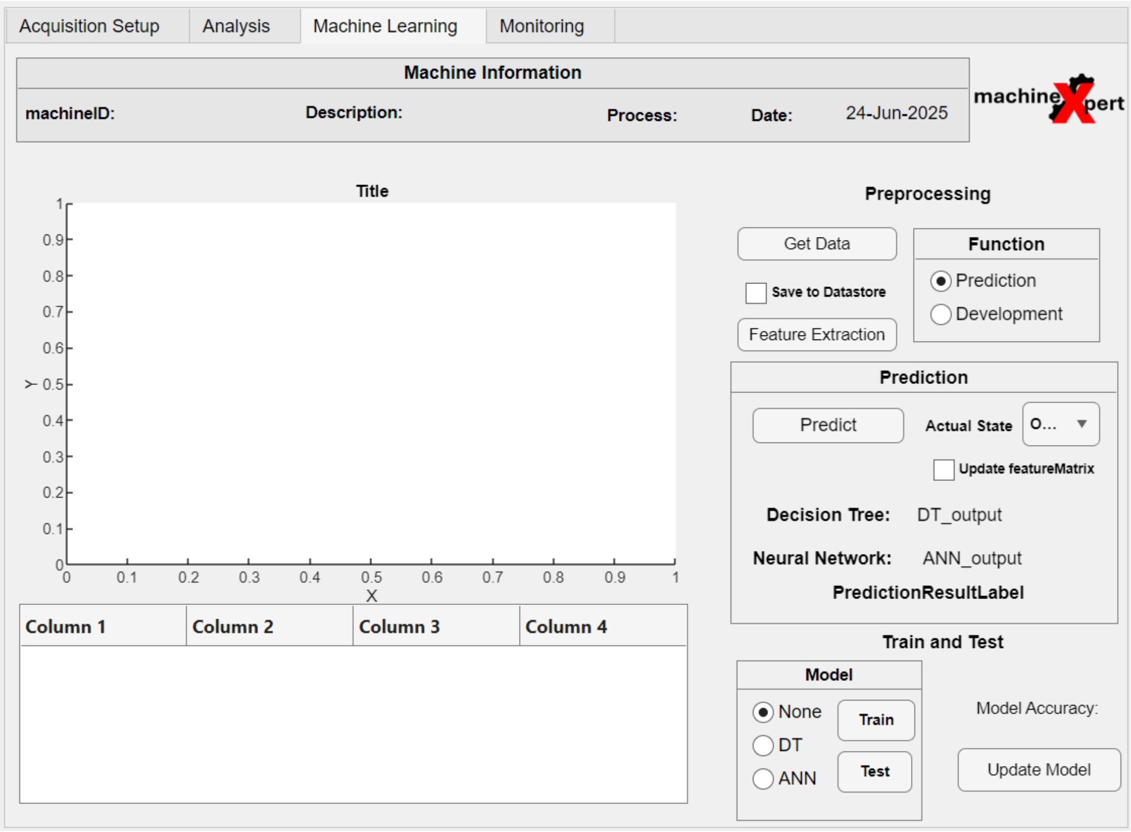

Figure 7.3-3. Graphical User Interface of the Machine Learning Tab of the Software

Function Group Panel

The function group panel allows the user to select the intended purpose of their analysis to control the functionality of other panels found in this GUI. The default selection of this panel is the ‘Prediction’ function. This assumes that most of the time this section of the GUI will be accessed to predict the operation status of the machine from the saved ML models. Alternatively, the user may opt to select the ‘Development’ option which focuses on training and testing of supervised Decision Tree (DT) and Artificial Neural Network (ANN) models. The selected option dictates what panels of the GUI are enabled to direct the user’s activity.

Preprocessing Panel

This panel is enabled by default as the function group panel is set to ‘Prediction’. This allows the user to collect data from a memory data storage area by pushing the ‘Get Data’ button. The app will then alert the user whether the process was successful, or whether to return to acquire data in the ‘Analysis Tab’. Once the data is collected, the user has an option of saving the raw data in the ensemble data store for future reference by selecting the ‘Save to Datastore’ checkbox. Otherwise, the user will then be required to click on the ‘Feature Extraction’ button to extract the required features from the data and normalise where necessary. This will then create a suitable feature matrix for use as inputs to machine learning models.

Prediction Panel

This panel becomes enabled when the 'Feature Extraction' button is pressed allowing passage of the feature matrix into machine learning models. Once the 'Predict' button in pushed, the stored DT and ANN models will make predictions on the input feature matrix and display their output at 'DT_output' and 'ANN_output', respectively. If the two outputs predict the same cavitation state, the 'PredictionResultLabel' will be populated with the predicted cavitation state while disagreement will populate this field with 'Expert Review Required!' text. This will be signalling that the user need to do their own analysis to ascertain the true state of the machine.

Once the true cavitation state is ascertained the actual state is selected from the 'Actual State' dropdown menu which append the cavitation status to the input feature matrix. Selecting the 'update featureMatrix' checkbox appends this data to the main 'featureMatrix' worksheet. Appending data to this worksheet is carried out in such a way that it circularly shifts observations of the same class to maintain the same number of observations in the file and achieves a balanced dataset over time by replacing the oldest observations with new ones. Moreover, the decision tree from the DT model will then be presented in the plot area to help with visualising the decision paths used by the model to make predictions. This is to formulate decision rules that the model followed supporting root cause analyses.

Train and Test Panel

The 'Train and Test Panel' serves as the ML model development space where the user selects the model they want to update between a DT and an ANN model. Pushing the 'Train' button starts the model training process using the training data which is a 70% portion of the 'featureMatrix', which has equal representation of the different cavitation states in the dataset. Once trained the validation accuracy is presented at the 'model accuracy' field while the confusion matrix is presented in table area below the plot area. Pushing the 'Test' button utilises the remaining 30% of the 'featureMatrix' to check the prediction accuracy of the developed model. Similarly, the table below the plot area presents the confusion matrix while the testing accuracy will be presented at the model accuracy area. Pushing the 'Update Model' button deletes the old ML models stored in the system and replaces them with newly trained and tested models. It is worth noting that both training, testing and updating the models should be done for one model at a time.

7.3.4. Monitoring Tab

The 'Monitoring' Tab implements the Health Monitoring Layer of the software. This tab can function on its own without the other tabs running. It ensures that the condition of the machine is monitored autonomously with little involvement of the user. Once the user sets it up including the monitoring frequencies of the machine condition it autonomously collects, analyses, classifies and trends important parameters for as long as the software is functional.

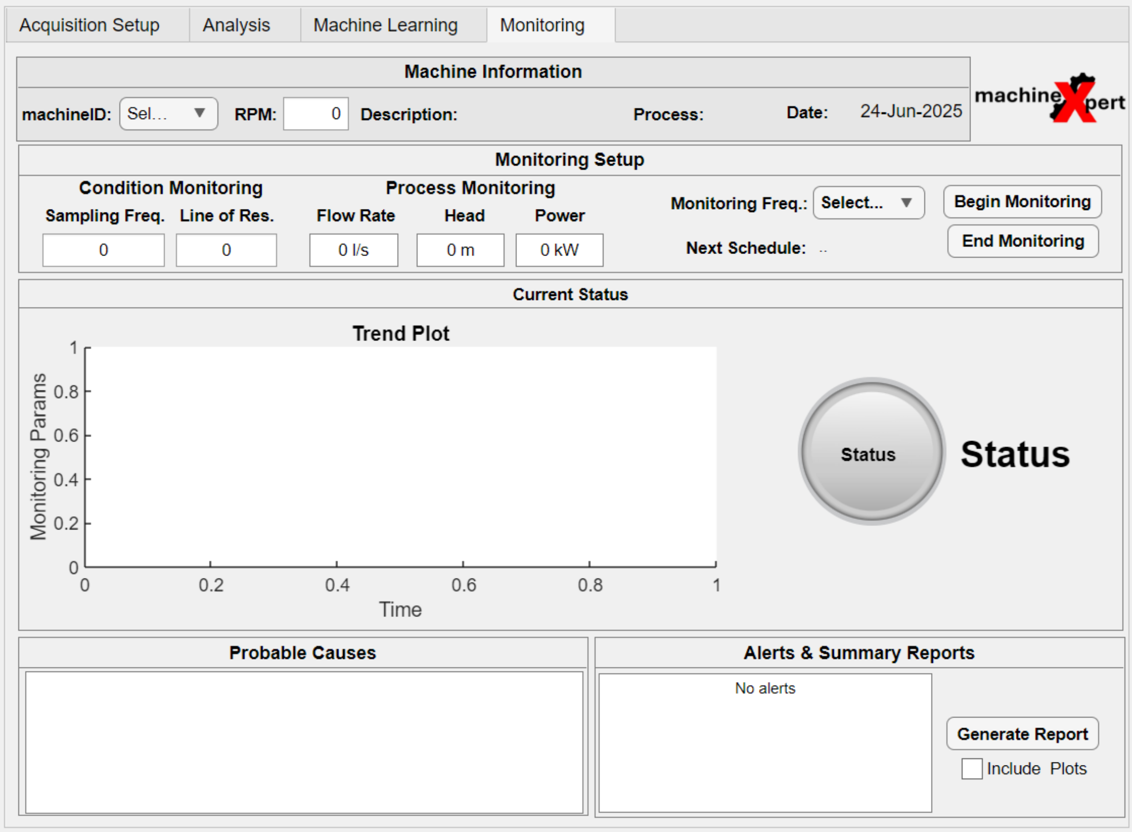

Figure 7.3-4. Graphical User Interface of the Monitoring Tab of the Software

The graphical user interface of this tab is presented in Fig. 7.3-4. The 'Machine Information' panel displays similar details about the machine presented in the other tabs with the exception that, in this tab it can be changed to run the 'Monitoring Tab' independently.

Monitoring Setup

Both condition monitoring and process monitoring parameters are populated when the respective DAQ sessions are running from the setup configured in the 'Acquisition Setup' tab. In this case, the values will be automatically populated and edit field disabled to avoid inadvertent changes. However, if there is no DAQ session running the 'sampling freq.' and 'Lines of Res.' edit fields are enabled to allow the user to enter the desired sampling frequency of the condition monitoring parameters, while the process monitoring parameters will be populated with their real-time values once the 'Begin Monitoring' button is pushed.

The 'Monitoring Freq.' dropdown menu allows the user to select the frequency of monitoring the condition of the machine. This is set to allow for monitoring daily, twice in a day, four times in a day, eight times in a day and hourly depending on the machine health status. The user initially selects the preferred frequency then the system would alter this depending on machine condition. Information on when the system will conduct a surveillance of the machine condition is provided adjacent to the 'Next Schedule:' label.

Pushing the 'Begin Monitoring' button pulls the monitoring history of important parameters such as the DND and the Overall Vibration from the historical data files and provides their trend in the trend plot. Conversely, pushing the 'End Monitoring' button stops the monitoring process allowing the panel to be reset again.

Current Status Panel

This panel consists of the machine health status indicator and a trend plot for monitoring important condition parameters. Trend plot also encompasses limits of these important parameters, which when exceeded the systems sends messages to the alert section to notify users. The status indicator receives diagnostic information from the Hybrid ML & Diagnostics framework and present it as a colour coded indication of the machine health status with green representing 'no cavitation' operation, orange indicating operation in the 'inception cavitation' region while red represent operation in the 'full cavitation' regime.

Probable Causes Panel

This panel presents decision tree logic into easy-to-understand rules that users can refer to when conducting a root cause analysis. These rules are only provided when the machine health status is detected to have changed from the 'no cavitation' state to other health conditions. This can be a detection by the Hybrid ML & Diagnostic framework of the platform or from the trending of key condition parameters. When a change of state is triggered by the changes in the monitored condition parameters, the probable causes panel indicates that also.

Alerts and Summary Reports

Any change of machine health status creates a status update that is presented to the user as alerts in this panel. The alerts are timestamped to easily create a record that can be linked with other information components about the machine health status. This makes it easier for the user to have information from different sources collated in a single location aiding in the generation of reports. By clicking the generate report, the information in the 'Probable Causes' panel and any alerts presented in this section are collated together in a downloadable document. To enrich the information on the report with different frequency plots and time waveform plot of the data that triggered the alerts, the 'Include Plots' check box must be selected.

7.4. LIMITATIONS OF THE DEVELOPED SOFTWARE PLATFORM

The developed software platform is currently tailored for the measurement and monitoring of machine vibration responses, in conjunction with key process parameters such as the PAT's head, flow rate and generated power. However, monitoring process parameters is limited to only low-resolution analysis, meaning it lacks the sensitivity and detail afforded to the vibration data. This restricts its ability to detect subtle changes in operational conditions. A further limitation is that the platform is designed to monitor only one machine at a time. To scale for multi-machine surveillance, the system would require an integrated scheduling and automation module that manages periodic assessments across different units without manual intervention.

Critically, the software is presently optimized exclusively for cavitation detection, assuming this is the sole failure mode. As a result, failure mechanisms outside cavitation may go undetected or be misclassified, leading to diagnostic inaccuracies. This is a recognized limitation. Future development will involve expanding the system's sensitivity to a wider range of failure modes. This will include testing current methodologies against datasets representing diverse fault conditions, thereby enabling the definition of new monitoring thresholds for each failure type.

From a data management standpoint, the software platform currently relies on a Microsoft Excel workbook as its storage layer. While useful during early development for integrating and testing system components, Excel is not suitable for handling large-scale datasets efficiently. To support long-term deployment and high-volume data processing (both raw and processed), the system must transition to scalable big data infrastructure capable of secure, fast and reliable storage.

Finally, the platform lacks a prognostic assessment layer, which is essential for full compliance with ISO 13374:2003 standards. Prognostic capability would allow the software to project future health states, predict failure modes and estimate remaining useful life (RUL) based on current condition and usage trends. This functionality is absent at present due to the focus on cavitation, a fluid dynamic disturbance whose effects accumulate over time rather than immediately cause structural deterioration.

Besides the above-described software-based limitations the following external factors that could affect the predictive capabilities of the proposed solution were not explicitly considered in the study but may influence the predictive capability and reliability of the proposed solution. These factors can affect signal quality, model generalisation and diagnostic accuracy when the system is deployed in real-world environments.

a. ***Variability of PAT geometry and design*** – the study focused on a single PAT geometry. In practice, PATs vary significantly in impeller design, blade number, volute geometry, clearance gaps and surface finish. These geometric differences can alter flow patterns, cavitation behaviour and vibration characteristics. As a result, vibration features and trained machine learning models may not generalise directly across different PAT designs without retraining or recalibration.
b. ***Installation and boundary conditions*** – field installations may introduce variability not captured in laboratory conditions, including pipe layouts, inlet flow distortions, positioning of valves, upstream bends and downstream pressure demands. These factors may have varying

impact on the flow stability and introduce additional vibration components unrelated to the occurrence of cavitation, potentially posing a challenge to the performance accuracy of the diagnostic models.

c. ***Structural mounting and foundation stiffness*** – differences in machine mounting, foundation stiffness and support structures can significantly influence vibration transmission paths. The same hydrodynamic phenomenon may produce different vibration amplitudes and frequency responses depending on how the PAT is installed. This affect feature consistency and may reduce classification reliability if not fully accounted for.

d. ***Sensor type, placement and mounting quality*** – the study assumed ideal sensor placement and mounting conditions. In real installations sensor orientation, mounting torque, surface condition and cable routing can introduce noise or attenuation. Variations in sensor sensitivity and frequency response may also affect feature extraction, particularly for higher-frequency vibration signatures.

e. ***Environmental and operational noise*** – external noise sources such as nearby pumps, valves, other electrical equipment and flow-induced structural vibrations can contaminate vibration signals. Electromagnetic interference and acoustic coupling may also influence measurements. These noise sources were assumed to be minimal in the laboratory setup but can be significant in operational environments.

f. ***Operational variability*** – the experiments were conducted under controlled and repeatable operating conditions. In the field, PATs may experience rapid load changes, intermittent operation, start-stop cycles and fluctuating head and flow conditions. These transient behavioural patterns can obscure cavitation signatures and reduce the robustness of detection and diagnosis systems.

g. ***Long-term degradation and ageing effects*** – the study did not consider long-term degradation mechanisms such as bearing wear, seal deterioration, surface roughening or material erosion due to operating under cavitating conditions. These failure mechanisms can alter baseline vibration characteristics over time, leading to model drift and potential misclassification if models are not periodically updated.

h. ***Cyber security and data integrity*** – moreover, the study did not consider cybersecurity threats or communication failures associated with real-time system monitoring. Data integrity issues could lead to incorrect diagnostics or loss of trust in the system.

These external factors highlight that reliable performance of the system is not solely determined by model accuracy, but by the entire monitoring ecosystem, including sensors, installation environment and operational context. While the platform provides a robust framework, real-world implementation would require site-specific calibration, continuous monitoring of data quality, adaptive model updating and integration with existing operational workflows.

7.5. SUMMARY

This chapter presented the final contribution of the thesis, the development of an integrated software platform for condition monitoring of PAT systems. Building on the experimental and analytical findings of previous chapters, the software brings together machine learning models, signal processing techniques and user-centred interface design into a unified tool that enables real-time, automated and actionable decision making for PAT health monitoring.

The platform was designed with a modular architecture consisting of four key functional layers namely Data Acquisition, Data Processing, Machine Learning & Diagnostics and Health Monitoring, each aligned with the principles and data flow requirements of ISO 13374:2003. Implemented in MATLAB App Designer, the system integrates both time-domain and frequency domain analysis, enabling accurate feature extraction and classification of cavitation states using a hybrid machine learning approach that balances prediction accuracy with interpretability.

Each interface tab mirrors a specific part of the system architecture, guiding users through the acquisition, analysis, diagnosis and monitoring process. Features such as the Decision Tree interpretability panel, real-time alerts and automated reporting ensure that the platform is not just technically robust but also practically valuable for end-users in micro- and pico-hydropower installations.

Nonetheless, several limitations were identified that provide a clear roadmap for future work. These include the software's current focus on a single fault mode, the absence of a multi-machines monitoring framework, limited sensitivity in process parameter acquisition and reliance on Excel-based data storage. Additionally, the lack of a prognostic layer restricts the platform's ability to forecast future system states or estimate the remaining useful life of components.

Lastly, the developed platform successfully achieves the fourth and final research objective of this thesis, thus, creating a real-time, user-friendly condition monitoring system tailored to the operational realities of PATs. While the current iteration is centred around cavitation detection, it lays a scalable foundation for a more comprehensive predictive maintenance system. Future enhancements, particularly those addressing broader fault classification, prognostics and scalable data management, will position the platform as a powerful digital solution for next generation hydropower asset management.

8. CONCLUSIONS AND RECOMMENDATIONS

8.1. CONCLUSIONS

The growing need for reliable and efficient small-scale hydropower systems, coupled with the evolution of a highly dynamic electric grid shaped by the integration of variable output renewable energy sources, has accelerated the adoption of pump-as-turbine (PAT) systems. This growth is largely driven by PAT's cost-competitiveness compared to conventional hydro turbines, the removal of historic feed-in tariffs, the rise in energy prices, the wide availability of PATs in various sizes suited to diverse application sites, and their competitive performance across operational ranges where traditional turbines may be less efficient.

However, despite the growing adoption of PAT systems, research and development efforts have not kept pace, particularly in the areas of operation and maintenance. Most studies to date have focused primarily on performance conversion from pump to turbine mode, as well as sizing and selection for specific application sites. This has left a significant gap in understanding the practical challenges of PAT operation and upkeep. Addressing these aspects is crucial to ensuring a safe and reliable energy generation, especially given that PATs serve as core components in micro-hydropower systems.

Building on this premise, this PhD thesis was dedicated to the development of a predictive maintenance system for PATs, with a particular focus on the hydrodynamic failure mechanism of cavitation. The research was guided by four core objectives aimed at systematically addressing the challenges involved namely, numerical analysis of cavitation in PATs, its investigation using experimentation, evaluation of machine learning algorithms for its detection and diagnosis, and lastly, implementing these algorithms as part of a software platform for predictive maintenance.

Firstly, Computational Fluid Dynamics (CFD) simulations were conducted across a range of operating conditions by varying the outlet pressure and flow rate through a PAT model to understand necessary conditions for cavitation, including the analysis of the associated pressure pulsations. The results revealed that cavitation primarily incepts early under the design flow conditions but with minimal impact on performance, while at off design conditions cavitation inception is a bit delayed but with severe consequences on the PAT performance.

Moreover, it was revealed that cavitation begins to occur on the blade suction side at the leading edge when operating at off-design flow conditions while at the design flow condition cavitation initiate at the impeller locking nut area. When cavitation progresses further it will build up at the blade pressure side where it starts to impact on performance. It was also observed that the developed cavity evolves from very small sized fast travelling vapour bubbles followed by the development of a sheet-like cavity, which subsequently evolves into a precessing vortex core ultimately developing into a torch-like structure.

The results of the frequency domain analysis of pressure pulsation data highlighted the complexity of cavitation in PATs, described by a frequency equivalent to one half the blade pass frequency at inception point. The energy of this frequency component will then shift towards lower frequencies as cavitation state deteriorates further, reaching frequencies closer to 0 Hz at its worst and a slight increase in amplitude. However, the amplitude of this frequency components remains lower than that of impeller speed related frequencies even though their effects could be exacerbated by coinciding with the system's natural frequency.

Secondly, experimental investigations were conducted to assess the vibration responses of PATs under cavitating conditions, alongside evaluating their hydraulic performance. The results demonstrated that, across all tested operating speeds, cavitation inception consistently occurred at a head of 29.65m, while the transition to 'full cavitation' was observed at a constant flow rate of 4.03 l/s. These findings indicate a relatively narrow safe operating range for PATs, underscoring the importance of accurate and timely cavitation detection.

Analysis of time-domain vibration signals led to the development of a modified Deviation from Normal Distribution (DND) method tailored for real-time cavitation detection. This method adapted the original DND technique, initially designed for gearbox failure detection, by calibrating it to the Gaussian distribution characteristics of the PAT's baseline vibration data under non-cavitating conditions, thus aligning the technique with the specific dynamics of PAT operation.

Additionally, frequency-domain analysis of the acquired vibration data revealed a frequency component at half the fundamental frequency at all operating speeds. The magnitude of this component showed a slight increase as the system approached 'full cavitation'. However, this component remained lower in magnitude than several other dominant rotating speed related harmonics, displaying a similar characteristic to the one observed for numerically obtained pressure pulsations. These observations highlight both the potential and limitations of frequency-based approaches for universal cavitation diagnosis in PATs, reinforcing the need for complementary approaches to cavitation detection and diagnosis.

Thirdly, three Machine Learning (ML) algorithms of Decision Trees (DT), Artificial Neural Networks (ANN) and Support Vector Machines were investigated for their applicability in a predictive maintenance framework aimed at the detection and diagnosis of cavitation in PATs. Among these, the ANN model demonstrated the highest predictive accuracy, making it particularly well-suited for high precision maintenance applications where early fault detection is critical. The DT model, while slightly less accurate, offered strong interpretability of its predictions, making it a valuable complementary model to ANN for explainability purposes. In contrast, the SVM model also produced competitive accuracy, however, it incurred a higher misclassification cost, which poses a risk to the safe and reliable operation of hydropower equipment.

To maximize the strengths of each model, a hybrid diagnostic framework was proposed. The approach combines the predictive power of ANNs with the interpretability of DT's, enabling both accurate and explainable cavitation diagnosis. The hybrid model was designed to enhance reliability in fault prediction while ensuring that operators can understand and trust the system outputs.

Building on these findings, a software platform was developed to operationalize the predictive maintenance strategy. Designed with a modular architecture, the platform consists of four core functional layers i.e., Data Acquisition, Data Processing, Machine Learning & Diagnostics and Health Monitoring. These layers were structured according to the ISO 13374:2003 standard for condition monitoring and diagnostics of machines, ensuring a robust and industry-compliant framework. The platform, implemented in MATLAB App Designer, integrates both time-domain and frequency-domain analysis, allowing for effective feature extraction and cavitation state classification using the hybrid ML approach.

The outcomes of this work contribute significantly toward improving the reliability, efficiency and sustainability of PAT-based micro-hydropower systems. Moreover, by translating the research into a practical, software-based solution, the study supports the digital transformation of hydropower. The predictive maintenance platform empowers operators to proactively manage failures, reduce downtime and optimise performance, aligning with global efforts to create resilient and intelligent renewable energy infrastructures.

8.2. CONTRIBUTIONS

The primary contribution of this research lies in the interdisciplinary integration of fluid dynamics, experimental vibration analysis and machine learning application for enhancing the operational reliability of PATs. Most notably, it addresses a critical gap in literature by focusing on the underexplored area of operation and maintenance in PAT-based micro-hydropower systems. This PhD research made several key contributions to the advancement of predictive maintenance in micro-hydropower systems, with a particular emphasis on cavitation-related failures in PATs;

a. Numerical Characterization of Cavitation Occurrence in PATs

The research provided a comprehensive numerical analysis of the conditions that lead to cavitation occurrence in PATs and described the various phases the developed cavity undergoes as conditions get worse. Through CFD simulations, the study identified specific pressure thresholds and flow regimes associated with cavitation onset and captured the resulting pressure pulsations, contributing valuable insights into the fluid dynamics of PAT operation under cavitating conditions.

b. Experimental detection of cavitation in PATs using time-domain vibration data

A detailed experimental investigation was conducted to characterise the vibration behaviour of PATs under varying cavitation states. The work led to the development of a modified Deviation from Normal Distribution (DND) method for real-time cavitation detection, adapted specifically for PAT applications. Additionally, the frequency-domain analysis revealed patterns linked to cavitation intensity, although with noted limitations in generalizability.

c. Evaluation and application of machine learning for cavitation diagnosis

The study evaluated and compared three machine learning algorithms of DT, ANN and SVM for automated detection and diagnosis of cavitation. It was found that ANN offers superior predictive accuracy, while DT provides transparent and interpretable outputs. A hybrid diagnostic framework for cavitation detection and diagnosis was proposed, combining both models to achieve high accuracy with explainable predictions.

d. Development of a modular predictive maintenance software platform

A complete predictive maintenance software platform was developed in MATLAB App Designer, integrating data acquisition, signal processing, machine learning and health monitoring functionalities. The architecture adheres to ISO 13374:2003 standard and incorporates both time and frequency-domain analysis, enabling comprehensive monitoring and diagnosis of cavitation in PATs.

e. Support for digital transformation in small-scale hydropower

By translating research outcomes into an applied software tool, this work contributes directly to the digitalization of hydropower systems. The proposed approach enhances operational reliability and enables proactive maintenance, aligning with broader global objectives for sustainability.

8.3. LIMITATIONS OF THE STUDY

While this thesis demonstrates the feasibility of a predictive maintenance approach for PAT systems, several limitations must be acknowledged to properly contextualise the findings and define the pathway toward practical exploitation. The experimental and machine learning investigations were conducted on a single laboratory-scale PAT under controlled conditions. Although this ensured repeatability and high-quality data, real-world installations introduce structural variability, background noise, hydraulic transients and operational fluctuations that may affect vibration signatures and model performance. Field validation across multiple installations is therefore necessary to assess robustness.

Moreover, the investigations were conducted on a single machine geometry thus affecting the generalisability of the resultant machine learning models. Supervised machine learning models depend on representative training data, and performance degradation may occur when applied to different PAT designs or operating regimes. Developing multi-machine datasets, incorporating physics-informed features and applying transfer learning techniques would improve generalisability.

Another limitation stems from basing cavitation classification on visual observations. While appropriate for experimental labelling, this introduces subjectivity, particularly near "*inception cavitation*". More objective quantification methods such as image-based vapour fraction estimation or pressure measurement-based cavitation indices would improve this limitation. Additionally, the proposed predictive maintenance solution focuses exclusively on cavitation excluding most of the mechanical failures that might be frequently experienced in actual operations.

In practice, PAT systems experience multiple failure modes, including bearing failure and misalignment. Expanding the methodology to multi-fault diagnostics would significantly enhance its industrial value. Furthermore, although integration with AI, IoT and digital twin concepts is discussed, full deployment would require scalable data infrastructure, cyber security considerations and long-term monitoring for model adaptation and prognostics.

Even though the described limitations affect the proposed solutions robustness, generalisation and reliability, the study provided a validated proof-of-concept under controlled conditions. Future work necessary to fully exploit the predictive maintenance solution in real world PAT application is further described in the next section.

8.4. FUTURE WORK

To ensure the wide adoption of the developed predictive maintenance system and its continued improvement enhancing its viability, generalisability and robustness, the following research areas are worth exploring further in the future.

a. Extending cavitation modelling to broader operating conditions

The conducted numerical analysis could be extended to cover a wider range of PAT designs, operating environments and transient flow conditions. Understanding scenarios where both flow rate and pressure changes simultaneously could yield deeper insights into complex flow behaviours during cavitation occurrence.

b. Adopting advanced experimental techniques for condition monitoring

Additional sensor types such as acoustic emission, high-speed imaging and ultrasound sensors could complement vibration-based diagnostics, enabling using several techniques to detect cavitation and other failure mechanisms. Long-term in-situ monitoring in actual micro-hydropower installations would also help validate and refine the developed detection techniques under real-world operating conditions.

c. Improving machine learning models and real-time implementation

While the hybrid ANN-DT model is characterised by high precision interpretable predictions, future work would explore more advanced machine learning techniques such as ensemble learning, deep learning and transfer learning to improve classification accuracy and adaptability across different PAT configurations. Moreover, deployment on embedded platforms or edge devices would also facilitate real-time diagnostics.

d. Integration of Artificial Intelligence (AI), Internet of Things (IoT) and Digital Twins

Future research and improvement initiatives should increasingly consider the integration of artificial intelligence, internet of things and digital twins to realise intelligent autonomous and adaptive monitoring of hydropower systems. Digital twins could enable continuous monitoring, simulation and optimization of system performance. IoT could support real-time connectivity, secure data exchange and remote access enhancing responsiveness while AI could represent a significant evolution in predictive maintenance towards continuous self-optimizing monitoring systems.

e. Incorporate various stakeholder insights in future revisions of the platform

Future iterations of the predictive maintenance platform should integrate feedback from diverse stakeholders, including micro-hydropower operators, maintenance technicians, software developers and policymakers. Engaging these potential end-users will help align the platform's functionality, usability and data presentation with real-world operational needs. This participatory approach can guide improvements in system design, enhance adoption and ensure tool supports practical decision-making in the field.

REFERENCES

[1] European Energy Agency. "Climate Change Policies." https://www.eea.europa.eu/themes/climate/policy-context (accessed 23 November, 2020).

[2] C. Nunez. "Renewable Energy, Explained." https://www.nationalgeographic.com/environment/article/renewable-energy#:~:text=Solar%2C%20wind%2C%20hydroelectric%2C%20biomass,warming%20effects%20of%20fossil%20fuels.&text=In%20any%20discussion%20about%20climate,worst%20effects%20of%20rising%20temperatures. (accessed 15 December 2019).

[3] H. Ritchie, M. Roser and P. Rosado, "Renewable Energy," 2020. [Online]. Available: https://ourworldindata.org/renewable-energy.

[4] Ofgem. "Feed-in Tarriffs (FIT)." https://www.ofgem.gov.uk/environmental-and-social-schemes/feed-tariffs-fit (accessed 8 October 2019).

[5] A. Carravetta, S. D. Househ, and H. H. Ramos, *Pumps as Turbines: Fundamentals and Applications*. Gewerbestrasse, Switzerland: Springer, 2018.

[6] A. McNabola *et al.*, "Energy Recovery in the Water Industry Using Micro-hydropower: An Opportunity to Improve Sustainability," *Water Policy,* vol. 16, pp. 168-183, 2014.

[7] L. Hernandez-Leal, H. Temmink, G. Zeeman, and C. J. N. Buisman, "Bioflocculation of Grey Water for Improved Energy Recovery Within Decentralised Sanitation Concepts," *Bioresource Technology,* vol. 101, no. 23, pp. 9065-9070, 2010.

[8] I. Martin, M. S. Pidou, A., S. Judd, and B. Jefferson, "Modelling the Energy Demands of Aerobic and Anaerobic Membrane Bioreactors for Wastewater Treatment," *Environmental Technology,* vol. 32, no. 9, pp. 921-932, 2011.

[9] R. Agathokloeous *et al.*, "Waste Heat Recovery in the EU Industry and Proposed New Technologies," *Energy Procedia,* vol. 161, pp. 489-496, 2019.

[10] C. Copeland and N. T. Carter, "Energy- Water Nexus: The Water Sector's Energy Use," Congressional Research Service, Washington DC, 2017.

[11] M. Gandiglio, A. Lanzini, A. Soto, P. Leone, and M. Santarelli, "Enhancing the Energy Efficiency of Wastewater Treatment Plants through Co-Digestion and Fuel Cell Systems," *Frontiers in Environmental Science,* vol. 5, no. 70, 2017.

[12] A. McNabola, P. Coughlan, and A. P. Williams, "The Technical & Economic Feasibility of Energy Recovery in Water Supply Networks," in *Proceedings of International Conference on Renewable Energy and Power Quality*, Las Palmas de Gran Canaria, Spain, 2011.

[13] T. C. Dublin. "Water and Wastewater." https://www.tcd.ie/provost/sustainability/initiatives/water/ (accessed 10 October, 2020).

[14] T. Lydon, P. Coughlan, and A. McNabola, "Pressure Management and Energy Recovery in Water Distribution Networks: Development of Design and Selection Methodologies using Three Pumps-as-Turbine Case Studies," *Renewable Energy,* vol. 114, pp. 1038-1050, 2017.

[15] D. Novara, A. Carravetta, A. McNabola, and H. M. Ramos, "Cost Model for Pumps as Turbines in run-of-river and In-pipe Micro-hydropower Applications," *Journal of Water Resources Planning & Management,* vol. 145, no. 5, pp. 1-9, 2019.

[16] S. V. Jain and R. N. Patel, "Investigations on Rump Running in Turbine Mode: A Review of the State of the Art," *Renewable and Sustainable Energy Reviews,* vol. 30, pp. 841-868, 2014.

[17] B. Nesbitt, *Handbook of Pumps and Pumping*. Oxford, UK: Elsevier, 2006.

[18] A. Bianchini, M. Pellegrini, and J. Rossi, "Maintenance Scheduling Optimization ofor Industrial Centrifugal Pumps," *International Journal of System Assurance Engineering and Management,* vol. 10, no. 4, pp. 848 - 860, 2019.

[19] J. L. Parrondo, S. Verlarde, and C. Santolaria, "Development of a Predictive Maintenance System for a Centrifugal Pump," *Journal of Quality in Maintenance Engineering,* vol. 4, no. 3, pp. 198 - 211, 1998.

[20] C. Alatorre-Frenk, "Cost Minimisation in Micro-hydro Systems Using Pump-as-Turbines," Univeristy of Warwick, Warwick, PhD Thesis 1994.
[21] K. A. K. D. Apostolou, "Hydropower," in *Power Engineering: Advances and Challenges, Part A: Thermal, Hydro and Nuclear Power*, 2018.
[22] A. McNabola *et al.*, "Energy recovery in the water industry using micro-hydropower: An opportunity to improve sustainability," *Water Policy,* vol. 16, no. 1, pp. 168-183, 2014.
[23] S. G. Rothausen and D. Conway, "Greenhouse-gas emissions from energy use in the water sector," *Nature climate change,* vol. 1, no. 4, pp. 210-219, 2011.
[24] C. Pandit and C. D. Thatte, "Hydropower: The Way Ahead," in *Water Governance: Challenges and Prospects*, A. Singh, D. Saha, and A. C. Tyagi Eds. Singapore: Springer Singapore, 2019, pp. 219-239.
[25] A. Gallo, J. R. Simões-Moreira, H. Costa, M. M. Santos, and E. M. Dos Santos, "Energy storage in the energy transition context: A technology review," *Renewable and sustainable energy reviews,* vol. 65, pp. 800-822, 2016.
[26] P. Punys, R. Baublys, E. Kasiulis, A. Vaisvila, B. Pelikan, and J. Steller, "Assessment of renewable electricity generation by pumped storage power plants in EU Member States," *Renewable and Sustainable Energy Reviews,* vol. 26, pp. 190-200, 2013.
[27] M. Chazarra, J. I. Pérez-Díaz, J. García-González, and R. Praus, "Economic viability of pumped-storage power plants participating in the secondary regulation service," *Applied energy,* vol. 216, pp. 224-233, 2018.
[28] J. Menendez, J. M. Fernandez-Oro, M. Galdo, and J. Loredo, "Pumped-storage hydropower plants with underground reservoir: Influence of air pressure on the efficiency of the Francis turbine and energy production," *Renewable energy,* vol. 143, pp. 1427-1438, 2019.
[29] D. K. Okot, "Review of small hydropower technology," *Renewable and Sustainable Energy Reviews,* vol. 26, pp. 515-520, 2013.
[30] P. Breeze, *Hydropower*. Academic Press, 2018.
[31] S. D. Houreh, A. Carravetta, and H. M. Ramos, *Pumps as turbines: Fundamentals and applications*. Springer International Publishing, 2018.
[32] D. Novara, "Hydropower energy recovery systems: Development of design methodologies for pumps as turbines in water networks," *University of Dublin, Trinity College Dublin,* 2020.
[33] B. S. Massey and J. Ward-Smith, *Mechanics of fluids*. Crc Press, 1998.
[34] D. Thoma and C. Kittredge, "Centrifugal pumps operated under abnormal conditions," *Power,* vol. 73, pp. 881-884, 1931.
[35] B. Nesbitt, *Handbook of pumps and pumping: Pumping manual international*. Elsevier, 2006.
[36] M. Rossi, M. Righetti, and M. Renzi, "Pump-as-Turbine for energy recovery applications: the case study of an aqueduct," *Energy Procedia,* vol. 101, pp. 1207-1214, 2016.
[37] T. Lydon, P. Coughlan, and A. McNabola, "Pressure management and energy recovery in water distribution networks: Development of design and selection methodologies using three pump-as-turbine case studies," *Renewable Energy,* vol. 114, pp. 1038-1050, 2017.
[38] S.-S. Yang, S. Derakhshan, and F.-Y. Kong, "Theoretical, numerical and experimental prediction of pump as turbine performance," *Renewable Energy,* vol. 48, pp. 507-513, 2012.
[39] A. Budris, "Using pumps as power recovery turbines," *Water World,* vol. 29, p. 2011, 2011.
[40] J.-M. Chapallaz, P. Eichenberger, and G. Fischer, "Manual on pumps used as turbines," 1992.
[41] S. Derakhshan and A. Nourbakhsh, "Experimental study of characteristic curves of centrifugal pumps working as turbines in different specific speeds," *Experimental thermal and fluid science,* vol. 32, no. 3, pp. 800-807, 2008.
[42] A. Williams, "The turbine performance of centrifugal pumps: a comparison of prediction methods," *Proceedings of the Institution of Mechanical Engineers, Part A: Journal of Power and Energy,* vol. 208, no. 1, pp. 59-66, 1994.

[43] D. Mitrovic, J. G. Morillo, J. A. Rodríguez Díaz, and A. Mc Nabola, "Optimization-based methodology for selection of pump-as-turbine in water distribution networks: Effects of different objectives and machine operation limits on best efficiency point," *Journal of Water Resources Planning and Management,* vol. 147, no. 5, p. 04021019, 2021.
[44] P. Singh and F. Nestmann, "An optimization routine on a prediction and selection model for the turbine operation of centrifugal pumps," *Experimental Thermal and Fluid Science,* vol. 34, no. 2, pp. 152-164, 2010.
[45] A. Carravetta, G. Del Giudice, O. Fecarotta, and H. M. Ramos, "Energy production in water distribution networks: A PAT design strategy," *Water resources management,* vol. 26, pp. 3947-3959, 2012.
[46] P. Suter, "Representation of pump characteristics for calculation of water hammer," *Sulzer Tech. Rev,* vol. 4, no. 66, pp. 45-48, 1966.
[47] E. B. Wylie, V. L. Streeter, and L. Suo, *Fluid transients in systems*. Prentice Hall Englewood Cliffs, NJ, 1993.
[48] J. F. Gülich, *Operation of centrifugal pumps*. Springer, 2008.
[49] O. Fecarotta, A. Carravetta, H. M. Ramos, and R. Martino, "An improved affinity model to enhance variable operating strategy for pumps used as turbines," *Journal of Hydraulic Research,* vol. 54, no. 3, pp. 332-341, 2016.
[50] E. Frosina, D. Buono, and A. Senatore, "A performance prediction method for pumps as turbines (PAT) using a computational fluid dynamics (CFD) modeling approach," *Energies,* vol. 10, no. 1, p. 103, 2017.
[51] J. D. Denton, "Some limitations of turbomachinery CFD," in *Turbo Expo: Power for Land, Sea, and Air*, 2010, vol. 44021, pp. 735-745.
[52] D. J. Smith, *Reliability, maintainability and risk: practical methods for engineers*. Butterworth-Heinemann, 2021.
[53] T. Tinga, "Failure Mechanisms," in *Principles of Loads and Failure Mechanisms: Applications in Maintenance, Reliability and Design*. London: Springer London, 2013, pp. 85-157.
[54] L. P. Anad, D.M., "Defect-Free Fatique," Massachusetts Institute of Technology, Cambridge, Massachusetts, 2004.
[55] A. Cubillo, "Physics-based approach to detect metal-metal contact in the hydrodynamic bearing of a planetary transmission," 2016.
[56] R. Ocampo, "Fatigue failures in pumps–part 1," *World Pumps,* vol. 2008, no. 500, pp. 42-45, 2008.
[57] R. Ocampo and B. Ruiz, "Fatigue failures in pumps – part 2," *World Pumps,* vol. 2008, no. 502, pp. 18-21, 2008/07/01/ 2008, doi: https://doi.org/10.1016/S0262-1762(08)70204-9.
[58] R. Ocampo, "Fatigue failures in pumps – part 3," *World Pumps,* vol. 2008, no. 505, pp. 38-42, 2008/10/01/ 2008, doi: https://doi.org/10.1016/S0262-1762(08)70346-8.
[59] C. E. Brennen, *Cavitation and bubble dynamics*. Cambridge university press, 2014.
[60] A. A. Abdel Fatah, M. A. Hassan, M. Lotfy, and A. S. Dimitri, "Health monitoring of centrifugal pumps using digital models," *Journal of Dynamic Systems, Measurement, and Control,* vol. 141, no. 9, p. 091014, 2019.
[61] T. Lei, Z. B. Shan, C. S. Liang, W. Y. Chuan, and W. B. Bin, "Numerical simulation of unsteady cavitation flow in a centrifugal pump at off-design conditions," *Proceedings of the Institution of Mechanical Engineers, Part C: Journal of mechanical engineering science,* vol. 228, no. 11, pp. 1994-2006, 2014.
[62] Q. Fu, F. Zhang, R. Zhu, and B. He, "A systematic investigation on flow characteristics of impeller passage in a nuclear centrifugal pump under cavitation state," *Annals of Nuclear Energy,* vol. 97, pp. 190-197, 2016.
[63] C. Ansys, "Solver Theory Guide. Release 2019 R3. Canonsburg: ANSYS," ed: Inc, 2019.
[64] F. Bakir, R. Rey, A. Gerber, T. Belamri, and B. Hutchinson, "Numerical and experimental investigations of the cavitating behavior of an inducer," *International Journal of Rotating Machinery,* vol. 10, no. 1, pp. 15-25, 2004.

[65] M. Rakibuzzaman, K. Kim, and S.-H. Suh, "Numerical and experimental investigation of cavitation flows in a multistage centrifugal pump," *Journal of Mechanical Science and Technology,* vol. 32, pp. 1071-1078, 2018.
[66] M. Rakibuzzaman, K.-Y. Jung, and S.-H. Suh, "A study on the use of existing pump as turbine," in *E3S Web of Conferences*, 2019, vol. 128: EDP Sciences, p. 06004.
[67] A. K. Singhal, M. M. Athavale, H. Li, and Y. Jiang, "Mathematical basis and validation of the full cavitation model," *J. Fluids Eng.,* vol. 124, no. 3, pp. 617-624, 2002.
[68] W. Li, "Validating full cavitation model with an experimental centrifugal pump," *TASK Quarterly: scientific bulletin of Academic Computer Centre in Gdansk,* vol. 18, 2014.
[69] P. J. Zwart, A. G. Gerber, and T. Belamri, "A two-phase flow model for predicting cavitation dynamics," in *Fifth international conference on multiphase flow*, 2004, vol. 152: Yokohama Japan.
[70] D. Wu, Y. Ren, J. Mou, Y. Gu, and L. Jiang, "Unsteady flow and structural behaviors of centrifugal pump under cavitation conditions," *Chinese Journal of Mechanical Engineering,* vol. 32, pp. 1-15, 2019.
[71] R. Tao, R. Xiao, F. Wang, and W. Liu, "Cavitation behavior study in the pump mode of a reversible pump-turbine," *Renewable Energy,* vol. 125, pp. 655-667, 2018.
[72] G. H. Schnerr and J. Sauer, "Physical and numerical modeling of unsteady cavitation dynamics," in *Fourth international conference on multiphase flow*, 2001, vol. 1: ICMF New Orleans New Orleans, LO, USA, pp. 1-12.
[73] M. Binama, W.-T. Su, X.-B. Li, F.-C. Li, X.-Z. Wei, and S. An, "Investigation on pump as turbine (PAT) technical aspects for micro hydropower schemes: A state-of-the-art review," *Renewable and Sustainable Energy Reviews,* vol. 79, pp. 148-179, 2017.
[74] M. Binama, A. Muhirwa, and E. Bisengimana, "Cavitation effects in centrifugal pumps-A review," *Int. J. Eng. Res. Appl,* vol. 6, pp. 52-63, 2016.
[75] J. Lu, S. Yuan, Y. Luo, J. Yuan, B. Zhou, and H. Sun, "Numerical and experimental investigation on the development of cavitation in a centrifugal pump," *Proceedings of the Institution of Mechanical Engineers, Part E: Journal of Process Mechanical Engineering,* vol. 230, no. 3, pp. 171-182, 2016.
[76] J. Lu, S. Yuan, P. Siva, J. Yuan, X. Ren, and B. Zhou, "The characteristics investigation under the unsteady cavitation condition in a centrifugal pump," *Journal of Mechanical Science and Technology,* vol. 31, pp. 1213-1222, 2017.
[77] J. Lu, S. Yuan, S. Parameswaran, J. Yuan, X. Ren, and Q. Si, "Investigation on the vibration and flow instabilities induced by cavitation in a centrifugal pump," *Advances in Mechanical Engineering,* vol. 9, no. 4, p. 1687814017696225, 2017.
[78] N. Zhang, B. Gao, Z. Li, and Q. Jiang, "Cavitating flow-induced unsteady pressure pulsations in a low specific speed centrifugal pump," *Royal society open science,* vol. 5, no. 7, p. 180408, 2018.
[79] N. Zhang, M. Yang, B. Gao, and Z. Li, "Vibration characteristics induced by cavitation in a centrifugal pump with slope volute," *Shock and Vibration,* vol. 2015, no. 1, p. 294980, 2015.
[80] J. Mais, "Spectrum analysis: the key features of analyzing spectra," *SKF USA, Inc,* 2002.
[81] E. Ayli, "Cavitation in Hydraulic Turbines," *International Journal of Heat & Technology,* vol. 37, no. 1, 2019.
[82] A. Minakov, D. Platonov, A. Dekterev, A. Sentyabov, and A. Zakharov, "The numerical simulation of low frequency pressure pulsations in the high-head Francis turbine," *Computers & Fluids,* vol. 111, pp. 197-205, 2015.
[83] P. Singh, "Optimization of internal hydraulics and of system design for pumps as turbines with field implementation and evaluation," Karlsruhe, Univ., Diss., 2005, 2005.
[84] C. Alatorre-Frenk, "Cost minimisation in micro-hydro systems using pumps-as-turbines," 1994.
[85] W. Li and Y. Zhang, "Numerical simulation of cavitating flow in a centrifugal pump as turbine," *Proceedings of the Institution of Mechanical Engineers, Part E: Journal of Process Mechanical Engineering,* vol. 232, no. 2, pp. 135-154, 2018.

[86] S. V. Jain, N. K. Patel, and R. N. Patel, "Experimental investigations of cavitation characteristics of pump running in turbine mode," *Journal of Energy Engineering,* vol. 143, no. 1, p. 04016034, 2017.
[87] D. Mitrovic *et al.*, "Multi-country scale assessment of available energy recovery potential using micro-hydropower in drinking, pressurised irrigation and wastewater networks, covering part of the eu," *Water,* vol. 13, no. 7, p. 899, 2021.
[88] J. Guelich and U. Bolleter, "Pressure pulsations in centrifugal pumps," 1992.
[89] X. Duan, F. Tang, W. Duan, W. Zhou, and L. Shi, "Experimental investigation on the correlation of pressure pulsation and vibration of axial flow pump," *Advances in Mechanical Engineering,* vol. 11, no. 11, p. 1687814019889473, 2019.
[90] L. R. Higgins and R. K. Mobley, "Maintenance engineering handbook," McGraw-hill, 2002.
[91] K. R. Mobley, *An Introduction to Predictive Maintenance*. United States of America: Butterworth-Heinemann, 2002.
[92] C. Soares, *Gas Turbines: A Handbook of Air, Land and Sea Applications*. Waltham, USA: Butterworth-Heinemann, 2015.
[93] British Standards Institute, *BS EN 9001: 2015 Quality Management System Requirements*, London, 2015.
[94] K. Mobley, L. R. Higgins, and D. J. Wikoff, *Maintenance Engineering Handbook*. United States of America: McGraw Hill Conpanies, Inc., 2008.
[95] Deloitte Consulting GmbH, *Predictive Maintenance*, Position Paper 2017.
[96] PWC, *Predictive Maintenance 4.0 Predict the Unpredictable*, Armsterdam, 2017.
[97] British Standards Institute, *Maintenance - Maintenance Terminology, BS EN 13306:2017*, UK, 2018.
[98] U. Leturiondo, "Hybrid Modelling in Condition Monitoring," Lulea University of Technology, Lulea, Sweden, Doctoral Thesis 2016.
[99] L. H. Chiang, E. L. Russell, and R. D. Braatz, *Fault Detection and Diagnosis in Industrial Systems*. London: Springer-Verlag, 2001.
[100] British Standards Institute, *Condition Monitoring and Diagnostics of Machines - Vibration Condition Monitoring - Part 1: General Procedures*, London, 2002.
[101] J. C. Robinson and J. E. Berry, "Description of PeakVue and Illustration of its Wide Array of Applications in Fault Detection and Problem Severity Assessment," in *Emerson Process Management Reliability Conference 2001*, 2001.
[102] A. R. Al-Obaidi, "Investigation of effect of pump rotational speed on performance and detection of cavitation within a centrifugal pump using vibration analysis," *Heliyon,* vol. 5, no. 6, 2019.
[103] R. B. Randall, *Vibration-based Condition Monitoring - Industrial, Automotive and Aerospace Applications*. Hoboken, NJ: John Wiley & Sons Ltd, 2021.
[104] British Standards Institution, *BS ISO 20816 -1: 2016 Mechanical Vibration - Measurement and Evaluation of Machine Vibration (Part 1 General Guidelines)*, UK, 2016.
[105] A. Brandt, *Noise and vibration analysis: signal analysis and experimental procedures*. John Wiley & Sons, 2010.
[106] V. P. Luciani, "Understanding Power Factor and Crest Factor," n.d. [Online]. Available: https://www.ametekesp.com/-/media/ametekesp/downloads/white-papers/esp-surgex_white-paper_understanding-power-factor-and-crest-factor.pdf?la=en&revision=2b8a5878-aab8-4630-930c-a5b43fc899bf&hash=CCF8C61B88A8EAE9F0C2A8BA151A4094
[107] S. Liu, S. Hou, K. He, and W. Yang, "L-Kurtosis and its application for fault detection of rolling element bearings," *Measurement,* vol. 116, pp. 523-532, 2018/02/01/ 2018, doi: https://doi.org/10.1016/j.measurement.2017.11.049.
[108] A. Parey, M. El Badaoui, F. Guillet, and N. Tandon, "Dynamic modelling of spur gear pair and application of empirical mode decomposition-based statistical analysis for early detection of localized tooth defect," *Journal of Sound and Vibration,* vol. 294, no. 3, pp. 547-561, 2006/06/01/ 2006, doi: https://doi.org/10.1016/j.jsv.2005.11.021.

[109] X. Wang, V. Makis, and M. Yang, "A wavelet approach to fault diagnosis of a gearbox under varying load conditions," *Journal of Sound and Vibration,* vol. 329, no. 9, pp. 1570-1585, 2010/04/26/ 2010, doi: https://doi.org/10.1016/j.jsv.2009.11.010.

[110] J. Vass, R. Šmíd, R. B. Randall, P. Sovka, C. Cristalli, and B. Torcianti, "Avoidance of speckle noise in laser vibrometry by the use of kurtosis ratio: Application to mechanical fault diagnostics," *Mechanical Systems and Signal Processing,* vol. 22, no. 3, pp. 647-671, 2008/04/01/ 2008, doi: https://doi.org/10.1016/j.ymssp.2007.08.008.

[111] N. Tandon, "A comparison of some vibration parameters for the condition monitoring of rolling element bearings," *Measurement,* vol. 12, no. 3, pp. 285-289, 1994/01/01/ 1994, doi: https://doi.org/10.1016/0263-2241(94)90033-7.

[112] P. Rzeszucinski, J. Sinha, R. Edwards, A. Starr, and B. Allen, "A new technique for condition monitoring of helicopter gearboxes," in *Proceedings of the 10 th International Conference on Vibration Problems Supplement*, 2011, pp. 407-412.

[113] E. Asnaashari and J. K. Sinha, "Crack detection in structures using deviation from normal distribution of measured vibration responses," *Journal of Sound and vibration,* vol. 333, no. 18, pp. 4139-4151, 2014.

[114] P. Rzeszucinski, J. Sinha, R. Edwards, A. Starr, and B. Allen, "Amplitude of probability density function (APDF) of vibration response as a robust tool for gearbox diagnosis," *Strain,* vol. 48, no. 6, pp. 510-516, 2012.

[115] R. B. Randall, *Vibration-based condition monitoring: industrial, automotive and aerospace applications*. John Wiley & Sons, 2021.

[116] C. R. Farrar and K. Worden, *Structural health monitoring: a machine learning perspective*. John Wiley & Sons, 2012.

[117] G. L. Boylan and B. R. Cho, "The normal probability plot as a tool for understanding data: A shape analysis from the perspective of skewness, kurtosis, and variability," *Quality and Reliability Engineering International,* vol. 28, no. 3, pp. 249-264, 2012.

[118] X. Escaler, E. Egusquiza, M. Farhat, F. Avellan, and M. Coussirat, "Detection of cavitation in hydraulic turbines," *Mechanical systems and signal processing,* vol. 20, no. 4, pp. 983-1007, 2006.

[119] M. Čdina, "Detection of cavitation phenomenon in a centrifugal pump using audible sound," *Mechanical systems and signal processing,* vol. 17, no. 6, pp. 1335-1347, 2003.

[120] S. V. Jain, N. K. Patel, and R. N. Patel, "Experimental Investigations of Cavitation Characteristics of Pump Running in Turbine Mode," *Journal of Energy Engineering,* vol. 143, no. 1, 2017, doi: 10.1061/(asce)ey.1943-7897.0000387.

[121] S. A. Al-Hashmi, "Detection and diagnosis of cavitation in centrifugal pumps," Doctor of Philosophy, School of Mechanical, Aerospace and Civil Engineering, University of Manchester, Manchester, 2005.

[122] B. W. Silverman, *Density estimation for statistics and data analysis*. Routledge, 2018.

[123] K. Umesh and R. Ganguli, "Composite material and piezoelectric coefficient uncertainty effects on structural health monitoring using feedback control gains as damage indicators," *Structural Health Monitoring,* vol. 10, no. 2, pp. 115-129, 2011.

[124] G. Blom, *Statistical estimates and transformed beta-variables*. Almqvist & Wiksell, 1958.

[125] V. Sharma and A. Parey, "Gearbox fault diagnosis using RMS based probability density function and entropy measures for fluctuating speed conditions," *Structural Health Monitoring,* vol. 16, no. 6, pp. 682-695, 2017.

[126] S. Nagarajaiah and B. Basu, "Output only modal identification and structural damage detection using time frequency & wavelet techniques," *Earthquake Engineering and Engineering Vibration,* vol. 8, no. 4, pp. 583-605, 2009.

[127] G. Heinzel, A. Rüdiger, and R. Schilling, "Spectrum and spectral density estimation by the Discrete Fourier transform (DFT), including a comprehensive list of window functions and some new at-top windows," 2002.

[128] J. K. Sinha, *Vibration analysis, instruments, and signal processing*. CRC press Boca Raton, FL, USA, 2015.

[129] R. B. Randall and J. Antoni, "Rolling element bearing diagnostics—A tutorial," *Mechanical systems and signal processing,* vol. 25, no. 2, pp. 485-520, 2011.
[130] T. Koivula, A. Ellman, and M. Vilenius, "Experiences on cavitation detection methods," *Tampere University of Technology, Institute of Hydraulics and Automation, Tampere,* 2000.
[131] A. Presas *et al.*, "Detection of erosive cavitation on hydraulic turbines through demodulation analysis," in *IOP Conference Series: Earth and Environmental Science*, 2019, vol. 240, no. 6: IOP Publishing, p. 062048.
[132] X. Escaler, E. Egusquiza, M. Farhat, and F. Avellan, "Cavitation erosion prediction in hydro turbines from onboard vibrations," in *Proceedings of the 22nd IAHR Symposium on Hydraulic Machinery and Systems, Stockholm, Sweden*, 2004, vol. 1: International Association For Hydraulic Research, pp. 1-10.
[133] X. Escaler, J. V. Ekanger, H. H. Francke, M. Kjeldsen, and T. K. Nielsen, "Detection of draft tube surge and erosive blade cavitation in a full-scale Francis turbine," *Journal of Fluids Engineering,* vol. 137, no. 1, p. 011103, 2015.
[134] D. Valentín, A. Presas, M. Egusquiza, C. Valero, and E. Egusquiza, "Transmission of high frequency vibrations in rotating systems. Application to cavitation detection in hydraulic turbines," *Applied Sciences,* vol. 8, no. 3, p. 451, 2018.
[135] G. Mousmoulis, C. Yiakopoulos, G. Aggidis, I. Antoniadis, and I. Anagnostopoulos, "Application of Spectral Kurtosis on vibration signals for the detection of cavitation in centrifugal pumps," *Applied Acoustics,* vol. 182, p. 108289, 2021.
[136] Y. Zhu *et al.*, "Research Progress on Identification and Suppression Methods for Monitoring the Cavitation State of Centrifugal Pumps," *Water,* vol. 16, no. 1, p. 52, 2023.
[137] X. Liu, J. Mou, X. Xu, Z. Qiu, and B. Dong, "A review of pump cavitation fault detection methods based on different signals," *Processes,* vol. 11, no. 7, p. 2007, 2023.
[138] W. Feng, Q. Cheng, Z. Guo, and Z. Qian, "Simulation of cavitation performance of an axial flow pump with inlet guide vanes," *Advances in Mechanical Engineering,* vol. 8, no. 6, p. 1687814016651583, 2016.
[139] M. Szala and D. Łukasik, "Cavitation wear of pump impellers," *Journal of Technology and Exploitation in Mechanical Engineering,* vol. 2, no. 1, pp. 40-44, 2016.
[140] B. Li, Q. Zhao, H. Li, X. Liu, J. Ma, and Z. Fan, "Analysis method of the cavitation vibration signals in poppet valve based on EEMD," *Advances in Mechanical Engineering,* vol. 13, no. 2, p. 1687814021998114, 2021.
[141] Z. Maizelis, M. Roukes, and M. Dykman, "Detecting and characterizing frequency fluctuations of vibrational modes," *Physical Review B—Condensed Matter and Materials Physics,* vol. 84, no. 14, p. 144301, 2011.
[142] D. Valentín, A. Presas, C. Valero, M. Egusquiza, and E. Egusquiza, "Detection of hydraulic phenomena in francis turbines with different sensors," *Sensors,* vol. 19, no. 18, p. 4053, 2019.
[143] A. Abdulaziz and A. Kotb, "Detection of pump cavitation by vibration signature," *Australian Journal of Mechanical Engineering,* vol. 15, no. 2, pp. 103-110, 2017.
[144] E. Vagnoni *et al.*, "The new role of sustainable hydropower in flexible energy systems and its technical evolution through innovation and digitalization," *Renewable Energy,* vol. 230, p. 120832, 2024.
[145] V. Brennmoen, "Predictive Maintenance and Analytics in Hydroelectric Power Plants," 2023.
[146] A. Betti, E. Crisostomi, G. Paolinelli, A. Piazzi, F. Ruffini, and M. Tucci, "Condition monitoring and predictive maintenance methodologies for hydropower plants equipment," *Renewable Energy,* vol. 171, pp. 246-253, 2021/06/01/ 2021, doi: https://doi.org/10.1016/j.renene.2021.02.102.
[147] V. Velasquez and W. Flores, "Machine learning approach for predictive maintenance in hydroelectric power plants," in *2022 IEEE Biennial Congress of Argentina (ARGENCON)*, 2022: IEEE, pp. 1-6.
[148] S. Xayyasith, A. Promwungkwa, and K. Ngamsanroaj, "Application of machine learning for predictive maintenance cooling system in Nam Ngum-1 hydropower plant," in *2018*

16th international conference on ICT and knowledge engineering (ICT&KE), 2018: IEEE, pp. 1-5.
[149] X. Lang, H. Nilsson, and W. Mao, "A machine learning based analysis of bearing vibrations for predictive maintenance in a hydropower plant," in *IOP Conference Series: Earth and Environmental Science*, 2024, vol. 1411, no. 1: IOP Publishing, p. 012046.
[150] J. Cen, Z. Yang, X. Liu, J. Xiong, and H. Chen, "A review of data-driven machinery fault diagnosis using machine learning algorithms," *Journal of Vibration Engineering & Technologies,* vol. 10, no. 7, pp. 2481-2507, 2022.
[151] S. Manikandan and K. Duraivelu, "Fault diagnosis of various rotating equipment using machine learning approaches–A review," *Proceedings of the Institution of Mechanical Engineers, Part E: Journal of Process Mechanical Engineering,* vol. 235, no. 2, pp. 629-642, 2021.
[152] D. Juying, J. Tang, H. Shuzhan, and Y. Wang, "Signal-Based Intelligent Hydraulic Fault Diagnosis Methods: Review and Prospects," *Chinese Journal of Mechanical Engineering= Ji xie gong cheng xue bao,* vol. 32, no. 1, 2019.
[153] W. Zhang, D. Yang, and H. Wang, "Data-Driven Methods for Predictive Maintenance of Industrial Equipment: A Survey," *IEEE Systems Journal,* vol. 13, no. 3, pp. 2213-2227, 2019, doi: 10.1109/JSYST.2019.2905565.
[154] C. E. Sunal, V. Dyo, and V. Velisavljevic, "Review of machine learning based fault detection for centrifugal pump induction motors," *IEEE access,* vol. 10, pp. 71344-71355, 2022.
[155] W. Jiang, Z. Li, J. Li, Y. Zhu, and P. Zhang, "Study on a fault identification method of the hydraulic pump based on a combination of voiceprint characteristics and extreme learning machine," *Processes,* vol. 7, no. 12, p. 894, 2019.
[156] H. A. Saeed, M.-j. Peng, H. Wang, and B.-w. Zhang, "Novel fault diagnosis scheme utilizing deep learning networks," *Progress in Nuclear Energy,* vol. 118, p. 103066, 2020.
[157] A. Mallak and M. Fathi, "Sensor and component fault detection and diagnosis for hydraulic machinery integrating LSTM autoencoder detector and diagnostic classifiers," *Sensors,* vol. 21, no. 2, p. 433, 2021.
[158] D. Z. Fawwaz and S.-H. Chung, "Real-time and robust hydraulic system fault detection via edge computing," *Applied Sciences,* vol. 10, no. 17, p. 5933, 2020.
[159] J. Liu, H. Xu, X. Peng, J. Wang, and C. He, "Reliable composite fault diagnosis of hydraulic systems based on linear discriminant analysis and multi-output hybrid kernel extreme learning machine," *Reliability Engineering & System Safety,* vol. 234, p. 109178, 2023.
[160] Q. Liu and M. Li, "Research on hydraulic system fault diagnosis method based on machine learning," *Engineering Research Express,* vol. 7, no. 1, p. 015401, 2025.
[161] N. E. Sepulveda and J. Sinha, "Parameter optimisation in the vibration-based machine learning model for accurate and reliable faults diagnosis in rotating machines," *Machines,* vol. 8, no. 4, p. 66, 2020.
[162] N. F. Espinoza Sepúlveda and J. K. Sinha, "Blind application of developed smart vibration-based machine learning (SVML) model for machine faults diagnosis to different machine conditions," *Journal of Vibration Engineering & Technologies,* vol. 9, pp. 587-596, 2021.
[163] K. M. Almutairi and J. K. Sinha, "Experimental vibration data in fault diagnosis: a machine learning approach to robust classification of rotor and bearing defects in rotating machines," *Machines,* vol. 11, no. 10, p. 943, 2023.
[164] K. Almutairi, J. K. Sinha, and H. Wen, "Fault Detection of Rotating Machines Using poly-Coherent Composite Spectrum of Measured Vibration Responses with Machine Learning," *Machines,* vol. 12, no. 8, p. 573, 2024.
[165] N. Sakthivel, V. Sugumaran, and S. Babudevasenapati, "Vibration based fault diagnosis of monoblock centrifugal pump using decision tree," *Expert Systems with Applications,* vol. 37, no. 6, pp. 4040-4049, 2010.

[166] N. Sakthivel, V. Sugumaran, and B. B. Nair, "Comparison of decision tree-fuzzy and rough set-fuzzy methods for fault categorization of mono-block centrifugal pump," *Mechanical systems and signal processing,* vol. 24, no. 6, pp. 1887-1906, 2010.
[167] M. B. Castellanos, A. L. Serpa, J. L. Biazussi, W. M. Verde, and N. d. S. D. A. Sassim, "Fault identification using a chain of decision trees in an electrical submersible pump operating in a liquid-gas flow," *Journal of Petroleum Science and Engineering,* vol. 184, p. 106490, 2020.
[168] A. K. Panda, J. S. Rapur, and R. Tiwari, "Prediction of flow blockages and impending cavitation in centrifugal pumps using Support Vector Machine (SVM) algorithms based on vibration measurements," *Measurement,* vol. 130, pp. 44-56, 2018.
[169] D. Goyal, A. Choudhary, B. Pabla, and S. Dhami, "Support vector machines based non-contact fault diagnosis system for bearings," *Journal of Intelligent Manufacturing,* vol. 31, pp. 1275-1289, 2020.
[170] Y. Wang, Q. Ma, Q. Zhu, X. Liu, and L. Zhao, "An intelligent approach for engine fault diagnosis based on Hilbert–Huang transform and support vector machine," *Applied acoustics,* vol. 75, pp. 1-9, 2014.
[171] S.-L. Lin, "Application of machine learning to a medium Gaussian support vector machine in the diagnosis of motor bearing faults," *Electronics,* vol. 10, no. 18, p. 2266, 2021.
[172] X. Zhu, J. Xiong, and Q. Liang, "Fault diagnosis of rotation machinery based on support vector machine optimized by quantum genetic algorithm," *IEEE Access,* vol. 6, pp. 33583-33588, 2018.
[173] P. Konar and P. Chattopadhyay, "Bearing fault detection of induction motor using wavelet and Support Vector Machines (SVMs)," *Applied Soft Computing,* vol. 11, no. 6, pp. 4203-4211, 2011.
[174] D. V. Carvalho, E. M. Pereira, and J. S. Cardoso, "Machine learning interpretability: A survey on methods and metrics," *Electronics,* vol. 8, no. 8, p. 832, 2019.
[175] C. Molnar, *Interpretable machine learning*. Lulu. com, 2020.
[176] R. Kumar, *Research Methodology: A Step-By-Step Guide for Beginners*. Pearson Education, 2018.
[177] M. Saunders, P. Lewis, and A. Thornhill, *Research Methods for Business Students*. Essex: Pearson Professional Limited, 2016.
[178] A. Ferrari, "Fluid dynamics of acoustic and hydrodynamic cavitation in hydraulic power systems," *Proceedings of the Royal Society A: Mathematical, Physical and Engineering Sciences,* vol. 473, no. 2199, p. 20160345, 2017.
[179] D. Dixon, "" Fish Friendly" Hydropower Turbine Development and Deployment. Alden Turbine Preliminary Engineering and Model Testing," Electric Power Research Institute, Palo Alto, CA (United States), 2011.
[180] T. Lei, Z. B. Shan, C. S. Liang, W. Y. Chuan, and W. B. Bin, "Numerical Simulation of Unsteady Cavitation Flow in a Centrifugal pump at Off-design Conditions," *Proc IMechE Part C: Journal of Mechanical Engineering Science,* vol. 228, no. 11, pp. 1994-2006, 2013.
[181] J. Lu, S. Yuan, Y. Luo, B. Zhou, and H. Sun, "Numerical anf Experimental Investigation on the Development of Cavitation in a Centrifugal Pump," *Journal of Process Mechanical Engineering,* vol. 0, no. 0, pp. 1-12, 2014.
[182] F. R. Menter, "Two-equation eddy-viscosity turbulence models for engineering applications," *AIAA journal,* vol. 32, no. 8, pp. 1598-1605, 1994.
[183] B. C. Ismail, G. Urmila, J. R. Patrick, J. F. Christopher, C. Hugh, and P. E. Raad, "Procedure for estimation and reporting of uncertainty due to discretization in CFD applications," *J. Fluids Eng,* vol. 130, no. 7, p. 078001, 2008.
[184] International Electrotechnical Commission, *IEC 60193 - Hydraulic Turbines, Storage Pumps and Pump-Turbines Model Acceptance Tests*, Geneva, Switzerland, International Standard 1999.
[185] W. Li and Y. Zhang, "Numerical simulation of cavitating flow in a centrifugal pump as turbine," *Proceedings of the Institution of Mechanical Engineers, Part E: Journal of*

Process Mechanical Engineering, vol. 232, no. 2, pp. 135-154, 2016, doi: 10.1177/0954408916686126.
[186] C. Alatorre-Frenk, "Cost minimisation in micro-hydro systems using pumps-as-turbines," Doctor of Philosophy, Department of Engineering, Faculty of Science, University of Warwick, Warwick, 1994.
[187] K. Shukla, S. Nefti-Meziani, and S. Davis, "A heuristic approach on predictive maintenance techniques: Limitations and scope," *Advances in Mechanical Engineering,* vol. 14, no. 6, p. 16878132221101009, 2022, doi: 10.1177/16878132221101009.
[188] A. Yunusa-Kaltungo, *Vibration-based condition monitoring of rotating machines*. The University of Manchester (United Kingdom), 2015.
[189] D. Novara and A. McNabola, "A model for the extrapolation of the characteristic curves of pumps as turbines from a datum best efficiency point," *Energy Conversion and Management,* vol. 174, pp. 1-7, 2018.
[190] K. Kan *et al.*, "Pump as turbine cavitation performance for both conventional and reverse operating modes: A review," *Renewable and Sustainable Energy Reviews,* vol. 168, p. 112786, 2022.
[191] J. N. Kutz, S. L. Brunton, B. W. Brunton, and J. L. Proctor, *Dynamic mode decomposition: data-driven modeling of complex systems*. SIAM, 2016.
[192] J. N. Kutz, *Data-driven modeling & scientific computation: methods for complex systems & big data*. OUP Oxford, 2013.
[193] B. Xu, L. Zhang, W. Zhang, Y. Deng, and T. N. Wong, "Data-Driven Modal Decomposition Methods as Feature Detection Techniques for Flow Fields in Hydraulic Machinery: A Mini Review," *Journal of Marine Science and Engineering,* vol. 12, no. 5, p. 813, 2024.
[194] P. Holmes, J. L. Lumley, and G. Berkooz, *Turbulence, Coherent Structures, Dynamical Systems and Symmetry* (Cambridge Monographs on Mechanics). Cambridge: Cambridge University Press, 1996.
[195] "SECTION 5-4 - Standard Responses," in *Op Amp Applications Handbook*, W. Jung Ed. Burlington: Newnes, 2005, pp. 325-348.
[196] R. Pintelon and J. Schoukens, "Real-time integration and differentiation of analog signals by means of digital filtering," *IEEE Transactions on Instrumentation and Measurement,* vol. 39, no. 6, pp. 923-927, 1990.
[197] H. Austerlitz, "CHAPTER 4 - Analog/Digital Conversions," in *Data Acquisition Techniques Using PCs (Second Edition)*, H. Austerlitz Ed. San Diego: Academic Press, 2003, pp. 51-77.
[198] O. Surucu, S. A. Gadsden, and J. Yawney, "Condition monitoring using machine learning: A review of theory, applications, and recent advances," *Expert Systems with Applications,* vol. 221, p. 119738, 2023.
[199] X. Ying, "An overview of overfitting and its solutions," in *Journal of physics: Conference series*, 2019, vol. 1168: IOP Publishing, p. 022022.
[200] D. J. Perangin-Angin and F. A. Bachtiar, "Classification of stress in office work activities using extreme learning machine algorithm and one-way anova f-test feature selection," in *2021 4th International Seminar on Research of Information Technology and Intelligent Systems (ISRITI)*, 2021: IEEE, pp. 503-508.
[201] B. Raufi and L. Longo, "Comparing ANOVA and PowerShap Feature Selection Methods via Shapley Additive Explanations of Models of Mental Workload Built with the Theta and Alpha EEG Band Ratios," *BioMedInformatics,* vol. 4, no. 1, pp. 853-876, 2024.
[202] N. O. F. Elssied, O. Ibrahim, and A. H. Osman, "A novel feature selection based on one-way anova f-test for e-mail spam classification," *Research Journal of Applied Sciences, Engineering and Technology,* vol. 7, no. 3, pp. 625-638, 2014.
[203] L. H. Chiang, E. L. Russell, and R. D. Braatz, *Fault detection and diagnosis in industrial systems*. Springer Science & Business Media, 2000.
[204] A. K. Nandi, C. Liu, and M. D. Wong, "Intelligent vibration signal processing for condition monitoring," in *Proceedings of the International Conference Surveillance*, 2013, vol. 7, pp. 1-15.

[205] S. J. Wright, "Numerical optimization," ed, 2006.
[206] L. Jack and A. Nandi, "Fault detection using support vector machines and artificial neural networks, augmented by genetic algorithms," *Mechanical systems and signal processing,* vol. 16, no. 2-3, pp. 373-390, 2002.
[207] A. Widodo and B.-S. Yang, "Support vector machine in machine condition monitoring and fault diagnosis," *Mechanical systems and signal processing,* vol. 21, no. 6, pp. 2560-2574, 2007.
[208] C. Rudin, "Stop explaining black box machine learning models for high stakes decisions and use interpretable models instead," *Nature machine intelligence,* vol. 1, no. 5, pp. 206-215, 2019.
[209] T. Hastie, R. Tibshirani, and J. Friedman, "The elements of statistical learning," ed: Citeseer, 2009.
[210] S. Martín del Campo Barraza, "Unsupervised feature learning applied to condition monitoring," Luleå University of Technology, 2017.
[211] I. H. Witten and E. Frank, *Data Mining: Practical Machine Learning Tools and Techniques, Second Edition (Morgan Kaufmann Series in Data Management Systems)*. Morgan Kaufmann Publishers Inc., 2005.
[212] W. Li, T. Shi, G. Liao, and S. Yang, "Feature extraction and classification of gear faults using principal component analysis," *Journal of Quality in Maintenance Engineering,* vol. 9, no. 2, pp. 132-143, 2003.
[213] H. Ahmed and A. K. Nandi, *Condition monitoring with vibration signals: Compressive sampling and learning algorithms for rotating machines*. John Wiley & Sons, 2020.
[214] Á. Gómez Asensio, "Unsupervised Learning for Condition Monitoring," 2019.
[215] S. Gupta, A. Kumar, and J. Maiti, "A critical review on system architecture, techniques, trends and challenges in intelligent predictive maintenance," *Safety Science,* vol. 177, p. 106590, 2024.
[216] A. Cachada *et al.*, "Maintenance 4.0: Intelligent and predictive maintenance system architecture," in *2018 IEEE 23rd international conference on emerging technologies and factory automation (ETFA)*, 2018, vol. 1: IEEE, pp. 139-146.
[217] M. Syafrudin, G. Alfian, N. L. Fitriyani, and J. Rhee, "Performance analysis of IoT-based sensor, big data processing, and machine learning model for real-time monitoring system in automotive manufacturing," *Sensors,* vol. 18, no. 9, p. 2946, 2018.
[218] Y. Bouabdallaoui, Z. Lafhaj, P. Yim, L. Ducoulombier, and B. Bennadji, "Predictive maintenance in building facilities: A machine learning-based approach," *Sensors,* vol. 21, no. 4, p. 1044, 2021.
[219] J. Lee, S. D. Noh, H.-J. Kim, and Y.-S. Kang, "Implementation of cyber-physical production systems for quality prediction and operation control in metal casting," *Sensors,* vol. 18, no. 5, p. 1428, 2018.
[220] L. Selak, P. Butala, and A. Sluga, "Condition monitoring and fault diagnostics for hydropower plants," *Computers in Industry,* vol. 65, no. 6, pp. 924-936, 2014.
[221] S. Jad, X. Desforges, K. Medjaher, P.-Y. Villard, and C. Caussidéry, "Condition monitoring and diagnostic of hydropower units based on machine learning techniques," *Renewable Energy,* p. 123210, 2025.

APPENDIX A – INSTRUMENTATION AND CALIBRATION CERTIFICATES

A1. Images of the instruments used for data acquisition

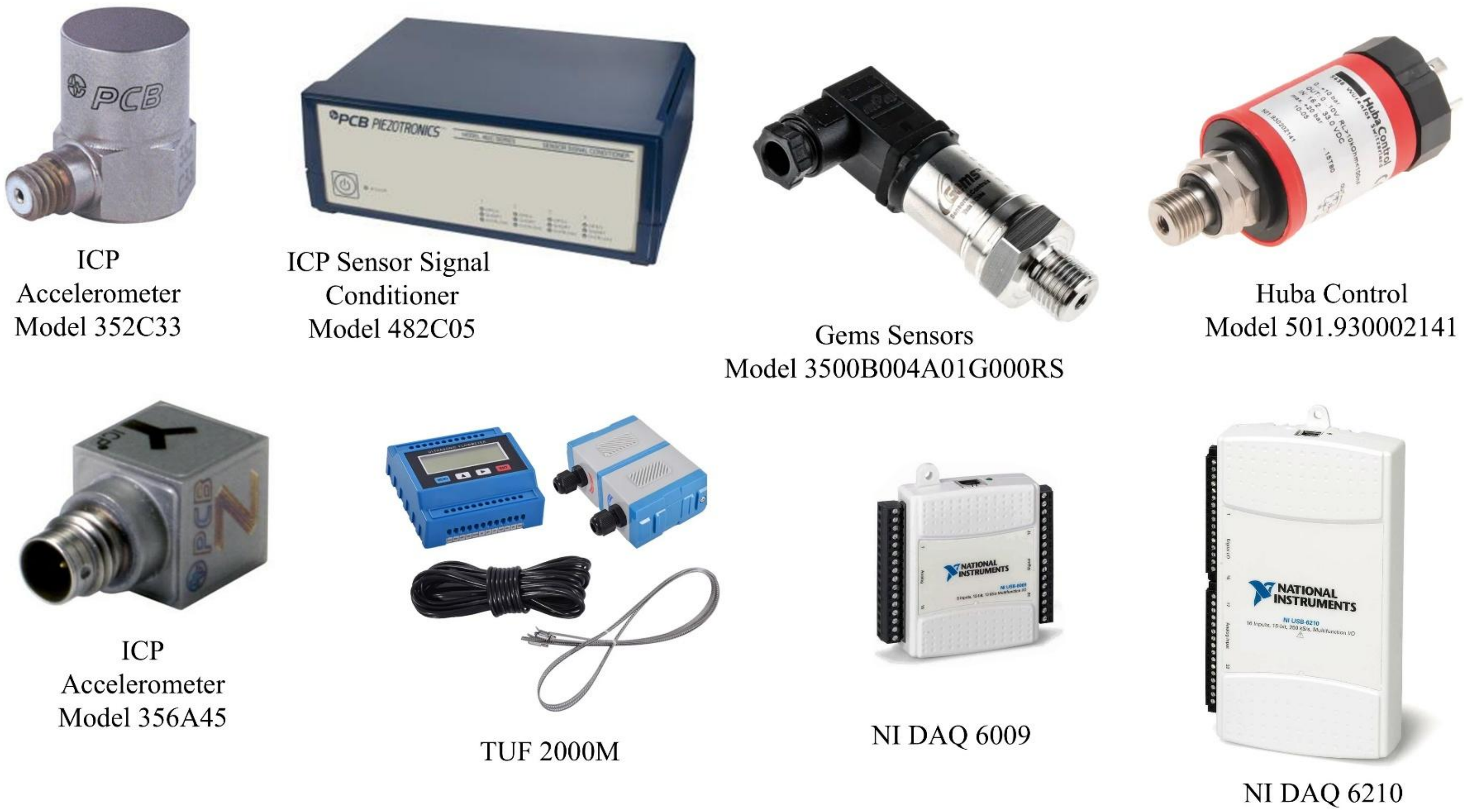

Figure A1. List of instrumentation equipment used for data acquisition

A2. Calibration Certificates for accelerometers and the signal conditioner unit

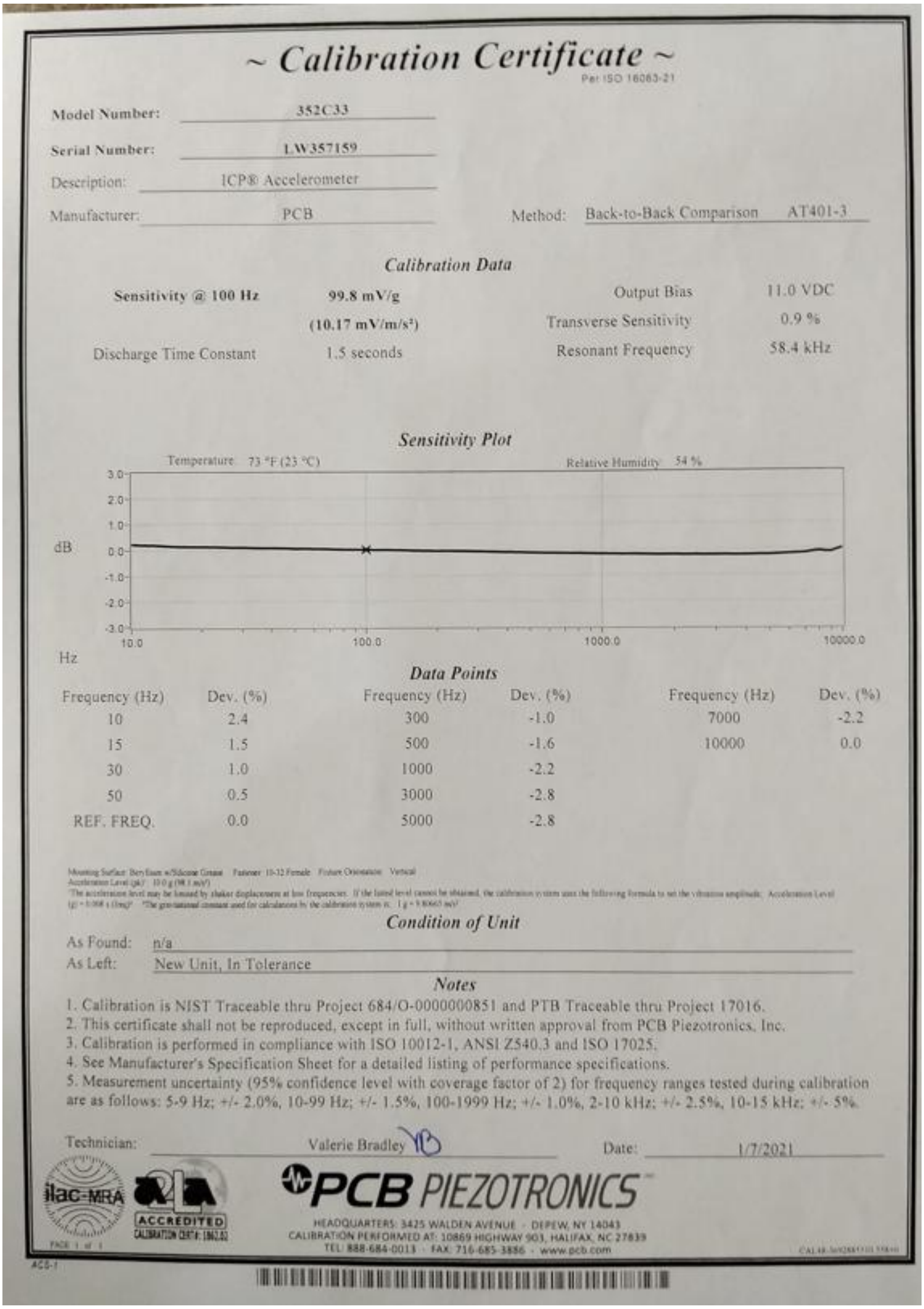

~ *Calibration Certificate* ~

Per ISO 16063-21

Model Number: 352C33

Serial Number: LW357159

Description: ICP® Accelerometer

Manufacturer: PCB

Method: Back-to-Back Comparison AT401-3

Calibration Data

Sensitivity @ 100 Hz	**99.8 mV/g**	Output Bias	11.0 VDC
	(10.17 mV/m/s²)	Transverse Sensitivity	0.9 %
Discharge Time Constant	1.5 seconds	Resonant Frequency	58.4 kHz

Sensitivity Plot

Data Points

Frequency (Hz)	Dev. (%)	Frequency (Hz)	Dev. (%)	Frequency (Hz)	Dev. (%)
10	2.4	300	-1.0	7000	-2.2
15	1.5	500	-1.6	10000	0.0
30	1.0	1000	-2.2		
50	0.5	3000	-2.8		
REF. FREQ.	0.0	5000	-2.8		

Condition of Unit

As Found: n/a

As Left: New Unit, In Tolerance

Notes

1. Calibration is NIST Traceable thru Project 684/O-0000000851 and PTB Traceable thru Project 17016.
2. This certificate shall not be reproduced, except in full, without written approval from PCB Piezotronics, Inc.
3. Calibration is performed in compliance with ISO 10012-1, ANSI Z540.3 and ISO 17025.
4. See Manufacturer's Specification Sheet for a detailed listing of performance specifications.
5. Measurement uncertainty (95% confidence level with coverage factor of 2) for frequency ranges tested during calibration are as follows: 5-9 Hz; +/- 2.0%, 10-99 Hz; +/- 1.5%, 100-1999 Hz; +/- 1.0%, 2-10 kHz; +/- 2.5%, 10-15 kHz; +/- 5%.

Technician: Valerie Bradley VB

Date: 1/7/2021

PCB PIEZOTRONICS

HEADQUARTERS: 3425 WALDEN AVENUE · DEPEW, NY 14043
CALIBRATION PERFORMED AT: 10869 HIGHWAY 903, HALIFAX, NC 27839
TEL: 888-684-0013 · FAX: 716-685-3886 · www.pcb.com

Figure A2. Calibration certificate for the bearing x-dir accelerometer

~ Calibration Certificate ~

Per ISO 16063-21

Model Number: 352C33

Serial Number: LW357647

Description: ICP® Accelerometer

Manufacturer: PCB

Method: Back-to-Back Comparison AT401-3

Calibration Data

Sensitivity @ 100 Hz	**100.1 mV/g**	Output Bias	10.9 VDC
	(10.21 mV/m/s²)	Transverse Sensitivity	1.2 %
Discharge Time Constant	1.9 seconds	Resonant Frequency	57.2 kHz

Sensitivity Plot

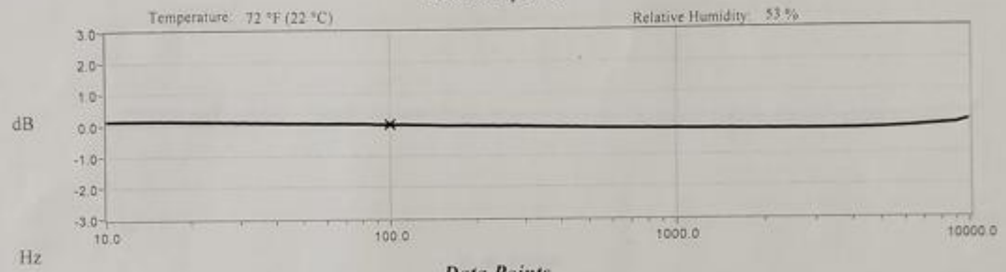

Data Points

Frequency (Hz)	Dev. (%)	Frequency (Hz)	Dev. (%)	Frequency (Hz)	Dev. (%)
10	1.5	300	-1.0	7000	-1.8
15	1.5	500	-1.6	10000	0.3
30	0.8	1000	-2.2		
50	0.4	3000	-2.7		
REF. FREQ.	0.0	5000	-2.6		

Mounting Surface: Beryllium w/Silicone Grease Fastener: 10-32 Female Fixture Orientation: Vertical
Acceleration Level (pk)[1]: 10.0 g (98.1 m/s²)
[1]The acceleration level may be limited by shaker displacement at low frequencies. If the listed level cannot be obtained, the calibration system uses the following formula to set the vibration amplitude: Acceleration Level (g) = 0.008 x (freq)². [2]The gravitational constant used for calculations by the calibration system is: 1 g = 9.80665 m/s².

Condition of Unit

As Found: n/a

As Left: New Unit, In Tolerance

Notes

1. Calibration is NIST Traceable thru Project 684/O-0000000851 and PTB Traceable thru Project 17016.
2. This certificate shall not be reproduced, except in full, without written approval from PCB Piezotronics, Inc.
3. Calibration is performed in compliance with ISO 10012-1, ANSI Z540.3 and ISO 17025.
4. See Manufacturer's Specification Sheet for a detailed listing of performance specifications.
5. Measurement uncertainty (95% confidence level with coverage factor of 2) for frequency ranges tested during calibration are as follows: 5-9 Hz; +/- 2.0%, 10-99 Hz; +/- 1.5%, 100-1999 Hz; +/- 1.0%, 2-10 kHz; +/- 2.5%, 10-15 kHz; +/- 5%.

Technician: Valerie Bradley   Date: 1/7/2021

ilac-MRA   ACCREDITED CALIBRATION CERT #: 1862.02

PCB PIEZOTRONICS

HEADQUARTERS: 3425 WALDEN AVENUE - DEPEW, NY 14043
CALIBRATION PERFORMED AT: 10869 HIGHWAY 903, HALIFAX, NC 27839
TEL: 888-684-0013 - FAX: 716-685-3886 - www.pcb.com

PAGE 1 of 1

ACS-1

Figure A3. Calibration certificate for the bearing y-dir accelerometer

~ Calibration Certificate ~

Per ISO 16063-21

Model Number: 352C33

Serial Number: LW357648

Description: ICP® Accelerometer

Manufacturer: PCB

Method: Back-to-Back Comparison AT401-3

Calibration Data

Sensitivity @ 100 Hz	100.1 mV/g	Output Bias	10.9 VDC
	(10.21 mV/m/s²)	Transverse Sensitivity	1.0 %
Discharge Time Constant	2.2 seconds	Resonant Frequency	57.8 kHz

Sensitivity Plot

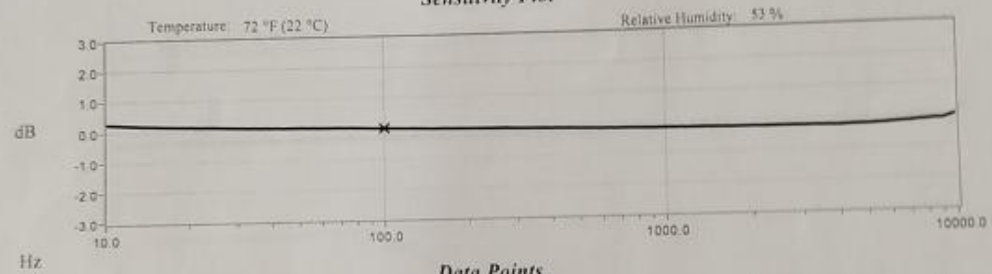

Data Points

Frequency (Hz)	Dev. (%)	Frequency (Hz)	Dev. (%)	Frequency (Hz)	Dev. (%)
10	3.0	300	-1.0	7000	-2.1
15	2.0	500	-1.6	10000	0.0
30	0.9	1000	-2.2		
50	0.5	3000	-2.8		
REF. FREQ.	0.0	5000	-2.8		

Mounting Surface: Beryllium w/Silicone Grease Fastener: 10-32 Female Fixture Orientation: Vertical
Acceleration Level (pk): 10.0 g (98.1 m/s²)
The acceleration level may be limited by shaker displacement at low frequencies. If the listed level cannot be obtained, the calibration system uses the following formula to set the vibration amplitude: Acceleration Level (g) = 0.008 x (freq)² The gravitational constant used for calculations by the calibration system is: 1 g = 9.80665 m/s²

Condition of Unit

As Found: n/a

As Left: New Unit, In Tolerance

Notes

1. Calibration is NIST Traceable thru Project 684/O-0000000851 and PTB Traceable thru Project 17016.
2. This certificate shall not be reproduced, except in full, without written approval from PCB Piezotronics, Inc.
3. Calibration is performed in compliance with ISO 10012-1, ANSI Z540.3 and ISO 17025.
4. See Manufacturer's Specification Sheet for a detailed listing of performance specifications.
5. Measurement uncertainty (95% confidence level with coverage factor of 2) for frequency ranges tested during calibration are as follows: 5-9 Hz; +/- 2.0%, 10-99 Hz; +/- 1.5%, 100-1999 Hz; +/- 1.0%, 2-10 kHz; +/- 2.5%, 10-15 kHz; +/- 5%.

Technician: Valerie Bradley VB

Date: 1/7/2021

ilac-MRA ACCREDITED CALIBRATION CERT# 1862.02

PCB PIEZOTRONICS

HEADQUARTERS: 3425 WALDEN AVENUE - DEPEW, NY 14043
CALIBRATION PERFORMED AT: 10869 HIGHWAY 903, HALIFAX, NC 27839
TEL: 888-684-0013 - FAX: 716-685-3886 - www.pcb.com

PAGE 1 of 1

ACS-1

Figure A4. Calibration certificate for the bearing z-dir accelerometer

~ Calibration Certificate ~

Per ISO 16063-21

Model Number: 356A45

Serial Number: LW300241 (x axis)

Description: ICP® Triaxial Accelerometer

Manufacturer: PCB

Method: Back-to-Back Comparison AT401-3

TEDS: This Sensor has been programmed with IEEE 1451.4 Template 25

Calibration Data

Sensitivity @ 100 Hz	**97.1 mV/g**	Output Bias	11.1 VDC
	(9.90 mV/m/s²)	Transverse Sensitivity	2.5 %
Discharge Time Constant	1.3 seconds		

Sensitivity Plot

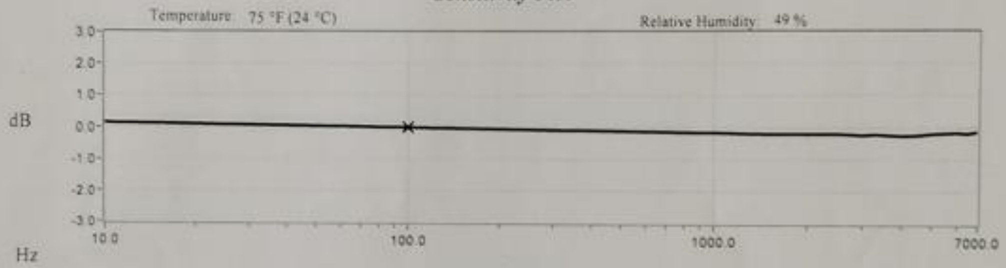

Data Points

Frequency (Hz)	Dev. (%)	Frequency (Hz)	Dev. (%)	Frequency (Hz)	Dev. (%)
10	1.5	300	-1.0	7000	-1.6
15	1.2	500	-1.3		
30	0.7	1000	-1.9		
50	0.4	3000	-2.8		
REF. FREQ.	0.0	5000	-2.3		

Mounting Surface: Beryllium Fastener: Adhesive Fixture Orientation: Inverted Vertical
Acceleration Level (pk): 10.0 g (98.1 m/s²)
The acceleration level may be limited by shaker displacement at low frequencies. If the listed level cannot be obtained, the calibration system uses the following formula to set the vibration amplitude: Acceleration Level (g) = 0.004 x (freq)² The gravitational constant used for calculations by the calibration system is: 1 g = 9.80665 m/s²

Condition of Unit

As Found: n/a

As Left: New Unit, In Tolerance

Notes

1. Calibration is NIST Traceable thru Project 684/O-0000000851 and PTB Traceable thru Project 17016.
2. This certificate shall not be reproduced, except in full, without written approval from PCB Piezotronics, Inc.
3. Calibration is performed in compliance with ISO 10012-1, ANSI Z540.3 and ISO 17025.
4. See Manufacturer's Specification Sheet for a detailed listing of performance specifications.
5. Measurement uncertainty (95% confidence level with coverage factor of 2) for frequency ranges tested during calibration are as follows: 5-9 Hz; +/- 2.0%, 10-99 Hz; +/- 1.5%, 100-1999 Hz; +/- 1.0%, 2-10 kHz; +/- 2.5%, 10-15 kHz; +/- 5%.

Technician: Alec Michalski AM 5269 Date: 12/9/2020

ilac-MRA ACCREDITED

PCB PIEZOTRONICS

3425 WALDEN AVENUE - DEPEW, NY 14043
TEL: 888-684-0013 - FAX: 716-685-3886 - www.pcb.com

Figure A5. Calibration certificate for the flange x-dir accelerometer

~ Calibration Certificate ~

Per ISO 16063-21

Model Number: 356A45

Serial Number: LW300241 (y axis)

Description: ICP® Triaxial Accelerometer

Manufacturer: PCB

Method: Back-to-Back Comparison AT401-3

TEDS: This Sensor has been programmed with IEEE 1451.4 Template 25

Calibration Data

Sensitivity @ 100 Hz	**99.1 mV/g**	Output Bias	11.2 VDC
	(10.10 mV/m/s²)	Transverse Sensitivity	1.6 %
Discharge Time Constant	1.1 seconds		

Sensitivity Plot

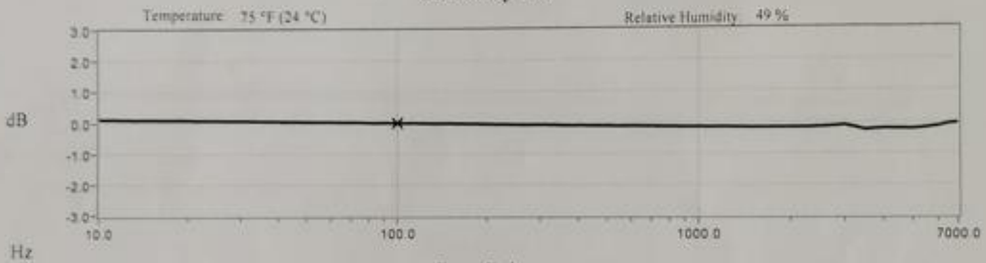

Data Points

Frequency (Hz)	Dev. (%)	Frequency (Hz)	Dev. (%)	Frequency (Hz)	Dev. (%)
10	1.3	300	-0.8	7000	-0.5
15	1.1	500	-1.2		
30	0.7	1000	-1.7		
50	0.4	3000	-1.3		
REF. FREQ.	0.0	5000	-2.6		

Condition of Unit

As Found: n/a

As Left: New Unit, In Tolerance

Notes

1. Calibration is NIST Traceable thru Project 684/O-0000000851 and PTB Traceable thru Project 17016.
2. This certificate shall not be reproduced, except in full, without written approval from PCB Piezotronics, Inc.
3. Calibration is performed in compliance with ISO 10012-1, ANSI Z540.3 and ISO 17025.
4. See Manufacturer's Specification Sheet for a detailed listing of performance specifications.
5. Measurement uncertainty (95% confidence level with coverage factor of 2) for frequency ranges tested during calibration are as follows: 5-9 Hz; +/- 2.0%, 10-99 Hz; +/- 1.5%, 100-1999 Hz; +/- 1.0%, 2-10 kHz; +/- 2.5%, 10-15 kHz; +/- 5%.

Technician: Alec Michalski AM 5269 Date: 12/9/2020

PCB PIEZOTRONICS

3425 WALDEN AVENUE - DEPEW, NY 14043
TEL: 888-684-0013 - FAX: 716-685-3886 - www.pcb.com

ilac-MRA A2LA ACCREDITED CALIBRATION CERT #1862.01

ACS-17

Figure A6. Calibration certificate for the flange y-dir accelerometer

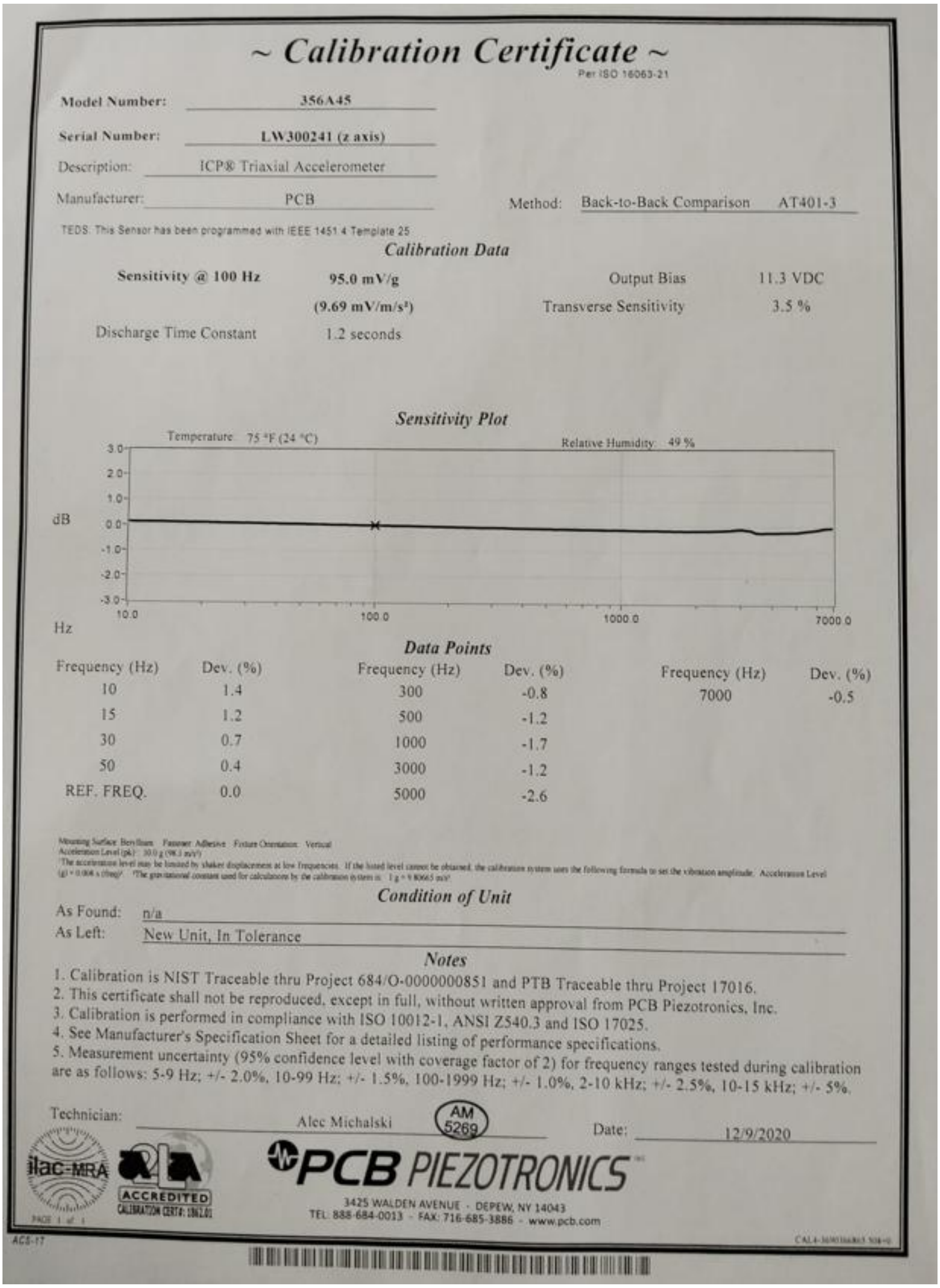

~ Calibration Certificate ~

Per ISO 16063-21

Model Number:	**356A45**		
Serial Number:	**LW300241 (z axis)**		
Description:	ICP® Triaxial Accelerometer		
Manufacturer:	PCB	Method:	Back-to-Back Comparison AT401-3

TEDS: This Sensor has been programmed with IEEE 1451.4 Template 25

Calibration Data

Sensitivity @ 100 Hz	**95.0 mV/g**	Output Bias	11.3 VDC
	(9.69 mV/m/s²)	Transverse Sensitivity	3.5 %
Discharge Time Constant	1.2 seconds		

Sensitivity Plot

Data Points

Frequency (Hz)	Dev. (%)	Frequency (Hz)	Dev. (%)	Frequency (Hz)	Dev. (%)
10	1.4	300	-0.8	7000	-0.5
15	1.2	500	-1.2		
30	0.7	1000	-1.7		
50	0.4	3000	-1.2		
REF. FREQ.	0.0	5000	-2.6		

Mounting Surface: Beryllium Fastener: Adhesive Fixture Orientation: Vertical

Condition of Unit

As Found: n/a

As Left: New Unit, In Tolerance

Notes

1. Calibration is NIST Traceable thru Project 684/O-0000000851 and PTB Traceable thru Project 17016.
2. This certificate shall not be reproduced, except in full, without written approval from PCB Piezotronics, Inc.
3. Calibration is performed in compliance with ISO 10012-1, ANSI Z540.3 and ISO 17025.
4. See Manufacturer's Specification Sheet for a detailed listing of performance specifications.
5. Measurement uncertainty (95% confidence level with coverage factor of 2) for frequency ranges tested during calibration are as follows: 5-9 Hz; +/- 2.0%, 10-99 Hz; +/- 1.5%, 100-1999 Hz; +/- 1.0%, 2-10 kHz; +/- 2.5%, 10-15 kHz; +/- 5%.

Technician: Alec Michalski AM 5269 Date: 12/9/2020

ilac-MRA A2LA ACCREDITED

PCB PIEZOTRONICS

3425 WALDEN AVENUE - DEPEW, NY 14043

TEL: 888-684-0013 - FAX: 716-685-3886 - www.pcb.com

PAGE 1 of 1

ACS-17

Figure A7. Calibration certificate for the flange z-dir accelerometer

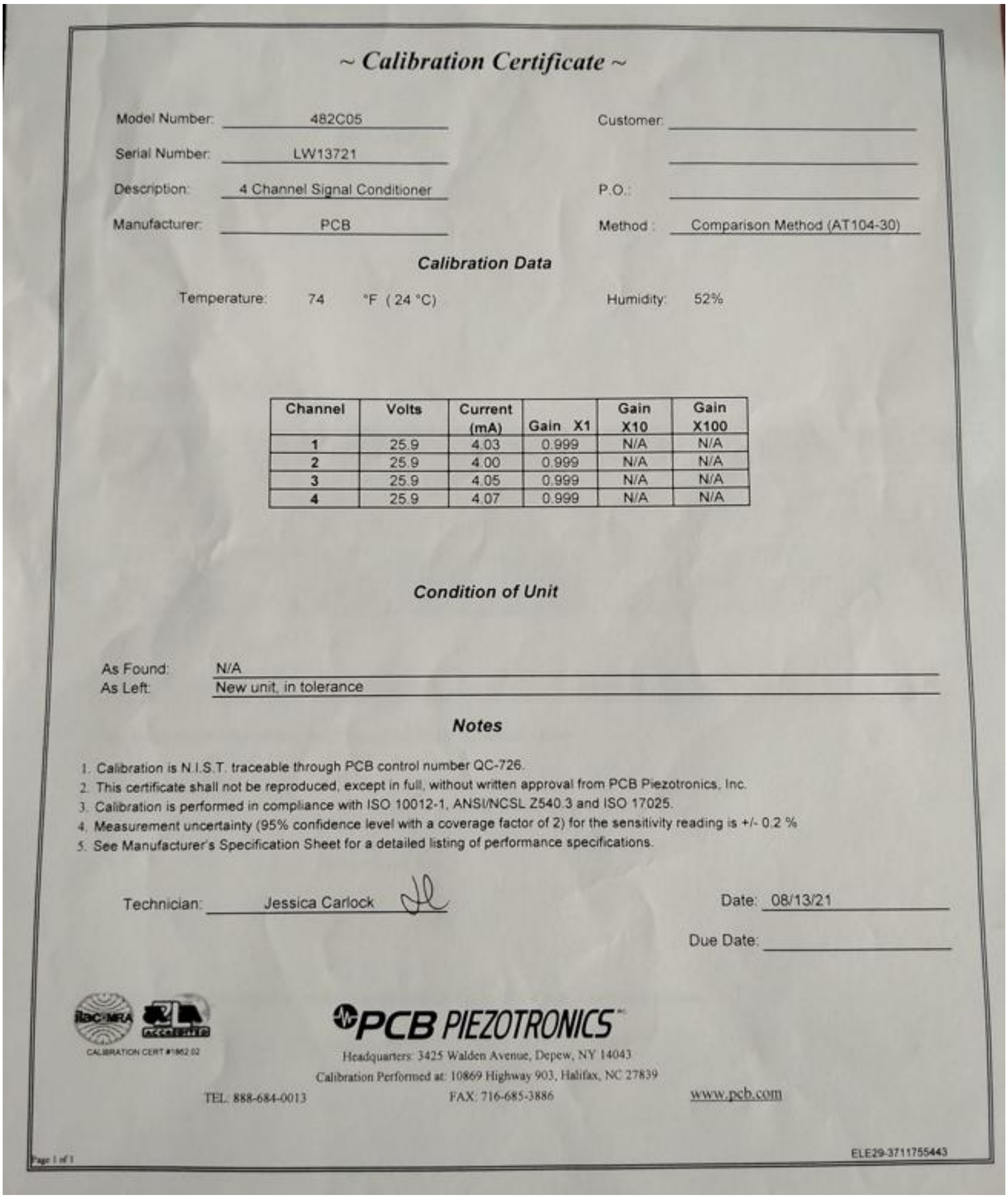

~ Calibration Certificate ~

Model Number: 482C05
Serial Number: LW13721
Description: 4 Channel Signal Conditioner
Manufacturer: PCB

Customer:
P.O.:
Method : Comparison Method (AT104-30)

Calibration Data

Temperature: 74 °F (24 °C) Humidity: 52%

Channel	Volts	Current (mA)	Gain X1	Gain X10	Gain X100
1	25.9	4.03	0.999	N/A	N/A
2	25.9	4.00	0.999	N/A	N/A
3	25.9	4.05	0.999	N/A	N/A
4	25.9	4.07	0.999	N/A	N/A

Condition of Unit

As Found: N/A
As Left: New unit, in tolerance

Notes

1. Calibration is N.I.S.T. traceable through PCB control number QC-726.
2. This certificate shall not be reproduced, except in full, without written approval from PCB Piezotronics, Inc.
3. Calibration is performed in compliance with ISO 10012-1, ANSI/NCSL Z540.3 and ISO 17025.
4. Measurement uncertainty (95% confidence level with a coverage factor of 2) for the sensitivity reading is +/- 0.2 %
5. See Manufacturer's Specification Sheet for a detailed listing of performance specifications.

Technician: Jessica Carlock
Date: 08/13/21
Due Date:

CALIBRATION CERT #1862.02

PCB PIEZOTRONICS

Headquarters: 3425 Walden Avenue, Depew, NY 14043
Calibration Performed at: 10869 Highway 903, Halifax, NC 27839
TEL: 888-684-0013 FAX: 716-685-3886 www.pcb.com

Page 1 of 1 ELE29-3711755443

Figure A8. Calibration certificate for the ICP Sensor Signal Conditioner

APPENDIX B – REPEATABILITY AND VARIABILITY ASSESSMENT OF MEASUREMENTS

To evaluate the repeatability of vibration measurements and assess result variability, a Power Spectral Density (PSD) comparison was conducted between two repeated trials acquired under identical operating conditions. Welch's method was used to compute the PSD of each trial using MATLAB, applying a Hanning window with 50% overlap to minimise spectral leakage. Both PSD plots were plotted in the same figure to visually assess similarity in amplitude and frequency distribution. Below are the results for each of the tested operating point.

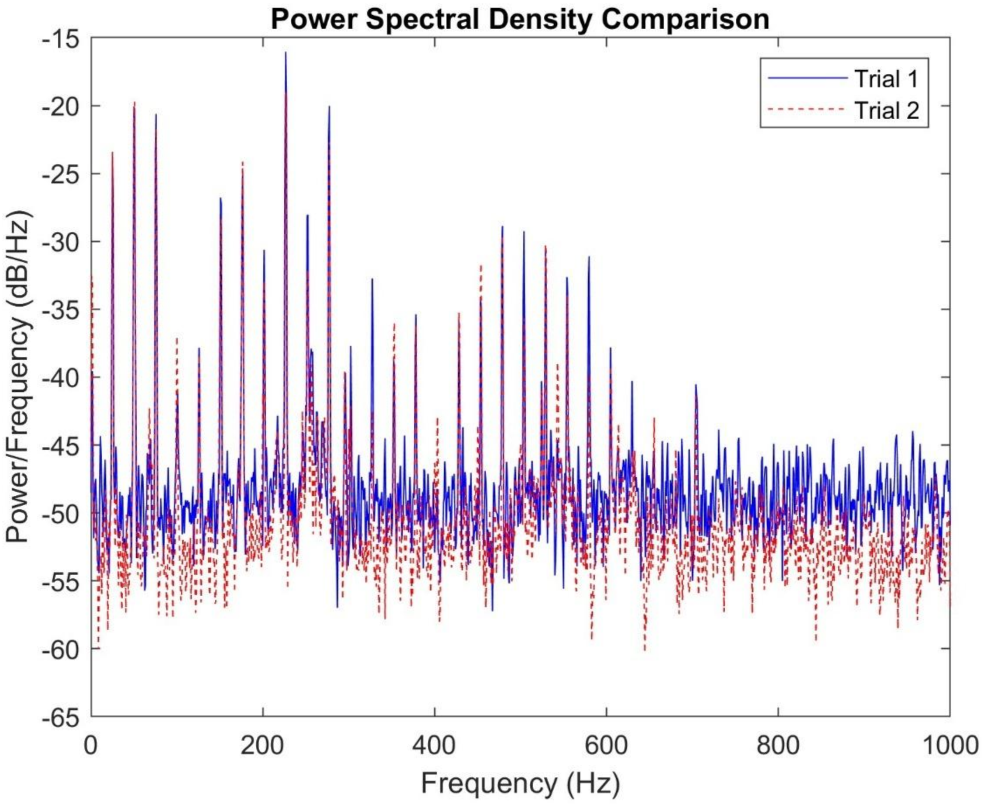

Figure B1. Comparison of trials at Operating point OP1

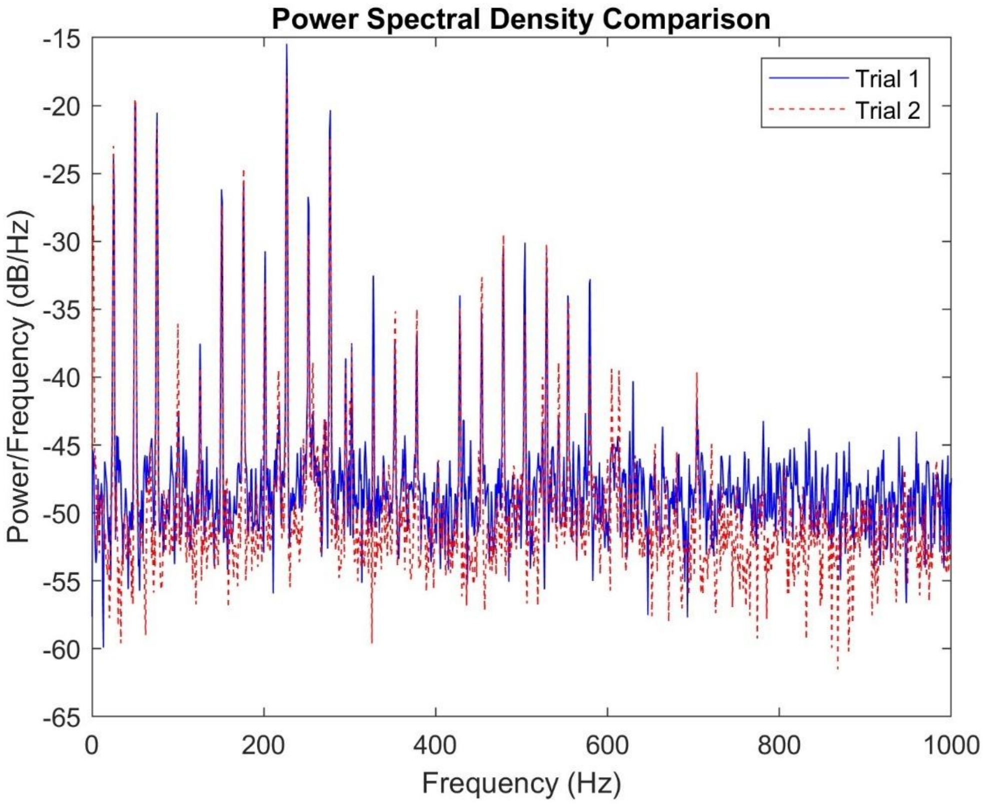

Figure B2. Comparisons at OP2

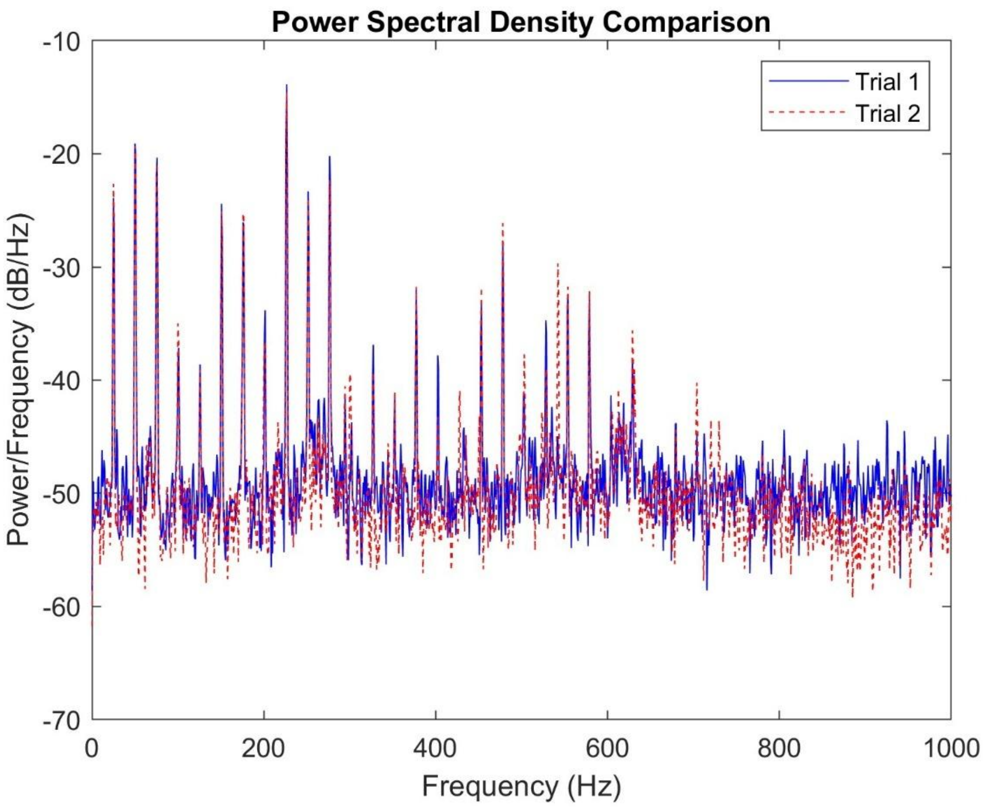

Figure B3. Comparisons at OP3

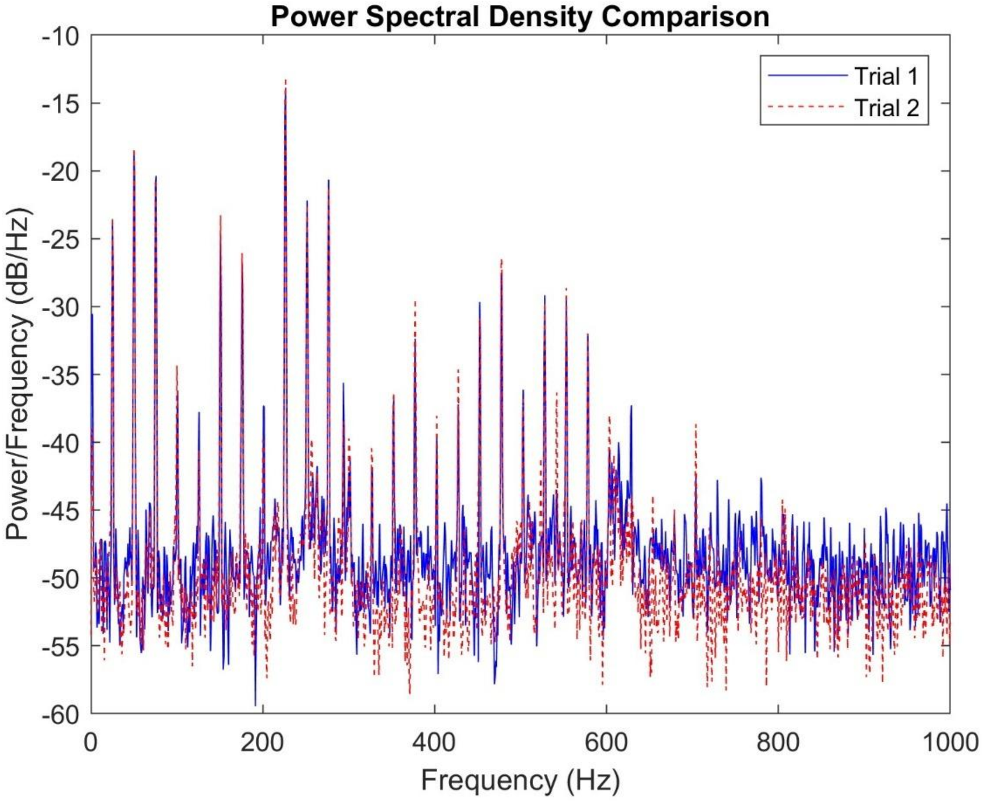

Figure B4. Comparisons at OP4

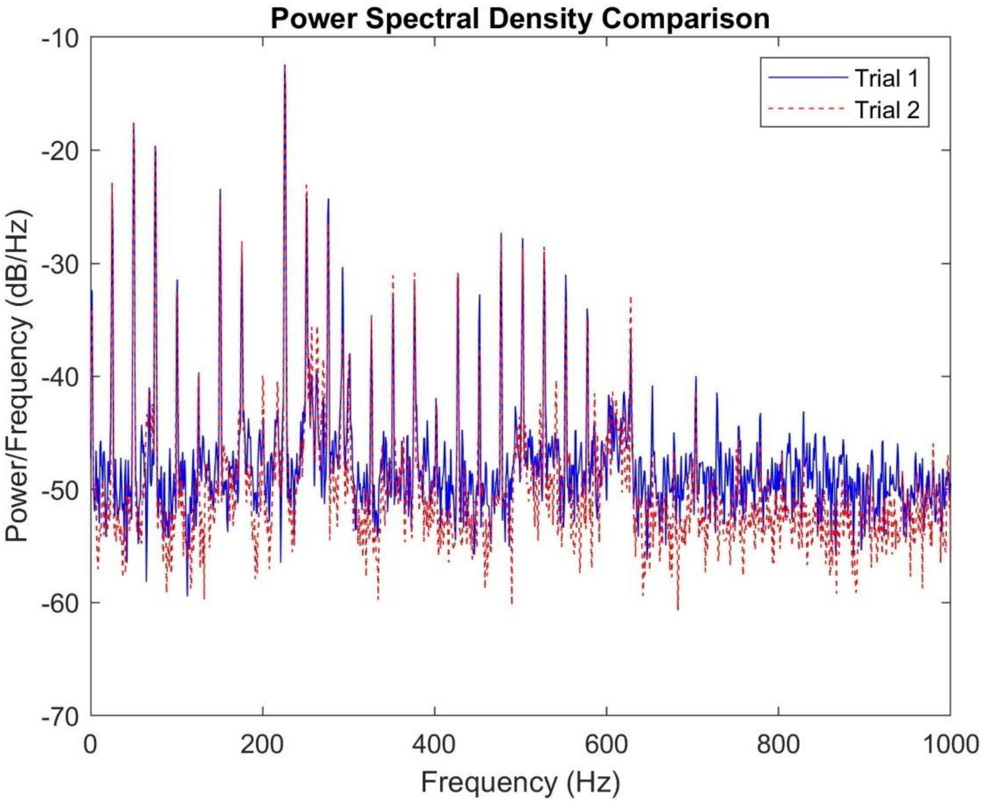

Figure B5. Comparison at OP5

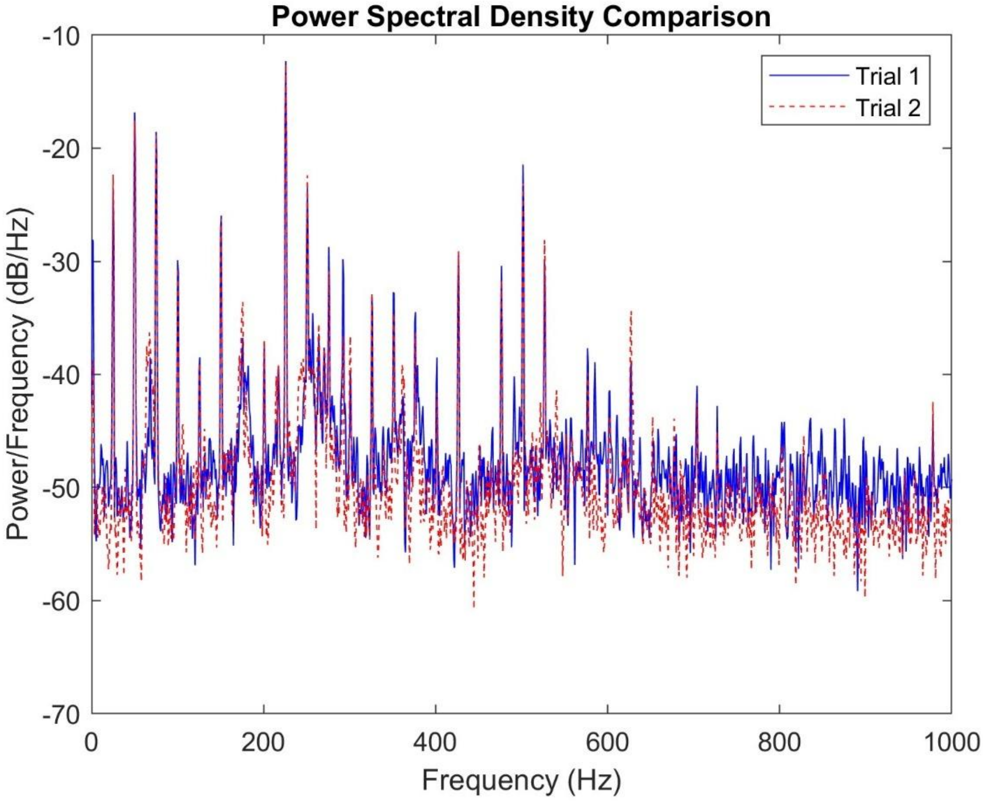

Figure B6. Comparison at OP6

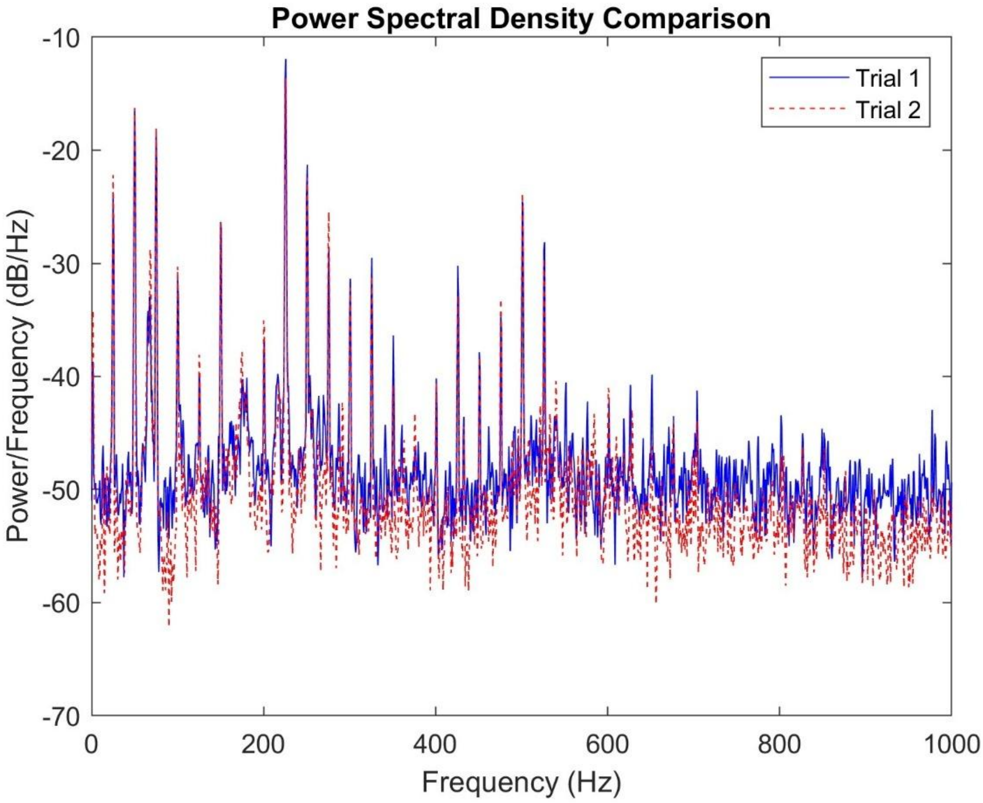

Figure B7. Comparison at OP7

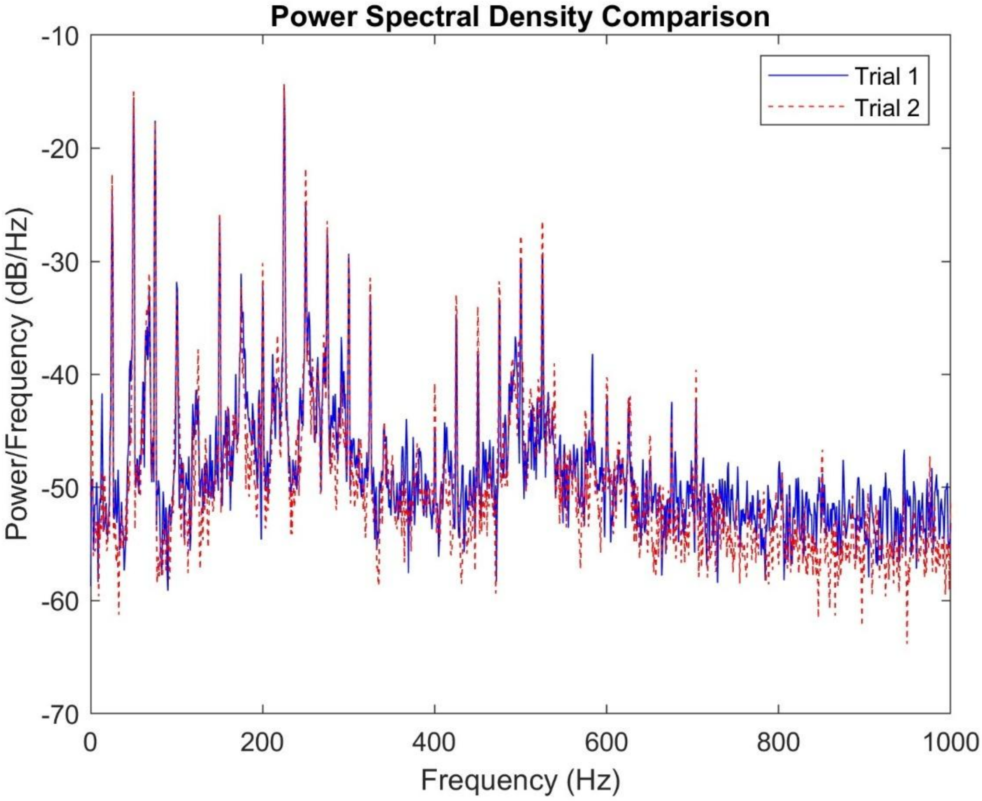

Figure B8. Comparison at OP8

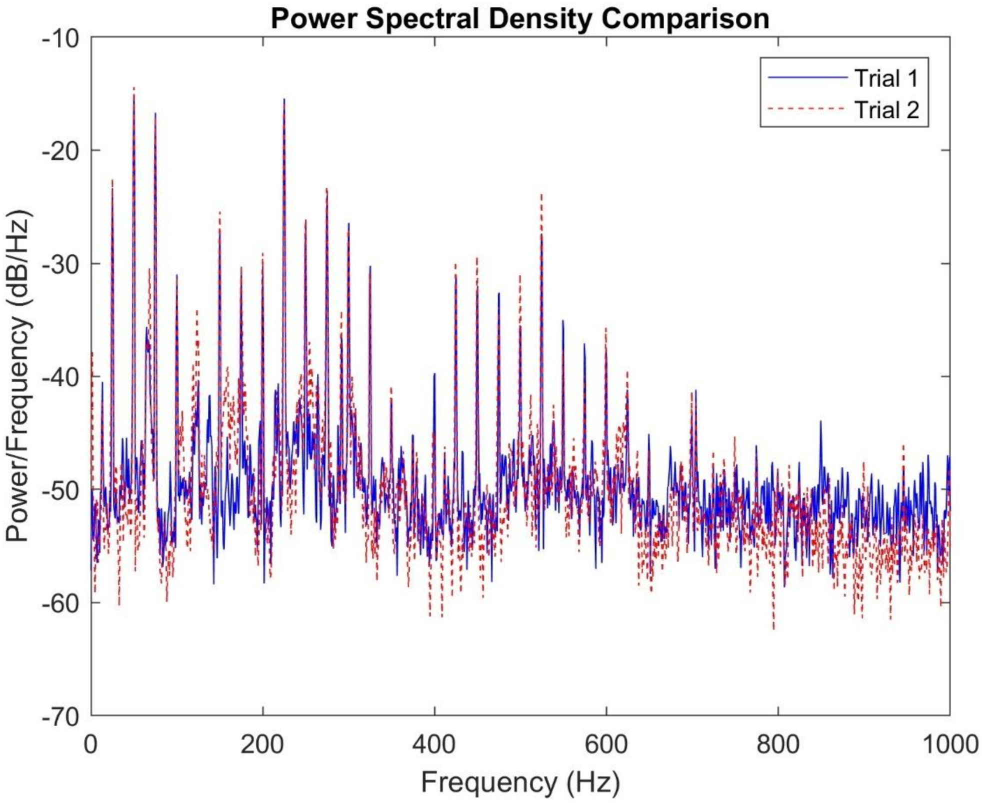

Figure B9. Comparison at OP9

These figures present a PSD comparison between two repeated vibration measurement trials, labelled Trail1 (blue solid line) and Trial 2 (red dashed line), over a frequency range of 0 to 1kHz. The y-axis shows the power per frequency bin (dB/Hz), indicating the energy content of the vibration signals at each frequency.

Overall, the two trials for each of the operating point strongly aligns with one another in the location and magnitude of dominant frequency peaks across the entire frequency spectrum. This close overlap demonstrates good repeatability, as the system consistently produced the same vibrational signature across both trials under identical conditions. The most prominent peaks, especially below 600 Hz, appear in the same position with nearly identical amplitudes. These correspond to structural or fluid induced frequencies that are characteristic of the system, further confirming measurement consistency. Minor deviations in PSD amplitude, particularly in the higher frequency region (above 600Hz) are visible. These are likely due to background noise or environmental fluctuations. However, they do not represent significant variability in the system's mechanical behaviour.

This description supports the conclusion that the vibration measurements are repeatable and exhibit minimal variability, validating the reliability of the experimental data for subsequent analysis. The PSD comparison effectively highlights consistency in system dynamics between repeated measurements.

APPENDIX C – VISUALIZATION OF MONITORING THRESHOLDS FOR THE MODIFIED DND METHOD

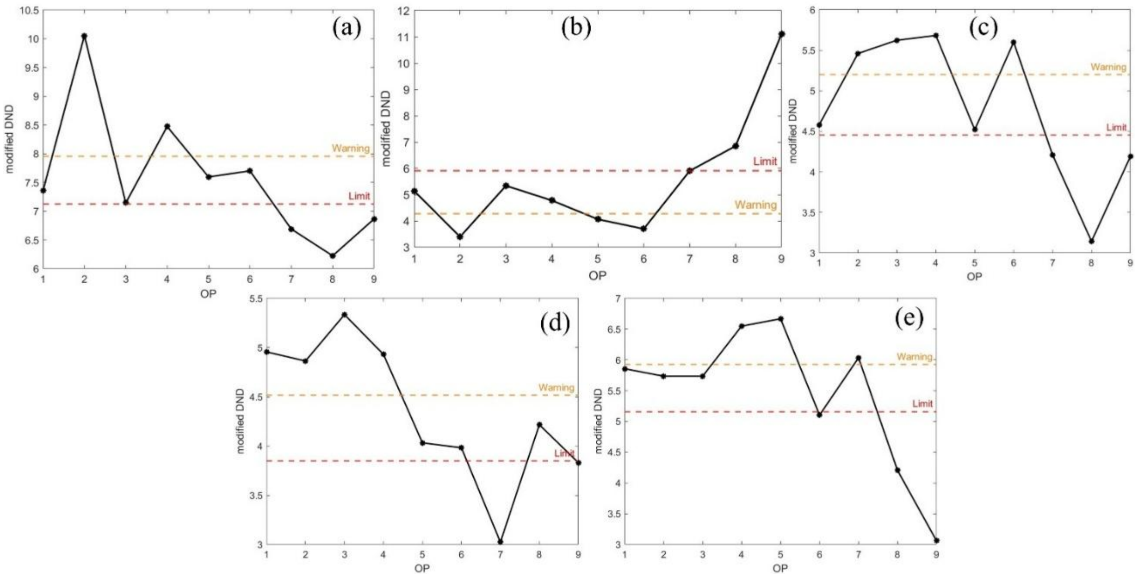

Figure C1. Trend plot with monitoring limits for N = 1800 rpm

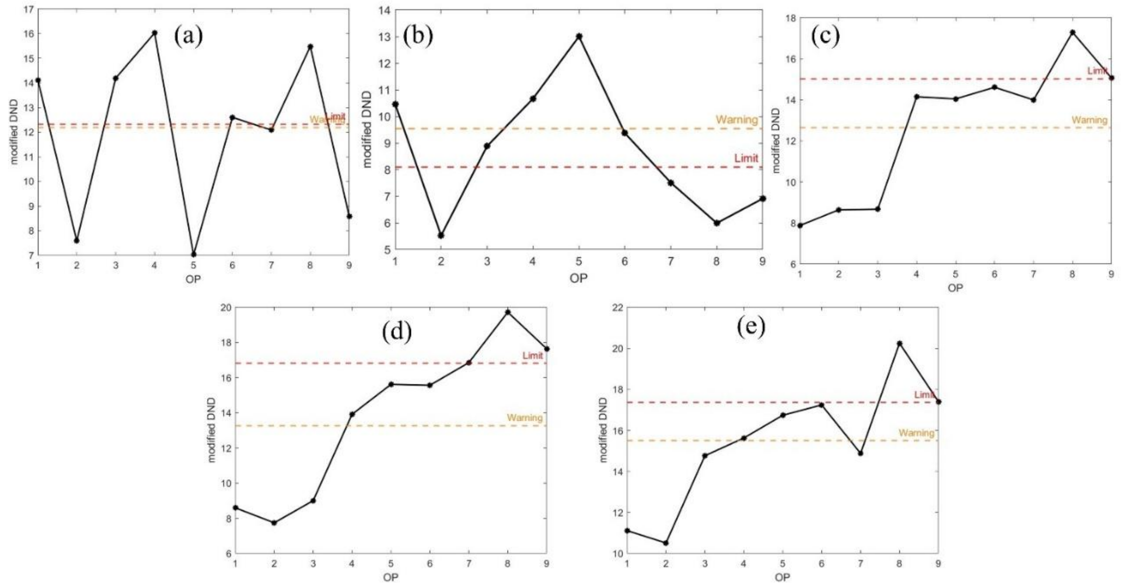

Figure C2. Trend plot with monitoring limits for N = 1650 rpm

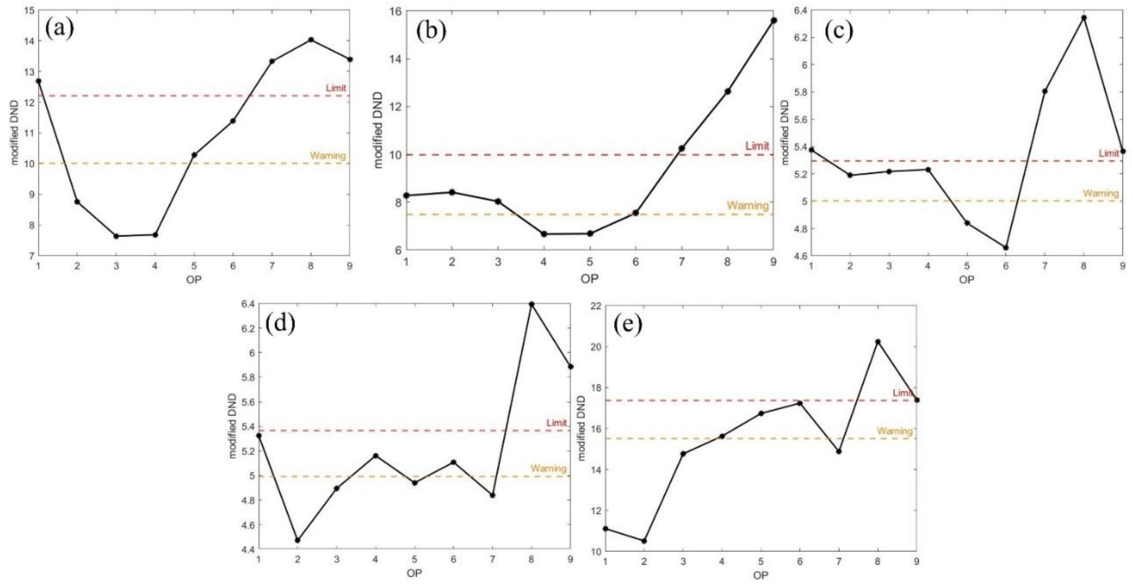

Figure C3. Trend plot with monitoring limits for N = 1500 rpm

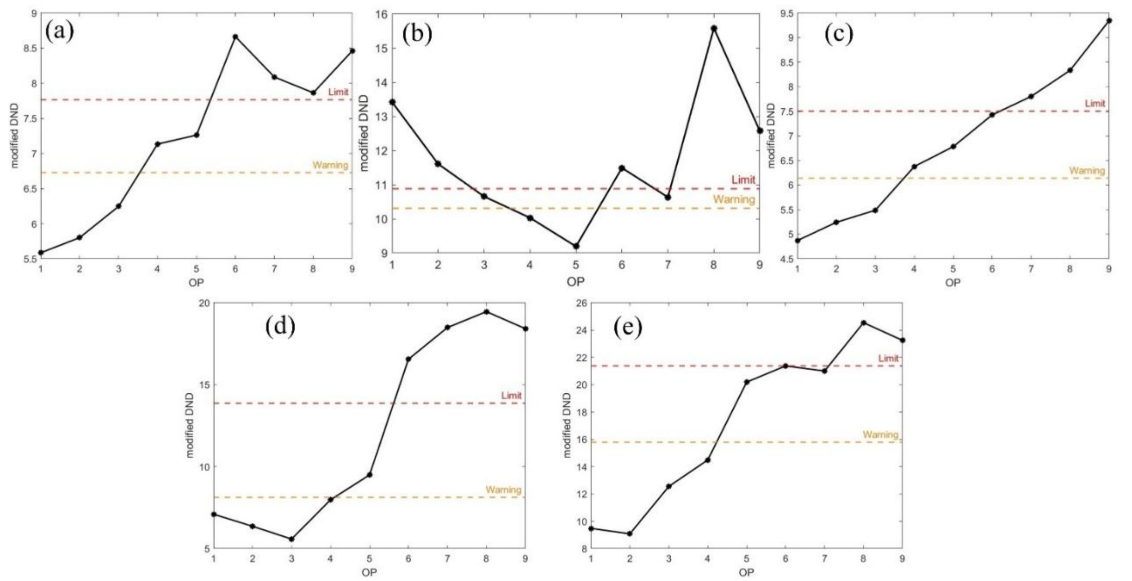

Figure C4. Trend plot with monitoring limits for N = 1350 rpm

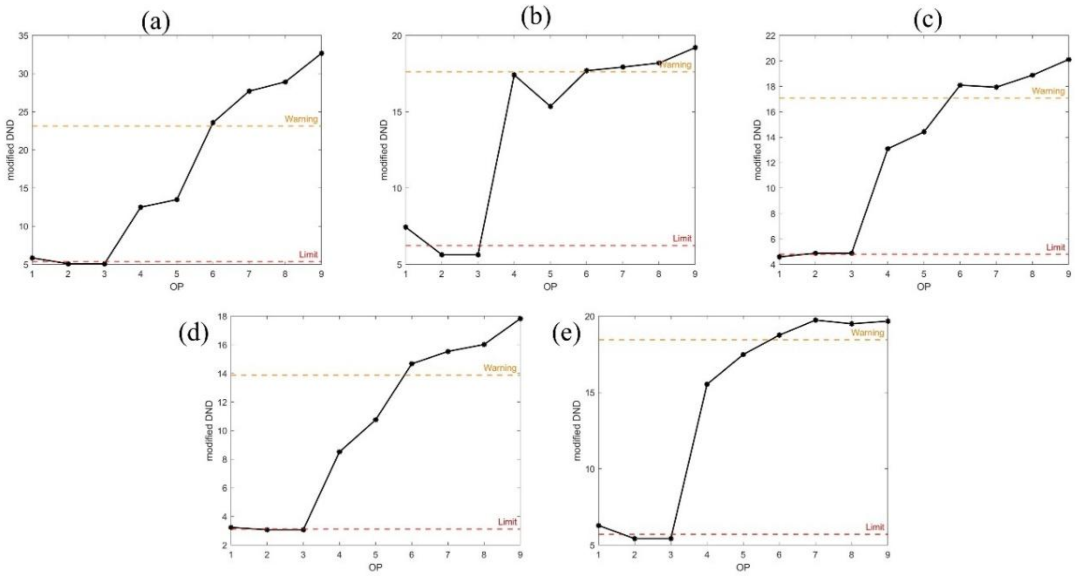

Figure C5. Trend plot with monitoring limits for N = 1200 rpm

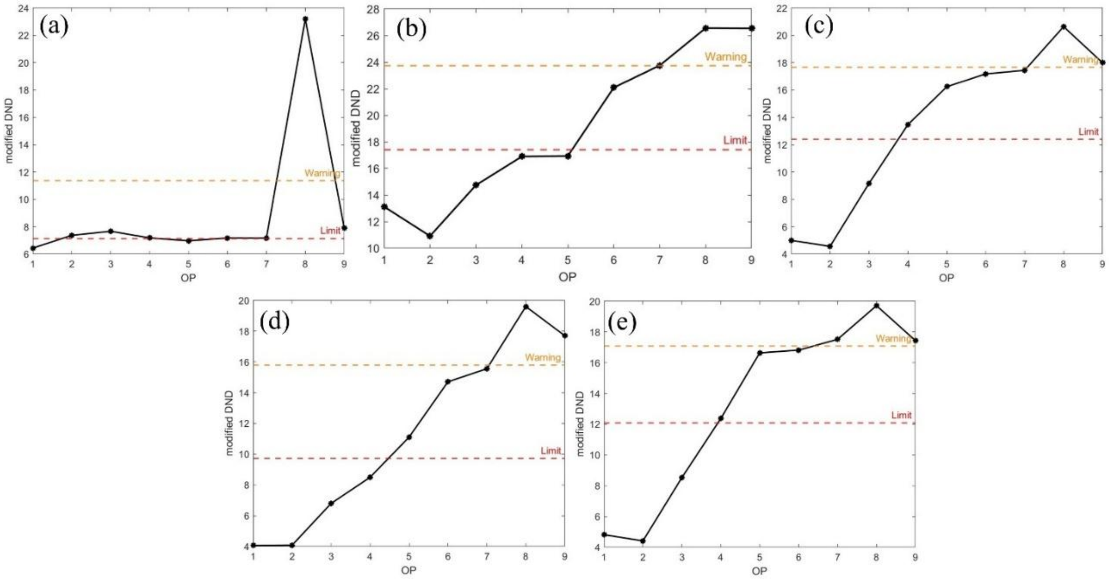

Figure C6. Trend plot with monitoring limits for N = 900 rpm

APPENDIX D – WATERFALL PLOTS FOR THE VIBRATION VELOCITY SIGNALS AT LOWER FREQUENCIES

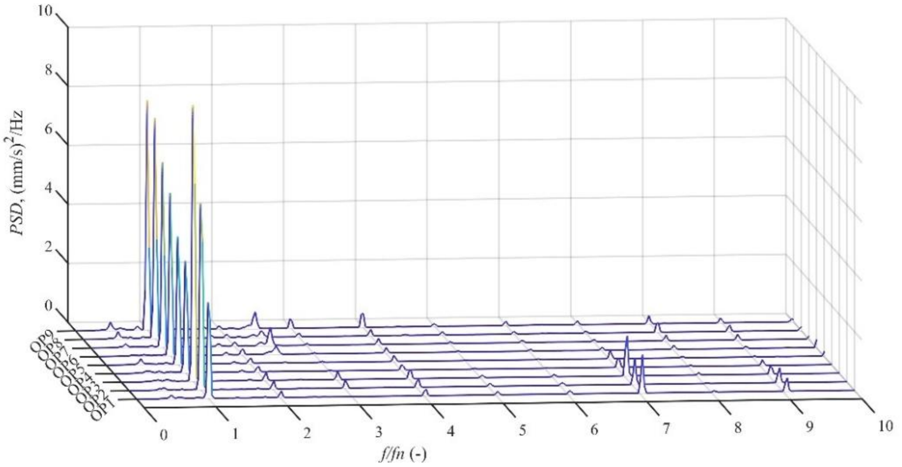

Figure D1. Horizontal vibration velocity waterfall plot for NDE bearing housing measurements at 1650 rpm

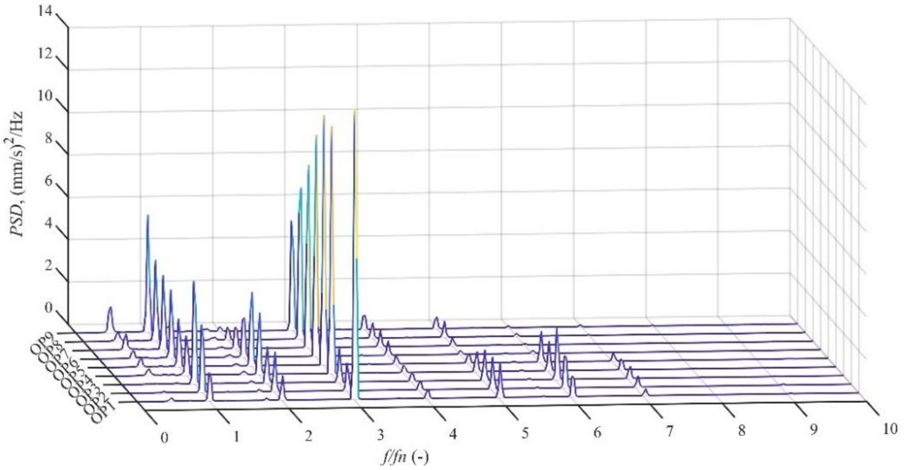

Figure D2. Vertical vibration velocity waterfall plot for NDE bearing housing measurements at 1650 rpm

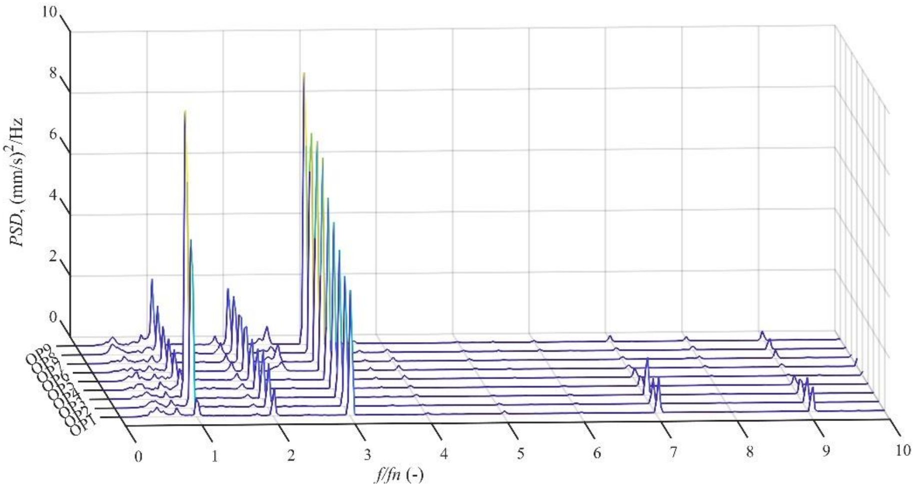

Figure D3. Horizontal vibration velocity waterfall plot for PAT outlet flange measurements at 1650 rpm

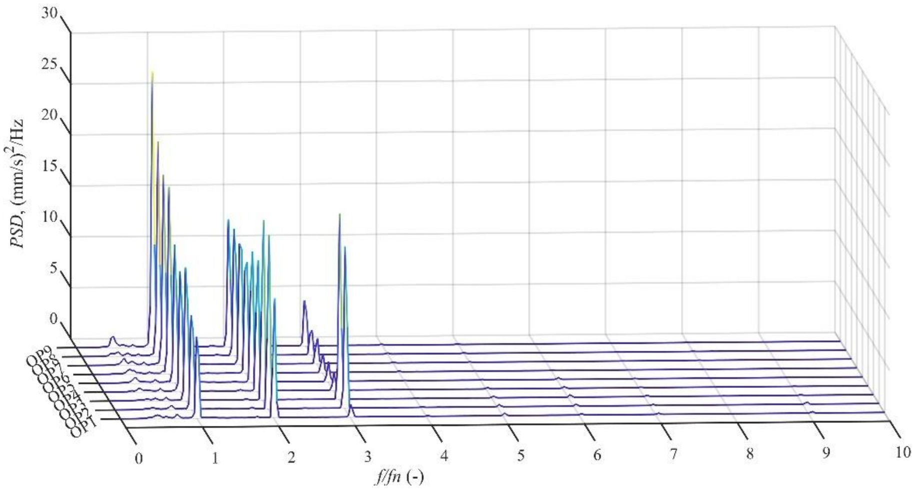

Figure D4. Vertical vibration velocity waterfall plot for PAT outlet flange measurements at 1650 rpm

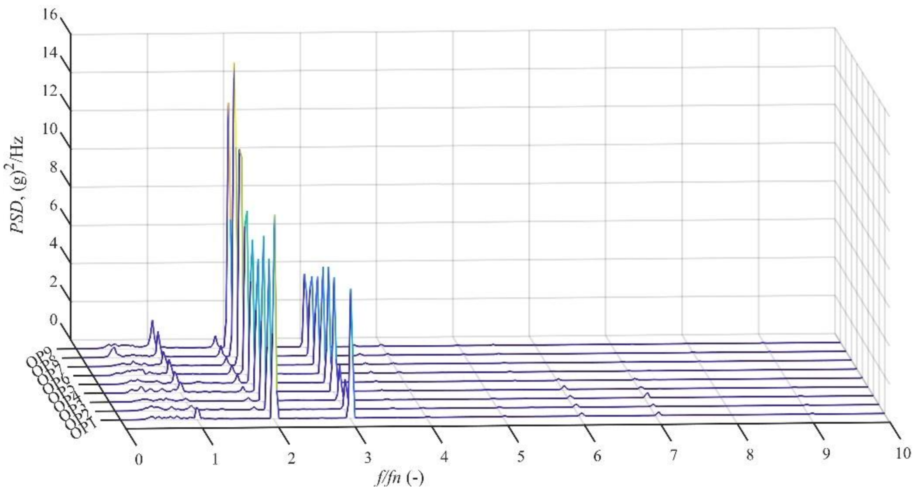

Figure D5. Axial vibration velocity waterfall plot for NDE bearing housing measurements at 1650 rpm

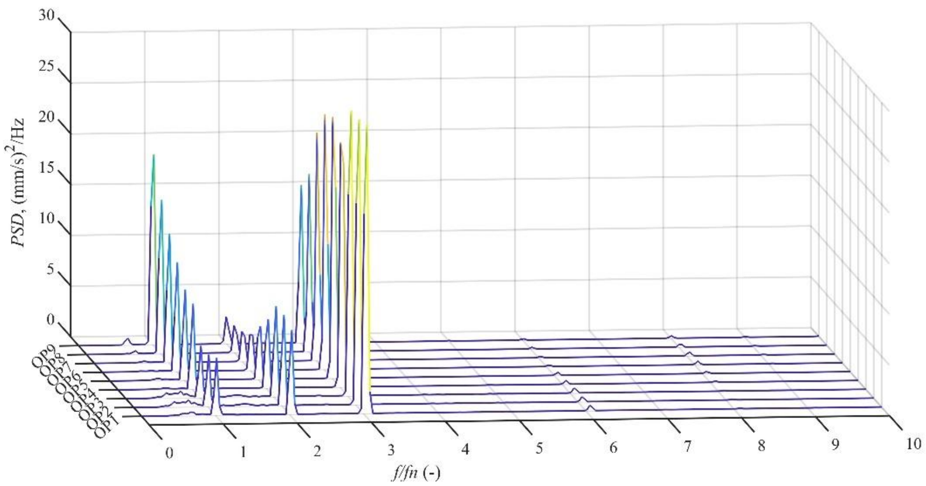

Figure D6. Horizontal vibration velocity waterfall plot for NDE bearing housing measurements at 1200 rpm

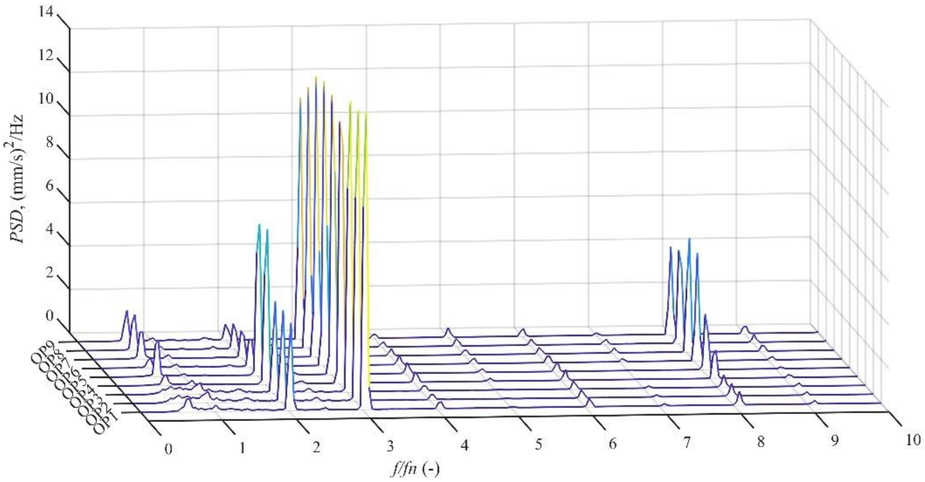

Figure D7. Vertical vibration velocity waterfall plot for NDE bearing housing measurements at 1200 rpm

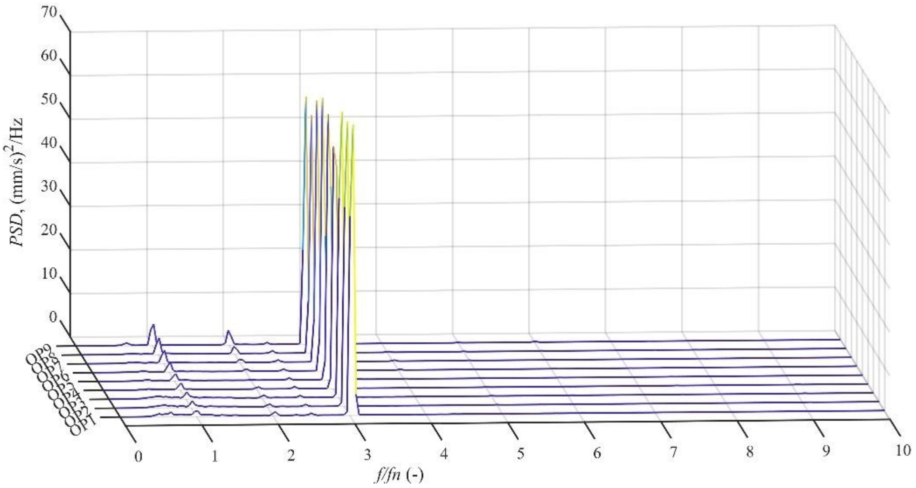

Figure D8. Horizontal vibration velocity waterfall plot for PAT outlet flange measurements at 1200 rpm

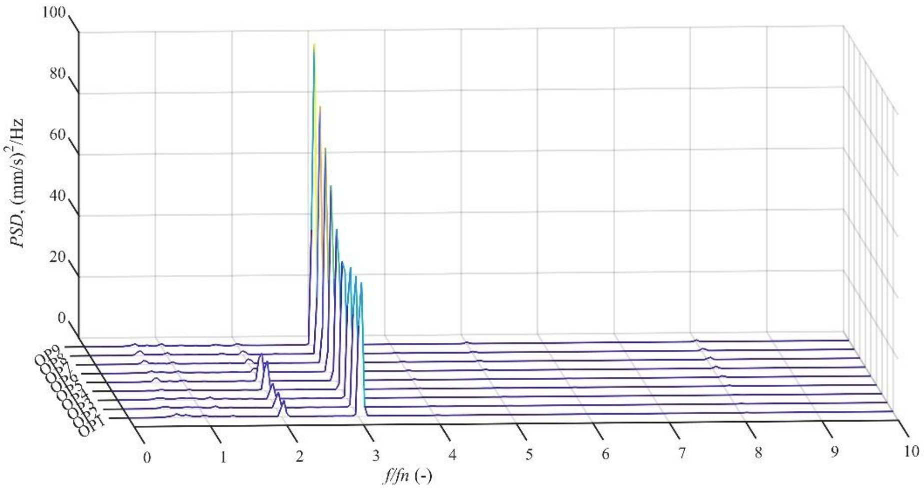

Figure D9. Vertical vibration velocity waterfall plot for PAT outlet flange measurements at 1200 rpm

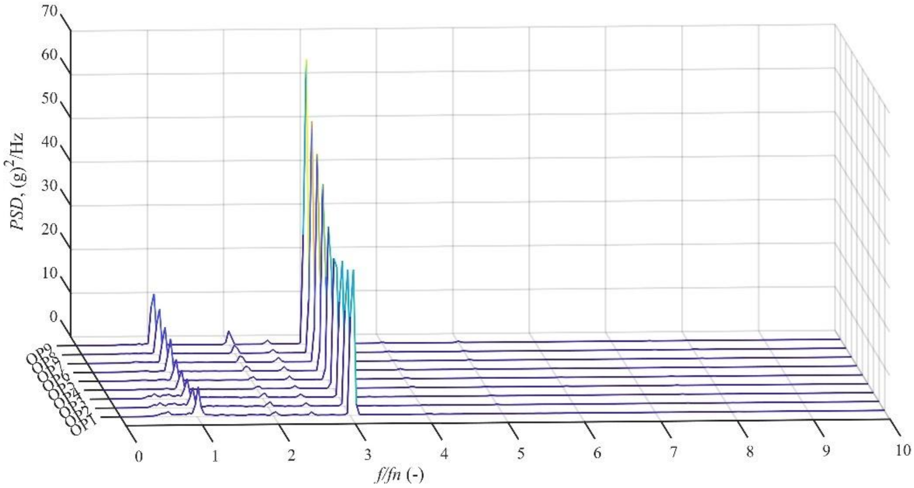

Figure D10. Axial vibration velocity waterfall plot for PAT outlet flange measurements at 1200 rpm

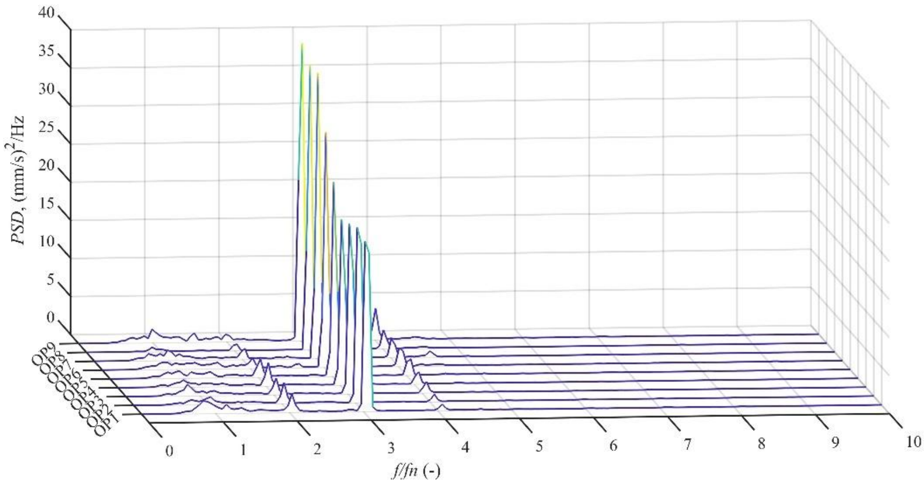

Figure D11. Horizontal vibration velocity waterfall plot for NDE bearing housing measurements at 900 rpm

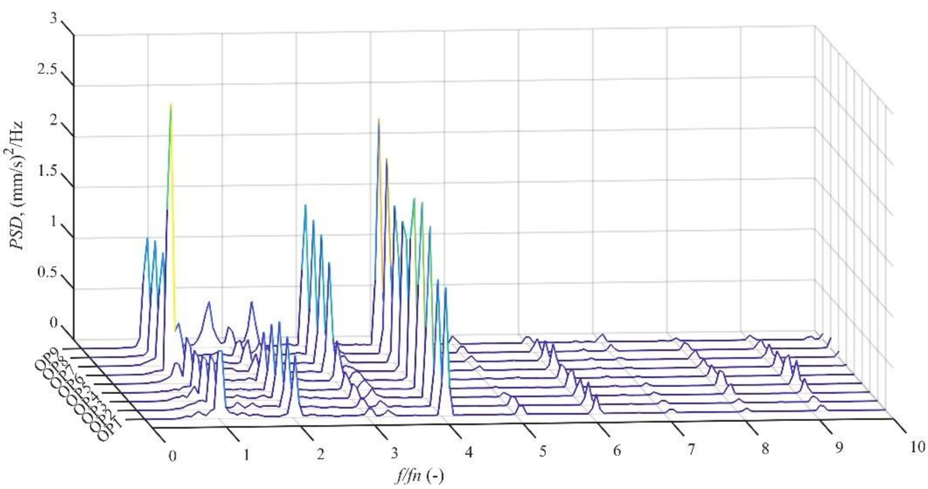

Figure D12. Vertical vibration velocity waterfall plot for NDE bearing housing measurements at 900 rpm

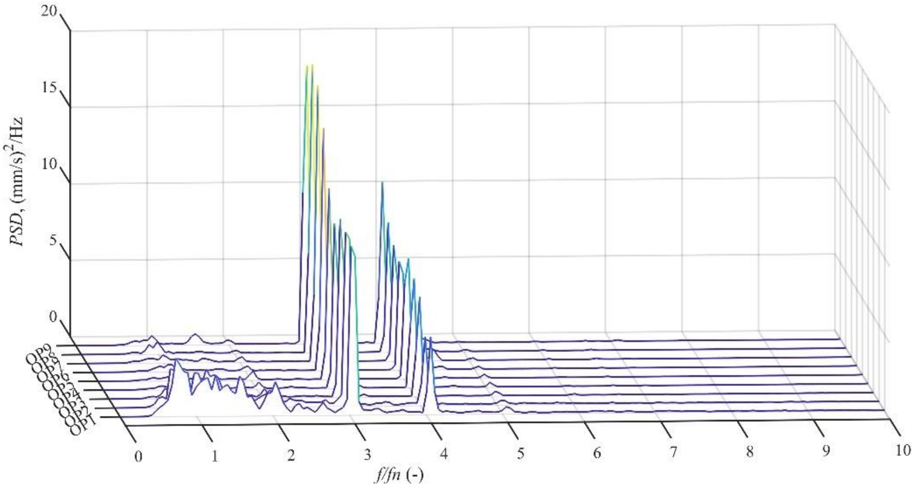

Figure D13. Horizontal vibration velocity waterfall plot for PAT outlet flange measurements at 900 rpm

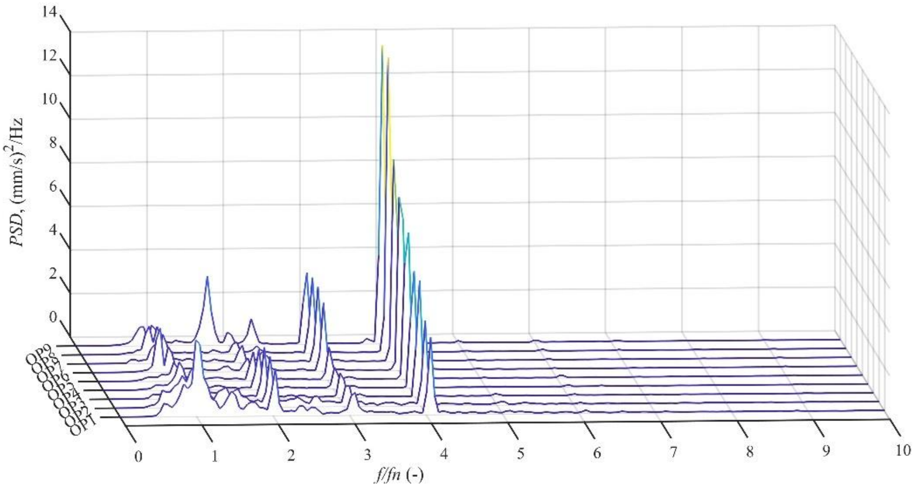

Figure D14. Vertical vibration velocity waterfall plot for PAT outlet flange measurements at 900 rpm

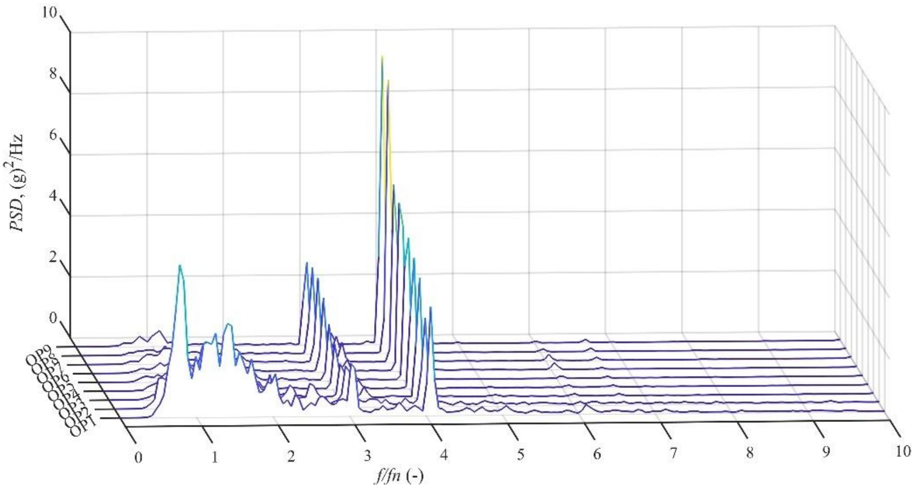

Figure D15. Axial vibration velocity waterfall plot for PAT outlet flange measurements at 900 rpm

APPENDIX E – WATERFALL PLOTS FOR THE VIBRATION ACCELERATION SIGNALS AT HIGHER FREQUENCIES

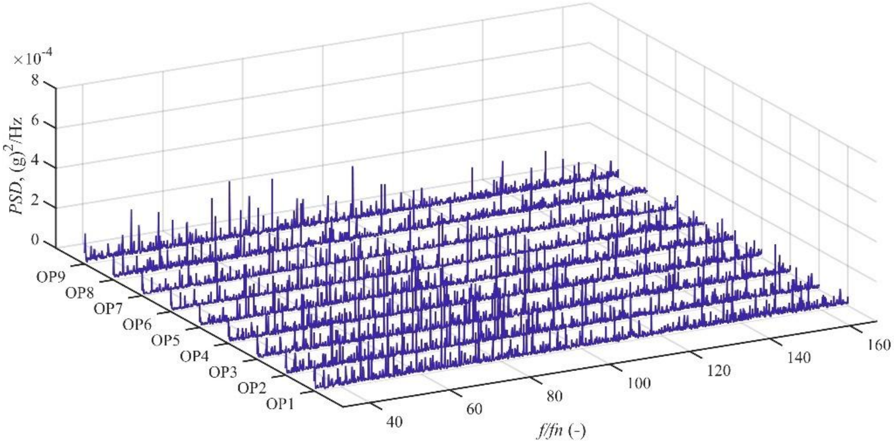

Figure E1. Horizontal vibration acceleration waterfall plot for PAT outlet flange measurements at 1800 rpm

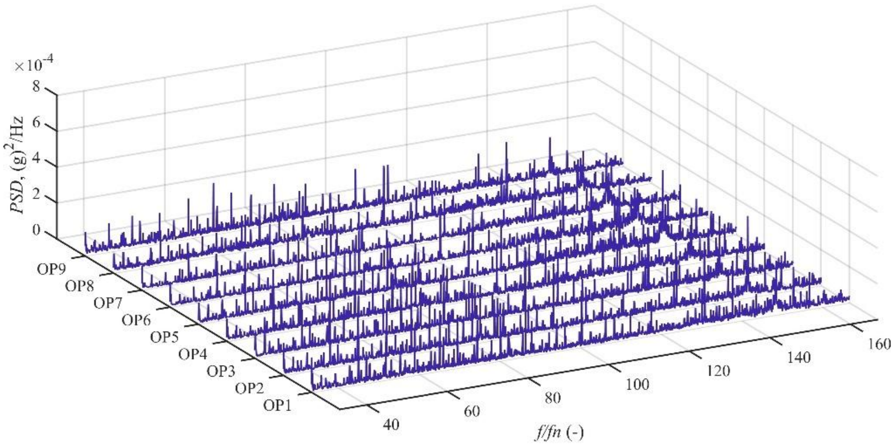

Figure E2. Vertical vibration acceleration waterfall plot for PAT outlet flange measurements at 1800 rpm

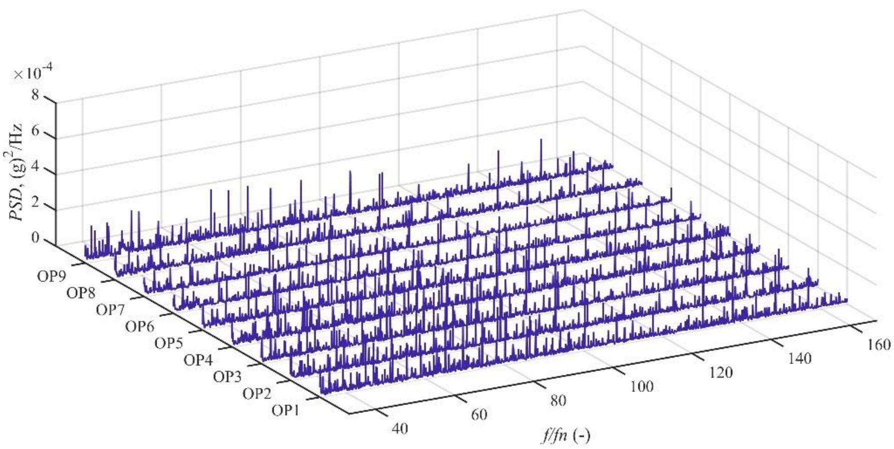

Figure E3. Axial vibration acceleration waterfall plot for PAT outlet flange measurements at 1800 rpm

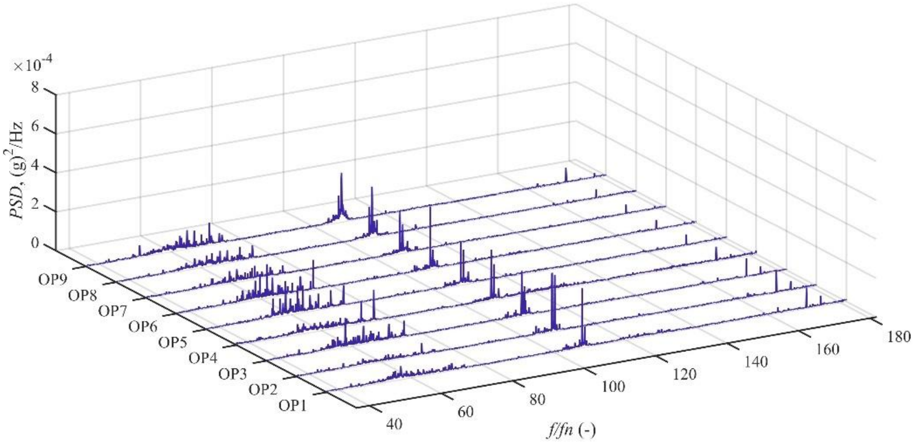

Figure E4. Horizontal vibration acceleration waterfall plot for NDE bearing housing measurements at 1650 rpm

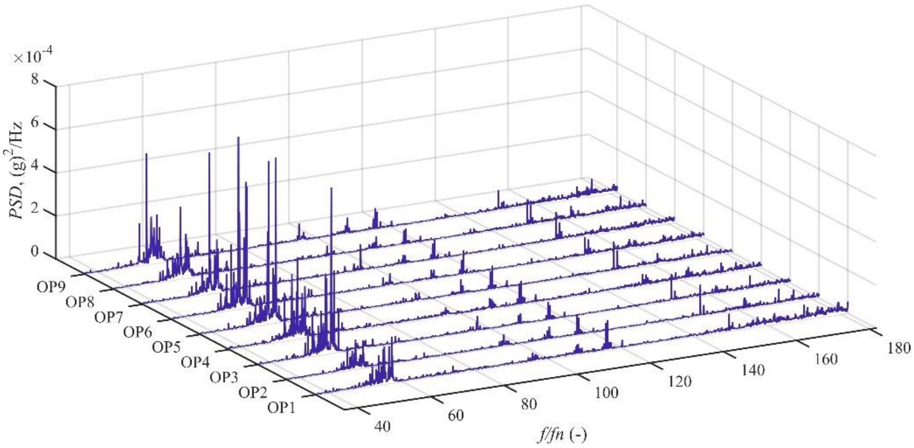

Figure E5. Vertical vibration acceleration waterfall plot for NDE bearing housing measurements at 1650 rpm

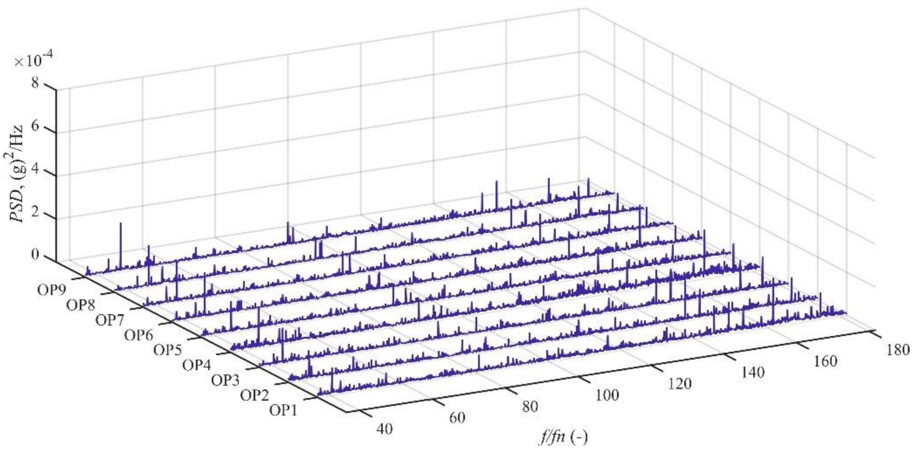

Figure E6. Horizontal vibration acceleration waterfall plot for PAT outlet flange measurements at 1650 rpm

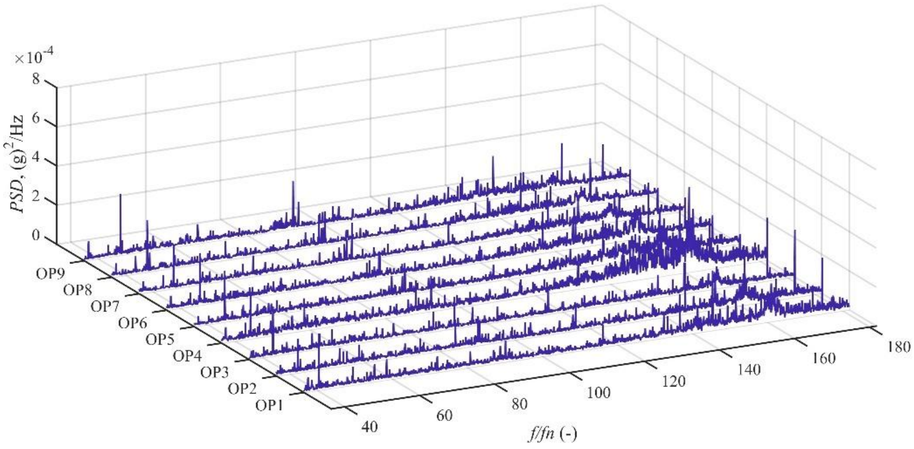

Figure E7. Vertical vibration acceleration waterfall plot for PAT outlet flange measurements at 1650 rpm

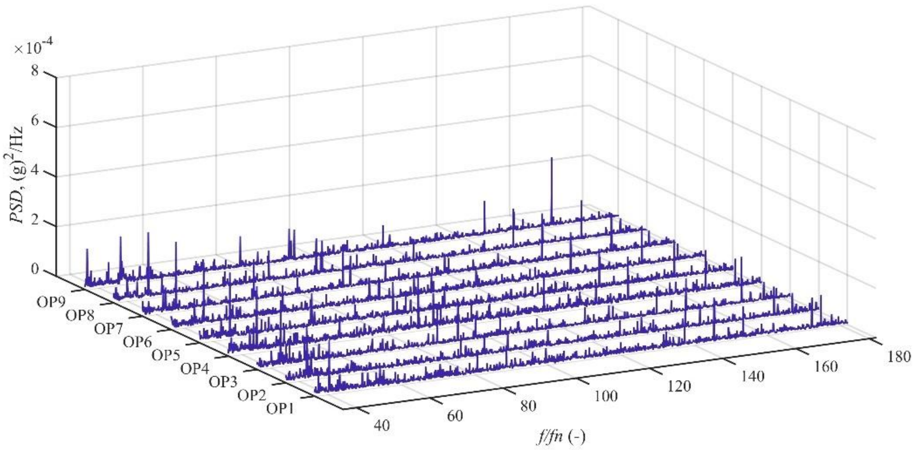

Figure E8. Axial vibration acceleration waterfall plot for PAT outlet flange measurements at 1650 rpm

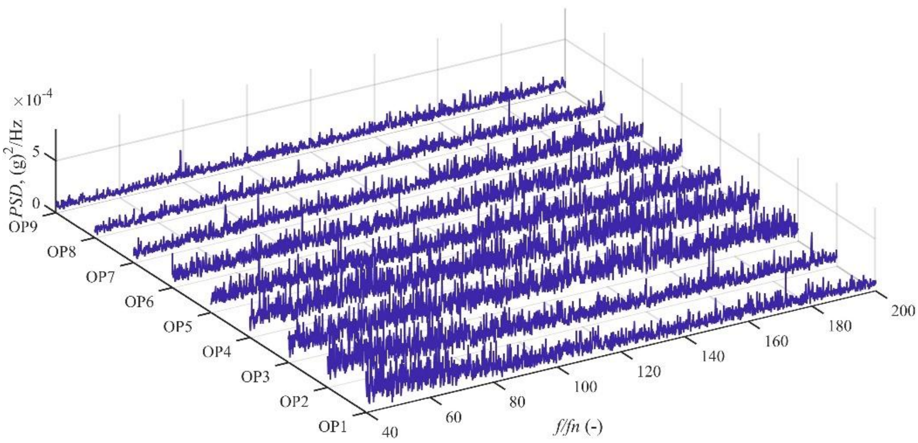

Figure E9. Vertical vibration acceleration waterfall plot for PAT outlet flange measurements at 1500 rpm

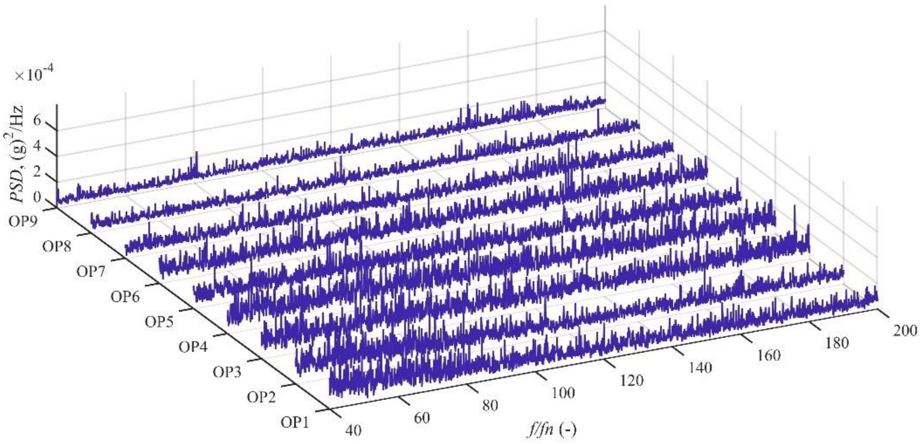

Figure E10. Axial vibration acceleration waterfall plot for PAT outlet flange measurements at 1500 rpm

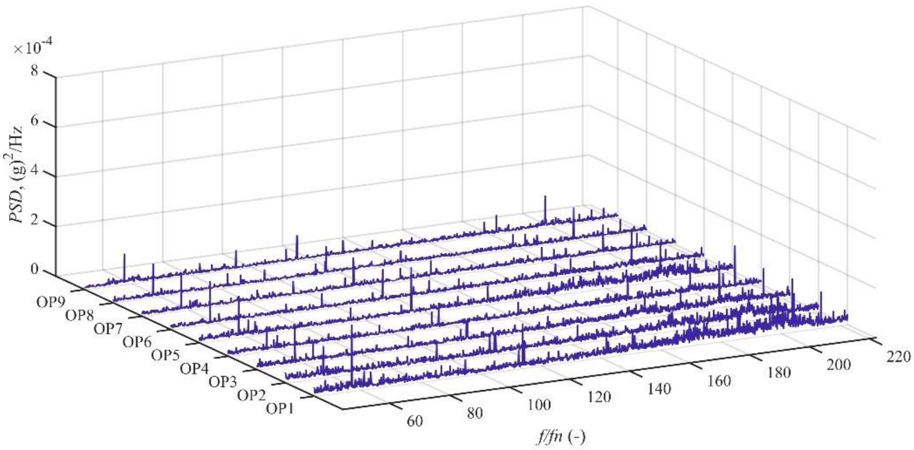

Figure E11. Horizontal vibration acceleration waterfall plot for PAT outlet flange measurements at 1350 rpm

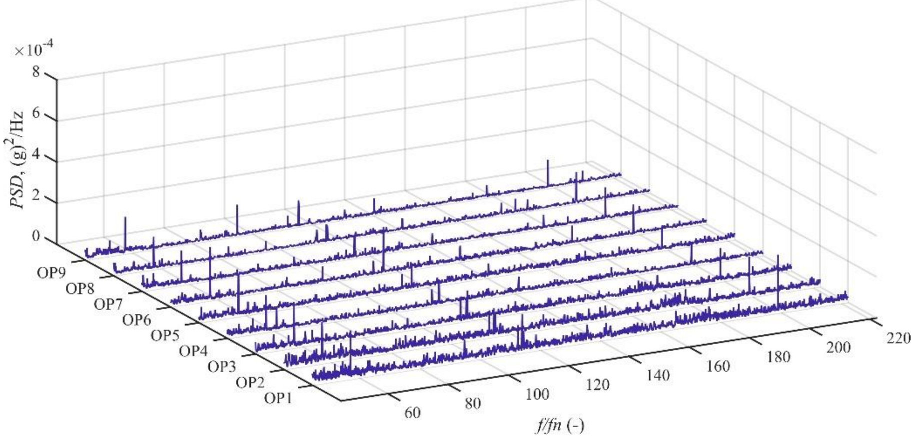

Figure E12. Axial vibration acceleration waterfall plot for PAT outlet flange measurements at 1350 rpm

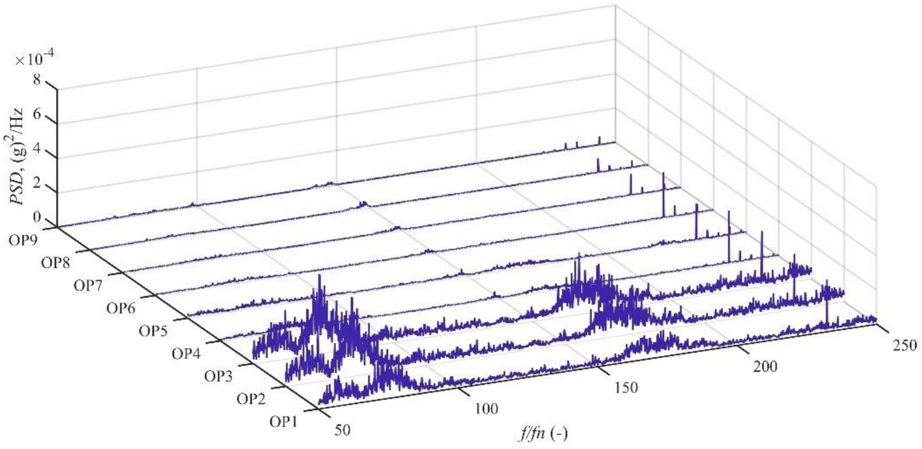

Figure E13. Horizontal vibration acceleration waterfall plot for NDE bearing housing measurements at 1200 rpm

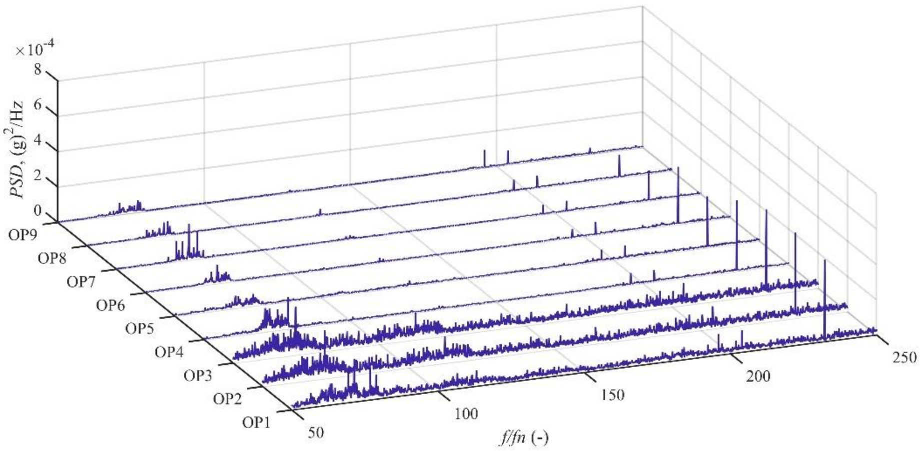

Figure E14. Vertical vibration acceleration waterfall plot for NDE bearing housing measurements at 1200 rpm

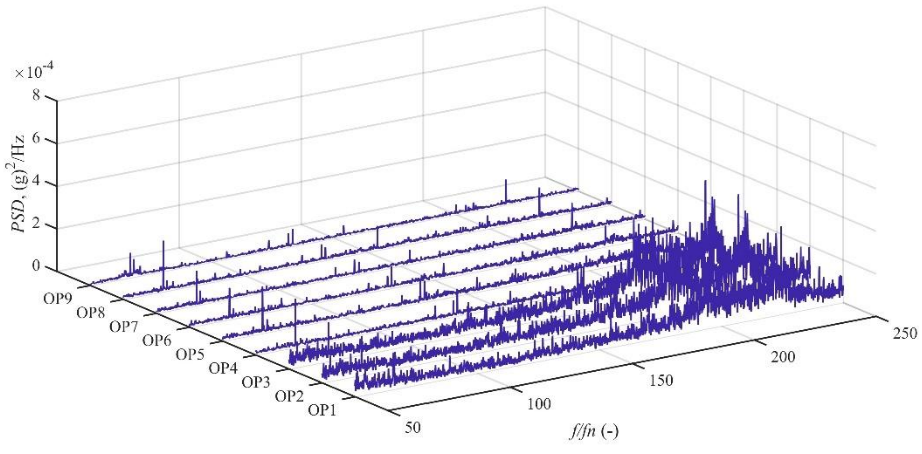

Figure E15. Horizontal vibration acceleration waterfall plot for PAT outlet flange measurements at 1200 rpm

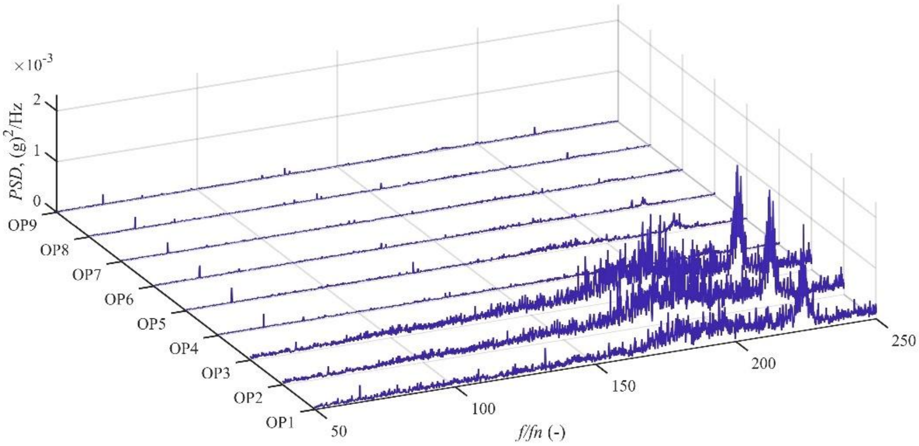

Figure E16. Vertical vibration acceleration waterfall plot for PAT outlet flange measurements at 1200 rpm

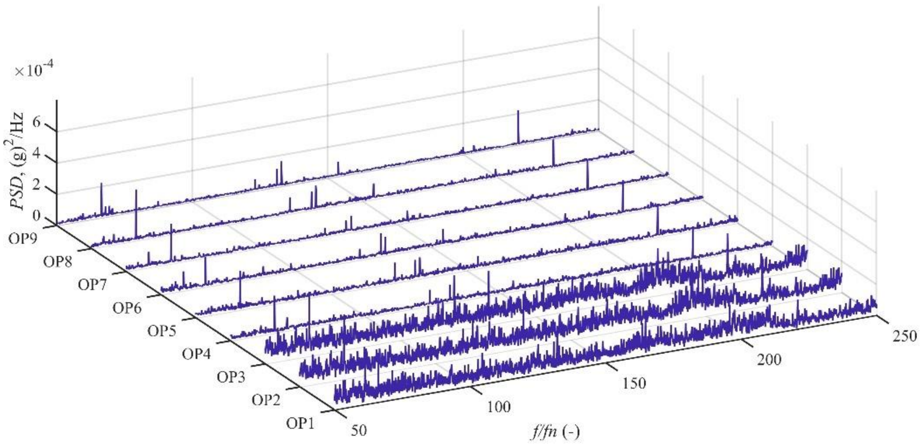

Figure E17. Axial vibration acceleration waterfall plot for PAT outlet flange measurements at 1200 rpm

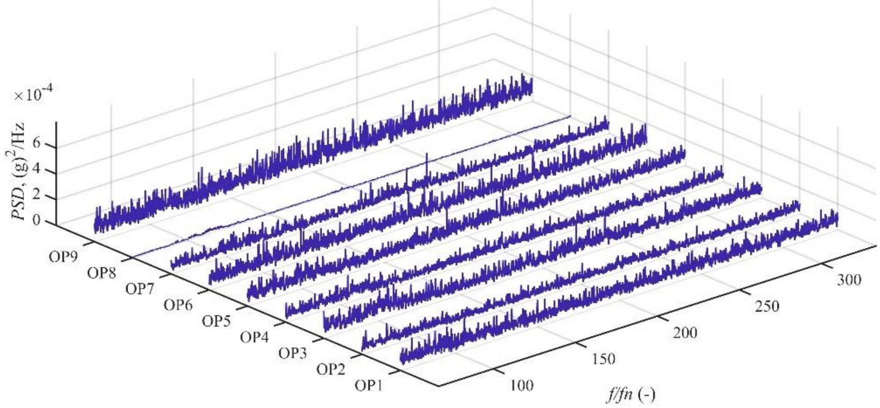

Figure E18. Horizontal vibration acceleration waterfall plot for NDE bearing housing measurements at 900 rpm

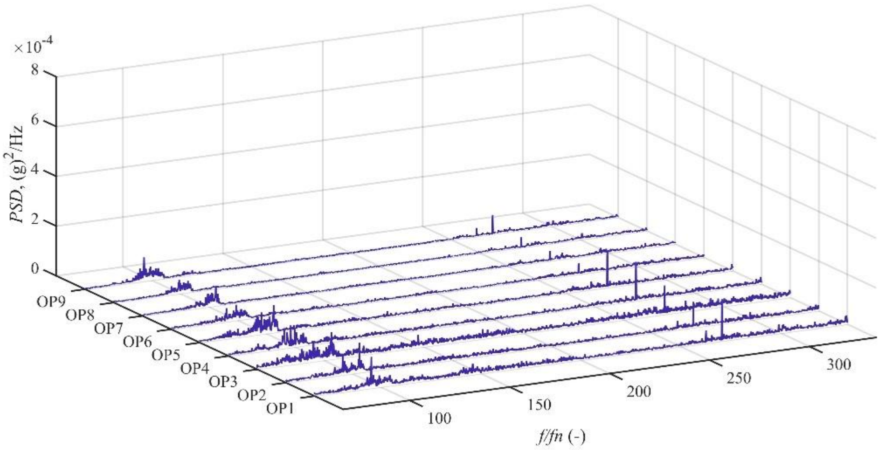

Figure E19. Vertical vibration acceleration waterfall plot for NDE bearing housing measurements at 900 rpm

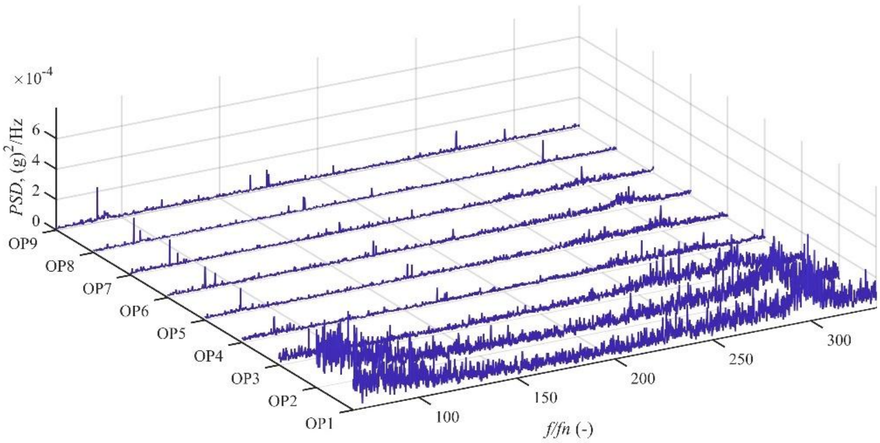

Figure E20. Horizontal vibration acceleration waterfall plot for PAT outlet flange measurements at 900 rpm

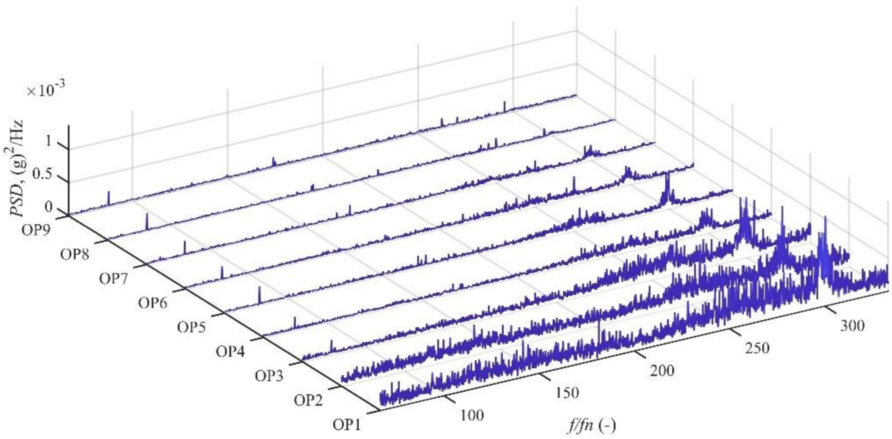

Figure E21. Vertical vibration acceleration waterfall plot for PAT outlet flange measurements at 900 rpm

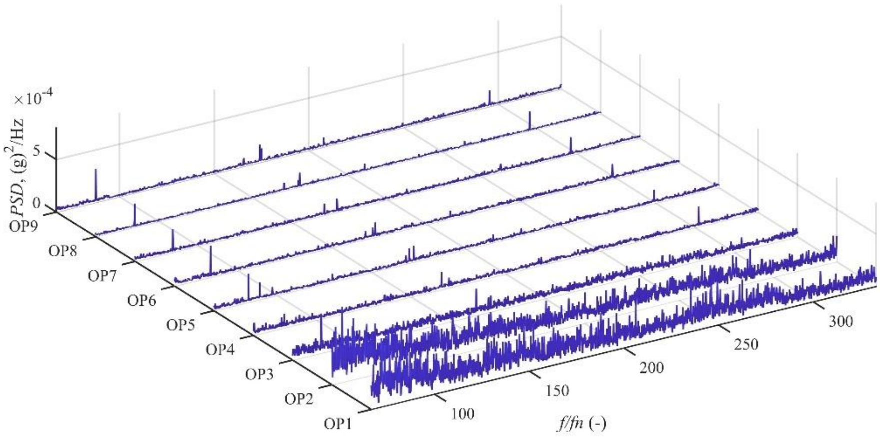

Figure E22. Axial vibration acceleration waterfall plot for PAT outlet flange measurements at 900 rpm

(This page is intentionally left blank)